Universidad de Cantabria

Departamento de Física Moderna

CSIC - Universidad de Cantabria

Instituto de Física de Cantabria

Estudio del Universo a Alto Redshift con Simulaciones de N-cuerpos

Memoria presentada por el Licenciado

Pier Paolo Ponente

dirigida por

Jose Maria Diego Rodriguez

2011

Jose M. Diego Rodriguez, Doctor en Ciencias Físicas y
Cientifico titular del Consejo Superior de Investigaciones Científicas,

CERTIFICA que la presente memoria

Estudio del Universo a Alto Redshift con Simulaciones de N-cuerpos

ha sido realizada por **Pier Paolo Ponente** bajo mi dirección.
Considero que esta memoria contiene aportaciones suficientes para construir la tesis Doctoral del interesado

En Santander,

Una parte di me
per sempre resterà qui
mentre la mia anima
vola sul fronte Est

Agradecimientos

Al primero al que quiero decir gracias es a mi jefe y director de tesis, Chema, quien me ha dado la oportunidad de empezar y acabar este proyecto de doctorado. Su ayuda en los primeros días en un nuevo país fue fundamental. También quiero darle las gracias a todos los colaboradores en este trabajo: Carlo, Ravi, Yago y Steffen.

Gracias a todo el grupo de cosmología por haberme enseñado tanto, por haberme apoyado en mi trabajo y sobre todo por permitirme que descubriera cómo de rica está la cocina cántabra.

Muchísimas gracias a todos aquellos que en estos años han sido mis compañeros de despacho, trabajo, casa y sobre todo amigos, tanto dentro como fuera del IFCA. No haré ninguna lista, ya que estoy seguro que me puedo olvidar de alguien y no quiero que se enfade. Vosotros sabéis quienes sois. Gracias por todo el tiempo pasado conmigo.

Además, gracias a todos los jugadores y jugadoras con los cuales he compratido pachangas, nunca en mi vida pensé que jugaría al fútbol. Gracias a mi equipo de Ultimate, si llegáis a leer estas palabras, nuestro grito de battalla siempre será "U.S. FENDISC!"

Un beso a Sabrina, que ha tenido la paciencia de esperarme durante casi tres años.

Grazie a tutti.

Universidad de Cantabria

Departamento de Física Moderna

CSIC - Universidad de Cantabria

Instituto de Física de Cantabria

Estudio del Universo a Alto Redshift con Simulaciones de N-cuerpos

A dissertation submited for the conferment of

the degree of Doctor of Philosophy in Physics by

Pier Paolo Ponente

2011

Prologue

The main motivation of this thesis is to study the distant Universe through alternative windows which are emerging in the most recent years. At high redshift, the large scale structure (LSS) undergoes an interesting phase called the reinoziation where the neutral matter gets ionized around the first generation of stars. This ionized medium can emit interesting signals among which I am interested in the weak free-free emission from diffuse gas and galaxy clusters present in the Universe after the era of the reionization. N-body simulations of this distant epoch can help understand the properties of the free-free and other siganls emerging from the reionization time. The free-free emission has been largely ignored in the literature with very few works paying attention to it. Part of this thesis will focus also on synchrotron signal from normal galaxies. Recent developements in technology start to reach the sensitivity needed to discern this weak signals from other more predominant ones. Also, my thesis will focus on the possible observational evidence of this signal, in particular in the excess signal found by the ARCADE2 experiment at radio wavelengths that could be partially explained by free-free emission from the reionization time.

ARCADE2 is a balloon-borne mission whose goal is to measure the radiobackground at frequencies lower than thiose explored by past and current Cosmic Microwave Background experiments. This regime of low frequencies are sensitive to interesting physical phenomena including some that coccured after the inflationary time and before the matter-radiation decoupling. The results of the ARCADE2 are surprising, with a significant excess of signal over previous estimations of the microwave-radio background temperature distortion (as measured by COBE/FIRAS). The authors claim that the results are free from systematics and that the excess signal is purely extragalactic, suggesting that free-free and synchrotron emissions could be the cause. This thesis explores both possibilities and throughs some light into this unsolved puzzle. The physics

involved in the sysnchrotron is far more complicated than in the free-free caee, needing a specific model for the Initial Mass Function (IMF), for the cosmic star formation rate (SFR), the rate of supernovae production and how they contribute to the magnetic field in galaxies. For these reasons, I concentrate my efforts on building a phenomenological model for the synchrotron emission, who shares some underlying mechanisms with the free-free model. The model is the first one (or one of the first ones) that uses the SFR to estimate the signal observed by ARCADE2 .

To achieve my goals, I make use of both analytical models (like the mass functions of Press-Schecther and Sheth-Tormen) and numerical simulations (making my own simulations with the GADGET-2 code).

The study of the radio Universe in the low GHz band offers a new window to explore the high redshift Universe. The results of my thesis will be relevant for future facilities such as ALMA as it deals with signals that could be potentially be studied with this facility.

My thesis work is completed with a study of the lensing problem. Gravitational lenses are an interesting tool to understand our Universe. On one hand they offer one of the best scenarios to see dark matter through their gravitational effects and on the other hand thay act as magnifying lenses that enhanced the flux of the background galaxies making it easier to detect them. This second feature is particularly interesting to study the first population of galaxies that emerge after the reionization time. I explore the capabilities of the gravitational mass reconstruction by studying one partiocular case that has triggered great debate in the last years, the galaxy cluster CL00254 and its alleged ring of dark matter. I explore the possible systematics in the lensing reconstruction of this cluster.

The work is organized as follows: in Chapter 1, I will give a short review of the basic cosmological concepts, the notions of the different distances involved, the mechanisms for the thermal and non-thermal emissions and a description of the standard geometry underlying the gravitational lensing. In the same chapter, I will provide an introduction to cosmological simulations and the codes used. In Chapter 2, I will treat the free-free emission, with the comparison between the N-body simulations and the analytical approach. Chapter 3 will extend radio signal with the synchrotron emission. Chapter 4 will be entirely dedicated to *non-parametric* cluster mass reconstruction using strong and weak lensing.

Finally, in Chapter 5, I will present the conclusions for the previous chapters. At the end of the thesis, a summary in *idióma castellano*, about the most important aspects and results, is given.

Contents

List of Figures

List of Tables

CHAPTER 1

Introduction

The first chapter of this thesis has the task to introduce the most important arguments that are necessary to understand the works presented in Chapter 2, 3 and 4. The task is non-trivial, because the topics in cosmologly and astrophysics are larger in number ans strictly correlated each others. I prefer to focus on the formation of structures, with a minor description of the radiation component and to leave outside all the properties of the anisotropies of the Cosmic Microwave Background.

I have found in the book of Peebles *Principles of Physical Cosmology*, [1], a balanced compromise between easiness and accuracy, with a very deep excursus in the history of cosmology. Naturally, some arguments have been integrated with other sources, [2–6].

The Chapter starts with the concept of the *Large Scale Structure* with some historical remarks. It follows with the introduction of the space-time metric describing distances in a static universe, then the same concepts are applied to a dynamical universe with different components. Will be given a syntetic description of the thermal history of the Universe, with the role of radiation and the introduction to the Cosmic Microwave Background. A section will be dedicated to the dark matter paradigm and to alternative theories. After the discussion on dark matter, the statistic of the density field is is introduced, along with the halo function and the basics to understand a cosmological simulation. A brief section is dedicated to the basic concpets of gravitational lensing, while the last section will focus on the radiation processes from ionized medium.

1.1 The Large Scale Structure of the Universe

This first section is introducing the *Large Scale Structure* through the historical remarks that arose at the beginning of the Twentieth century. That was not a case that the knowledges about the nature of the Universe were expanding first under the pulse of the theory of General Relativity and then with the discovering of distant galaxies. The observations were the proof for the theory and the theory was changing after the feedbacks from observations. Nowadays, the Large Scale Structure is well understood within the Standard Model for structure formations, that relies on accepted paradigms like inflation, dark matter and dark energy.

1.1.1 The meaning of *Large Scale Structure*

The term *Large Scale Structure* was introduced in astronomy in the second decade of the twentieth century. At that time astronomers were only familiar with the concept of *local Universe*, since their observations were limited to the Milky Way. At the beginning of the past century, Albert Einstein proposed his theory on the general gravitation, General Relativity (GR). He was strongly influenced by Ernst Mach (1838 - 1916) who claimed the non-existence of the Newtonian concept of the absolute motion. An observer could only sense an inertial frame in the presence of a fixed reference frame. Apparent forces produced by the inertia have not an absolute character, but related to fixed masses. In General Relativity, this was the concept of the line element connecting two events,

$$ds^2 = \sum_{ij} g_{ij} dx^i dx^j \tag{1.1.1}$$

where the differences in the space-time dx^i, dx^j and the metric tensor g_{ij} depend on the coordinate labels. The metric tensor has ten independent functions, and these are known as Einstein's *field equation*, describing the matter distribution acting like the generator of the space-time curvature.

A special case of the metric tensor are the Minkowski coordinates,

$$\eta_{ij} = (1, -1, -1, -1) \tag{1.1.2}$$

for $i = j$ and 0 elsewhere. This metric locally describes a Newtonian inertial frame and, more importantly, is the unique non-singular spherically symmetric

solution to Einstein's field equations in absence of matter. That is, the metric can extend indefinitely far away from the matter, defining absolute inertial frames. This contradiction was slowly solved with the help of Willem de Sitter in 1916, that suggested to Einstein a way to pass from the Minkowski form $g_{ij} \sim \eta_{ij}$ to a metric tensor that would not define an inertial frame far from matter. But where is it supposed to exist such passage? De Sitter argued that there is no change due to the fixed stars and the objects called at that time *spiral nebulae*, since there were no gravitational effects observed in their spectra. Einstein accepted the ideas of de Sitter, but he was brought to think to the existence of exotic matter at the boundaries of the Universe, that was not observed. But soon, he proposed another scheme: there was no mass at the boundaries of the Universe, but the whole Universe is filled, *homogeneously*, with matter. The matter density itself is responsible to curve the space-time and leave, locally the Minkowski form, unchanged.

That was a ground-breaking idea for the astronomers. The concept of the Universe and its size and geometry was strongly limited by the observations. For example, Eddington in 1914 titled his book *Stellar Motions and the Structure of the Universe* and described the main features of the Milky Way, considered like a structure filled with stars but alone in an empty space. The objects referred as spiral nebulae where thought to belong to the same structure, and only in a later moment they were identified as galaxies, replicas of the Milky Way. Nonetheless, the following two decades were critical for the affirmation of the concept of homogeneous Universe on large scale: surveys revealed a larger number of objects in increasing distance, that were definitely recognized as galaxies of stars (e.g. Fig. 1.1 where is shown the map of Charlier 1922, [7]). Alongside, an uniform and extended matter distribution drastically simplified the mathematical problem of solving the field equations of GR.

A complementary concept that came embodied in the homogeneity of the Universe and not violating Mach's principle is the one regarding the *isotropy*: there is no observer in privileged reference systems, nor absolute direction for the bulk motion of the galaxies. *The Einstein's Cosmological Principle* (Milne, 1935) is nowadays accepted as a condition that is consistent with the observations.

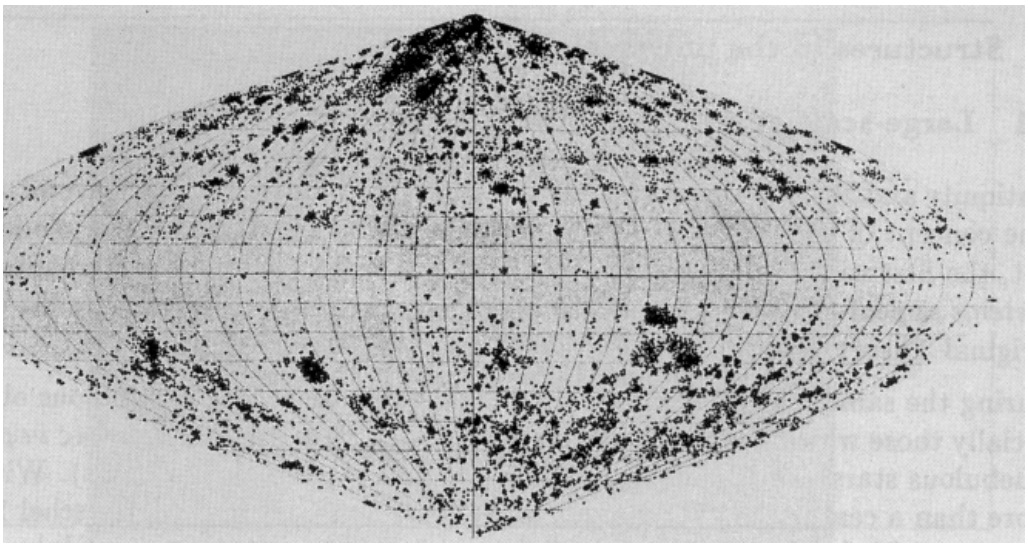

Figure 1.1 Map of the nebulae, from Charlier (1922), [7].

1.1.2 The Hubble's experience

Common sense would suggest us a question: how is it possible to obtain a space distribution of matter if we can only observe a two-dimensional picture? The empirical law that links the flux of an object to its distance from us, is due to Edwin Hubble (1889 - 1953). Hubble applied basic concepts from surveys of stars to galaxies, essentially the relation between the intrinsic luminosity of the source and the observed energy flux:

$$f = \frac{L}{4\pi r^2}\,, \tag{1.1.3}$$

where r denotes the distance from the observer. If galaxies had the same brightness L, then higher fluxes f would correspond to closer distances r. In astronomy, fluxes and brightnesses are expressed through the quantity *magnitude*:

$$m = -2.5 \log f + \text{ constant} \tag{1.1.4}$$

is the apparent magnitude and

$$M = -2.5 \log L + \text{ constant} \tag{1.1.5}$$

is the absolute magnitude. From 1.1.3 one could derive the relation called the *distance modulus*:

$$m - M = 5 \log r_{\text{Mpc}} + 25. \tag{1.1.6}$$

Hubble thought, as opposedto stars, galaxies were distributed uniformly on average. The number of galaxies emitting fluxes higher than f is proportional to f:

$$N(>f) \propto f^{-3/2}, \tag{1.1.7}$$

that combined with the Eq. 1.1.4 yields the differential counts for homogeneous mean distribution of galaxies:

$$\frac{dN(m)}{dm} \propto 10^{0.6m}. \tag{1.1.8}$$

Hubble, [8], proved that the galaxies counts agree with the power law of Eq. 1.1.7, demonstrating the uniform distribution on large scales.

1.1.3 The standard definition of the Redshift

The concept of *redshift* is fundamental for the description of cosmological distances and times. The basic formulation, indeed, relies on the observed frequencies. The redshift z of an object is the fractional *Doppler shift* of its emitted light resulting from radial motion, [5]

$$z \equiv \frac{\nu_e}{\nu_0} - 1 = \frac{\lambda_0}{\lambda_e} - 1 \tag{1.1.9}$$

where ν_e and λ_e are the emitted frequency and wavelength, and ν_0 and λ_0 are the observed ones. In Special Relativity, the redshift is related to the radial velocity of an object:

$$1 + z = \frac{\sqrt{1 + v/c}}{\sqrt{1 - v/c}}. \tag{1.1.10}$$

The radial velocity v is the sum of two components: the peculiar velocity $v_{\rm pec}$, that is related to the proper motion of an object respect other objects in the neighborhood and the *Hubble flow* motion, due to the stream caused by the expansion of the Universe. The velocity due to the mean flow is directly proportional to the distance, with a factor known as the *Hubble constant*, H_0:

$$v = H_0 d \tag{1.1.11}$$

The Hubble constant H_0 refers to the value it has at the present time (the subscript 0 is always referred to the present time, except where differently stated), as it is expected to change with time. The velocity v is expressed in km s^{-1}, the distance d is expressed in Mpc, hence H_0 is expressed in units of km s^{-1} Mpc^{-1}.

Usually, in the literature, any observable related to H_0 is given as a function of a dimensionless constant, h

$$h = \frac{H_0}{100 \text{ km sec}^{-1} \text{ Mpc}^{-1}}. \tag{1.1.12}$$

In the last few decades, the value of H_0 has been constantly refined, due to the possibilities to measure it with different techniques (measurement of Cepheid variable stars, gravitational lensing, rich catalogs of distant objects, microwave relic radiation). All the techniques point to a concordance value for H_0, that is $H_0 = 72 \text{ km sec}^{-1} \text{ Mpc}^{-1}$ (e.g. the value reported by the released 7-year WMAP data is $h = 0.71 \pm 0.025$, [9]). Two related constants can be easily derived from H_0: the *Hubble time*

$$t_H \equiv \frac{1}{H_0} = 9.78 \times 10^9 \, h^{-1} \text{ yr} \tag{1.1.13}$$

and the *Hubble distance*

$$D_H \equiv \frac{c}{H_0} = 3000 \, h^{-1} \text{ Mpc}. \tag{1.1.14}$$

In next section I will give the notion of redshift as related to the expansion of the Universe, that is not possible to introduce without the introduction of the metric describing the topography. Nonetheless, the notion of redshift is basically the on here presented, since it is related to quantities directly observable as the curves of light of emitting objects. Only after some assumptions, redshift can been used as a measure of the expansion of the Universe.

1.2 The Static Universe

1.2.1 The line element

Describing the geometry of the Universe and the path that any observer follows within it is a non trivial exercise for anyone's mind, due to the high degree of abstraction needed to imagine a four-dimension coordinates system. One can divide the spatial part from the time part, threat them separately and then blend them in a unique metrics.

Since one can always use the Minkowski metric tensor in our neighborhood, we can see how to separate the form in Eq. 1.1.1 in a time part and a space part. Consider some observers that move along with the mean flow of the matter in the Universe. Each observer has assigned a set of three numbers, x^α, $\alpha = 1, 2, 3$

and each observer is carrying a clock. If we assign to an event the three numbers of the observer passing for that event and the time coordinate $x^0 = t$, where t is the time measured by the clock that observer is carrying, then we have assigned a four coordinates system to the space-time. Two events that belong to the same world line of a comoving observer will have only the time coordinate changing with the amount dt, whose metric is

$$dt^2 \equiv ds^2 = g_{ij}dx^i dy^j = g_{00}dt^2. \tag{1.2.1}$$

The last equality derives from the statement that two events separated only by time interval have dx^α $(\alpha = 1, 2, 3)$, and we have $g_{00} = 1$. The off-diagonal elements have to be zeros, $g_{0\alpha} = 0$, since for the Einstein's cosmological principle, there is no preferred direction for $g_{0\alpha}$ to point. The line element can thus be rewritten in the form

$$\begin{aligned} ds^2 &= dt^2 + g_{\alpha\beta}dx^\alpha dx^\beta \\ &= dt^2 - dl^2 \end{aligned} \tag{1.2.2}$$

with dl^2 is the proper spatial separation between events at the same world time, t.

Now we must use the above extrapolation, thinking of the space-time as a four-dimension space. A line element on a three-dimensions spehere is the line connecting two points on a surface, whose equation is

$$R^2 = x^2 + y^2 + z^2, \tag{1.2.3}$$

the same has to be thought for a three-dimensions surface embedded in a four-dimensions space:

$$R^2 = x^2 + y^2 + z^2 + w^2, \tag{1.2.4}$$

with the line element described by

$$dl^2 = dx^2 + dy^2 + dz^2 + dw^2. \tag{1.2.5}$$

Now, renaming the three independent space variables $r^2 = x^2 + y^2 + z^2$, the fourth variable is fixed by the relation $w^2 = R^2 - r^2$, whose differential leads to

$$dw = \frac{rdr}{(R^2 - r^2)^{-1/2}}. \tag{1.2.6}$$

Introducing the last equation in the Eq. 1.2.5, we obtain the general form of four-dimensions line element in Cartesian coordinates

$$dl^2 = dx^2 + dy^2 + dz^2 + \frac{r^2 dr^2}{R^2 - r^2}. \tag{1.2.7}$$

Common sense would suggest that a set of polar coordinates $r,\ \theta,\ \phi$ is more appropriate to describe a spherical surface. Substituting the usual relations

$$\begin{aligned} z &= r\cos\theta, \\ x &= r\sin\theta\cos\phi, \\ y &= r\sin\theta\sin\phi, \end{aligned} \tag{1.2.8}$$

in Eq. 1.2.7, we finally get the space line element for a four-dimensional curved surface:

$$dl^2 = \frac{dr^2}{1 - r^2/R^2} + r^2\left(d\theta^2 + \sin^2\theta d\phi^2\right). \tag{1.2.9}$$

Introducing the time coordinate is straightforward, giving the complete expression for the line element in a static Universe

$$ds^2 = dt^2 - \frac{dr^2}{1 - r^2/R^2} + r^2\left(d\theta^2 + \sin^2\theta d\phi^2\right). \tag{1.2.10}$$

In the next subsections I will introduce some basic equations on the dynamics of Einstein's model, then I will introduce the concept of scale factor that combined to Eq. 1.2.10 will give a more precise description of the metric in an expanding Universe.

1.2.2 Dynamical properties of Einstein's model

We ha ve seen that the metric tensor $g_{ij}(x)$ is the entity describing distance between elements in the space-time. The Einstein's field equation (EFE) is the equation describing the behavior of the metrics in the presence of matter

$$R_{ij} - \frac{1}{2}g_{ij}R = 8\pi G T_{ij}. \tag{1.2.11}$$

The first term, the second-order tensor R_{ij} is the Ricci tensor and describes the amount of deviations of a curved surface in a generic Riemann manifold from the same curved surface in Euclidean space. The quantity R is the Ricci scalar and in this case is the trace of the Ricci tensor. On the right hand of the equation we have the stress-energy tensor. It describes the flux of the energy density and momentum in the space-time. Usually, it has sixteen (4×4) elements, but in the local Minkowski coordinate system in which the fluid is at rest, it has the form

$$T_{ij} = \begin{bmatrix} \rho & 0 & 0 & 0 \\ 0 & p & 0 & 0 \\ 0 & 0 & p & 0 \\ 0 & 0 & 0 & p \end{bmatrix}, \tag{1.2.12}$$

where ρ is the energy density (matter, radiation and non-gravitational force fields) and p is the pressure.

In Newtonian dynamics, the Poisson's equation indicates the mass density as the source for gravital acceleration. But in presence of high pressure, a more general way to indicate the source of gravitational force is

$$\nabla \mathbf{g} = -4\pi G(\rho + 3p), \tag{1.2.13}$$

where we can indicate with $\rho_g = (\rho + 3p)$ the source of gravitational acceleration.

Considering a spherically symmetric distribution of mass with radius l, using the Birkhoff theorem (the mass in a flat space acts under Newtonian dynamics), we get that the acceleration of the mass surface is

$$\ddot{l} = -\frac{GM}{l^2} = -\frac{4}{3}\pi G(\rho + 3p)l \tag{1.2.14}$$

where the single and double dot sign mean first and second order time derivative respectively. The net energy inside the sphere is given by the mass, $U = \rho V$. Changing in the net energy is a consequence of the movement of matter inside the radius l, due to the change of pressure work on the surface

$$\begin{aligned} dU &= -pdV \\ &= d\rho V + V d\rho, \end{aligned} \tag{1.2.15}$$

where the second line is the differential of the energy-mass relation. Since $V \propto l^3$ and $dV = \dot{V}dt$, $d\rho = \dot{\rho}dt$, the second relation in Eq. 1.2.15 yields

$$\dot{\rho} = -(\rho + p)\frac{\dot{V}}{V} = -3(\rho + p)\frac{\dot{l}}{l}. \tag{1.2.16}$$

Using the equation above, we can eliminate the pressure p in Eq. 1.2.14:

$$\ddot{l} = \frac{8}{3}\pi G\rho l + \frac{4}{3}\pi G\dot{\rho}\frac{l^2}{\dot{l}}. \tag{1.2.17}$$

The last equation has the great advantage that multiplied by $\dot{l}$ has the integral in the form:

$$\dot{l}^2 = \frac{8}{3}\pi G\rho l^2 + K, \tag{1.2.18}$$

with K the constant of integration.

In a static Universe, with l constant (and zero time derivatives), the constant of integration is $K = -l^2/R^2$, with R the same curvature seen in Eq. 1.2.9. Eqs.

1.2.14 and 1.2.18, for a static, homogeneous and isotropic Universe are

$$\frac{4}{3}\pi G(\rho + 3p) = 0 \tag{1.2.19}$$

and

$$\frac{8}{3}\pi G\rho - \frac{1}{R^2} = 0. \tag{1.2.20}$$

1.2.3 Introduction of the cosmological constant

With no doubt, one of the biggest puzzle in cosmology is the nature of the so called *dark energy*. Historically, the existence of an extra component besides matter and radiation arose by the evident contradiction in Eq. 1.2.19. In a static Universe, for a positive density (naturally expected for ordinary matter and radiation), pressure has to be negative, $p = -\rho/3$. To avoid this, Einstein modified the EFE, with the integration of an additional term on the left hand:

$$R_{ij} - \frac{1}{2}g_{ij}R - \Lambda g_{ij} = 8\pi G T_{ij}, \tag{1.2.21}$$

where Λ is called *cosmological constant*. Comparing the metric tensor g_{ij} with the stress-energy tensor T_{ij}, Eq. 1.2.12, we get

$$\rho_\Lambda = \frac{\Lambda}{8\pi G} \tag{1.2.22}$$

and

$$p_\Lambda = -\rho_\Lambda. \tag{1.2.23}$$

The nature of constant arises instantly if we substitute the relation in Eq. 1.2.23 in Eq. 1.2.16, we get $\dot{\rho}_\Lambda = 0$. Finally, using the relations in Eqs. 1.2.22 and 1.2.23 in Eqs. 1.2.19 and 1.2.20, we see how the cosmological constant acts as a source for gravity and curvature:

$$4\pi G\rho = \Lambda = \frac{1}{R^2}. \tag{1.2.24}$$

Einstein introduced the cosmological constant for consistency with the accepted idea of a statical Universe. In fact, the mean mass density, $\bar{\rho}$ is set equal to a constant, $\Lambda/4\pi G$. Larger (lower) values of the the mean mass density will cause the Universe to contract (expand) under its own gravity (vacuum pressure).
In the next section, I will introduce the dynamics of an expanding Universe, which, in principle, makes the cosmological constant useless. Nonetheless, the accelerated expansion that the Universe is undergoing is caused by the density of the Dark Energy, that relies on the same formulation introduced for the cosmological constant.

1.3 The expanding Universe

1.3.1 The scale factor

We indicate with l the proper physical separation between two objects, namely two galaxies, distant enough to not attract themselves under their mutual gravitational force. The expansion of the Universe says that this proper distance is a function of time, $l(t)$:

$$l(t) = l_0 a(t), \tag{1.3.1}$$

where the proper distance has been separated into a constant part l_0 and a *scale factor* $a(t)$ that carries the expansion part. The cosmological principle makes the scale factor $a(t)$ the same for every part of the Universe. The rate of the recession is obtained differentiating the above relation:

$$v = \dot{l} = l_0 \dot{a} = l\frac{\dot{a}}{a} \equiv Hl. \tag{1.3.2}$$

The Hubble's parameter is a function of time, $H = \dot{a}/a$, and the value it has at the present, H_0, refers to the expansion scale factor at the present epoch, a_0.

1.3.2 The Robertson-Walker metric

From Eq. 1.3.1 we can easily apply the expansion factor to the line element in Eq. 1.2.2:

$$ds^2 = dt^2 - a^2(t) g^0_{\alpha\beta} dx^\alpha dx^\beta. \tag{1.3.3}$$

Using the prescription in Sect.1.2.1, we get the general metric describing the space-time:

$$ds^2 = dt^2 - a^2(t)\left[\frac{dr^2}{1-Kr^2} + r^2(d\theta^2 + \sin^2\theta d\phi^2)\right], \tag{1.3.4}$$

where the spatial part between square brackets is expanded by the scale factor $a(t)$. The metric in the Eq. 1.3.4 is called the Robertson-Walker line element, and is the most general form of the line element in a spatially homogeneous and isotropic space-time, independently of the gravitational framework. The constant K is the curvature, $K = 1/R^2$. It defines spatial hyper-surface with positive, zero or negative curvature, $K = +1, 0, -1$. We can introduce the coor-

dinate χ:

$$\chi = \int \frac{dr}{\sqrt{1-Kr^2}} = \begin{cases} \sin^{-1} r & (\text{for } K=1) \\ r & (\text{for } K=0) \\ \sinh^{-1} r & (\text{for } K=-1) \end{cases}, \tag{1.3.5}$$

and its function $S_K(\chi)$,

$$S_K(\chi) = \begin{cases} \sin\chi & (\text{for } K=1) \\ \chi & (\text{for } K=0) \\ \sinh\chi & (\text{for } K=-1) \end{cases}, \tag{1.3.6}$$

that allows us to compact the spatial part of the metric:

$$dl^2 = a^2 \left[d\chi^2 + S_K(\chi)(d\theta^2 + \sin^2\theta d\phi^2) \right]. \tag{1.3.7}$$

We have already seen the case in which $K = 1$, that describes the case of a three-sphere embedded in an abstract flat four-dimensional Euclidean space (Sect. 1.2.1). The interval for the coordinate χ is $0 \leq \chi \leq \pi$, where the other angles take the usual values for the spherical coordinates. Hence the $K = 1$ model has finite volume, and is referred as *close*. The case $K = 0$ is the simplest one, that describe the flat Euclidean three-space. This model is referred as *flat*. The last case with $K = -1$ describes the geometry of a hyperboloid embedded in an abstract four-dimensional space. The spatial element of the hyperboloid is

$$dl^2_{k=-1} = a^2 \left[d\chi^2 + \sinh^2\chi(d\theta^2 + \sin^2\theta^2 d\phi^2) \right]. \tag{1.3.8}$$

Note that the passage from a positive curvature to a negative one is obtained with the transformation $R \mapsto iR$. On a three-sphere, any point can be mapped onto another with a rotation, while on three-hyperboloid any point can be mapped onto another with a rotation by an imaginary angle. These transformations leave the metric unchanged, demonstrating that all the points and directions are equivalent, accordingly to the cosmological principle.

1.3.3 Dynamics in the expansion

The basic equation of the expansion

$$l(t) = l_0 a(t) \tag{1.3.9}$$

is applied to the concepts exposed in Sect. 1.2.2 to describe fundamental laws of the expanding Universe. Since $l(t) \propto a(t)$, the Eq. 1.2.14 transforms in

$$\frac{\ddot{a}}{a} = -\frac{4}{3}\pi G(\rho + 3p) + \frac{\Lambda}{3}, \tag{1.3.10}$$

where we have added the cosmological constant. The energy conservation Eq. 1.2.16 transforms into

$$\dot{\rho} = -3(\rho + p)\frac{\dot{a}}{a}. \tag{1.3.11}$$

Eliminating the pressure, we obtain the corresponding of Eq. 1.2.18:

$$\left(\frac{\dot{a}}{a}\right)^2 = \frac{8}{3}\pi G\rho + \frac{K}{a^2} + \frac{\Lambda}{3}, \tag{1.3.12}$$

that can be rewritten introducing the Hubble's parameter and the curvature model

$$H^2 = \left(\frac{\dot{a}}{a}\right)^2 = \frac{8}{3}\pi G\rho \pm \frac{1}{a^2R^2} + \frac{\Lambda}{3}, \tag{1.3.13}$$

where the the sign for the curvature model is negative in case of closed model and positive for open model.

The Eq. 1.3.13 gives us important information on the behavior of the different components of the Universe. First, if matter presents negligible pressure, the energy conservation Eq. 1.3.11 states that matter density scales as

$$\rho \propto \frac{1}{a(t)^3}, \tag{1.3.14}$$

accordingly to the common sense that a volume scales as $a(t)^3$ and the mass is conserved. Then, we consider the different behaviors of the components with the scale factor in Eq. 1.3.13. Matter density varies as a higher power of the expansion parameter $a(t)$ then the Λ term and the curvature term. Tracing back the scale factor to smaller values, the mass term dominates. We can neglect the last two terms in Eq. 1.3.13 and write

$$\left(\frac{\dot{a}}{a}\right)^2 = \frac{8}{3}\pi G\rho, \tag{1.3.15}$$

which yields

$$a \propto t^{2/3} \tag{1.3.16}$$

and

$$t = \frac{2}{3H} = \frac{1}{(6\pi G\rho)^{1/2}}. \tag{1.3.17}$$

When $t \to 0$, we have $a \to 0$, and $\rho \to \infty$, that represents a singularity.

1.3.4 The cosmological redshift

First of all, we show how the cosmological principle applies to the recession law. In vector form, the recession velocity of a galaxy at distance l is

$$\mathbf{v} = H_0\mathbf{l}. \tag{1.3.18}$$

Another observer, recessing from us with a velocity $\mathbf{v}'$ will see the recession of the same galaxy with velocity

$$\hat{\mathbf{v}} = \mathbf{v} - \mathbf{v}' = H_0(\mathbf{l} - \mathbf{l}') = H_0\hat{\mathbf{l}}, \tag{1.3.19}$$

where $\hat{\mathbf{l}}$ is the distance between the second observer and the galaxy and the Hubble law is clearly applied in case of non-relativistic velocities.

For the redshift, imagine an observer measuring at time t some radiation emitted in the past. For that observer, the radiation has a certain wavelength $\lambda(t)$. Another comoving observer will observe the same radiation after a time $t + \delta t$, at a proper distance $l = \delta t$ (with $c = 1$). The first observer sees the second moving with a recession speed of $v = Hl = (\dot{a}/a)\delta t$. The wavelength measured by the second observer is Doppler shifted

$$\lambda(t + \delta t) = \lambda(t)(1 + v) = \lambda(t)[1 + (\dot{a}/a)\delta t], \tag{1.3.20}$$

that is reduced to

$$\frac{\dot{\lambda}}{\lambda} = \frac{\dot{a}}{a} \tag{1.3.21}$$

with the solution

$$\lambda(t) \propto a(t). \tag{1.3.22}$$

In Sect. 1.1.3 the redshift has been defined through the Eq. 1.1.9. Using the above relation, we get

$$1 + z = \frac{\lambda_0}{\lambda_e} = \frac{a_0}{a_e}, \tag{1.3.23}$$

where the subscript o refers to the observed wavelength and scale factor at the present and the subscript e refers to the wavelength at the emission and the scale factor of the Universe at that time. In this thesis, we often refer to the redshift in term of emitted and observed frequencies

$$\frac{\nu_o}{\nu_e} = \frac{a_e}{a_o} = \frac{1}{1+z} \tag{1.3.24}$$

or in the preferred form $\nu_e = \nu_o(1 + z)$ (sometimes, the subscript 0 is used in place of o). The redshift loses its nature of measuring how distant is an object from us, and assumes the slightly different meaning of measuring the epoch of a certain event.

1.3.5 Parameters

The expansion factor $H = \dot{a}/a$ is a function of time. We can define it as the relation among different parameters, each one describing the behavior of a component of the Universe, which density evolves with time:

$$H^2 = \left(\frac{\dot{a}}{a}\right) = \left(\frac{\dot{z}}{1+z}\right) = H_0^2[\Omega(1+z)^3 + \Omega_R(1+z)^2 + \Omega_\Lambda], \tag{1.3.25}$$

where H_0 is the Hubble constant at the present time and the parameters inside the square brackets, Ω, Ω_R and Ω_Λ are constants who evolves explicitly with time (redshift). These parameters are the *density parameter*

$$\Omega = \frac{8\pi G\rho_0}{3H_0^2}, \tag{1.3.26}$$

related to the mean matter density ρ_0. As we already know, the mean mass density scales as the inverse cube of the scale factor, $\rho \propto a^{-3} \propto (1+z)^3$. The second parameter is the *curvature parameter*

$$\Omega_R = \frac{1}{(a_0 H_0 R)^2}. \tag{1.3.27}$$

This parameter is positive when R is real (positive curvature, closed space) and negative with open space (R is imaginary). For flat space, $R \to \infty$ and $\Omega \to 0$. The last term is the *cosmological constant parameter*

$$\Omega_\Lambda = \frac{\Lambda}{3H_0^2}. \tag{1.3.28}$$

At the present epoch, the equality between H and H_0 in Eq. 1.3.25 is obtained through the relation:

$$\Omega + \Omega_R + \Omega_\Lambda = 1 \tag{1.3.29}$$

since $z = 0$ cancels the power laws of the first two parameters.

1.3.6 The Einstein-de Sitter solution

The discovery of a non-static Universe, moved Einstein to reject the idea of the cosmological constant. Accordingly with the idea of de Sitter, Einstein declared that the simplest reasonable case was considering the only mass density, the only one at that time having observable evidence and hence not negligible. The scale factor and time relations for an Universe filled only with matter are given in Eqs. 1.3.16 and 1.3.17, while the line element is

$$ds^2 = dt^2 - a^2(t)[dr^2 + r^2 d\Omega]. \tag{1.3.30}$$

Since the expression inside square brackets is the ordinary flat space, the Einstein-de Sitter model is often referred as a flat model.

Even in the case that the others two parameter, Ω_R and Ω_Λ are non-zero, at high redshifts the dominant term is the matter density. At the early stages, the Universe was in a Einstein-de Sitter state,

$$H = \frac{\dot{a}}{a} = \frac{\dot{z}}{1+z} = H_0 \Omega^{1/2} (1+z)^{3/2}, \tag{1.3.31}$$

with the solution

$$t = \frac{2}{3} \frac{1}{H_0 \Omega^{1/2} (1+z)^{3/2}} \tag{1.3.32}$$

independently of the cosmological constant and space curvature.

From Eq. 1.3.26 and Eq. 1.1.12, we can derive the numerical value of the mean matter density:

$$\begin{aligned} \rho_0 = 3\Omega H_0^2/(8\pi G) = \Omega \rho_{\rm crit} &= 2.78 \times 10^{11} \Omega h^2 \mathcal{M}_\odot \ {\rm Mpc}^{-3} \\ &= 1.88 \times 10^{-29} \Omega h^2 \ {\rm g \ cm}^{-3}. \end{aligned} \tag{1.3.33}$$

1.3.7 Distances in cosmology

The following concepts are fundamental tools when dealing with redshift and the metrics associated to distant events in the space-time. The following auxiliary function enters in most of the calculations

$$E(z) \equiv \sqrt{\Omega (1+z)^3 + \Omega_R (1+z)^2 + \Omega_\Lambda}. \tag{1.3.34}$$

The Hubble's constant at any redshift can be expressed via the Eq. 1.3.34, $H(z) = H_0 E(z)$ that is a generalization of the Eq. 1.3.31. The quantity $dz/E(z)$ is the proper distance that a photon travels in the interval dz, divided by the scale factor, hence is a comoving distance. The integration along the line-of-sight (LOS) is the the total LOS comoving distance

$$D_C = \frac{c}{H_0} \int_0^z \frac{dz'}{E(z')} \tag{1.3.35}$$

The *transverse* comoving distance D_M is related to the LOS comoving distance

$$D_M = \begin{cases} \frac{c}{H_0} \frac{1}{\sqrt{\Omega_R}} \sinh[\sqrt{\Omega_R} \frac{H_0}{c} D_C] & \text{for} \quad \Omega_R > 0 \\ D_C & \text{for} \quad \Omega_R = 0 \\ \frac{c}{H_0} \frac{1}{\sqrt{|\Omega_R|}} \sin[\sqrt{|\Omega_R|} \frac{H_0}{c} D_C] & \text{for} \quad \Omega_R < 0. \end{cases} \tag{1.3.36}$$

The comoving distance between two elements that take place in the same time (or redshift) and are seen separated by the angle $\delta\theta$ is $\delta\theta D_M$. The comoving distance is the *proper motion distance* defined in Weinberg 1972, [10].
The *angular diameter distance* for an object is the defined as the ratio between its physical transverse size to its angular size (i.e., measured by a telescope). It is the comoving diameter distance multiplied by the scale factor

$$D_A = a(t)D_M = \frac{D_M}{1+z}. \tag{1.3.37}$$

The angular diameter distance between two objects is not the the difference between their angular diameter distances, but

$$D_{A12} = \frac{1}{1+z_2}\left[D_{M2}\sqrt{1+\Omega_R\frac{H_0^2 D_{M1}^2}{c^2}} - D_{M1}\sqrt{1+\Omega_R\frac{H_0^2 D_{M2}^2}{c^2}}\right] \tag{1.3.38}$$

that is valid only for $\Omega_R \geq 0$.

Another fundamental tool is the *luminosity distance* D_L that is defined as the ratio between the emitted bolometric luminosity L and bolometric flux S

$$S = \frac{L}{4\pi D_L^2} \tag{1.3.39}$$

(see Eq. 1.1.3), where

$$D_L = (1+z)D_M = (1+z)^2 D_A. \tag{1.3.40}$$

The *comoving volume* V_C is defined as the volume in which the number density of non-evolving objects locked in the Hubble flow is constant. The element of the volume is

$$dV_C = \frac{c}{H_0}\frac{(1+z)^2 D_A^2}{E(z)}d\Omega dz \tag{1.3.41}$$

in the solid angle element $d\Omega$ and redshift interval dz. Integrated, we get the comoving volume of the sky

$$V_C = \begin{cases} \frac{4\pi}{2\Omega_R}\left(\frac{c}{H_0}\right)\left[\Xi(D_M,\Omega_R) - \Theta(D_M,\Omega_R)\right] & \text{for} \quad \Omega_\mathrm{R} \neq 0 \\ \frac{4\pi}{3}D_M^3 & \text{for} \quad \Omega_\mathrm{R} = 0 \end{cases} \tag{1.3.42}$$

where the functions $\Xi(D_M,\Omega_\mathrm{R})$ and $\Theta(D_M,\Omega_R)$ are

$$\Xi(D_M,\Omega_\mathrm{R}) = \frac{D_M}{(c/H_0)}\sqrt{1+\Omega_\mathrm{R}\frac{D_M^2}{(c/H_0)^2}}, \tag{1.3.43}$$

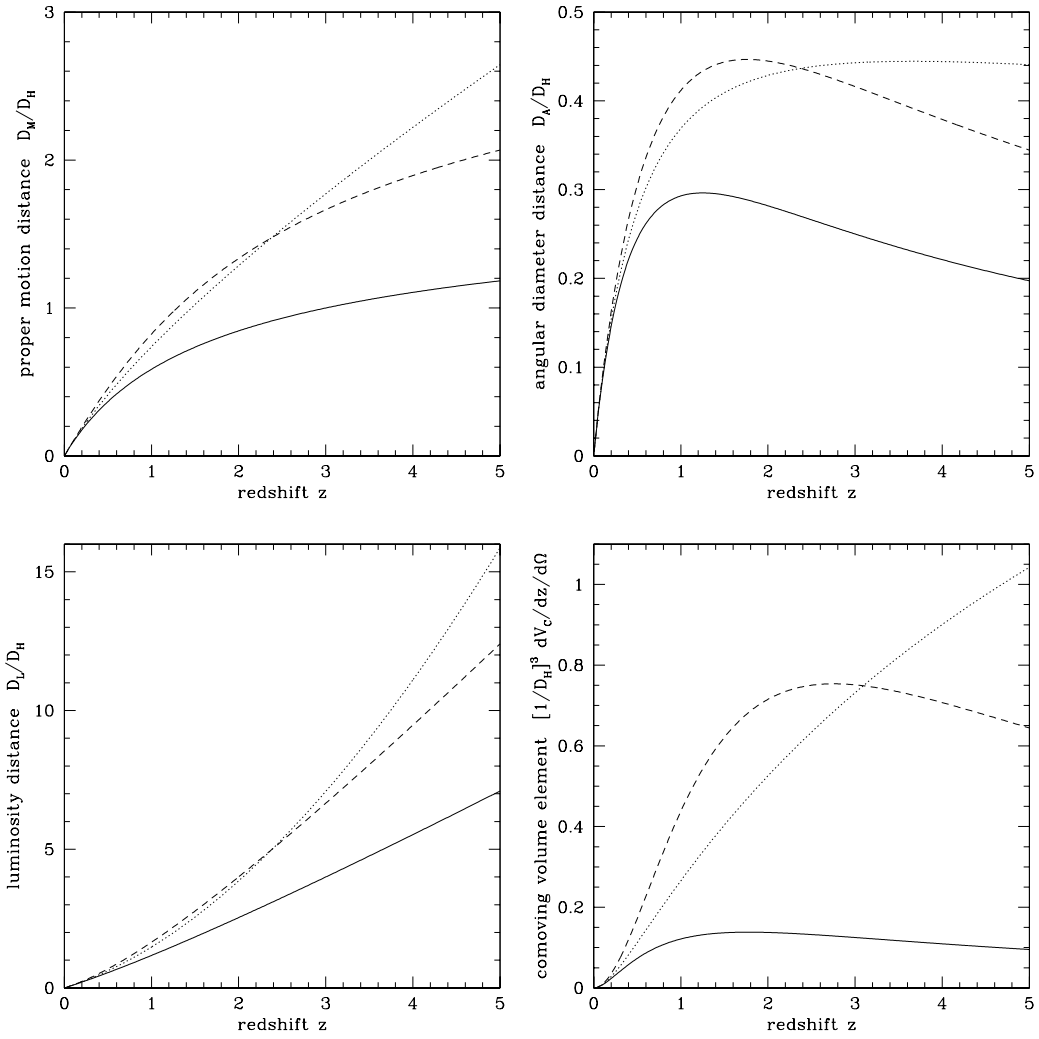

Figure 1.2 Relevant distances in cosmology. *Solid line*: $\Omega = 1, \Omega_\Lambda = 0$; *dotted lines*: $\Omega = 0.05, \Omega_\Lambda = 0$; *dashed line*: $\Omega = 0.2, \Omega_\Lambda = 0.8$. All plots from Hogg (1999), [5].

and

$$\Theta(D_M, \Omega_R) = \begin{cases} \frac{1}{\sqrt{\Omega_R}} \text{arcsinh}\left(\sqrt{|\Omega_R|}\frac{D_M}{(c/H_0)}\right) & \text{for} \quad \Omega_\text{R} > 0 \\ \frac{1}{\sqrt{\Omega_R}} \arcsin\left(\sqrt{|\Omega_R|}\frac{D_M}{(c/H_0)}\right) & \text{for} \quad \Omega_\text{R} < 0. \end{cases} \tag{1.3.44}$$

In Fig. 1.2 are plotted distances for different models of Universe. All the plot and references in this section are from Hogg (1999), [5].

1.3.8 The k-correction

Bolometric quantities do not discern among frequencies or wavelengths of the emitted radiation. Band luminosities are converted to band fluxes through the

k − correction

$$S_\nu = (1+z)\frac{L_{\nu_e}}{L_\nu}\frac{L_\nu}{4\pi D_L^2} \tag{1.3.45}$$

when observing in a frequency interval and

$$S_\lambda = \frac{1}{(1+z)}\frac{L_{\lambda_e}}{L_\lambda}\frac{L_\lambda}{4\pi D_L^2} \tag{1.3.46}$$

when observing in a wavelength interval. The quantities with the subscript e are the frequency and wavelengths at the rest frame of the emitter, $\nu_e = \nu(1+z)$ and $\lambda_e = \lambda/(1+z)$, where ν and λ are the observed quantities. The k-correction is fundamental in observation astronomy, since it has to be taken into account for each emission with a non-constant νL_ν.

1.4 Growth through gravitational instability

The Universe appears homogeneous on large scales. In contrast to the static model, the expanding Universe has been close, in the past, to the homogeneity observed today. On smaller scales, the structures we observer (galaxy groups, clusters and filaments) are a departure from the homogeneity. At the position $\mathbf{x}$ and at time t, we define the density as

$$\rho(\mathbf{x}, t) = \rho_b(t)[1 + \delta(\mathbf{x}, t)]. \tag{1.4.1}$$

Here, $\rho_b(t)$ is the mean background density and $\delta(\mathbf{x}, t)$ is the *density contrast*, a number that measures the departure from the homogeneity. The spatial coordinate $\mathbf{x}$ is the coordinate of the observer that records the density contrast at proper time t. A hypothetical collection and comparison of the records from all the observers freely moving in the Universe can be done even if some of them are separated by the Hubble length.

1.4.1 Newtonian equations of motion

The Newtonian mechanics approach to perturbation theory is better suited to study the growth of large structures such as galaxy clusters. These structures present typical sizes R to be much smaller than the Hubble length H^{-1}, hence the velocities involved are non-relativistic and the treatment through the Newtonian laws is justified, [1].

The baryonic matter is considered as a pressureless ideal fluid. Indicating with $\mathbf{u}$ the velocity field in an inertial coordinate system at the proper position $\mathbf{r}$, the mass conservation equation is

$$\left(\frac{\partial \rho}{\partial t}\right)_{\mathbf{r}} + \nabla_{\mathbf{r}} + (\rho \mathbf{u}) = 0 \tag{1.4.2}$$

while the Eulerian equation of motion is

$$\left(\frac{\partial \mathbf{u}}{\partial t}\right)_{\mathbf{r}} + (\mathbf{u} + \nabla_{\mathbf{r}})\mathbf{u} = -\nabla_{\mathbf{r}}\Phi \, . \tag{1.4.3}$$

The Poisson's equation for the potential Φ is $\nabla^2_{\mathbf{r}}\Phi = 4\pi G\rho$.

1.4.2 Comoving coordinates

In Eq. 1.3.1 we have already seen the relation between proper coordinates and comoving. The same relation is applied to the comoving coordinate $\mathbf{x}$ respect the proper one $\mathbf{r}$,

$$\mathbf{x} = \mathbf{r}/a(t) \, . \tag{1.4.4}$$

The gradient $\nabla_{\mathbf{r}}$ is computed with respect to the proper coordinate. Passing to the comoving coordinate and removing the subscript:

$$\nabla = a\nabla_{\mathbf{r}} \, . \tag{1.4.5}$$

Furthermore, the velocity can be seen as a sum of two separate velocities:

$$\mathbf{u} = \dot{a}\mathbf{x} + \mathbf{v}(\mathbf{x}, t), \tag{1.4.6}$$

where the first part is the the Hubble flow and the second part is the peculiar velocity of the object relative to the general expansion. The time derivative of any function $f = f(\mathbf{x}, t)$ with respect the proper coordinate is

$$\left(\frac{\partial f}{\partial t}\right)_{\mathbf{r}} = \left(\frac{\partial f}{\partial t}\right)_{\mathbf{x}} - \frac{\dot{a}}{a}\mathbf{x} \cdot \nabla f, \tag{1.4.7}$$

where the gradient is with respect to $\mathbf{x}$ (Eq. 1.4.5). Differentiating with respect the comoving coordinate the Eq. 1.4.2

$$\left(\frac{\partial}{\partial t} - \frac{\dot{a}}{a}\mathbf{x} \cdot \nabla\right)[\rho_b(t)(1+\delta)] + \frac{\rho_b}{a}\nabla \cdot [(1+\delta)(\dot{a}\mathbf{x} + \mathbf{v})] = 0 \tag{1.4.8}$$

where we can use the differential 1.3.14 with respect to t, $\dot{\rho}_b = -3\rho_b\dot{a}/a$ to get the simpler form:

$$\frac{\partial \delta}{\partial t} + \frac{1}{a}\nabla \cdot [(1+\delta)\mathbf{v}] = 0. \tag{1.4.9}$$

The potential Φ can be rewritten in terms of the comoving potential $\phi(\mathbf{x}, t)$

$$\Phi = \phi(\mathbf{x}, t) + \frac{2}{3}\pi G\rho_b a^2 x^2 - \frac{1}{6}\Lambda a^2 x^2, \tag{1.4.10}$$

useful for the Poisson's equation in which enters the density contrast

$$\nabla^2\phi = 4\pi G\rho_b a^2 \delta. \tag{1.4.11}$$

Reminding the notation for the time derivative in Eq. 1.4.7, we can use the above expression in the Eq. 1.4.3:

$$\left(\frac{\partial}{\partial t} - \frac{\dot{a}}{a}\mathbf{x}\cdot\nabla\right)(\dot{a}\mathbf{x} + \mathbf{v}) + \frac{1}{a}(\dot{a}\mathbf{x} + \mathbf{v})\cdot\nabla(\dot{a}\mathbf{x} + \mathbf{v}) = -\frac{1}{a}\nabla\phi - \frac{4}{3}\pi G\rho_b a\mathbf{x} + \frac{1}{3}\Lambda a\mathbf{x}. \tag{1.4.12}$$

Finally, using the relation between the expansion velocity $\ddot{a}$ and the sources for gravitation (Eq. 1.3.10), we can simplify the above equation

$$\frac{\partial\mathbf{v}}{\partial t} + \frac{\dot{a}}{a}\mathbf{v} + \frac{1}{a}(\mathbf{v}\cdot\nabla)\mathbf{v} = -\frac{1}{a}\nabla\phi. \tag{1.4.13}$$

The set of Eqs. 1.4.9, 1.4.11 and 1.4.13 represents the evolution in an expanding universe of mass fluctuations, where the pressure is negligible with respect to the density.

1.4.3 Linear evolution

On small scales, neglecting the pressure is not so well justified, but comes to a realist approach when averaging on larger scales. In this regime, we can compute δ and $\mathbf{v}$ in linear perturbation theory, neglecting terms of order δv or δ^2. Thus, Eqs. 1.4.9 and 1.4.13 have simplest forms:

$$\frac{\partial\delta}{\partial t} + \frac{1}{a}\nabla\cdot\mathbf{v} = 0, \tag{1.4.14}$$

$$\frac{\partial\mathbf{v}}{\partial t} + \frac{\dot{a}}{a}\mathbf{v} + \frac{1}{a}\nabla\phi = 0. \tag{1.4.15}$$

Deriving with respect to time the first equations and subtracting the divergence of the second, where we can substitute the Poisson's expression in Eq. 1.4.11, we get the time evolution of the mass density contrast

$$\frac{\partial^2\delta}{\partial t^2} + 2\frac{\dot{a}}{a}\frac{\partial\delta}{\partial t} = 4\pi G\rho_b\delta. \tag{1.4.16}$$

For the Einstein-de Sitter model, where the density is the dominant component with respect to the curvature and the cosmological constant, the scale factor scales as $t^{2/3}$ and the time evolution becomes

$$\frac{\partial^2\delta}{\partial t^2} + \frac{4}{3t}\frac{\partial\delta}{\partial t} = \frac{2}{3t^2}\delta, \tag{1.4.17}$$

that has the solution

$$\delta = At^{2/3} + Bt^{-1}. \tag{1.4.18}$$

The two coefficients A and B are functions of the comoving coordinate $\mathbf{x}$, while the two functions in t are linearly independent. The first term is the *growing mode* of a density perturbation, while the second term is known as the *decaying mode*.

The growing mode corresponds to the gravitational instability and it is the mechanism at the base of the structures formation in the Universe. Indicating with $D(t)$ the function upon which depends the δ in Eq. 1.4.18, Eq. 1.4.14 becomes

$$\nabla\cdot\mathbf{v} = -a\frac{\partial\delta}{\delta t} = -a\delta\frac{\dot{D}}{D}, \tag{1.4.19}$$

since the coefficient A depends only on the position. We define the velocity factor

$$f = \frac{a}{\dot{a}}\frac{\dot{D}}{D} = \frac{1}{H}\frac{\dot{D}}{D} \tag{1.4.20}$$

and we compare Eq. 1.4.19 to the Poisson's equation for the peculiar gravitational acceleration $\mathbf{g} = -\nabla\phi/a$

$$\mathbf{v} = \frac{fH}{4\pi G\rho_b}\mathbf{g} = \frac{2}{3}\frac{f}{\Omega H}\mathbf{g}, \tag{1.4.21}$$

that for Einstein-de Sitter model ($\Omega = 1 = f$), has the usual form $\mathbf{v} = \mathbf{g}t$. For a negligible cosmological constant or curvature, the velocity factor has an phenomenological value

$$f \approx \Omega^{0.6}. \tag{1.4.22}$$

1.4.4 The Jeans scale

When the photons-baryons gas is not negligible, the pressure affects the solution. The pressure force per unit volume is

$$\mathbf{F} = -\frac{1}{a}\nabla p = -\frac{dp}{d\rho}\frac{\nabla\rho}{a} = -c_s^2\rho_b\frac{\nabla\delta}{a}, \tag{1.4.23}$$

where $c_s^2 \equiv dp/d\rho$ is the velocity of sound. The equation 1.4.13 for the velocity evolution becomes

$$\frac{\partial \mathbf{v}}{\partial t} + \frac{\dot{a}}{a}\mathbf{v} + \frac{1}{a}(\mathbf{v}\cdot\nabla)\mathbf{v} = -\frac{1}{a}\nabla\phi - c_s^2\frac{\nabla\delta}{a}. \tag{1.4.24}$$

The density perturbation in Eq. 1.4.16 takes an additional term:

$$\frac{\partial^2\delta}{\partial t^2} + 2\frac{\dot{a}}{a}\frac{\partial\delta}{\partial t} = 4\pi G\rho_b\delta + \frac{c_s^2}{a^2}\nabla^2\delta. \tag{1.4.25}$$

The role of the pressure is to counterbalance the effects of gravity. To identify the size of the overdensities that collapse under the gravitational force, the density contrast can be decomposed in Fourier series:

$$\delta = \sum \delta_{\mathbf{k}} e^{-i\mathbf{k}\cdot\mathbf{x}}, \tag{1.4.26}$$

where $\mathbf{k}$s are the wavenumbers and $\delta_{\mathbf{k}}$ are the amplitudes of the series. For each amplitude $\delta_{\mathbf{k}}(t)$, the evolution of the density perturbation yields

$$\frac{d^2\delta_{\mathbf{k}}}{dt^2} + 2\frac{\dot{a}}{a}\frac{d\delta_{\mathbf{k}}}{dt} = \left(4\pi G\rho_b - \frac{k^2c_s^2}{a^2}\right)\delta_{\mathbf{k}}. \tag{1.4.27}$$

The evolution of each amplitude of the overdensity is zero when the term in brackets is zero. This is obtained at a certain wavenumber k_{J}

$$k_{\mathrm{J}} = \frac{2a}{c_s}(\pi G\rho_b)^{1/2}, \tag{1.4.28}$$

which correspond to the *Jeans wavelength*

$$\lambda_{\mathrm{J}} = \frac{2\pi a}{k_{\mathrm{J}}} = \left(\frac{\pi c_s^2}{G\rho_b}\right)^{1/2}. \tag{1.4.29}$$

The role of the Jeans wavelength is clear: at wavelengths larger than this value, the pressure wave velocity cannot counteract the gravitational fall and hence the perturbation grows as it was in absence of pressure. For shorter wavelengths, the contrast oscillates as a sound wave.

1.4.5 The Zeldovich approximation

The Zeldovich approximation, [11], is a further step beyond the linearity of the motion equations. Basically, the proper position can be seen as the product between the scale factor and the comoving position plus a perturbation term

$$\mathbf{r}(t) = a(t)\mathbf{q} + b(t)\mathbf{f}(\mathbf{q}), \tag{1.4.30}$$

where $\mathbf{q}$ is the usual comoving coordinate, $b(t)$ is a scale function for the time-independent displacement field $\mathbf{f}(\mathbf{q})$, representing a strain. The vectorial field $\mathbf{f}(\mathbf{q})$ is irrotational, hence the gradient of a scalar field $\mathbf{f}(\mathbf{q}) = \nabla\psi(\mathbf{q})$. The relation with the linearized density perturbation is

$$\delta = -\frac{b}{a}\nabla\mathbf{f}. \tag{1.4.31}$$

The above equation represents a first-order Lagrangian perturbation theory. When the density perturbation is small, the Lagrangian approach and the linear Eulerian approach gives the same results. In fact, we can see that $b(t)/a(t) = D(t)$, where $D(t)$ is the same linear relation of Eq. 1.4.18. We can rewrite the proper coordinate as

$$\mathbf{r}(t) = a(t)[\mathbf{q} + D(t)\mathbf{f}(\mathbf{q})]. \tag{1.4.32}$$

The Zeldovich approach is a method used to set up quasi-linear initial conditions for N-body simulations.

1.4.6 Spherical collapse

The spherical collapse is a very useful way to describe overdensity that are much greater than unity. A spherical distribution of matter behaves as a closed universe. The matter density of the sphere has not to be uniformly distributed, as the collapse is driven by the mean density.

In a matter-dominated Universe, the relation between the proper radius and time is the solution for a cycloid

$$\begin{aligned} r &= A(1-\cos\theta); \\ t &= B(\theta-\sin\theta), \end{aligned} \tag{1.4.33}$$

where A and B are constants. The perturbation within the sphere is

$$\delta \simeq \frac{3}{20}\left(\frac{6t}{B}\right)^{2/3} \tag{1.4.34}$$

that for early times is the growing mode for linear evolution. Breakdown from linearity occurs at later times. The first departure is found at *turnaround*. From the first of Eqs. 1.4.33 we see that a maximum for r is reached at $\theta = \pi$ and $t = \pi B$. In this case $r = 2A$, while from the cycloid solution $A^3 = GMB^2$, where M is the mass enclosed in the sphere of radius r. The mean density inside the sphere is $\bar{\rho} = 3M/4\pi r^3$, while the background density is $\rho_b = 1/(6\pi G t^2)$,

as the solution is in a matter-dominated Universe (Eq. 1.3.17). The density contrast at the time of the turnround is

$$\frac{\bar{\rho}}{\rho_b} = \frac{9}{16}\pi^2 \simeq 5.6 \tag{1.4.35}$$

Linear evolution would predict $\delta_{\rm lin} = (3/20)(6\pi)^{2/3} \simeq 1.06$. After the turnaround, the system collapses under the gravity, reaching a singularity for $\theta = 2\pi$. This occurs when

$$\delta_{\rm lin} = (3/20)(12\pi)^{2/3} \simeq 1.69. \tag{1.4.36}$$

The collapse never occurs, but rather the system encounters a state of equilibrium according to the *virial theorem*, with a kinetic energy K related to the potential energy V with the relation $V = -2K$. The virialization state means the end of the gravitational collapse for a given system, reached at $\theta = 3\pi/2$ with an overdensity of $\simeq 147$. If the collapse is taken as the point the system reaches the virialization, with $\theta = 2\pi$, then the overdensity is taken to have a value of 178.

1.5 Radiation

One could easily argue that there is a huge amount of radiation in the Universe: the one proceding from stars, from hot gas clouds, from catastrophic events such supernovae. Nonetheless, the radiation density from these events is not even comparable to the matter density or the cosmological constant. In a steady-state Universe, the presence of radiation as one of the components of the Universe has not been taken into account. But for theorists facing the steady-state with the Big Bang model, the radiation would have an important role in the early stage of the Universe. After the Big Bang (a proper image of the Big Bang is a high density state where new physics is expected), the Universe was incredibly hot and dense, presenting a high energy density and pressure. In this state elemental particles were coupled. As the Universe expanded and cooled, elemental particles were capable to form neutrons and protons, in a continuous process of formation and destruction. Photons were at thermal equilibrium with matter, and the streaming path was limited by the frequent collisions and absorptions. The universe was totally opaque to the light. As the plasma further expanded, the first light nuclei formed and the corresponding temperature

lowered to the point that the photons were free to escape. The sphere subtended by the free streaming path of the photons originary on a single point is known as the *horizon* of that single point, while all the parts of the Universe that can interacts with these are said to be *causally* connected.

In a thermal equilibrium, the plasma behaves as a *black body*, an entity that emits all the radiation absorbed with a spectral distribution that only depends on its temperature. The mean number of photons per oscillation mode is

$$\begin{aligned} \mathcal{N} &= \frac{1}{e^{\hbar\omega/kT}-1} \\ &= \frac{1}{e^{hc/kT\lambda}-1} \end{aligned} \tag{1.5.1}$$

where $\omega = 2\pi\nu$ is the angular frequency, $\hbar = h/2\pi$ is the reduced Planck constant and k is the Boltzmann constant. For the adiabaticity (no interactions with other fields occur because the frequencies of radiation are much more larger than the expansion rate, [1]) $\mathcal{N}$ is independent of time, but the expansion of the universe stretches the wavelength as $\lambda \propto a(t)$. This implies, as the Universe expands, that the temperature scales as

$$T \propto \frac{1}{a(t)}, \tag{1.5.2}$$

that means that the temperature of the radiation is proportional to $1+z$,

$$T(t) = T_0 a_0/a(t) = T_0(1+z). \tag{1.5.3}$$

In order to derive the radiation spectrum for the radiation energy, we report the expression for the number of photons per unit volume with (angular) frequency ω in the interval $d\omega$ moving in any direction ($d\Omega = 4\pi$)

$$dN = n(\omega)d\omega = \frac{1}{\pi^2 c^3}\frac{\omega^2 d\omega}{e^{\hbar\omega/KT}-1} \tag{1.5.4}$$

This number density function does not change its shape even during the expansion of the Universe.

The blackbody radiation energy $u(\omega)d\omega$ is the Eq. 1.5.4 times the energy of each photon $\hbar\omega$

$$u(\omega)d\omega = \frac{\hbar}{\pi^2 c^3}\frac{\omega^3 d\omega}{e^{\hbar\omega/kT}-1}, \tag{1.5.5}$$

that is known as the *Planck distribution*. Usually in astrophysics, this quantity is given in unit of erg sec $^{-1}$ cm^{-3} Hz^{-1}. The same quantity is often referred as emission per solid angle, then divided by 4π. Another way to express the

radiation spectrum is the *surface brightness*, that is the Eq. 1.5.5 divided by 4π and multiplying by the speed of light c

$$i(\nu)d\nu = \frac{2h}{c^2}\frac{\nu^3 d\nu}{e^{h\nu/kT}-1}, \tag{1.5.6}$$

where the $\nu = \omega/2\pi$ is the change between angular frequency and frequency. When $h\nu \ll kT$, Eq. 1.5.6 can be approximated with a Taylor series to the first order

$$i(\nu) = 2kT\nu^2/c^2, \tag{1.5.7}$$

that is known as the *Rayleigh-Jeans approximation*. Later we will discuss better these quantities, introducing unities to measure them.

Integrating over frequencies we get the radiation energy per unit volume

$$u = \int_0^\infty u(\omega)d\omega = \frac{\pi^2}{15}\frac{(kT)^4}{(\hbar c)^3} = a_B T^4, \tag{1.5.8}$$

where $a_B = 7.56 \times 10^{-15}$ erg cm^{-3} K^{-4}.

The radiation density is obtained dividing Eq. 1.5.8 by c^2

$$\rho_{\rm rad} = \frac{a_B T^4}{c^2} = \frac{a_B}{c^2}T_0^4(1+z)^4. \tag{1.5.9}$$

We have seen in Eq. 1.3.14 that the matter density scales as a function of $(1+z)^3$, thus there has been an epoch at high redshift that the Universe was dominated by radiation. We can find the value of the corresponding scale factor recalling that the matter density is

$$\rho(t) = \frac{1}{a(t)^3}\frac{3H_0^3}{8\pi G} \tag{1.5.10}$$

and

$$a(t) = \frac{8\pi G a_B T_0^4}{3H_0^2 c^2}\frac{1}{\Omega} \simeq 2.5 \times 10^{-5}\Omega^{-1}h^{-2}, \tag{1.5.11}$$

which has redshift

$$1 + z_{eq} = \frac{1}{a(t)} \simeq 4 \times 10^4 \Omega h^2. \tag{1.5.12}$$

The most recent value for z_{eq} has been given by the 7-years WMAP data, $z_{eq} = 3196^{+134}_{-133}$, [9]. We can calculate the time at which matter density and radiation density were equivalent (from Eq. 1.3.32)

$$t(z_{\rm eq}) = \frac{2}{3}\frac{1}{\Omega^{1/2}H_0(1+z_{\rm eq})} \simeq 2.6 \times 10^{10}\Omega^{-2}h^{-4} \text{ seconds} \tag{1.5.13}$$

Before this time, the expansion of the Universe has been dominated by the radiation, after this time it is matter dominated.

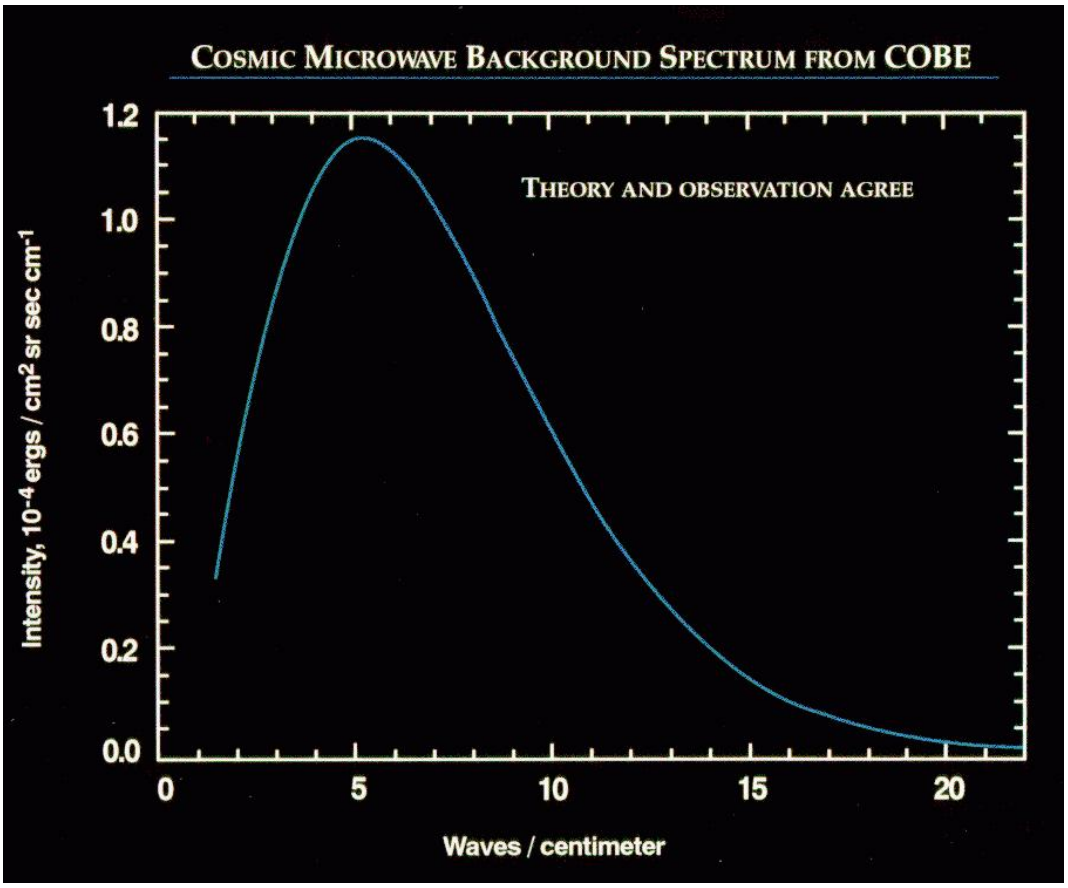

Figure 1.3 Spectrum of the Cosmic Microwave Background from the FIRAS instrument at the north Galactic pole.

1.5.1 The Cosmic Microwave Background

We have mentioned the radiation temperature in Eq. 1.5.9, where the temperature T_0 is some certain value that is measurable and that can tell us what was the temperature at the time of equivalence. The temperature T_0 is the temperature of the *Cosmic Microwave Background*, or CMB

$$T_0 = 2.735 \pm 0.06 \text{ Kelvin}, \tag{1.5.14}$$

that is the result of the FIRAS instrument mounted on the COBE satellite, that is the first generation of satellite for the measurement and the study of the CMB and its features, [12]. The measurement has confirmed that the CMB is a perfectly thermalized blackbody at the temperature T_0 (see Fig. 1.3).

The discovery of the CMB has one curious aspect: the debate on the evolution of the Universe (steady-state model or expansion) has taken place for decades, and the same theorists of the evolution struggled between a hot early

universe (the Big Bang) and a cold one. The abundance of helium observed in the universe (about 26%) was a heritage of a hot and dense primordial universe, as pointed out in the paper of Gamow and Alpher (the famous $\alpha - \beta - \gamma$ paper) who first described the potential physics that could be involved. In 1948 Alpher and Herman published a paper with the description of a relic radiation, filling the whole space with blackbody distribution, cooled at 5 K as proof of the expansion of the Universe. After several years, Robert Dicke from Princeton University and his collaborator P.J.E. Peebles concentrated their effort not only on the calculation of the temperature (they gave a value of 10 K) but also in the possible way to find the relic radiation. That was in 1964. In the same year, a couple of radio astronomers, A. Penzias and R. Wilson working for the Bell Telephone Company, started some calibration works on a radio antenna in Holmdel, New Jersy, not very far from Princeton. They were continuously receiving a signal, independently of the direction of the antenna. After one year trying to understand the nature of such excess signal, they came across the Peebles work and invited Dicke to Holmdel for a demonstration. The Cosmic Microwave Background was finally discovered, meaning the victory of the Big Bang model over other models. Penzias and Wilson were granted the Nobel's prize in 1978.

The discovery of the CMB has opened the door to the *cosmology* science, since the radiation itself is full of information on the early stages of the Universe.

1.5.2 Thermal properties

In the hot plasma that constitutes the early Universe, radiation and matter are strictly coupled and the high radiation pressure keeps the matter fully ionized, in a continuous reaction

$$e + p \leftrightarrow \mathrm{H} + \gamma \tag{1.5.15}$$

where the net balance of the chemical potential is

$$\mu(e) + \mu(p) = \mu(\mathrm{H}). \tag{1.5.16}$$

The chemical potential comes useful in the calculation of the number density of particles per unit volume

$$n = g\frac{(2\pi mkT)^{3/2}}{(2\pi\hbar)^3}e^{(\mu - mc^2)/kT}, \tag{1.5.17}$$

where g is the number of the spin states (2 for protons and electrons and 4 for the hydrogen atom in its ground state). The Saha *thermal ionization equilibrium equation* relates the number densities to the ionization fraction $x = n_e/n$:

$$\frac{n_e n_p}{n_H n} = \frac{x^2}{1-x} = \frac{(2\pi m_e kT)^{3/2}}{n(2\pi\hbar)^3} e^{-B/kT}, \tag{1.5.18}$$

where $B = 13.60$ eV is the binding energy of the electron and proton respect the hydrogen atom. Beside the Ω parameter for the matter, we must introduce a restricted parameter for only baryon matter content, Ω_b, related to the number density through the relation

$$n = 1.12 \times 10^{-5} \Omega_B h^2 (1+z)^3 \text{ cm}^{-3}. \tag{1.5.19}$$

Using the scale relation for the temperature of Eq. 1.5.14, we can calculate $d\log x/d\log z$,

$$\log[x^2/(1-x)] = 20.99 - log[\Omega_b h^2 (1+z)^{3/2}] - 25050/(1+z). \tag{1.5.20}$$

For a ionization fraction of $x = 0.5$, we can calculate the redshift at *decoupling*

$$z_{\text{dec}} \sim 1300, \tag{1.5.21}$$

with a temperature of

$$T_{\text{dec}} = T_0 z_{\text{dec}} \sim 3000 \text{ K}. \tag{1.5.22}$$

Recent releases of WMAP data report the precise measurement of the redshift for the decoupling, $z_{\text{dec}} = 1088.2 \pm 1.2$, [9].

The decoupling is maybe the most important event in observational cosmology. Photons, previously coupled to matter, are now free to stream away, with a typical path compared to the horizon of the Universe at that time. The redshift at which the coupling happens is usually referred as the *Last Scattering Surface*, the light emerging is what we observe in the present as CMB.

1.5.3 Recombination

The recombination is the transition phase that follows decoupling. It refers to the formation of hydrogen atoms via the capture of the electron in the coulombian field of the proton. But there was no previous catch in the thermal history of the universe and the term 'recombination' is used improperly. Through expansion and cooling, the primeval plasma is free to combine to atomic hydrogen at the same redshift of the decoupling phase.

The electron can be captured in the ground state: in this case, the loss of energy of the electron gives birth to a photon that ionizes another atom, leaving no net change. The production of atomic hydrogen passes through the capture in an excited state. If the electron is captured in the metastable state $2s$, the atomic hydrogen is formed with the two-photon decay, [13]

$$\begin{aligned} p + e &\rightarrow \mathrm{H}^* + \gamma_1, \\ \mathrm{H}^* &\rightarrow \mathrm{H} + \gamma_2. \end{aligned} \tag{1.5.23}$$

This transition is parametrized through the rate $\Lambda = 8.23\,\mathrm{s}^{-1}$ (not to be confused with the cosmological parameter). Besides the two-photon decay, it is present the allowed transition $2p \rightarrow 1s$ that gives birth to a Lymann-α (Lyα) emission. The net rate of production of hydrogen per unit volume is

$$\alpha_b n_e^2 - \beta_e n_{2s} = R + \Lambda \left(n_{2s} - n_{1s} e^{h\nu_\alpha / kT} \right), \tag{1.5.24}$$

where $\alpha_b = 2.6 \times 10^{-13}\mathrm{cm}^3\mathrm{s}^{-1}$ is the *case B* recombination coefficient, R is the rate for the allowed Lyα transition and ν_α is the frequency. The factor β_e is just the Saha relation for the thermal equilibrium between the states n_{2s} and n_e^2, found in Eq.1.5.18 but with the binding energy $B_2 = 3.4$ eV of the level $n = 2$. From the above equation is possible to calculate the time variation of the ratio between electron density and baryon density

$$-\frac{d}{dt}\frac{n_e}{n} = \left(\frac{\alpha_b n_e^2}{n} - \frac{\beta_e n_{1s}}{n} \right) C. \tag{1.5.25}$$

The constant C takes into account the expansion of the Universe that introduces a redshift in the wavelength of the Lyα photons.

In the absence of reionization sources, at low redshifts the Universe is almost completely neutral. Scaling formula can be found in Peebles (1993), [1].

Residual electrons give birth to molecular hydrogen H_2, via the reaction chains

$$\begin{aligned} \mathrm{H} + e &\leftrightarrow \mathrm{H}^- + \gamma \\ \mathrm{H}^- + \mathrm{H} &\leftrightarrow \mathrm{H}_2 + e \end{aligned} \tag{1.5.26}$$

and

$$\begin{aligned} \mathrm{H} + p &\leftrightarrow \mathrm{H}_2^+ + \gamma \\ \mathrm{H}_2^+ + H &\leftrightarrow \mathrm{H}_2 + p. \end{aligned} \tag{1.5.27}$$

The first reaction has a binding energy of $B_- = 0.75$ eV and can produce molecular hydrogen at relatively low redshift, while the second chain has a binding energy of $B_+ = 2.65$ eV and requires higher redshifts. The second case reaches the equilibrium, described by the Saha equation

$$\frac{n_{2+}}{n_p} = \frac{n(2\pi\hbar)^3}{(2\pi m_p kT)^{3/2}} e^{B_+/kT}, \tag{1.5.28}$$

that reaches the unity at a redshift $z_f = 200$ in an expanding universe, [14].

1.5.4 Helium and light nuclei

Last step in this brief summary of the thermal history of the Universe is the production of helium, one of the constituent of the diffuse gas. The nucleus of helium consists in two protons and two neutrons, hence the necessity for a chain to form neutrons out from protons:

$$\begin{aligned} e^- + p &\leftrightarrow n + \nu, \\ \bar{\nu} + p &\leftrightarrow n + e^+, \\ n &\leftrightarrow p + e^- + \bar{\nu}. \end{aligned} \tag{1.5.29}$$

The ratio between neutron and proton is kept in thermal equilibrium for plasma temperatures grater than $Q = (m_n - m_p)c^2 = 1.2934$ MeV (1 MeV $\sim 1.1 \times 10^{10}$ Kelvin)

$$n/p = q^{-Q/kT}. \tag{1.5.30}$$

In the reaction 1.5.29, the pair neutrino-antineutrino plays a determinant role and the final abundance of helium is strictly related to the number of species of neutrino, that in the standard model is set to be $N_\nu = 3$. The reaction between a proton and a neutron creates deuterium (a stable isotope of the hydrogen formed by a proton and a neutron in its nucleus)

$$n + p \leftrightarrow d + \gamma \tag{1.5.31}$$

. The inverse process (photo-dissociation) destroys deuterium faster than its formation, until temperature drops below $kT \sim 100$ KeV. At this point, the formation of helium ^{4}He is favored through the intermediate production of tritium (isotope of the hydrogen, which nucleus has two neutrons and one proton) and

the isotope ^{3}He:

$$\begin{aligned} d + d &\leftrightarrow t + p, \\ d + d &\leftrightarrow {}^3\mathrm{He} + n, \\ t + d &\leftrightarrow {}^4\mathrm{He} + n, \\ {}^3\mathrm{He} + d &\leftrightarrow {}^4\mathrm{He} + p. \end{aligned} \tag{1.5.32}$$

Through the reactions in 1.5.29, 1.5.31 and 1.5.32 is worth noting that the formation of helium and light nuclei is the result of a fine balance of different equilibria, involving temperatures that favor different reactions, relative abundance and recombination times respect the Hubble time. Details are to be found in Bernstein, Brown & Feinberg (1989), [15], and Peebles (1983), [1]. Here, it is worth mentioning the neutron abundance respect baryons:

$$\frac{n_n}{n_n + n_p} \equiv x(t) = x_0 e^{-\int_{t_0}^{t} (\lambda + \hat{\lambda}) dt'} + \int_{t_0}^{t} \frac{\lambda}{\lambda + \hat{\lambda}} de^{-\int_{t_0}^{t} (\lambda + \hat{\lambda}) dt''} \tag{1.5.33}$$

where $\lambda = \lambda_1 + \lambda_2$ and $\hat{\lambda} = \hat{\lambda}_1 + \hat{\lambda}_2 + \lambda_d$. Here, λ_1 and $\hat{\lambda}_1$ are respectively the probabilities per unit time of the reactions $p + e^- \leftrightarrow n + \nu$ (λ_1 for the production, $\hat{\lambda}_1$ for the decay), while λ_2 and $\hat{\lambda}_2$ are the probabilities for the reactions $p + \bar{\nu} \leftrightarrow n + e^-$. Finally λ_d is the probability for the decay of neutron through the reaction $n \rightarrow p + e^- + \nu$. Number of species of the neutrinos play an important role in the numerical integration of Eq. 1.5.33. The equilibrium for the deuterium for the reaction $n + p \leftrightarrow d + \gamma$ is found via the Saha equation

$$\frac{n_p n_n}{n_d n} = \frac{4}{3} \left(\frac{m_p m_n}{m_d} \right)^{3/2} \frac{(2\pi k T)^{3/2}}{(2\pi\hbar)^3 n} e^{-B/kT}, \tag{1.5.34}$$

where $n = 1.124 \times 10^{-5} \Omega_B h^2$ cm^{-3} is the actual number density for baryons and $B = 2.225$ MeV is the binding energy for deuteron. The number N_ν of neutrino families is the parameter that fixes the neutron abundance at different temperatures, along with the baryon density Ω_B. The value for the baryon density has been refined in the last cross-measurements from WMAP seventh years, $\Omega_B h^2 = 0.02258^{+0.00057}_{-0.00056}$, while the primordial helium fraction is $Y_{\mathrm{He}} = 0.28^{+0.14}_{-0.15}$, that is higher than the previous estimation of $Y_{\mathrm{He}} = 0.249$, [16]. For N_ν has been estimated a lower limit $N_\nu > 2.7$(95% CL), accordingly with N_ν reported in Peebles (1993).

1.6 Dark Matter

All the previous sections have treated the ordinary matter, matter that is formed by baryons and that is often associated to a luminous emission such as stars or gas clouds. But it has been known from the 1930s that a *missing mass* is responsible for bounding the Virgo and Coma clusters, [17, 18]. Since then, the term of missing mass has been gradually substituted by the term *dark matter* and with time has begun one of the most discussed paradigms in astrophysics, since it appears to be the largest contribution to the matter density. Furthermore, the dark matter paradigm is puzzling not only for cosmologists, but even also for particle physics, it is deeply involved in finding and defining limits for the candidates.
For quite a long time, the dark matter has been associated to a baryonic component not directly measurable, as low mass stars, stars remnants and planets. Anyway, in Gott et al. (1974), [19], the authors noticed that if $\Omega_B \sim 1$, this could not explain the observed deuterium abundance that would have burnt into helium due to the high density of matter in primeval state of Universe. From this consideration, leaving a reasonable fraction of dark matter as still baryonic, most of it has to be something exotic, that does not participate in element-building reactions.

A hypothetical non-baryonic dark matter candidate was a particular family of massive neutrinos (few tens of eV) that can be produced in nuclear beta decay. This neutrino could be a perfect non-baryonic candidate to explain some properties of rich galaxy clusters, but it is not able to explain some behavior of dwarf galaxies. Some of the problems of massive neutrinos were: first, the refinement of the measure of the Hubble's constant h, that was no more compatible with the mass of a family of neutrinos, that needs to be smaller, second, a primeval universe were fluctuations in radiation, baryons and neutrinos are Gaussian, scale-invariant and adiabatic, would encounter a real problem to form structures. Anyway these critics could be removed by considering another family of massive neutrinos or shifting the formation of structures in a non-adiabatic scheme. Nonetheless, the combination of the two critics found a better solution in realizing that particle physics would offer different candidates to maintain both the initial adiabatic conditions and the robust galaxy formation model.

Because neutrinos were relativistic and exhibited a pressure at $z \sim z_{\rm eq}$, they are

indicated with the term *hot dark matter* (HDM), while pressureless candidates are indicated with the term *cold dark matter* (CDM).
Baryonic matter in non-emitting form has been ruled out on the basis of the observable mass-to-light ratio of our galaxy ($\mathcal{M}/L = 2.2(\mathcal{M}_\odot/L_\odot)$). The presence of high quantity of hydrogen in brown dwarfs and neutron stars is ruled out by the fact that most of the mass of the preceding stars is expelled and then reprocessed in new stars formation. The capture of an important fraction of molecular hydrogen in cometlike snowballs has to be ruled out. Comets form by elements that *are not* hydrogen via chemical reactions that bind them together. The only way for molecular hydrogen to form comets is through gravitational attraction, but at the temperature of the CMB, $T_0 = 2.725$ K, the minimum mass required for a stable hydrogen formation is six orders of magnitude grater than the observed comets of the solar system (see calculations in Peebles 1993, [1]). Similar mass-to-light ratios to the one reported for the Milky Way have been found for the cores of other galaxies in the neighborhood, indicating that baryonic matter cannot widely exceed the luminous matter. This indicates that the bulk for the dark matter is still to be found in non-baryonic matter.

1.6.1 Cold Dark Matter

CDM is today accepted as the most plausible candidate for fulfilling the matter parameter Ω. The shift of attention from the HCD (neutrinos) to the CDM is mainly due to elegant way to explain galaxy formation. The particles to be thought as CDM would have to be nonrelativistic at the time first fluctuations formed, in order to allow them to grow until dark matter becomes self-gravitating at $z \sim z_{\rm eq}$. Dark matter is at equilibrium with the CMB at the temperature T, with small chemical potential respect kT, and the occupation number of the particles for the energy ϵ is

$$\mathcal{N} = \frac{1}{e^{\epsilon/kT} \pm 1}, \tag{1.6.1}$$

After a first phase of equilibrium between creation and annihilation, the expansion of the Universe brings the suppression of the annihilation, and the number n_f of particles is *frozen* at time t_f, at equilibrium with radiation temperature T_f. In case of non-relativistic particles, the energy can be expressed as

$\epsilon = mc^2 + p^2/2m$, and the number density at freezing is

$$\begin{aligned} n_f &= \int \frac{4d^3p}{(2\pi\hbar)^3} e^{-p^2/2mkT_f} e^{-mc^2/kT_f} \\ &= \left(\frac{mkT_f}{2\pi\hbar}\right)^{3/2} e^{-mc^2/kT_f}. \end{aligned} \tag{1.6.2}$$

This number is diluted through the expansion, and an estimate for present value holds

$$\rho_d = \frac{n_f m}{(1+z_f)^3} = \frac{3H_0^2\Omega_d}{8\pi G}, \tag{1.6.3}$$

where the mass m is to be estimated. The density parameter Ω_d is of the order of unity for masses between 2 and 10 GeV.

A candidate in this range of mass are the *weakly interacting massive particles* or WIMPs. WIMPs are been introduced in the framework of the supersimmetry (SUSY), a step ahead of the standard model of particle physics. To the *lightest supersimmetric particle* (LSP) has been given the name of neutralino, and is the candidate for the WIMP CDM. Neutralino must have very small, but a still measurable cross section with ordinary matter, provided by weak force. Mass range for the neutralino spans from 10 to 1000 GeV. Experiments for the detection and measurements of WIMPs are on going or planned. A indirect measurement consists of the detection of some neutrinos produced by the annihilation of WIMPs captured in great quantity by the Sun. But the most promising experiments has been the *cryogenic dark matter search* (CDMS) in Sudan Mine (Minnesota, US), where two events between supposed WIMPs and an array of detectors (made up by germanium and silicon cooled at 50 μK) have been recorded. Despite the uncertainty of the nature of the detections (that might have been produce by some sort of decay in the background particles), the reported mass is in the range 7 - 11 GeV, as the same order expected for the WIMP dark matter.

The other accepted candidate for cold dark matter is the *axion*. The axion is a lightweight boson. Standard model in particle physics predicts the violation of the either charge (C) and parity (P, together CP) for strong nuclear interactions. If the CP is violated, an electric dipole momentum in neutrons is expected, but this has never been observed. In 1977, Peccei and Quinn have introduced a new symmetry that violates the CP spontaneously, [20], but this involves a massless quark. Massless quarks have never be endemonstrates to exist, hence later the axion has been introduced to take that role. Axions are expected to have very

light masses, $10^{-6} - 1$ eV, and to interact very weakly with ordinary matter. Due to its low mass, axions must be present in the Universe in the state of a Bose-Einstein condensate (BEC), confined in a potential and cooled to almost 0 K. Several experiments are operating for the detection of axions: the Italian *Polarizzazione del Vuoto con LAser* (PVLAS) has succesfully announced in recent years the detection of axions, but soon after, international particle physics community and the same PVLAS team announced that the result had to be rejected. The *CERN Axion Solar Telescope* (CAST) tries to detect axions produced in the interior of the Sun by the scattering of X-rays over electrons and protons in the presence of strong electric fields. These axions are then reconverted into X-rays in the laboratory using strong magnetic fields. A first phase has been accomplished without any trace of the particle, but restricting the range of mass. A second phase is running. Another experiment is the *Axion Dark Matter Experiment* (ADMX), that consists of a *haloscope*, an instrument capable to detect the axions filling the halo dark matter around our galaxy. The axions would be converted into photons by strong magnetic fields, and the photons detected in a vacuum chamber at resonance frequency of 460 - 810 MHz. Detection of relevant events are still expected. A review of latest results on the axion dark matter theory can be found in Duffy & van Bibber (2009), [21].

1.6.2 Alternatives to the Dark Matter

One of the most decisive evidences in favor of the DM model is the rotational curve of spiral galaxies. In Fig. 1.4 is reported the result from van Albada et al. (1985), [22], where the radial velocity of the gas in the galaxy NGC 3198 is measured as a function of the radius. The only disk, which is accounted for all the matter in the classical model without DM, cannot reproduce the data points. The rotation elements in a spiral galaxy are in equilibrium where gravitational attraction counterbalances the centripetal force

$$\frac{GM_{\rm disk}m}{r^2} = \frac{m}{r}v^2 \tag{1.6.4}$$

and velocity has to show an inverse law $v = \sqrt{GM/r}$. But the rotation curve in the figure is flat, and is explained with the introduction of the *halo* of DM that surrounds the galaxy.

In the effort to explain this behavior, Mordehai Milgrom proposed a modifica-

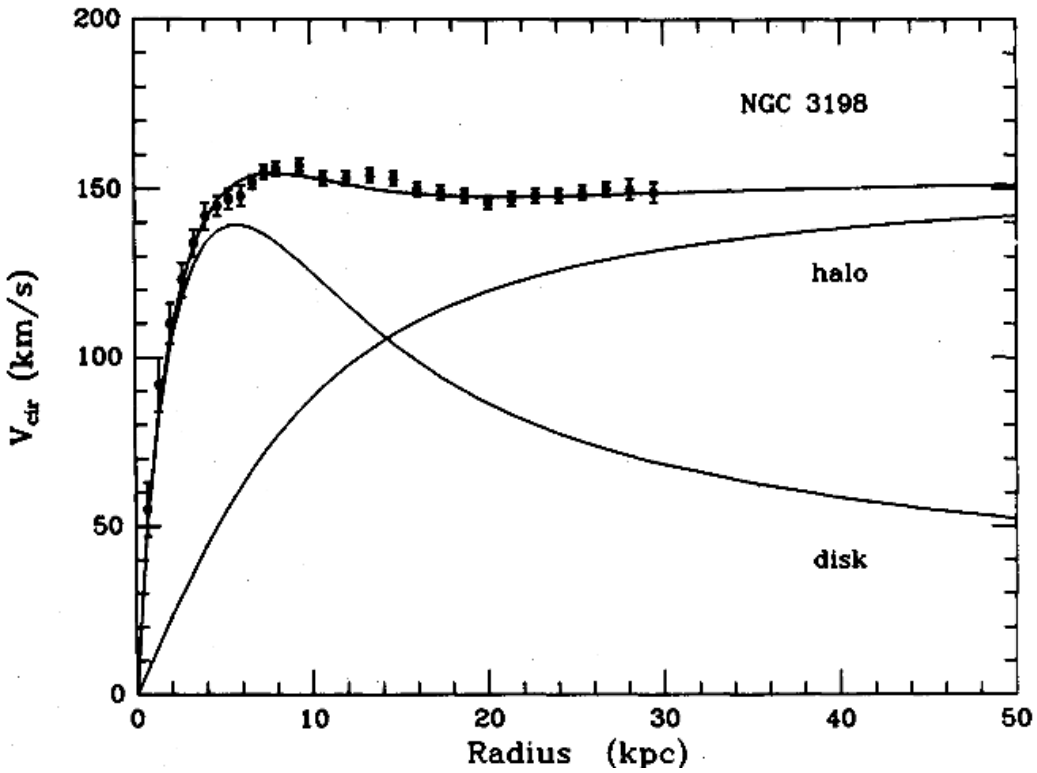

Figure 1.4 Rotation curve for NGC 3198, from van Albada et al. (1985), [22]. The data points describe a flat curve, that is a superposition of two components: the baryonic matter (disk) and the dark matter component (halo).

tion of the Newton physics [23–25]. The proposed modification is

$$\frac{GMm}{r^2} = m\mu(x)a, \tag{1.6.5}$$

where $\mu(x \gg 1) \approx 1$, $\mu(x \ll 1) \approx x$ and $x = a/a_0$. The classical Newtonian acceleration is a, while $a_0 \approx 10^{-10}$ m sec^{-2}. Hence, when the ordinary acceleration is much greater than a_0, we get the usual second law of Newton $F = ma$. But in the external part of galaxies, the acceleration a induced by the central disk can drop to values lower than a_0. In this case, eliminating m in Eq. 1.6.5

$$\frac{GM}{r^2} = \frac{a^2}{a_0} \tag{1.6.6}$$

then, considering the acceleration in a central field

$$a = \frac{v^2}{r} = \frac{(GMa_0)^{1/2}}{r}. \tag{1.6.7}$$

The velocity of rotation curve is

$$v = (GMa_0)^{1/4} \tag{1.6.8}$$

that is a naturally flat curve.

MOND is an interesting alternative to DM, as it can fit the rotation curves of galaxies with high accuracy, regardless of their type. Some applications to fit MOND's critical acceleration a_0 to different scales have been successful, [26]. Nonetheless MOND seems to fail when predicting accelerations on galaxy cluster and cosmological scale.
Another alternative conceptually similar to the MOND is the *theory of modified gravity* or MOG, proposed by Moffat in 2006, [27]. The author introduces a composed potential $\Phi(r) = \Phi_N(r) + \Phi_Y(r)$, where $\Phi_N(r)$ is the classical Newtonian potential and

$$\Phi_Y(r) = \sigma \frac{e^{-\mu r}}{r}, \tag{1.6.9}$$

is the Yukawa potential, derived from particles physics. In this potential, σ is a function of the mass M_0, a parameter to be estimated according to the mass of the system one is interested with and μ is the effective mass of the particle vector in the scalar-tensor-vector gravity (STVG). The gravity acceleration, for a spherical symmetry, depends on a function $G(r)$, instead of the usual Newton's constant G

$$a(r) = -\frac{G(r)M(r)}{r^2}, \tag{1.6.10}$$

where the function $G(r)$ depends on the MOG mass scale M_0 and on the MOG range scale r_0. When r tends to zero, $G(r)$ tends to the Newtonian value of G. The author examines different cases of interest in astrophysics and cosmology and claims that remarkably successes has been achieved. MOG seems to fit well for a single galaxy as well as a galaxy cluster and it is the only theory (stated by the author) capable to explain the anomalous acceleration of the Pioneer 10 and 11 spacecrafts outside the Solar system. The frame is completed by the MOG's prediction of the acoustic peaks featured in the angular power spectrum of the Cosmic Microwave Background.

Since its formulation, MOG gives an excess of mass to the baryons. Since dark matter is strictly coupled to baryons, in principle there is no way to distinguish the two theories. Fortunately, in recent years, a powerful dark matter test has been observed.

Figure 1.5 The reconstructed image of the cluster 1E0657-558, commonly named *Bullet cluster* for its unique feature to show a merger between two subclusters on the plane of the sky. The emission from the hot ICM gas is shown in red color (false) from the central region, while the convergence map which indicates the potential, is shown in blue.

1.6.3 A laboratory for the Dark Matter: the Bullet Cluster

The Fig. 1.5 shows the cluster 1E0657-558, in a reconstructed image that enhance its unique feature, the separation between the collisionless component (dark matter and galaxies) and the collisional component, the ICM gas.

The cluster, located at $z = 0.296$, has been identified by Tucker et al. (1998), [28] and a deeper analysis has been carried out by Clowe et al. (2006), [29]. The analysis consists of a X-ray observation through the *Chandra* satellite, and a set of optical observation performed with various telescopes, the 2.2 meters at ESO/MPG, the 6.5 meters at the Magellan IMACS and the Advanced Camera for Surveys (ACS) mounted on the Hubble Space Telescope (HST). The cluster is composed of two components, a main cluster (east-side in figure) and a subcluster (west-side), separated by 0.72 Mpc on the sky. The X-ray image, though,

gives a different picture, with a huge concentration of hot ICM gas located between the two clusters. Even if this configuration appears to be very special, it is no surprising since the galaxy component and the gas have two different behaviors when a merger between clusters occurs. In fact, galaxies are to be treated as collisionless, due to the large separation between them. Gas has to be treated properly as a viscous component with phenomena of friction when the two clouds cross.

The test for the dark matter arises when reconstructing the convergence map. As will be explained in the section about gravitational lensing, huge gravitational potentials produce a coherent distortion (*shear*) of the image of the background galaxies. The shear can be measured and makes it possible to reconstruct the radial profile of the mass density. Clowe et al. (2006) analyzed the shear field. Since the mass of the gas component for a cluster (see later) is higher than the combined mass of the galaxies, one could expect that the radial density profile will be centered on the ICM cloud. Surprisingly, the shear analysis confirms that the radial profile is split and centered on the two clusters visible in the optical images. This leads to the conclusion that the main mass is not the ICM, but neither can be the galaxies. Clowe et al. (2006) state that this is a direct empirical proof of the existence of dark matter, since its collisionless nature will locate its peaks at the same location of the galaxies.

The Bullet cluster remains the only observed cluster merger where the components separation appears so distinctive. The discovery has open a new window in different fields: hydrodynamical simulations have been run to test the initial velocities of the two clusters before merging to simulate the shock fronts that are observed, large ΛCDM simulations (see later) with high spatial resolution have evidenced that a similar separation between components is expected in 1-2% of the clusters with masses larger than $10^{14}\mathcal{M}_{\odot}$, [30]. A supposed similar merger has been observed for the cluster CL0024 through the lensing analysis performed by Jee et al. (2007), [31] (see Chapter 4), but along the line of sight and not on the plane of the sky. Moreover, the theories that propose an alternative to the Dark Matter have tried to explain the dynamical state of the Bullet cluster. MOND seems to fail in the prediction of the observed convergence map, while in a recent paper by Brownstein and Moffat (2007), [32], the modified gravity (MOG) has been applied successfully to reconstruct the surface mass density. Nonetheless, the dark matter paradigm remains the most

robust workframe for the observed separation of the two components.

1.7 Statistics of density field

The basic quantity to study the statistics for the density field is the variance $< \delta^2 >$. The variance is calculated sampling the same event in several repetitions of a process. But our observations are limited to a single Universe, hence it does not constitute an *ensemble*. Nonetheless, the density fluctuations in different parts of the sky are non-correlated, hence they can be treated as independent and the average can be done over a volume rather than over the number events of the ensemble.

1.7.1 Correlation function

The first quantity to be defined is the *two-point correlation function*, $\xi(r)$, [1] defined through the probability that two point processes (galaxies or overdensity) are found in the two volume elements dV_1 and dV_2 placed at a separation r

$$dP = n^2 dV_1 dV_2 [1 + \xi(r)]., \tag{1.7.1}$$

where n is the number density. Giving a function dependent on the position $\mathbf{r}$, for which $dP = f(\mathbf{r})dV_1 dV2$ and $n = \langle f \rangle$, we can find

$$n^2 \xi(r_{12}) = \langle f_1 f_2 \rangle - n^2 = \langle (f_1 - n)(f_2 - n) \rangle, \tag{1.7.2}$$

where $f_1 = f(r_1)$ and $r_{12} = |\mathbf{r}_1 - \mathbf{r}_2|$. We can consider our function f, the density at the position $\mathbf{r}$, $\rho(\mathbf{r})$. The average over a volume is $\langle \rho(\mathbf{r}) \rangle = \rho_b$, and substituting into Eq. 1.7.2 we get

$$\xi(|\mathbf{r}_1 - \mathbf{r}_2|) = \frac{\langle (\rho(\mathbf{r}_1) - \rho_b)(\rho(\mathbf{r}_2) - \rho_b) \rangle}{\rho_b^2}, \tag{1.7.3}$$

that is the *dimensionless autocorrelation function*. The quantity expressed above is the product between two overdensities, and a simple change of variables $\mathbf{r} = \mathbf{r}_2 - \mathbf{r}_2$ results in

$$\xi(\mathbf{r}) = \langle \delta(\mathbf{r}) \delta(\mathbf{r}_1 + \mathbf{r}) \rangle \tag{1.7.4}$$

that is the standard expression for the correlation function of the density field, where the angle brackets indicate the average over a volume V with periodic boundary conditions. The boundary conditions are formally expressed by the

wavevectors $\mathbf{k} = 2\pi\mathbf{n}/L$, where L is the side of the volume and the vector $\mathbf{n}$ is a triplet of integers, positive or negative.

1.7.2 Power spectrum

It is possibleto compute the Fourier transform of the correlation function (see Eq. 1.4.26)

$$\xi(\mathbf{r}) = \left\langle \sum_{\mathbf{k}} \sum_{\mathbf{k}'} \delta_{\mathbf{k}} \delta^*_{\mathbf{k}'} e^{i(\mathbf{k}-\mathbf{k}')\cdot\mathbf{r}_1} e^{-i\mathbf{k}\cdot\mathbf{r}} \right\rangle. \tag{1.7.5}$$

The periodic boundary conditions of the volume make the cross term $\mathbf{k} \neq \mathbf{k}'$ to cancel on average, while the real field $\delta(\mathbf{r})$ has the property $\delta_{\mathbf{k}}(-\mathbf{k}) = \delta^*_{\mathbf{k}}(\mathbf{k})$, [2]. Passing to the integral

$$\xi(\mathbf{r}) = \frac{V}{(2\pi)^3} \int |\delta_{\mathbf{k}}|^2 e^{-i\mathbf{k}\cdot r} d^3k, \tag{1.7.6}$$

where is evident that the correlation function is the Fourier transform of the quantity

$$\mathcal{P}(k) \equiv \langle |\delta_{\mathbf{k}}|^2 \rangle, \tag{1.7.7}$$

which is the *power spectrum*. The vector notation $\mathbf{k}$ can be dropped because the isotropy of the space, $\langle |\delta_{\mathbf{k}}|^2(\mathbf{k}) \rangle = |\delta_k|^2(k)$. The last step is to express the integral in 1.7.6 in polar coordinates, $d^3k = k^2 dk d\Omega$. The spherical symmetry makes it trivial to integrate over the angular part

$$\xi(r) = \frac{V}{(2\pi)^3} \int 4\pi \mathcal{P}(k) \frac{\sin kr}{kr} k^2 dk. \tag{1.7.8}$$

Alternatively, the power spectrum can be expressed in the form

$$\Delta^2(k) \equiv \frac{V}{(2\pi)^3} 4\pi k^3 P(k). \tag{1.7.9}$$

A featureless power spectrum has the form

$$\langle |\delta_k|^2 \rangle \propto k^n, \tag{1.7.10}$$

and is the simplest form to represent the power spectrum in the absence of a functional form. The variance of the density contrast, when filtering the density field in a box of comoving length x is

$$\langle \delta^2 \rangle \propto \int_0^{1/x} k^n 4\pi k^2 dk \propto x^{-(n+3)}, \tag{1.7.11}$$

from which

$$\delta_{\rm rms} \propto x^{-(n+3)/2}. \tag{1.7.12}$$

A *scale invariant power spectrum* is obtained for $n = 1$, to have $\Delta^2 \propto k^4$. This spectrum is also referred as the *primordial power spectrum*, since it arises in the era of *inflation* (see details in Sect. 17 of Peebles 1993, [1]). A scale invariant power spectrum assumes that the the density perturbation evolves linearly with the Hubble length and the Universe looks always the same when seen on the Hubble length (describing the Universe similar to a fractal). A scale invariant power spectrum is the primordial power spectrum for the density fluctuations during the inflationary era.

1.7.3 CDM model

We recall some basic concepts: $z_{\rm eq}$ and $t_{\rm eq}$ are the redshift and time when the universe passes from the radiation-dominated phase to the matter-dominated phase. In the radiation era, scale factor is $a \propto 1/T$ (Eq. 1.5.2), while the expansion rate is

$$\left(\frac{\dot{a}}{a}\right)^2 = \frac{8\pi G a_b T^4}{3c^2}, \tag{1.7.13}$$

that gives $a \propto t^{1/2}$. In the radiation era, we can divide the modes of perturbation in two branches: those that are larger than the horizon (larger wavelengths, smaller ks) and those that reside inside the horizon. Conceptually, the pressure gradient force prevents the growth, while the scale factor is expanding. Indicating with k_x the breakthrough wavenumber, we have

$$\mathcal{P}(k) \sim \begin{cases} A(k_x/k)^3 & \text{for} \quad k \gg k_x\,, \\ Ak/k_x & \text{for} \quad k \ll k_x\,, \end{cases} \tag{1.7.14}$$

where A is the amplitude term.
There is another approach to describe the evolution from a primordial power spectrum Ak to a decaying mode Ak^{-n}. We consider a perturbation $h_{\alpha,\beta}$ to the line element, [1],

$$ds^2 = dt^2 - a(t)^2(\delta_{\alpha,\beta} - h_{\alpha,\beta})dx^\alpha dy^\beta. \tag{1.7.15}$$

The time evolution of the perturbation in the line of the light path is a consequence of the overdensities, either in radiation (coupled to baryons) ($\rho_{\rm r}$ and $p_{\rm r} = \rho_{\rm r}/3$) and dark matter (only density ρ_x)

$$\frac{d^2h}{dt^2}\frac{\dot{a}}{a}\frac{dh}{dt} = 8\pi G(2\rho_r\delta_r + \rho_x). \tag{1.7.16}$$

The dark matter component has the only condition for the energy conservation

$$\frac{d\delta_x}{dt} = \frac{1}{2}\frac{dh}{dt}, \tag{1.7.17}$$

while for the matter radiation fluid, there are the energy-momentum conservation equations

$$\frac{d\delta_r}{dt} = \frac{4}{3}\left(\frac{kv}{a} + \frac{1}{2}\frac{dh}{dt}\right), \tag{1.7.18}$$

and

$$\frac{dv}{dt} = -\frac{k\delta_r}{4a}. \tag{1.7.19}$$

In Peebles (1982), [33], details are given for the numerical integration of the above equations, with a resulting parametric form for the power spectrum in the era of radiation $z \ll z_{\rm eq}$

$$\mathcal{P}(k) = \frac{Ak}{(1+\alpha k+\beta k^2)^2} \tag{1.7.20}$$

where the numerator is the primordial power spectrum and the denominator is the *transfer function*. The factors α and β do depend on the matter parameter Ω and have the sizes of Mpc and Mpc^2 respectively. In Appendix A, illustrating our computations for the halo function, we use the different transfer function from Bardeen et al. (1986), [34], and we give the value for the normalization term A.

The power spectrum $\mathcal{P}(k)$ is a fundamental quantitys in cosmology and astrophysics and it can be tested with observations. A very good picture of this is shown in Fig. 1.6, from Tegmark et al. (2004), [35]. The shape of the power spectrum evolves in this way: we start from a linear, primordial power spectrum, on all scales. The inflation has expanded the overdensities to scale larger than the horizon. Fluctuations are growing on all scales, but soon as a mode enters the horizon, the growth is counterbalanced by the radiation pressure and starts to oscillate as a sound wave and smoothed by the Silk damping (see next section). This length scale corresponds to the Jeans scale seen previously (see Eq. 1.4.29). This corresponds to the right hand side of Fig. 1.6, but imagine that the overall amplitude is lower and the scale affected by the suppression is just the far end of the tail. As soon as the horizon expands, more scales enter it and get suppressed, while the modes outside the horizon keep growing. This creates the observed peak. The peak moves leftward (from higher wavenumbers to lower). The transition to the matter dominated era freezes the power spectrum since all modes now are free to grow linearly.

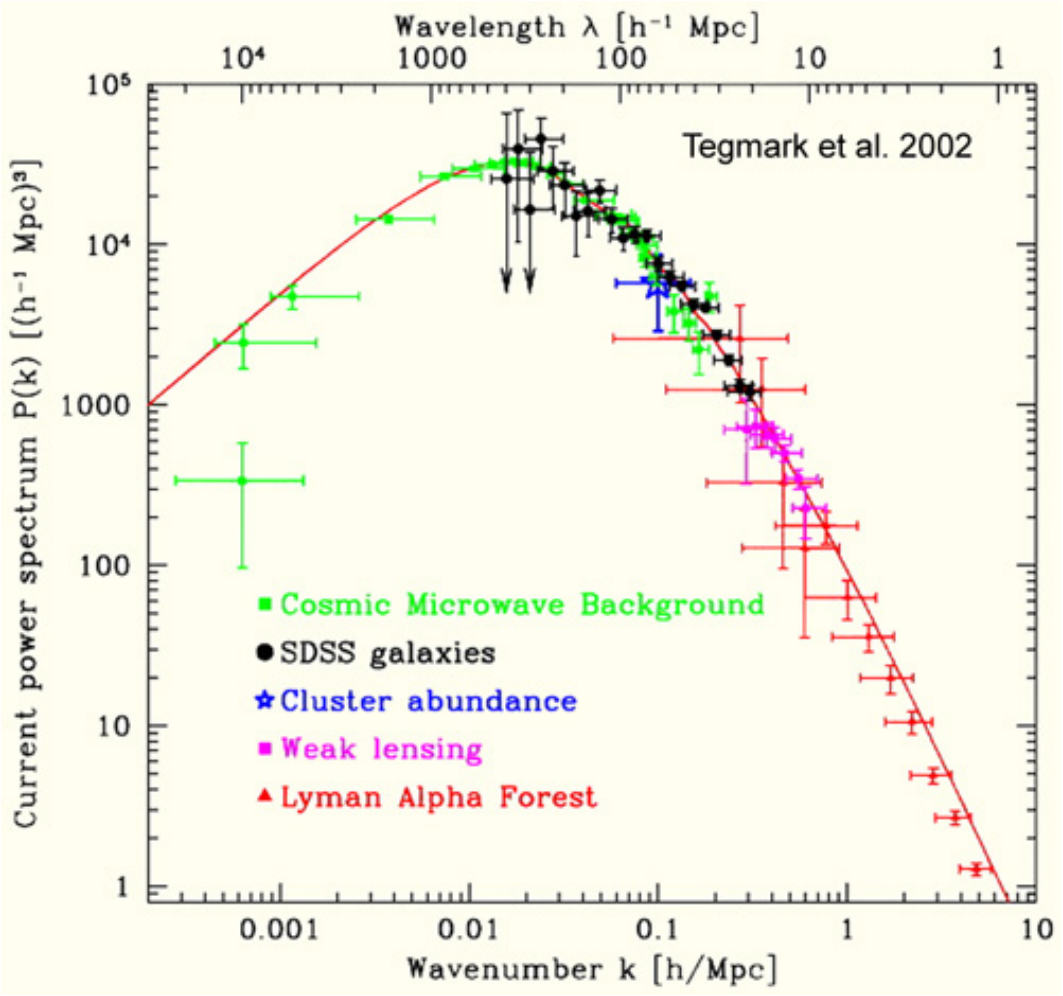

Figure 1.6 Matter power spectrum reconstruction through observations, from Tegmark et al. (2004), [35]. Visible is the peak that corresponds to the Jeans scale at the equivalence.

1.7.4 Silk damping

For scale factors $a < a_{\rm dec}$, only dark matter overdensities can grow in presence of radiation pressure. For baryons, the only growing modes are the ones outside the horizon, that are stopped by the pressure action as they enter it. Baryonic modes inside the horizon could potentially start to grow again after $t_{\rm eq}$ (as matter dominates the expansion), but this is not going to happen because the effect of the radiation drag. Photons are tight coupled to baryons, and this limits their streaming path. But photons can *diffuse*, moving from overdense regions to underdense ones. Baryons follow photons, and this dragging smooths the overdensities on scales smaller that the diffuse scale $l_{\rm diff}$, [3]. The diffuse scale is given the name of Silk scale and to the associated mass the name of Silk

mass, [36]

$$M_S \simeq 6.2 \times 10^{12} \mathcal{M}_\odot \left(\frac{\Omega_{\rm tot}}{\Omega_{\rm bar}}\right)^{3/2} (\Omega_{\rm tot} h^2)^{-5/4}. \tag{1.7.21}$$

Silk mass varies as $M_S \propto a^{15/4}$ in the period $a_{\rm eq} < a < a_{\rm dec}$, while for $a > a_{\rm dec}$ the effect is not present anymore. Silk mass, hence, represents the minimum mass for baryonic objects forming after the decoupling, because smaller fluctuations are wiped out by the radiation drag.

1.7.5 Cluster of galaxies

This section focuses on one of the most important issues of this thesis, the galaxy clusters. These structures are the biggest gravitationally bounded objects. A large gravitationally bounded system, that does not show some of the typical properties of the clusters is referred to be a *galaxy groups*. Differences between the two different aggregations are to be found first in the mass range, groups are in the order of $10^{11} - 10^{13} \mathcal{M}_\odot$, while clusters are typically $10^{14} - 10^{15} \mathcal{M}_\odot$. A characteristic feature of clusters is the presence of the *intracluster medium* (ICM), sometimes referred also as *intergalactic medium* (IGM), that is baryonic matter in the gas state, mainly formed of primordial hydrogen and helium. The typical temperature of the gas is a few keV ($\sim \times 10^7$ Kelvin). The gas is an important tracer of the mass of the cluster, since it emits in the radio 21-cm line when in neutral state, or emits through *bremsstrahlung* and *synchrotron* when ionized. The ICM gas is discussed in the next Chapter.

Galaxy clusters have one, important, intrinsic information: they show the strict correlation that exists between the collapse of dark matter clumps and the distribution of baryons (gas and stars). Galaxy clusters have shown (rotation curves, gravitational lensing) that they are formed prevalently of dark matter, and that the baryonic matter has been coupled with it because of the high gravitational potential. For the underlying dark matter distribution, both for clusters and groups, we give the generic name of *halo*.

A statistic for the number density of halos was first proposed by Press and Schechter (1974), [37], lately revisited by Sheth and Tormen (1999), [38]. If we indicate with δ the mass density contrast at decoupling, we can derive the standard deviation (rms) of the density contrast smoothed over a comoving window r_s

$$\sigma = \langle \delta^2 \rangle^{1/2}. \tag{1.7.22}$$

We have seen in linear theory that the collapse of an overdensity occurs at $\delta_{\rm lin} = 1.69$ (Eq. 1.4.36). We need to project this quantity at the redshift of decoupling. For an Einstein-de Sitter universe ($\Omega = 1$) this is straightforward since density scales with the scale factor

$$\delta_c = \frac{\delta_{\rm lin}}{(1+z_{\rm dec})}. \tag{1.7.23}$$

For a flat Universe with cosmological constant $\Omega + \Omega_\Lambda = 1$, the computation is quite different and can be found in Appendix A (for reference, see Mathiesen & Evrard 1998, [39]). Any overdensity that at decoupling has a mass density contrast larger than δ_c will collapse in a halo. Since the fluctuations are Gaussian distributed, the probability that this occur is

$$P(>\delta_c) = \frac{1}{(2\pi)^{1/2}\sigma}\int_{\delta_c}^{\infty} e^{-\delta^2/2\sigma^2} d\delta, \tag{1.7.24}$$

where $\sigma = sigma(\mathcal{M})$ and fixes the radius of the window where the contrast is averaged. The above equation indicates the probability that a spherical volume of radius r_s (window) is placed on a protocluster of mass $\mathcal{M}$ or smaller. The same probability in Eq. 1.7.24 can be applied with the variance $\sigma(\mathcal{M}-\delta\mathcal{M})$, and the difference between the two expressions (P in $\sigma(\mathcal{M})$ and P in $\sigma(\mathcal{M}-\delta M)$) is the probability that a halo of mass between $\mathcal{M}$ and $\mathcal{M}-\delta\mathcal{M}$ is formed. The volume of the window is $V_s = \mathcal{M}/\rho_0$ and defining the quantity

$$\nu_c \equiv \left[\frac{\delta_c}{\sigma}\right]^2, \tag{1.7.25}$$

we can compute the number density of object forming at the present with mass between $\mathcal{M}-\delta\mathcal{M}$ in the Press-Schecther formalism

$$\mathcal{M}\frac{dn}{d\mathcal{M}} = \left(\frac{2}{\pi}\right)^{1/2}\frac{d\ln\sigma^{-1}}{d\ln\mathcal{M}}\nu_c^{1/2}e^{-\nu_c/2}. \tag{1.7.26}$$

The seven-year fit of the WMAP data has fixed the value for the rms fluctuation over a radius of $8h^{-1}$ Mpc to be $\sigma_8 = 0.801 \pm 0.030$, [9].

The role of the mass function has been intensely used in the next Chapter, where an estimation of the halos produced per unit volume and per unit of redshift has been used to model the free-free emission from groups and clusters. More details on the used Sheth-Tormen mass function (a revisited version of the Press-Schechther), on the rms fluctuation σ, on the transfer function and the window function are given in the Appendix A. We only advise that the role of the halo mass function has demonstrated its importance among the cosmological hydrodynamical simulation sets.

1.7.6 The observation of the bottom-up formation

We have not mentioned the formation of structures in case the dark matter is constituted by relativistic particles, like neutrinos (HDM). HDM theory has two branches, the adiabatic model and the isocurvature model. The adiabatic HDM is the simplest model. Neutrinos coupled with baryons exhibit a strong pressure force that does not allow the gravitational collapse of small coherent lengths. Hence, the collapse occurs only for objects on scales larger than the ones predicted by CDM scenario. Then isolated galaxy or groups have to be formed out through a fragmentation, or *top-down*. Nonetheless, the observation of the isolated galaxies in our neighborhood seems to indicate that no fragmentation has occurred, since the peculiar velocity does not indicate a motion from out the Virgo cluster. Furthermore, our Galaxy is older than others in the same group, indicating a process of aggregation instead of fragmentation. Cold dark matter (CDM) supplies an accordance model for the observed *hierarchic* structure formation. Groups, clusters and filaments are the result of gravitational attraction of smaller clumps.
Even if the observations seem to role out the adiabatic model for the HDM, the isocurvature model is still an open question, since the bottom-up formation is not in contradiction with it. Here, we limit to say that in this scenario, hot dark matter is still formed up by relativistic neutrinos, but the clumps have been originated by baryons after the decoupling. Only at later time, neutrinos cool down and fall in the gravitational potential of the baryonic clumps.

1.7.7 N-body simulations

In recent years, cosmology has taken enormous advantage of the processing power of modern computers. There is no better way to test a model than to replicate it in a virtual universe, especially when the involved physics are in the non-linear regime. Of course, many limitations have to be considered in this task, but final picture of the large scale structure from a simulation clearly resembles the matter distribution from observations.

In this thesis, for the part of the bremsstrahlung emission from halos, we have used a set of simulations based on the cosmological code GADGET-2 , by Volker Springel, [40]. The code has been run on local facilities and further details are

given in the next Chapter. Here, we will briefly mention the basic underlying the cosmological code, as extracted from the work of the author.

A simulation basically consists of the evolution of two types of matter under mutual interaction: collisionless matter that acts only under a gravitational field, and a collisional matter, for which it is necessary to develop some hydrodynamical properties besides gravity. Collisionless matter is the dark matter, collisional matter consists of gas that develops friction and viscosity. Both types are subjected to the gravitational field.

Collisionless dynamics is based on the collisionless Boltzmann equation (CBE) coupled to the Poisson equation in an Friedman-Lemâitre model (expanding background universe with a Robertson-Walker metric). We assume that the matter is discretized as a finite number of particles, each one has assigned a mass m_i. Given a single particle phase-space $(\mathbf{x}, \mathbf{p})$, where $\mathbf{x}$ is the comoving coordinate (three-vector) and $\mathbf{p}_i = a^2 m_i \dot{\mathbf{x}}_i$. The function $f(\mathbf{x}, \mathbf{p}, t)$ is the mass density for a single particle in phase-space, and the BCE defines the evolution of the that function under the gravitational force and in the presence of no collisions:

$$\frac{df}{dt} \equiv \frac{\partial f}{\partial t} + \mathbf{p}\frac{\partial f}{\partial \mathbf{x}} - \frac{\partial \Phi}{\partial \mathbf{x}}\frac{\partial f}{\partial \mathbf{p}} = 0 \tag{1.7.27}$$

where $\Phi(\mathbf{x})$ is the peculiar potential for each particle, defined as

$$\Phi(\mathbf{x}) = \sum_i m_i \phi(\mathbf{x} - \mathbf{x}_i). \tag{1.7.28}$$

Particles are distributed inside a cube of size L with periodic boundaries conditions, the interaction potential $\phi(\mathbf{x})$ is the solution of the Poisson equation

$$\nabla^2 \phi(\mathbf{x}) = 4\pi G \left[-\frac{1}{L^3} + \sum_n \tilde{\delta}(\mathbf{x} - \mathbf{n}L) \right]. \tag{1.7.29}$$

The density particle function $\tilde{\delta}(\mathbf{x})$ is a Dirac δ-function convolved with a spline kernel, which depends on a comoving softening length ϵ, $\tilde{\delta}(\mathbf{x}) = W(|\mathbf{x}|, 2.8\epsilon)$, [41]. For large numbers of particles N, the computation of the gravitation force is a heavy task. GADGET-2 can use approximated force computations with a set of modification to the main method, since the errors in the force accuracy are comparatively small. However, this assumption is valid only for collisionless particles. Collisional gas particles require high accuracy computation, limiting the execution of cosmological codes involving gas only to powerful clusters of processors.

The gas component of the simulation has to be supplied with a full set of equations for the computation of the pressure and viscosity. The *smoothed particle hydrodynamics* (SPH) method considers a discrete set of particles with coordinates $\mathbf{r}_i$, velocities $\mathbf{v}_i$ and mass m_i. The thermodynamic state of each particle is expressed through the entropy per unit mass, s_i, or more accurately, by an entropic function $A \equiv P/\rho^\gamma$. The density estimation makes use of the smoothing kernel

$$\rho_i = \sum_{j=1}^{N} m_j W(|\mathbf{r}_{ij}|, h_i). \tag{1.7.30}$$

The smoothing length h_i is the length in which is contained the same amount of mass of the smoothing neighbors

$$\frac{4\pi}{3} h_i^3 \rho_i = N_{\mathrm{SPH}} \overline{m}, \tag{1.7.31}$$

where $\overline{m}$ is the average particle mass. From a Lagrangian point of view, the equation of motion for a particle is

$$\frac{dv_i}{dt} = -\sum_{j=1}^{N} m_j \left[f_i \frac{P_i}{\rho_i^2} \nabla_i W_{ij}(h_i) + f_j \frac{P_j}{\rho_j^2} \nabla_i W_{ij}(h_j) \right] \tag{1.7.32}$$

with the coefficients f_i defined as

$$f_i = \left(+ \frac{h_i}{3\rho_i} \frac{\partial \rho_i}{\partial h_i} \right)^{-1}. \tag{1.7.33}$$

The kernel function in Eq. 1.7.32 is defined as $W_{ij} = W(|\mathbf{r}_i - \mathbf{r}_j|, h)$ and $P_i = A_i \rho_i^\gamma$.

The time evolution of the motion of the particles due to viscosity needs another system of N equations

$$\frac{dv_i}{dt}|_{\mathrm{visc}} = -\sum_{j=1}^{N} m_j \Pi_{ij} \nabla_i \overline{W}_{ij}, \tag{1.7.34}$$

where Π_{ij} is the artificial viscosity term and a parametrization depending on $\mathbf{v}_{ij}$, $\mathbf{r}_{ij}$ and h_{ij} is given in Gingold & Monaghan (1982), [42] and Balsara (1995), [43]. The term $\overline{W}_{ij}$ is the arithmetic average of the two kernels $W_{ij}(h_i)$ and $W_{ij}(h_j)$.

All the basic equations for the gravitational field and the hydrodynamics are evolved in time, but some algorithms are required to speed the computation. GADGET-2 uses a combination of Fourier mesh and the tree algorithm for the

computation of the gravitational field. Through this method, the problem is solved as a N-body system, in which dark matter and gas are represented with particles. Usually, each particle feels the force of the other $N-1$ particles, but the tree algorithm decompose the space in adaptive multipoles: distant particles are grouped as a single entity exerting just one force. The simplest implementation of the tree is considering the box as root cube, then dividing it in eight sub-nodes of half box length each. The algorithm chooses, based on a threshold, if the partial gravitational force in the node is accurate for the computation. If it is, the force inside the node is used, and then other node is taken into account. If it is not, the node is opened, again in eight sub-nodes and the algorithm analyzes each of them. This will reduce the computation to a $\mathcal{O}(\log N)$.

An example of the open criterion adopted in GADGET-2 is to open the node if the the following relation is satisfied

$$\frac{GM}{r^2}\left(\frac{l}{r}\right)^2 \leq \alpha|\mathbf{a}|, \tag{1.7.35}$$

where M is the mass of the node, l is its side length and r is the distance from the particle for which is asked the open-criterion. The total amount of the acceleration obtained in the last time-step is $|\mathbf{a}|$ an α is a tolerance parameter. The error in the force accuracy that this open-criterion introduces is kept constant, and adapted to the dynamical state of the simulation where required.

The walking tree algorithm is adopted and adapted for the search of SPH neighbors too. In this case, at a position $\mathbf{r}_i$ is applied a sphere of radius h_i. If this sphere overlaps the node, then the node is open, otherwise the node is discarded. This method limits the walking tree process only at local regions around the particle of interest, allowing CPU power saving.
On smallest scales, the tree algorithm can be implemented with a *Particle Mesh* (PM) development, which has been given the name of treePM. TreePM decomposes the potential in Eq. 1.7.28 into $\phi_k = \phi_k^{\text{long}} + \phi_k^{\text{short}}$, where

$$\phi_k^{\text{long}} = \phi_k e^{-\mathbf{k}^2 r_s^2}, \tag{1.7.36}$$

and the real-space of the short range is

$$\phi^{\text{short}}(\mathbf{x}) = -G\sum_i \frac{m_i}{r_i}\text{erfc}\left(\frac{r_i}{2r_s}\right). \tag{1.7.37}$$

The scale r_s is the scale of the force split and $r_i = \min(\mathbf{x} - \mathbf{r}_i - \mathbf{n}L)$, where $\mathbf{x}$ is the point in the space where the potential is computed and $\mathbf{r}_i$ is the coordinate

of the particle. The force is rapidly suppressed by the error function for scales grater than r_s, accounting only for the particles in the short range. The force expressed by the short scale potential can be computed with the tree algorithm. Since the suppression to the large scale, for each target particle the walk has to be performed only on restricted spatial regions. The treePM guaranties that the force is computed with the same accuracy on all scales of the volume.

The integration scheme used for the GADGET-2 simulation code is the sympletic leapfrog (a trasformation which maintains a global stability of the system) introduced by Quinn et al. (1997), [44]. The Hamiltonian structure of the system is preserved in time integration if each step of it is formulated as a canonical transformation. For the time-step Δt, the transformations are obtained through the *drift* operator and the *kick* operator

$$D_t(\Delta t) : \begin{cases} \mathbf{p}_i & \mapsto & \mathbf{p}_i \\ \mathbf{x}_i & \mapsto & \mathbf{x}_i + \frac{\mathbf{p}_i}{m_i} \int_t^{\Delta t} \frac{dt}{a^2}, \end{cases} \tag{1.7.38}$$

$$K_t(\Delta t) : \begin{cases} \mathbf{x}_i & \mapsto & \mathbf{x}_i \\ \mathbf{p}_i & \mapsto & \mathbf{p}_i + f_i \int_t^{\Delta t} \frac{dt}{a}, \end{cases} \tag{1.7.39}$$

where

$$f_i = -\sum_j m_i m_j \frac{\partial \phi(\mathbf{x}_{ij})}{\partial \mathbf{x}_i} \tag{1.7.40}$$

is the force on the particle i. The time evolution operator can be approximated as a combination of the above operators, like drift-kick-drift (DKD) or kick-drift-kick (KDK). The advantage of this system over similar time integration schemes like Runge-Kutta is, for a Hamiltonian system, that no perturbations are introduced in the long term behavior.

Gas particles constitutes a Hamiltonian system if no viscosity arises. However, long-time perturbations arise only under some circumstances, and when this occurs a thermal energy components is added to the Hamiltonian of the system

$$H_{\text{therm}} = \frac{1}{\gamma - 1} \sum_i m_i A_i \rho_i^{\gamma}, \tag{1.7.41}$$

for which the leapfrog scheme can be used. Further notions and details are to be found in [40] and the references therein.

1.7.8 The Standard Model

A cosmological simulation like GADGET-2 is a powerful test not only for the dark matter paradigm, but for the entire *Standard model*. We can briefly summarize it. The Universe is in a dynamical state of expansion and has been originated in a hot and density state about 13 billions years ago. Its age is concordant with a model of flat universe with the total density parameter $\Omega_{\rm tot} \simeq 1$. In the early stage, quantic fluctuations were stretched by an accelerated expansion which theorists give the name of *inflation*. Isotropy and homogeneity are a result of this primordial expansion, which can be invoked to give an answer to the problems of the horizon and flatness. The first problem concerns different patches of the sky, separated by large angular distances, that seem to be causally connected in the past. The flatness problem is more puzzling. We observe today a high grade of flatness, $|\Omega_{\rm tot} - 1| \sim 0.01$. This indicates that in the past, the flatness had to be *stronger* than the value it has today, exactly $|\Omega_{\rm tot} - 1| \sim 10^{-62}$. A slightly different value in the past would translate today into a non-flat universe, hence the extremely little order of magnitude represents a clear problem of *fine-tuning*. Inflation resolves the problem with the introduction of a constant density for the inflationary field, even in the case of an accelerated expansion where the scale factor $a(t)$ rises exponentially. This will lead to a merely flat geometry independently of the initial curvature. Moreover, the scale-invariant-spectrum ($n = 1$ for the spectral index of Eq. 1.7.10) predicted by inflation has been confirmed by the WMAP observations.

The matter content of the Universe accounts only for a fraction of the total density parameter, $\Omega \simeq 0.27$. The baryonic percentage is lower, $\Omega_{\rm bar} \simeq 0.0449$. The matter is almost totally dark, and the standard model prescripts it is cold. Evidence of the non collisional nature of the dark matter has been mentioned in the previous sections. The dark energy, commonly associated with the initial guess of Einstein's cosmological constant and hence indicated with Λ is driving the accelerated expansion with a density parameter $\Omega_\Lambda \simeq 0.73$. The standard model is often referred as *flat ΛCDM model*.

Another fundamental aspect of the standard model is the *reionization*: after the recombination redshift $z_{\rm rec} \simeq 1300$, the primordial gas was in a neutral phase. The first luminous objects injected UV photons into the IGM, which slowly went through a new ionization phase. When all the bubbles around ionization objects overlapped, the reionization process was completed. The beginning and

Name	symbol	value
Hubble's constant	H_0	70.4 ± 2.5 km sec^{-1} Mpc^{-1}
Age of Universe	t_0	13.77 ± 0.13 Gyr
Baryon density	Ω_b	0.0449 ± 0.0028
Dark matter density	$\Omega_{\rm DM}$	0.222 ± 0.026
Dark energy density	Ω_Λ	0.734 ± 0.029
Primordial power spectrum index	n_S	0.963 ± 0.014
Optical depth	τ	0.088 ± 0.015
End of reionization redshift	$z_{\rm reion}$	10.6 ± 1.2

Table 1.1 ΛCDM parameters. From the seventh year fit of the WMAP analysis, [9].

the duration of the process are not well understood, since it depends on the first class of luminous objects and on their physical properties, nor has been understood that reionization has occurred once with the actual older population of stars or it has been a first reionization carried out by the so called *Population III stars*, massive stars formed only of primordial gas and that have left no traces today. Anyway, the redshift of reionization has been measured through the optical depth τ.

The Tab. 1.1 resumes the concordance model.

Running a cosmological simulation according to the standard model is the most standard case. ΛCDM simulations have been proved to replicate the large scale structure quite accurately. In Borgani and Kravtsov (2009), [45], the authors review all the progresses and still open problems for the simulation of galaxy clusters, hence, simulations for which is required a high spatial resolution and in which the physics due to the hydrodynamics plays a fundamental role. Nonetheless, the authors state: "*Many of the salient observed properties of clusters, such as scaling relations between observables and total mass, radial profiles of entropy and density of the intracluster gas and radial distribution of galaxies are reproduced quite well*". Excepts the inner regions of the clusters where the simulations predict a higher star formation rate, generally a cluster is a structure whose formation is well framed in the ΛCDM model. The Fig. 1.7, from page 14 of Borgani and Kravtsov (2009), reports three *snapshots* for the dark matter density, where is visible the bottom-up hierarchical formation.

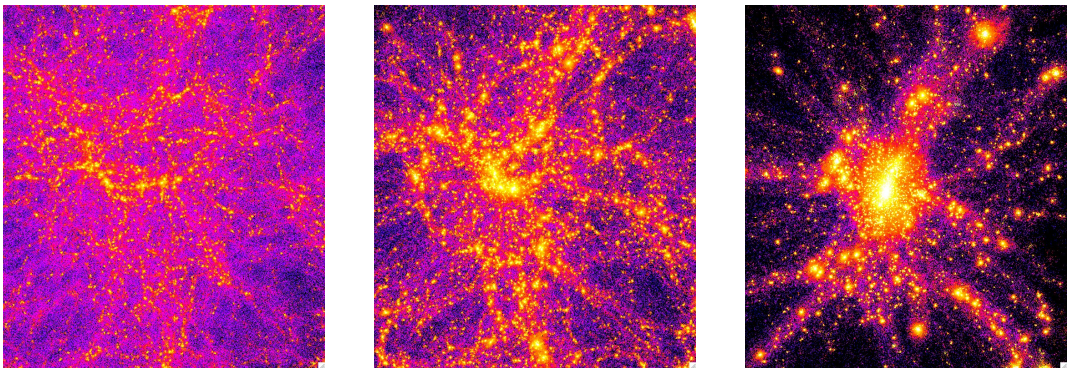

Figure 1.7 Three snapshots from a GADGET-2 simulation from [45]. The snapshots represent the dark matter density in a comoving volume of $24h^{-1}$ Mpc, at redshifts (from left to right) $z = 4$, $z = 2$, $z = 0$.

1.8 Gravitational lensing

This section treats about the theory framework of the gravitational lensing, related to Chapter 4.

1.8.1 Basics

In gravitational lensing, it is usual to adopt the thin lens approximation because the cosmological distances between the observer, the lens, and the sources are much greater than the size of the lens. Hence, the lens can be treated as a plane. All the other elements in the lensing problem are also assumed to be located in planes. When there are multiple background galaxies, each one is assumed to be in a different plane with redshift z_i (in the case of strong lensing) or in the same plane at the average redshift z (in the case of weak lensing). All these planes are perpendicular to the line of sight and the deflection is assumed to occur instantly when the light crosses the lens plane.
We define D_{ls} as the angular diameter distance between the source plane and the lens plane and D_{ol} and D_{os} as the angular diameter distances from the observer to the lens and from the observer to the sources, respectively. With respect to the line of sight, the sources are located at angular positions β_i ($i = 1, 2, ..., n$ with n the number of sources), while the lensed images are located at positions θ_i ($i = 1, 2, ..., m$ with m the number of images). We define the equation of the lens

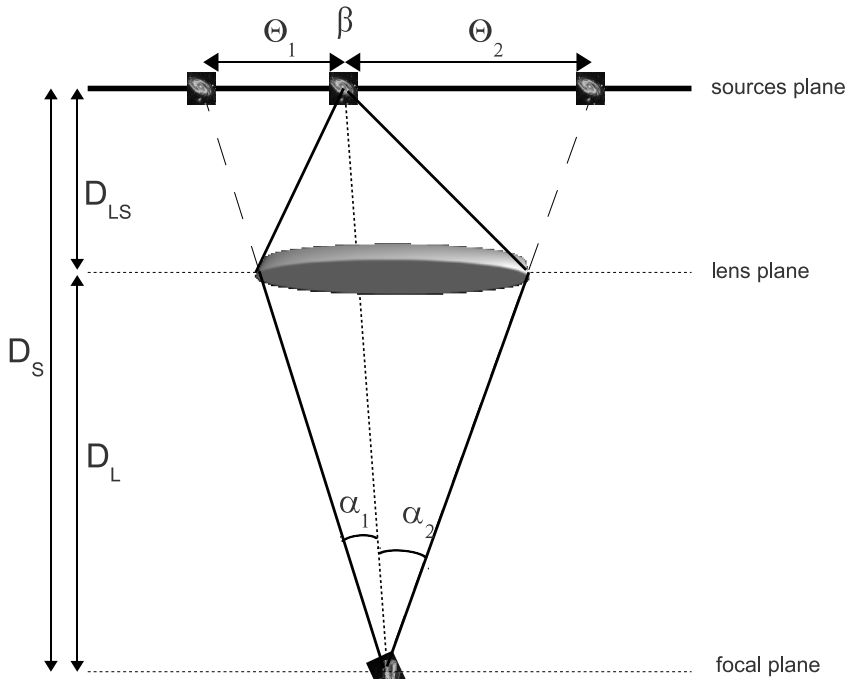

Figure 1.8 Simplified geometry of *strong* gravitational lensing through the *thin lens* approximation. The thickness of the lens is negligible with respect to the cosmological distances involved. D_S, D_L and D_{LS} are the angular diameter distances from observer to background galaxies, from observer to lens and from lens to background galaxies respectively. Note that the distance D_{LS} is *not* the difference between D_S and D_L, but is computed through the Eq. 1.3.38. The positions θs represent the positions of the lensed images on the plane of the sources. The unlensed position β of the background galaxy is function of θs and of the deflection angles αs.

$$\beta = \theta - \frac{D_{ls}}{D_{os}}\alpha(\theta). \tag{1.8.1}$$

We denote by $\psi(\theta)$ the two-dimensional potential produced by all the masses located at θ'

$$\psi(\theta) = \frac{4GD_{ol}D_{ls}}{c^2 D_{os}} \int d^2\theta' \Sigma(\theta') ln(|\theta - \theta'|), \tag{1.8.2}$$

where $\Sigma(\theta')$ is the surface density of the cluster at the given position θ'. The part outside the integral is related to the *critical density*

$$\Sigma_{crit} \equiv \frac{c^2}{4\pi G}\frac{D_{os}}{D_{ol}D_{ls}}. \tag{1.8.3}$$

The above equation is used in the definition of the *convergence*

$$\kappa = \frac{\Sigma(\theta)}{\Sigma_{crit}} \tag{1.8.4}$$

The deflection angle α and the convergence can be expressed as derivatives of the two-dimension potential

$$\alpha = \nabla\psi, \tag{1.8.5}$$

$$\kappa = \frac{1}{2}\nabla^2\psi. \tag{1.8.6}$$

The magnification that the lens produces on the source is quantified by the determinant of the matrix describing the variation in the image position $\delta\theta$ for a small variation in the source position $\delta\beta$

$$\mu = \det\left|\frac{\partial\theta}{\partial\beta}\right| = \left[\det\left|\frac{\partial\beta}{\partial\theta}\right|\right]^{-1}. \tag{1.8.7}$$

From Eq. (1.8.1), we get

$$\mu^{-1} = 1 - \frac{\partial\alpha_x}{\partial\theta_x} - \frac{\partial\alpha_y}{\partial\theta_y} + \frac{\partial\alpha_x}{\partial\theta_x}\frac{\partial\alpha_y}{\partial\theta_y} - \frac{\partial\alpha_x}{\partial\theta_y}\frac{\partial\alpha_y}{\partial\theta_x}. \tag{1.8.8}$$

The strong lens regime is most sensitive to the central mass of the cluster, where the mass surface density is normally higher than the critical surface mass density ($\kappa > 1$). When the surface mass density drops significantly below the critical density ($\kappa << 1$), we are in the regime of weak lensing. Weak lensing cannot produce multiple images, but useful information about the distribution of the mass in the cluster can be extracted from the *shear* of the distortion (γ_1 and γ_2). Differentiating Eq. (1.8.1), we obtain

$$H = \delta_{ij} - \frac{\partial\psi}{\partial\theta_i\partial\theta_j} = \begin{pmatrix} 1-\kappa-\gamma_1 & -\gamma_2 \\ -\gamma_2 & 1-\kappa+\gamma_1 \end{pmatrix} \tag{1.8.9}$$

where

$$\gamma_1(\theta) = \frac{1}{2}(\psi_{11} - \psi_{22}), \tag{1.8.10}$$

$$\gamma_2(\theta) = \psi_{12} = \psi_{21}, \tag{1.8.11}$$

where the double subscripts indicate the second order partial derivative. Equations (1.8.10) and (1.8.11) can be expressed in the complex notation

$$\gamma = \gamma_1 + \mathbf{i}\gamma_2 \tag{1.8.12}$$

to obtain the amplitude and the orientation of the deformation. The *reduced shear* is defined (in complex notation) $\mathbf{g} = \gamma/(1-\kappa)$. The shear measures coherent shape distortions of source galaxies.

The detection of multiple images and/or the measurement of the shear can be used to constrain the mass distribution of the cluster. In cases where the number of constraints is large the mass of the cluster expressed in Eq. (1.8.2) can be reconstructed using a non-parametric method (see Chapter 4).

1.9 Radiation processes

This section is the last part of the introduction Chapter. The aim here is to give some basics on the emission processes that are developed in Chapters 2 and 3. Even if occurring in a cosmological contest, the radiation mechanisms as free-free and synchrotron are correlated to structures that are already formed. However, a last, important, step in the thermal history of the Universe has to be analyzed, the reionization process.

1.9.1 Cosmic reionization

Reionization has been observed both in high-z absorption line studies and with the CMB experiments. However, many aspects of the reionization remain unclear. First of all, the role of the first stars and quasars. We have already mentioned the debate about the existence or not and the efficiency of the first massive stars, the Population III. But this is just one of the multiple aspects to be clarified. In Ferrara and Ciardi (2005), [6], they discuss the uncertainty of another parameter, the escape fraction of ionizing photons, $f_{\rm esc}$. It is generally accepted that $f_{\rm esc} = 7\% - 14\%$ for a Milky Way type galaxy. Some studies have considered the escape fraction from high-z galaxies, with the result that $f_{\rm esc}$ could drop to lower than 1% at $z \approx 10$. At the same redshift, the role of miniquasars can be relevant.
An accurate model of the reionization of the IGM has to consider a radiative process

$$\mathrm{H} + \gamma \leftrightarrow \mathrm{p} + \mathrm{e}, \tag{1.9.1}$$

and an electron collision

$$\mathrm{H} + \mathrm{e} \rightarrow \mathrm{p} + \mathrm{e} + \mathrm{e}. \tag{1.9.2}$$

The inverse reaction of the photoionization is the photon capture

$$\mathrm{p} + \mathrm{e} \leftrightarrow \mathrm{H} + \gamma, \tag{1.9.3}$$

while the inverse reaction of the electron collision is the electron capture of the electron by the proton

$$\mathrm{p} + \mathrm{e} \rightarrow \mathrm{H}. \tag{1.9.4}$$

The recombination coefficient α is estimated through the product of the electron capture cross section, σ_r and the velocity of the electron v_e,

$$\alpha = \langle \sigma_r v_e \rangle = \int \frac{4\pi p^2 e^{-p^2/2mkT}}{(2\pi mkT)^{3/2}} \frac{p}{m} \frac{2\hbar^2\omega^2}{c^2 p^2} \frac{\sigma_1 \omega_1}{\omega^3}, \tag{1.9.5}$$

where ω_1 is the angular frequency of the Lyman series $1s \rightarrow np$ with the value $\omega_1 = 7.9 \times 10^{-18}$ cm^2. An interpolation of the α coefficient has been given in Osterbrock (1989), [46],

$$\alpha = 4 \times 10^{-13} T_4^{-0.7} \text{ cm}^3 \text{ s}^{-1}, \tag{1.9.6}$$

where $T_4 = T/10^4$ K. This temperature is the reference temperature to consider the IGM ionized. The ionized fraction x is determined by the balance between the recombination rate α and the rate of ionization by radiation or collision.
Gnedin (2000), [47], has modeled the cosmic reionization through a numerical simulation, identified three stages: a pre-overlap stage where hydrogen is in neutral form (HI) and ionized bubbles exist only around isolated objects, an overlap stage where the bubbles expand to ionize the medium and a post-overlap stage where a small fraction of neutral hydrogen still exists in clumps. Gnedin identifies the end of the reionization when the neutral hydrogen fraction is less than 10^3. We have already mentioned that this happens at $z_{\text{reion}} \approx 10$. Once ionized, the IGM is left in a state of free ions and electrons, which interact with each other (free-free). This interaction is also extended to the CMB photons (inverse Compton) and with magnetic winds (synchrotron). Clumpy regions of neutral hydrogen emit through the hyperfine transition at 21-cm wavelength.

After reionization, we can start talking about HII regions. With n_e we indicate the number density of electrons in units of cm^{-3}. The reionization is measured through the optical depth (see Tab. 1.1)

$$\tau(z) = c\sigma_T \int_{z_{\text{reion}}}^{0} dz n_e(z) \frac{dt}{dz}, \tag{1.9.7}$$

where $\sigma_T = 6.65 \times 10^{-25}$ cm^2 is the Thomson scattering cross-section. The electron density at a given redshift scales as $(1+z)^3$

$$n_e(z) = n_{\mathrm{H},0}(1+z)^3 x(z), \tag{1.9.8}$$

where $n_{\mathrm{H},0}$ is the hydrogen density at the present epoch, and $x(z)$ is the ionized fraction, [48].

1.9.2 Free-free emission

The effect is properly named *thermal bremsstrahlung*, from the German word meaning *brake radiation*.The name free-free is given because the state of the electron before and after the collision. The term free-free is also used to distinguish the less energetic bremsstrahlung visible at radio and microwaves bands from the more energetic interactions in the X-ray band.
The mechanism is straightforward to understand: nonrelativistic electrons, moving free in the plasma, have a coulombian collision with the ionized hydrogen and helium nuclei. Interactions between electrons and electrons do not occur due to the very small cross-section.

A single collision has two parameters: the velocity of the incoming electron v and the impact parameter b, defined as the minimum distance l between the electron and the ion. The energy radiated by a single electron-ion interaction is

$$W = \frac{\pi Z^2 e^6}{4c^3 m_e^2}\left(\frac{1}{b^3 v}\right), \tag{1.9.9}$$

emitted in a single pulse of duration $t \approx b/v$. The pulse power spectrum is nearly flat for frequencies lower than a maximum frequency

$$\nu_{\max} = (2\pi t)^{-1} = v/(2\pi b), \tag{1.9.10}$$

then it decreases rapidly. For typical HII regions at $T = 10^4$ K, the cutoff frequency is estimated to be $\nu_{\max} \approx 10^{14}$ Hz $\equiv 10^5$ GHz.
In HII regions, we can estimate the number of electrons with a velocity range between v and $v + dv$ that collide with the ions within an impact parameter between b and $b + db$ per unit volume and per unit time

$$N(v,b) = (2\pi b db)[v f(v) dv] n_e n_i \tag{1.9.11}$$

where $f(v)$ is the velocity distribution for the electrons that for a nonrelativistic plasma in local thermal equilibrium (LTE) is the Maxwell distribution

$$f(v) = \frac{4v^2}{\pi}\left(\frac{m}{2kT}\right)^{3/2} e^{-mv^2/kT}. \tag{1.9.12}$$

The *isotropic spectral power* is the integral over the parameter b, in the velocity v, over the whole solid angle

$$\begin{aligned} 4\pi\epsilon_\nu &= \int_{b=0}^{\infty}\int_{v=0}^{\infty} W_\nu(v,b)N(v,b)dvdb \\ &= \frac{\pi^3 Z^2 e^6 n_e n_i}{c^3 m_e^2}\int_{v=0}^{\infty}\frac{f(v)}{v}\int_{b=0}^{\infty}\frac{db}{b} \end{aligned} \tag{1.9.13}$$

in units of $\mathrm{cm}^{-3}\,\mathrm{sec}^{-1}\,\mathrm{Hz}^{-1}$. The integral in db diverges for both extremes $b = 0$ and $b = \infty$, and hence it is necessary to define a range for the impact parameter $b_{\min} \leq b \leq b_{\max}$. The *free-free emission coefficient* is

$$\epsilon_\nu = \frac{\pi^2 Z^2 e^6 n_e n_i}{4c^3 m_e^2}\left(\frac{2m_e}{\pi kT}\right)^{1/2}\ln\left(\frac{b_{\max}}{b_{\min}}\right). \tag{1.9.14}$$

A simple estimation of the ratio in the last term yields

$$\frac{b_{\max}}{b_{\min}} \approx \left(\frac{3kT}{m_e}\right)^{3/2}\frac{m_e}{3\pi Z e^2 \nu}. \tag{1.9.15}$$

For a pure hydrogen plasma we can make a numeric evaluation for the free-free coefficient in Eq. 1.9.14. For a full ionized medium, the number densities of ions and electrons are to be equal $n_i = n_e$, while the effective nucleus charge is $Z = 1$. The weak dependence on the frequency is absorbed in the free-free Gaunt factor, [49],

$$g_{\mathrm{ff}} \approx \ln\left[4.355\times 10^{-2}\left(\frac{\nu}{\mathrm{GHz}}\right)^{-1}\right] + 1.5\ln\left(\frac{T_e}{\mathrm{K}}\right). \tag{1.9.16}$$

The numerical estimation of the free-free coefficient used in the calculation in the next Chapter is

$$\epsilon_\nu = 5.4\times 10^{-39} n_e^2 T_e^{-1/2} g_{\mathrm{ff}}(\nu, T_e) e^{-h\nu/kT_e}, \tag{1.9.17}$$

in units of $\mathrm{erg}\,\mathrm{cm}^{-3}\,\mathrm{sec}^{-1}\,\mathrm{Hz}^{-1}\,\mathrm{srad}^{-1}$.

1.9.3 Synchrotron radiation

Synchrotron radiation is the dominant mechanism for normal galaxies in the radio band. By normal galaxy we mean a galaxy whose center does not have a supermassive black hole, or, if present, there is no matter falling onto it and radiating. The emission is originated by free electrons accelerated to relativistic velocities in magnetic fields. Consider an electron with velocity $\mathbf{v}$ moving in a magnetic field $\mathbf{B}$. The electric field measured in the rest frame of the charge

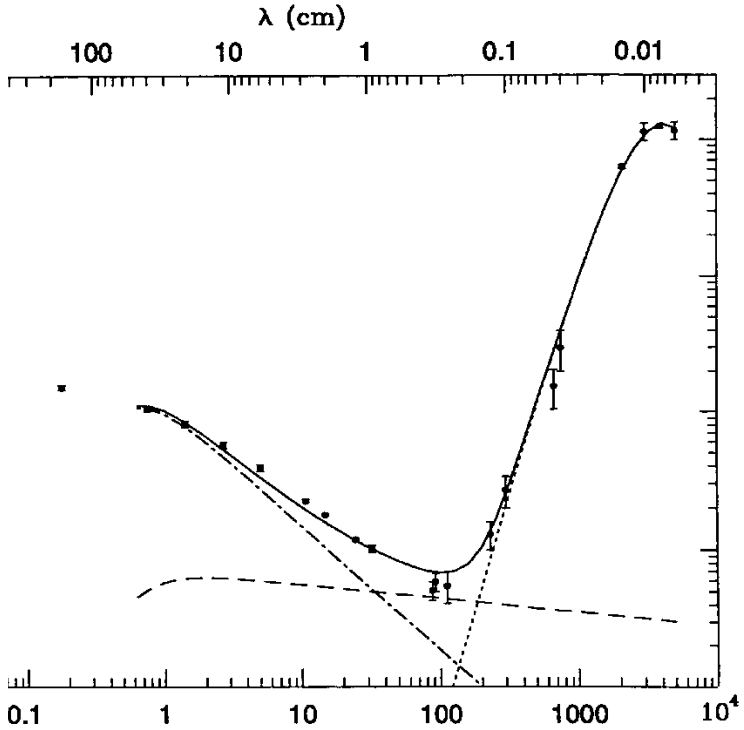

Figure 1.9 Spectrum of galaxy M82 in radio/far infrared, presented by Condon 1992, [50], using data from Klein et al. 1988, [51] and Carlstrom & Kronberg 1991, [52]. The spectrum is the sum of the free-free emission (*dashed line*,) synchrotron radiation (*dot-dashed line*) and dust components (*dotted line*). In the radio band, free-free and synchrotron are the dominant effects, with the latter dominating at lower frequencies, due to the slope $S_\nu \propto \nu^{-0.7}$. The weaker frequency dependence of the free-free, $S_\nu \propto \nu^{-0.1}$, makes it possible to observe only in a narrow window.

is $E' \propto \gamma B$, with an acceleration $a' = (qE'/m_e)$. The radiated energy by the accelerated particle is

$$\frac{d\mathcal{E}}{dt} = \frac{d\mathcal{E}'}{dt'} = \frac{2}{3}\frac{q^2}{c^3}(a')^2 = \frac{2}{3}\frac{q^2}{c^3}\left(\frac{q^2}{m_e^2}\gamma^2 B^2\right), \tag{1.9.18}$$

where the first equivalence is between the lab frame and the charge rest frame and $\gamma = \sqrt{1 - v^2/c^2}$. The power radiated by a single electron of energy $E = \gamma\, m_e c^2$ is $(d\mathcal{E}/dt) \propto \epsilon^2 B^2$. The energy density of a magnetic field is $U_b = (B^2/8\pi)$, then the

$$\frac{d\mathcal{E}}{dt} = \frac{16\pi}{3}\left(\frac{q^2}{m_e c^2}\right)^2 \gamma^2 c U_b \simeq (\sigma_T c U_b)\gamma^2, \tag{1.9.19}$$

where σ_T is the Thomson scattering cross section. When the electron is relativistic, its effective mass is $m_e\gamma$ and for a spiral motion in a magnetic field, the angular frequency is $\omega = (qB/m_e c\gamma) = (qcB/E)$. For relativistic effects, the angular frequency sets the critical frequency of the emitted radiation

$$\omega_{\text{crit}} \approx \omega\gamma^3 \propto B\gamma^2 \propto B\epsilon^2 \tag{1.9.20}$$

(details to be found in Chapters 1 and 3 of *Theoretical Astrophysics, Volume I: Astrophysical Processes* by Padmanabhan 2000, [3]). The total radiation emitted is

$$\epsilon_\omega \propto B^2E^2N(E)(dE/d\omega), \tag{1.9.21}$$

where B^2E^2 is the energy emitted by a single particle, $N(E)$ is the number of particle with energy E and $(dE/d\omega)$ is the Jacobian from E to ω_{crit}. The energy spectrum of the electrons has the form of a power law

$$N(E) = CE^{-p}, \tag{1.9.22}$$

then the radiation spectrum is

$$\epsilon_\nu \approx \frac{e^3}{m_e c^2}\left(\frac{3e}{4\pi m_e^3 c^5}\right)^{(p-1)/2} CB^{(p+1)/2}\nu^{-(p-1)/2}. \tag{1.9.23}$$

Indicating with $\alpha = (p-1)/2$, the Eq. 1.9.23, the emission spectrum of synchrotron is a power law of type $\epsilon_{\text{synch}} \propto \nu^{-\alpha}$.
For the computation in Chapter 3, we have adopted a value $\alpha = 0.7$, that is suitable when the spectrum contribution is mostly from normal galaxies. Both free-free and synchrotron are the main mechanism for the emission in radio band by normal galaxies. However, the difference in the spectral indexes, $\alpha = 0.1$ for free-free and $\alpha = 0.7$ allows the two emission to not be completely overlapped. More, the deep analysis carried out in Condon (1992), [50], shows how synchrotron is at last one decade higher than free-free. Both effect are strictly connected to the rate of star formation (SFR) in the galaxies: on the left hand, the ionization of the interstellar medium is function of the escape fraction f_{esc} of ionizing photons, on the right hand, magnetic fields in galaxies are mainly produced by supernovae remnants (SNR), which number is again related to the number and charateristics of the stars formed in the burst. A third kind of emission is peculiar for normal galaxies and is the IR radiation from spinning dust. The empirical relation between a $\lambda = 10$ μm emission and a 1415 MHz emission was first pointed out by van der Kruit (1971), [53], and was soon extended to

universal law for normal galaxies. The definition of the FIR/radio correlation will be given in Chapter 3. To illustrate the typical spectrum emission of normal galaxies, Fig. 1.9 shows the emission spectrum of galaxy M82 as a composition of the three main radiation mechanism, free-free, synchrotron and dust.

CHAPTER 2

The cosmological free-free signal from galaxy groups and clusters

Using analytical models and cosmological N-body simulations, we study the free-free radio emission from ionized gas in clusters and groups of galaxies. The results obtained with the simulations are compared with analytical predictions based on the mass function and scaling relations. Earlier works based on analytical models have shown that the average free-free signal from small haloes (galaxies) during and after the reionization time could be detected with future experiments as a distortion of the CMB spectrum at low frequencies ($\nu < 5$ GHz). We focus on the period after the reionization time (from redshift $z = 0$ up to $z = 7$) and on haloes that are more massive than in previous works (groups and clusters). We show how the average signal from haloes with $M > 10^{13} h^{-1} M_{\odot}$ is less than 10% the signal from the more abundant and colder smaller mass haloes.However, the individual signal from the massive haloes could be detected with future experiments opening the door for a new window to study the intracluster medium.

2.1 Introduction

In the near future, new high sensitivity experiments observing at radio and millimeter wavelengths will open a new window to study the high redshift Universe and in particular the re-ionization period. Among these experiments,

the *Square Kilometer Array* (or SKA hereafter, [54]) and the *Atacama Large Millimeter Array* (or ALMA hereafter, [55]) are the most relevant ones due to their sensitivity and angular resolution. These experiments will be able, for the first time, to trace in detail the distribution of neutral hydrogen before re-ionization (through the 21 cm line, see e.g. Schneider et al. 2008, [56]), and the transition between a neutral and ionized Universe at the time of reionization (ALMA could see the first galaxies emerging at the reionization time).

The study of the re-ionization period will offer a unique window to help us understand the formation of the first stars and galaxies. The possibilities of this new window for astronomy has motivated many studies that focus, for instance, on the 21-cm line radiation from neutral gas, [57–66], or on the kinematic Sunyaev-Zeldovich effects (kSZ, [67]) from inhomogeneous (patchy) reionization on large scales, [68–70]. In Oh (1999), [71], it is proposed that the reionization can be studied also through the H-α emission, useful to trace young star formation regions.

Another signal emerging from the ionized regions will be the free-free from interactions between the electrons and ions in the plasma. The photons emerging from these interactions can be observed in the radio and microwave bands. The distortion that free-free induces on the background temperature in the Rayleigh-Jeans part of the spectrum, [72], is actually constrained by the ground based measurement of Bersanelli et al. (1994), [73], at 2 GHz, $Y_{\rm ff} < 1.9 \times 10^{-5}$ (95% CL).

Most of the efforts focus on the study of the 21-cm line and the interaction between the CMB photons and the ionized clouds but little has been done in relation to the free-free signal. In this paper we focus on the free-free emission and its ability to trace the ionized medium. The free-free emission (or *bremsstrahlung*) can be potentially observed in the local Universe and up to the re-ionization era. UV radiation emerging from the first stars and quasars ionized the neutral hydrogen creating expanding bubbles of ionized plasma. During a free-free interaction between two charged particles (free electrons and ionized atoms), the electron loses part of its kinetic energy by emitting a photon. The energy of the photon ranges from the radio to the X-ray wavelength depending on the electron temperature. Since this interaction involves two particles, its intensity depends on the square of the free electron (or equivalently

the ion) density, n_e. This n_e^2 dependence makes the free-free signal an interesting candidate for cross-correlations with other signals like the SZ effect where the signal amplitude depends linearly on n_e.

In the late 90's, an experiment was designed to measure the distortion of the CMB spectrum due to the cosmological free-free signal; the Absolute Radiometer for Cosmology, Astrophysics and Diffuse Emission (or ARCADE, see Fixsen et al. 2004, Kogut et al. 2006, Fixsen et al. 2011 and Seiffert et al. 2011, [74–77] for details). Its goal is to detect the average free-free signal at frequencies around 1 GHz. Studying the distortion of the CMB spectrum at these frequencies would allow, in principle, to set strong constraints on the history of reionization of the Universe. Recently, the ARCADE team presented the results of the ARCADE2 mission that studies both Galactic and extragalactic signals, [76]. They detect a signal that is significantly larger than the expected extragalactic radio background (a factor ~ 5 brighter than the estimated contribution from radio point sources). The ARCADE team is currently exploring the possible causes of such a signal like for instance possible foreground contamination, synchrotron emission from Earth's magnetic field or CII lines. In the latest review of the results of the mission, [77], the authors still report that the excess detection remains unexplained, even though the three main sources of errors, Galactic emission, instrumental systematic errors and radio emission from the faint end of the distribution of known sources, are carefully taken into account. Sharpe (2009), [78], has suggested that the observed excess is produced by synchrotron radiation emerging from an optically thin low density magnetized plasma region in the heliosphere of the Sun.

Oh (1999), [71], presents an exhaustive treatment of the different sources of radiation that could be detected with SKA and ALMA in the range of the radio frequencies. He pays special attention to the free-free signal from small haloes and the intergalactic medium (or IGM) and concludes that the IGM signal is subdominant when compared with the signal from haloes. Another interesting work is presented in Cooray & Furlanetto (2004), [79], where the authors use a halo model to predict the amount of free-free signal from haloes. The authors also compute the angular power spectrum of the signal produced by the free-free below 2 GHz and make predictions in the context of the ARCADE mission.

Burigana et al. (1995), [80], discusses different physical processes involving the CMB photons and the ionized medium, including also the free-free signal. In Burigana et al. (2004), [65], the authors discuss about the possibility of detecting the individual sources of free-free signal.

All these works have focused on the signal from small and cold haloes, largely ignoring the signal coming from larger and hotter haloes (groups and clusters). In this paper we will study the regime of more massive haloes and focus on the period after reionization. Also, an important advantage of working with more massive haloes is that their modeling is much simpler than in the case of smaller haloes. The cooling time is significantly larger for massive haloes and one can more easily ignore highly non-linear phenomena like radiative cooling.

2.2 Free-Free emission

In a hot plasma with temperature T, the electrons move with kinetic energy $E_e = 3/2 k_b T$ where k_b is the Boltzmann's constant (1.38×10^{-23} J/K). The minimum T required to ionize a plasma is $\approx 2 \times 10^4$ K, [81]. This is also the temperature at which most of the cooling radiation occurs in a typical galaxy halo, [82]. This temperature can be translated into a kinetic energy for the free electrons, typically in the order of 2×10^{12} erg ($\sim$ 1 eV). The collisions between opposite charged particles within the plasma modify the paths of the electrons that lose a few percent of their kinetic energy (*bremsstrahlung* or *brake radiation*). The net effect is the bulk emission of photons in the radio frequency range ($1 \sim 10$ GHz), strongly dependent on the square of the electron density. Note that this square dependence implies a crucial role of the density contrast pattern inside the haloes.

The bremsstrahlung, or free-free signal, can be parametrized in terms of the electron density n_e and temperature T_e as, [60, 79, 83],

$$\epsilon_\nu = 5.4 \times 10^{-39} n_e^2 T_e^{-1/2} g_{\rm ff}(\nu, T_e) \exp\left(\frac{-h\nu}{k_b T_e}\right), \tag{2.2.1}$$

in units of ergs cm^{-3} s^{-1} Hz^{-1} sr^{-1}. The Gaunt factor, [80, 84], $g_{\rm ff}$, is computed for the observed frequency but it has a weak dependency on the temperature of the gas. In the Rayleigh-Jeans limit (where the free-free radiation is more relevant) the exponential part can be safely neglected. From Eq. (2.2.1) it is clear

that the free-free emissivity depends mostly on the electron density n_e. The inverse dependence with the root square of temperature is a direct consequence of the thermal Maxwellian distribution.

The luminosity of an ionized volume of space with constant n_e and T_e can be obtained from Eq. (2.2.1) by integrating the electron density and temperature over that volume. By dividing this luminosity by the corresponding luminosity distance, the flux (or brightness) in Jy can be derived (1 Jy $= 10^{-23}$ergs/s cm^2 Hz). In terms of the temperature distortion, the brightness can be transformed into equivalent temperature. In the Rayleigh-Jeans limit we have that

$$\Delta T \propto F\lambda^2 \tag{2.2.2}$$

where F is the free-free flux and $\lambda = c/\nu$. Thus, at 1 GHz, while the flux does not change much with frequency, the free-free temperature distortion is expected to be higher than at 10 GHz by a factor 100. This simple scaling shows the convenience of looking for the free-free signal at lower frequencies. Several attempts have been made in the past to measure the free-free distortion at low frequencies as a deviation of the nearly perfect CMB blackbody energy spectrum. The first accurate measurements of the spectrum of the CMB were made by the FIRAS and have shown no departure from the blackbody spectrum (within the error bars) in the frequency range of $60 - 600$ GHz. It is expected that new experiments will detect the average free-free contribution at lower frequencies in the shape of a distortion of the CMB energy spectrum.

2.3 Predictions from analytical models

Through analytical halo models it is possible to explore a wide range of cases. Oh (1999), [71], shows that the free-free contribution coming from the diffuse IGM is significantly smaller than the signal from ionized haloes so it can be safely ignored. Two ingredients are needed in order to compute the average free-free signal from haloes. First, the mass function, $n(M, z)$, that predicts the average number of haloes per redshift, z, and mass, M, intervals and, second, a model for the internal gas distribution (and temperature) inside the haloes. The abundance of haloes can be computed from the mass function given a cosmological model. We use the mass function of Sheth & Tormen (1999) (or ST mass function hereafter, [38]) for this purpose. The ST mass function reproduces well

the results obtained with large N-body simulations. For the internal distribution of the gas in the haloes and temperature we assume a standard isothermal β-model with $\beta = 2/3$. The gas density profile plays an important role since steeper profiles can produce a larger free-free signal with the same amount of gas (as it happens in the X-ray band with gas in galaxy clusters). Other more realistic models can be found in the literature (see for instance Ascasibar et al. 2003, [85], Ascasibar & Diego 2008, [86]) but for simplicity we will use the β-model as this model requires only three parameters (T_o for the temperature and R_c, and n_o for the β-model).

2.3.1 Predictions for a single halo

The β-model is widely used in the context of galaxy clusters to describe the electron density as a function of radius, [87, 88]:

$$n_e(R) = \frac{n_o}{1 + \left(\frac{R}{R_c}\right)^2}, \tag{2.3.1}$$

where n_o is the electron density at the center of the halo and R_c is the core radius and we have assumed $\beta = 2/3$.

For the β-model, the free-free luminosity can be computed integrating Eq. (2.2.1) over the volume of a sphere of radius $R_{\rm vir}$

$$\begin{aligned} L_\nu &= \int_V \epsilon_\nu dV \\ &= C n_o^2 R_c^3 \left(\tan^{-1}\sqrt{p} - \frac{\sqrt{p}}{p+1} \right) \end{aligned} \tag{2.3.2}$$

where $C = 5.4 \times 10^{-39} 2\pi T_e^{-1/2} g_{\rm ff}(\nu, T_e)$ and the argument p is the ratio $R_{\rm vir}/R_c$. For simplicity we have dropped the negligible term $exp(-h\nu/(k_b T_e))$ in Eq. (2.2.1).

The halo luminosity can be transformed into flux given the luminosity distance, D_L, from the halo at redshift z to the observer (at $z = 0$).

$$S_\nu({\rm Jy}) = \frac{L_\nu}{4\pi D_L(z)^2}. \tag{2.3.3}$$

The values of n_o, R_c and T can be computed from scaling relations. In order to establish these relationships we assume that the total mass of the halo, M, and the total mass of the gas, $M_{\rm gas}$, are proportional to each other with the

proportionality constant being the universal baryon fraction, $f_b = M_{\rm gas}/M$. Given a virial mass for the halo, the virial radius can be expressed as, [89, 90],

$$R_{\rm vir} = 1.3 M_{15}^{1/3} (1+z)^{-1}, \tag{2.3.4}$$

where M_{15} is the halo total mass expressed in $10^{15} h^{-1} M_\odot$ and the radius is scaled with the expansion factor $(1+z)^{-1}$. Within the virial radius, the relation between the baryonic mass and the electron density profile (given in Eq. (2.3.1)) is

$$\begin{aligned} M_{\rm gas} &= \int_V \mu m_p n_e(R) dV \\ &= 4\pi\mu m_p \int_0^{R_{\rm vir}} n_e(R') R'^2 dR'. \end{aligned} \tag{2.3.5}$$

Then, a relationship between n_o and the total mass of virialized halo, $M_v \approx M_{\rm gas}/f_b$, can be established:

$$n_o = \frac{M_v f_b}{[p - tan^{-1}(p)]\, 4\pi\mu m_p R_c^3}, \tag{2.3.6}$$

where $p = R_{\rm vir}/R_c$. The ratio between $R_{\rm vir}$ and R_c is assumed to be constant ($R_{\rm vir}/R_c = 10$). For f_b we assume $f_b = 0.13$. Finally, for the temperature we use the relation obtained by Diego et al. (2001), [91], which was shown to be consistent with X-ray measurements

$$T({\rm keV}) = 10 M_{15}^{4/7}. \tag{2.3.7}$$

Once n_o, R_v, R_c and T are known, it is possible to compute the total free-free luminosity, flux and temperature distortion of the halo at redshift z from equations (2.3.2), (2.3.3) and (2.2.2) respectively.

2.3.2 The abundance of haloes: the mass function

In this work we use Sheth & Tormen (ST hereafter) mass function, [38], see A .

We compute the mass function between the masses $10^8 \leq M \leq 10^{16} h^{-1} M_\odot$. This mass interval covers the range from the smallest ionized haloes to the largest galaxy clusters. We include the small haloes in our calculation for comparison purposes with earlier works and with the more massive haloes. In our simple model we will make the assumption that all haloes included in the mass function are fully ionized. This is not properly true in the low end of the

mass interval since, as it was discussed in Oh (1999), [71], the low mass haloes will stay ionized only for a limited amount of time. Consequently, at a given redshift, only a fraction of the low mass haloes are *active* or fully ionized. The conclusions derived from our calculations should be then considered as an upper limit in the low mass range ($M \lesssim 10^{12} h^{-1} M_{\odot}$). On the other hand, the high mass end haloes can be considered as fully ionized as most the gas in these massive haloes (clusters) will remain ionized by the high temperatures of the plasma in the clusters. Regarding the redshift range we will consider only the contributions up to redshift $z = 7$. The reionization period was studied in Loeb (1996), [92], Oh (1999), [71], Oh & Mack (2003), [60]. In Fig. 2.1 we show how

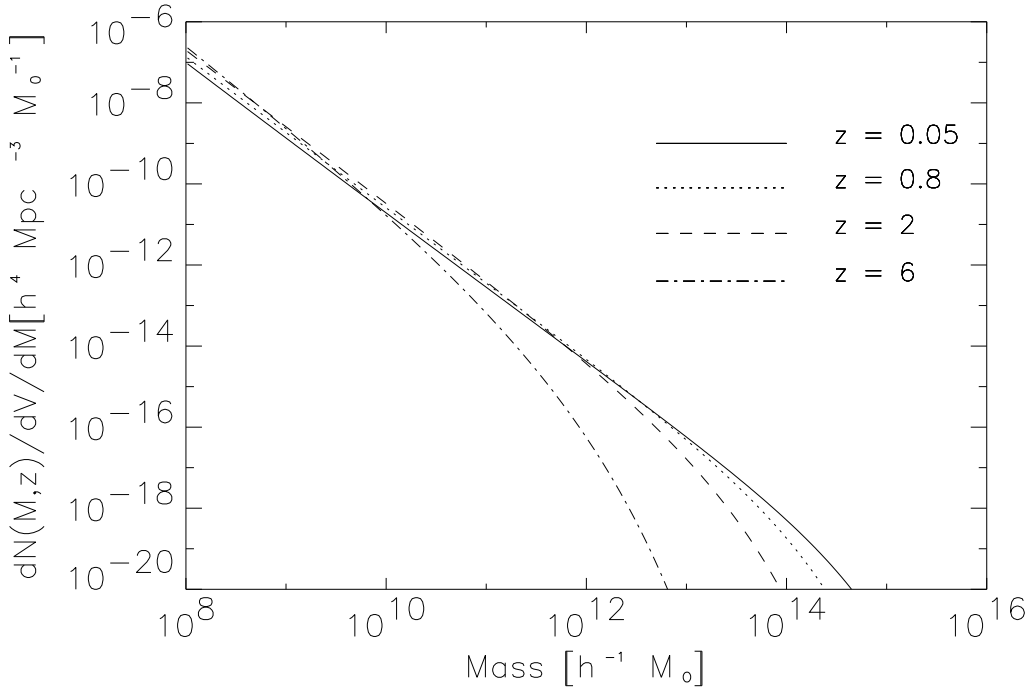

Figure 2.1 Mass function for different redshift intervals. Note how small haloes are common at all redshifts (their population drops at redshifts larger than the ones shown here).

the mass function behaves for different redshifts. The low mass haloes ($\sim 10^8$ solar masses) show a nearly constant abundance at all redshifts while the number of massive haloes decreases with redshift.

In the next subsection we will combine the predicted flux of the β-model from

one halo with the mass function to compute the mean free-free signal from a cosmological volume.

2.3.3 Average free-free emission from an analytical halo model

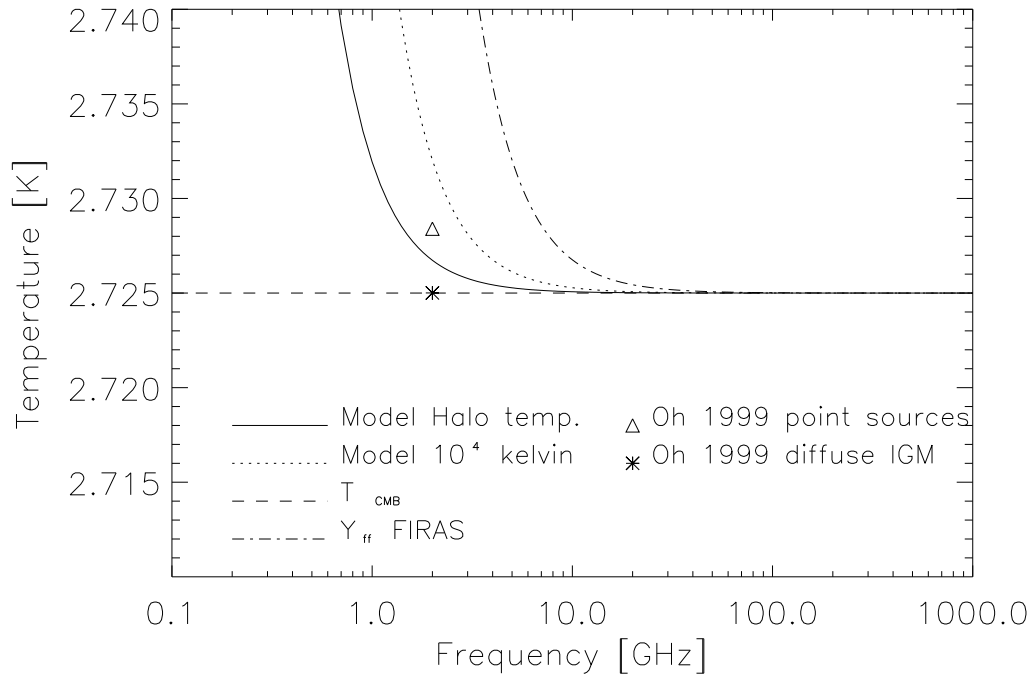

Figure 2.2 Average temperature distortion due to free-free as a function of frequency for our analytical model. The solid line shows the distortion obtained assuming that the temperature of each halo was computed with the scaling law $T(\mathrm{keV}) = 10 M_{15}^{4/7}$; for reference, we show as a dotted line the distortion corresponding to a fixed temperature of 10^4 K for all haloes. The dot-dashed line represents the 95% confidence level observational upper limit derived from Bersanelli et al. (1994), [73]. The star and the triangle represent the results from Oh (1999), [71] related to the diffuse IGM ($\Delta T = 6.0 \times 10^{-6}$ K) and to point sources ($\Delta T = 3.4 \times 10^{-3}$ K) respectively.

Combining a model for the gas distribution inside a halo, like the β-model, with the abundance of haloes as a function of mass and redshift, it is possible to compute the mean free-free signal in a solid angle as a function of redshift and/or mass. We can also integrate this information in the redshift-mass space and estimate the mean free-free signal from all these haloes.

Given a redshift and mass interval, we compute the number of haloes in the

interval and compute the free-free flux from those haloes. After integrating over the entire redshift range ($0 < z < 7$) and mass range ($10^8 < M < 10^{16}$) we compute the mean free-free flux from all the haloes. The flux is converted into thermodynamic temperature to compute the $\Delta T/T$ as a function of the frequency. The resulting distortion from our analytical model is shown in Fig. 2.2. When comparing our results with those obtained by Oh (1999), [71], we find that our model (solid line) falls below the predicted value by Oh (1999). This can be explained by the fact that we are assuming a higher temperature for the haloes. Fixing the temperature to $T = 10^4$ K (like in Oh 1999), our model predicts more signal than in Oh (1999). A possible explanation is that, in Oh (1999), only a fraction of the haloes were *active* while in our case all haloes are ionized.

It is interesting to show how the free-free signal depends on the redshift and the mass of the haloes. In Fig. 2.3 we show the free-free signal for different mass intervals. In each interval, we compute the mean free-free distortion as a function of redshift. The smaller but more abundant haloes give a larger signal. Also, as we show earlier, smaller haloes have more or less the same abundance at all redshifts and hence their average free-free contribution shows a slow dependence with redshift. Note how the simulation predicts significantly less average signal than the analytical model. As we will see later, this is a direct consequence of the lack of resolution in the simulation that is not able to capture the contribution from the smallest haloes.

This prediction, however, should be taken with care since on one hand we assumed that haloes remain ionized at all times and the temperature of the gas corresponds to the virial temperature of the halo. In small systems, the cooling time is short and the gas can cool down significantly, become neutral and form stars. Our assumptions are only valid for the most massive haloes (groups and clusters) and the model predictions are robust only in that regime. For these objects, the average free-free distortion is of the order of a few to several tens of μK at 1 GHz. Also, the plot shows the average free-free signal obtained from simulations (see below) as a function of redshift (stars). As we will see later, the smaller range of halo masses of the simulation predicts a smaller average free-free signal.

In Fig. 2.4 we show more explicitly the dependency of the average free-free distortion with the mass range but for different redshift intervals. Again, smaller

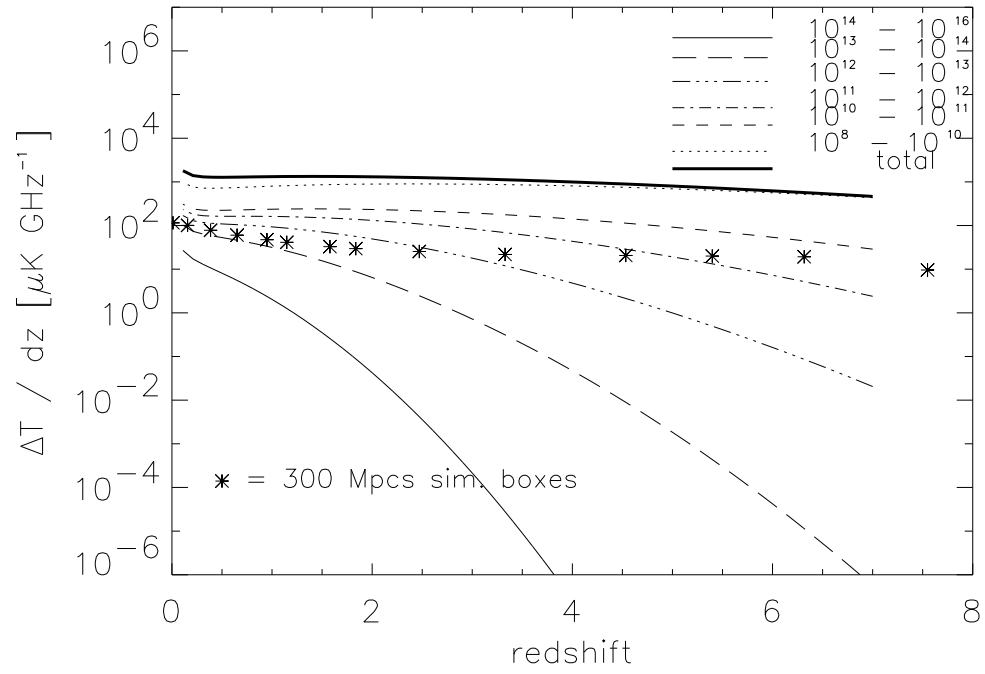

Figure 2.3 Free-free signal for different mass intervals as a function of redshift and for $\nu = 1$ GHz. The points represent the distortion ΔT computed from a cosmological simulation of 300 Megaparsecs (see Sect. 2.4 below). The minimum mass resolved in the simulation at $z = 1.57$ is $M_{\rm min,sim} = 1.14 \times 10^{11}$ and the maximum mass is $M_{\rm max,sim} = 8.21 \times 10^{13}$.

haloes contribute more to the average signal than massive ones at all redshifts. This result is strengthened by the the model proposed in Miniati et al. 2004, [93]. The authors, referring to the component of the UV luminosity produced by the thermal emission from gas accreting on to dark matter haloes, calculate that the most contribution is produced by haloes with temperatures between 10^6 K and a few $\times 10^7$ K, corresponding to masses $10^{11} - 10^{13}$ solar masses.

It is important to note, though, that cooling and star formation play a critical role in determining the actual contribution of galaxy-sized haloes ($M < 10^{12} h^{-1} M_\odot$) to the temperature distortion of the CMB. On the one hand, the temperature of the ionized gas will be around 10^4 K, much lower than predicted by Eq. (2.3.7), and its density will be considerably higher than predicted by the β-model. The combined action of both effects can boost the expected free-free

signal by a large factor. On the other hand, a significant fraction of the gas will be transformed into stars and most of the interstellar medium will be in neutral rather than ionized form, and therefore it will not emit any bremsstrahlung radiation. The net effect is difficult to quantify, and Oh (1999), [71], has resorted to a phenomenological parameter describing the fraction of *active* galaxies or, equivalently, the average ionization fraction of the gas. These works focus on the signal from small and cold systems, where UV radiation from stars and quasars ionizes the surrounding neutral hydrogen and creates expanding bubbles of ionized plasma.

Gas cooling, star formation, and feedback processes determine the amount of ionized gas, its characteristic density, its temperature, and thus the total bremsstrahlung luminosity.
We discuss in more detail the regime of hotter, more massive objects, where the gas is heated collisionally rather than photo-ionized. These systems contribute only to a small fraction of the overall cosmological signal. In this work, we provide robust lower limits for the signal produced by massive objects, based on a simply physical modeling. A more detailed treatment of cooling and photo-ionization of the interstellar medium will be addressed in a future work.

2.4 N-body simulations

In the previous section we have shown how the average free-free signal from haloes depends on their redshift and mass distributions. We also discussed how these predictions depend on the internal gas distribution inside the haloes. In this section we use numerical simulations to compute the free-free signal. Through N-body simulations we can obtain the distribution of the electron density, its temperature and ultimately the free-free effect which can be projected into sky maps.

We use the GADGET-2 code, [40], see Sect. 1.7.7 in Introduction. The code is a combination of a Particle Mesh Refinement algorithm and the TreeSPH method by Hernquist and Katz (1989),[94]. For the cosmological parameters we use the concordance model: $\Omega_\Lambda = 0.73$, $\Omega_M = 0.27$, $\Omega_b = 0.039$, $\Omega_K = 0$, $\sigma_8 = 0.79$, $h = H_0/(100\ \mathrm{Km\ s^{-1}Mpc^{-1}}) = 0.72$ where σ_8 is the RMS mass fluctuation on a sphere of a radius of 8 Mpc.

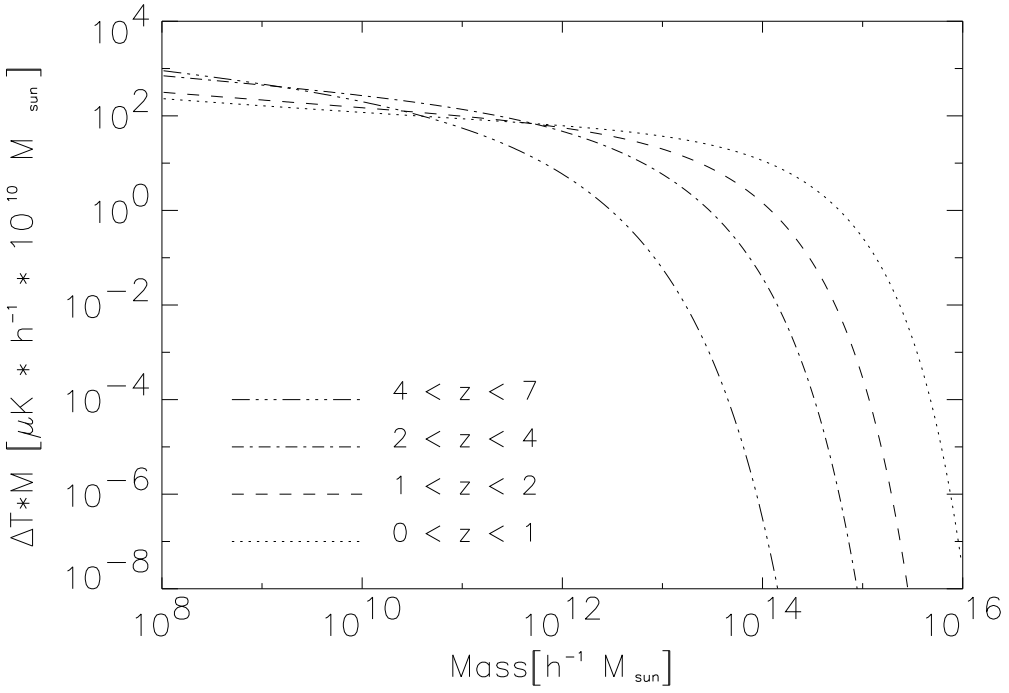

Figure 2.4 Free-free signal as a function of the halo mass and for different redshift intervals.

We create the initial conditions at redshift z=49 with the code 2LPT, [95], based on a second-order Lagrangian perturbation theory. The initial condition is evolved with GADGET-2 from $z = 49$ until $z = 0$. For the main simulation, we use a cosmological volume with 512^3 particles of dark matter and 512^3 particles of gas distributed in a box size of $(300h^{-1}\ \mathrm{Mpc}\ )^3$. The force smoothing parameters has been set to 1/30 of the inter particle distance, and corresponds to 20 Kpc for the $300h^{-1}$ Mpc simulation.

The outputs (or snapshots using the GADGET-2 terminology) of the $300h^{-1}$Mpc box were chosen at redshifts for which the comoving distance between both ends of the box would overlap between consecutive redshifts. Each snapshot is analyzed independently from the others. We assume that the Universe is fully ionized below z=7 and we concentrate on this regime. The masses for the dark matter and gas particles are $M_{\mathrm{DM}} = 1.165 \times 10^{10} h^{-1} M_{\odot}$ and $M_{\mathrm{gas}} = 0.17 \times 10^{10} h^{-1} M_{\odot}$ respectively.

The minimum and maximum masses of the structures found in our simulation depend on the simulated volume, particle mass, and of course the redshift. As

discussed earlier, the free-free signal has a wide dynamical range in mass.

The choice of the comoving volume of the simulation box is important: on one hand we want to have the largest possible box so we can include more massive haloes, on the other hand, the small structures have a very significant impact on the average free-free signal and is also important to capture the small scale signal.

To address the issue of resolution in the N-body simulation we make a different simulation (with the same cosmology) but with higher resolution. The use of different box sizes and resolutions is useful to study a wider range of masses (or resolutions) with N-body simulations (see for instance Refregier & Teyssier 2002, [96] and Trenti & Stiavelli 2008, [97]).

The box size of the second simulation is $(50h^{-1}\ \mathrm{Mpc})^3$ (that is 6^3 times smaller in volume). We maintain the same number of particles (512^3 for dark matter and 512^3 for gas). The resulting dark matter and gas particle masses are $M_{\mathrm{DM}} = 6.1 \times 10^7 h^{-1} M_\odot$ and $M_{\mathrm{gas}} = 0.873 \times 10^7 h^{-1} M_\odot$ respectively. The masses of the particles are proportional to the volume of the simulation boxes divided by the number of particles, that is, since the number of particles is the same in both simulations, the particle masses are 6^3 times larger in the 300 h^{-1} Mpc box than in the 50 h^{-1} Mpc one.

Our simulations do not include cooling nor radiative transfer. In a future work we plan to include these mechanisms and improve the predictions. We also plan to extend the redshift range into the reionization period. For the present work, our intention is to explore the redshift range $0 < z < 7$ and focus on the most massive haloes for which the above effects are not so relevant.

2.4.1 Range of halo masses in the N-body simulation

We use a halo finder to map the distribution of haloes in mass and to associate each simulations with a proper free-free emissivity mass range (Fig. 2.3 and Fig. 2.4).

In order to identify haloes and subhaloes in our simulations we have run the MPI+OpenMP hybrid halo finder AHF[1]. A detailed description of AHF is given in the code description paper, ([98]). We provide a brief summary of

[1] AMIGA halo finder, to be downloaded freely from `http://www.popia.ft.uam.es/AMIGA`

the mode of operation. By virtue of the adaptive mesh hierarchy employed to sample the density field, AHF locates overdensities as prospective halo centers. The local potential minima are computed for each of these density peaks and, treating the prospective halo in isolation, the gravitationally bound particles are determined. Only peaks with at least 20 bound particles are considered as haloes and retained for further analysis. For each halo, we compute the virial radius $r_{\rm vir}$, that is the radius r at which the density $M(< r) = (4\pi r^3/3)$ drops below $\Delta_{\rm vir}\bar{\rho}$. Here $\bar{\rho}$ is the cosmological background density. The threshold $\Delta_{\rm vir}$ is computed using the spherical top-hat collapse model and is a function of both cosmological model and time. Applying the AHF to the 300 Mpc simulation, we have found that the mass of the inside haloes only span between $M \approx 10^{11}h^{-1}M_{\odot}$ and $M \approx 10^{14}h^{-1}M_{\odot}$. Low mass haloes are not present in the simulation due to the resolution. On the high end mass, the limited volume of our simulation prevents us from having the most massive clusters in our simulation.

2.4.2 Average free-free from the simulation

For each gas particle in the volume, we compute the free-free luminosity assuming that the electron density is approximately constant over the volume of the particle. Then, the integral of the squared of the electron density can be computed as:

$$\int_V n_e^2 dV \approx n_e \int_V n_e dV = n_e \frac{M_{\rm gas}}{\mu m_p}. \tag{2.4.1}$$

The gas density, n_e, at the position of the particle is extracted from GADGET-2 and then transformed into convenient cm^{-3} units.

Eq. (2.4.1) is used to compute the particle luminosity from Eq. (2.2.1). The particle luminosity is transformed into particle flux given the luminosity distance, D_L, from the particle at redshift z to the observer (at $z = 0$).

$$S_{\rm ff}({\rm Jy}) = \frac{e_\nu}{4\pi D_L^2}. \tag{2.4.2}$$

The internal energy is given by GADGET-2 in units of [km sec^{-1}]^2 which is converted into K with the factor:

$$C_K = 10^6(\gamma - 1)\mu\frac{m_p}{k_b}, \tag{2.4.3}$$

where $\gamma = 5/3$ is the adiabatic index for a monoatomic ideal gas. The scale factor 10^6 accounts for GADGET-2 's internal units, and k_b is the Boltzmann constant.

After the flux per particle is computed, the fluxes are projected along the line of sight into a pixelized 2D map. Since the apparent angular size of each box depends on the redshift, we have to restrict our analysis to the smallest field of view that in our case corresponds to the apparent size of the most distant box (about 3 degrees for the 300 h^{-1} Mpc box). Because we want to compare the distortion that our model induces on the CMB temperature as a function of frequency, we extract a mean flux, $\bar{S}_{\rm ff}$, from all the projected maps. The resulting mean brightness is converted into temperature in K (antenna or thermodynamic, since we are considering low frequencies):

$$\Delta T(\nu) = \frac{c\bar{S}_{\rm ff}}{2k_b\nu^2} \tag{2.4.4}$$

In Fig. 2.5 we show the result obtained from Eq. (2.4.4). We plot, based on the actual constraint of $Y_{\rm ff}$ (*dashed line*), the corresponding upper limit distortion produced by the free-free emission over the CMB temperature. The solid line shows the mean temperature distortion of the projected map in the sky from the simulation while the dot-dashed line refers to the assumption of a constant temperature for all particles of $T = 10^4$ K (see Oh 1999, [71]). Because in Eq. (2.2.1) the strength of the signal depends inversely on the temperature, the lower the temperature of the gas, the higher the signal.

From Fig. 2.5, we conclude that the average free-free distortion predicted from our 300 h^{-1} Mpc N-Body is well below the current observational constraint (*dashed* line). A much lower temperature for the gas (10^4 K) in Eq. (2.2.1) does not change the effect too much showing the anticipated weak dependency of the free-free distortion with the temperature.

The signal from the simulation is also significantly smaller than the value predicted using the analytical model. As we will see below, the most likely reason for this is the fact that the simulation does not include the small mass haloes that give most of the signal in the analytical case. A limiting factor of the N-body simulations is that by construction there is a minimum mass for the haloes. This can have a large impact on the predicted average signal as smaller haloes are expected to be much more numerous than massive ones and they can boost the average signal. In the next subsection we explore the range of masses present

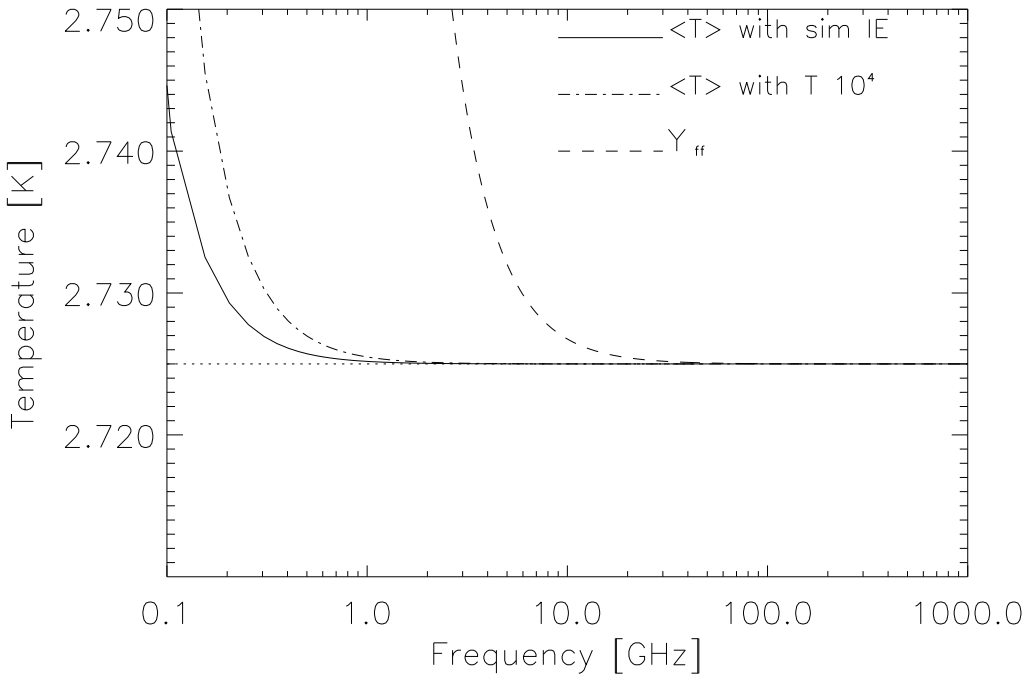

Figure 2.5 Free-free emission distortion from the 300 h^{-1} Mpc simulation. The emission is computed from 20 snapshots within the interval $0 < z < 7$. The field of view covers 2.7 degrees. The solid line shows the distortion in the case where the emissivity has been computed with the temperature derived from the simulation. The dash-dotted line corresponds to the case where the temperature for all particles has been fixed to 10^4 K. The dashed line shows the observational upper limit constraints (95% CL) from Bersanelli et al. (1994), [73].

in the simulation.

2.4.3 Dependency with the resolution

In the previous sections, we have shown the results obtained with the 300 Mpc simulation. In this section we compare the results obtained with the $50h^{-1}$ simulation that has a much higher resolution.

When we compare the mass functions, we find that, as expected, the 50 h^{-1} Mpc box contains less massive haloes, but it has many more small haloes. A halo must contain of the order of 20 particles to be considered a halo. Therefore the minimum mass of a halo depends on the resolution of the simulation.

On the other hand, the maximum mass of a halo depends on the volume of the simulation. Large haloes are truncated by the boundary conditions of the simulation that suppress the power on scales larger than the box side. In other words, there is a minimum k-mode in the Fourier modes which is directly related with the dimension of the box.

We compare the average free-free effect in the 300 h^{-1} Mpc and 50 h^{-1} Mpc boxes. Since the 50 h^{-1} Mpc box is 6^3 times smaller in volume than the 300 h^{-1} Mpc one, we renormalize the average free-free to the same volume. As expected, due to the presence of smaller haloes in the 50 h^{-1} Mpc simulation, the smaller box produces a larger free-free signal. Considering a slice of 50 h^{-1} Mpc at redshift 1.57 in both cases; in the 300 h^{-1} Mpc box the average ΔT is $\Delta T \approx 10^{-6}$ K at 1 GHz while in the 50 h^{-1}Mpc box $\Delta T \approx 5 \times 10^{-6}$ K also at 1 GHz. This is a factor 5 more signal in the higher resolution case. As shown earlier, this extra signal comes from the lower mass haloes although we should keep in mind that in our model we are not including neither radiative cooling nor partial ionization of the low mass haloes. These effects compensate each other partially (in terms of the free-free signal) but they will change the amount of free-free predicted by our model (again, in the low mass haloes more than in the massive ones).

2.5 Free-free from a single massive halo. A new window for cluster science ?

In the previous section we have shown how the average contribution of the massive haloes (groups and clusters) to the mean free-free signal is significantly smaller than the contribution from the smaller but more numerous low mass haloes. In this section we explore the signal of an individual halo comparing the prediction from the β-model with the result obtained from the numerical simulation.

Using the high resolution simulation (50 h^{-1} Mpc box, $M_{\rm gas} = 0.8 \times 10^7 h^{-1} M_\odot$ per particle) presented in Sect. 4, we extract the most massive cluster from it in order to compare its free-free flux with an analytical model. The redshift of the simulation is $z = 1.6$ but the same conclusions can be extracted at other redshifts. It is however interesting to explore the high redshift regime since

the free-free signal could be potentially useful to detect clusters in their earlier stages of formation and before the gas is too hot to be seen through X-rays. In this sense, the free-free emission could extend the actual X-ray science in clusters to the range of the radio waves. Similarly, the same cluster could be seen through the SZ effect but its detection will be harder if the cluster is not hot enough. On the contrary, a lower temperature in the cluster makes the free-free signal stronger.

The halo boundaries are defined as $R_{\rm vir}$ or the radius where the over-density equals 200 times the average density in the box (according to the common assumption of the virial radius r_{200}, adopted to our simulation). For the most massive halo in our simulation, this radius corresponds to $R_{\rm vir} = 560$ kiloparsecs (co-moving) and the corresponding total mass of the halo within this radius is $M_{\rm halo} = 9 \times 10^{12} h^{-1} M_{\odot}$. This mass corresponds to a group of galaxies. We add the flux per particle and compute the flux and temperature distortion (see Eqs. (2.2.1) and (2.4.1)). In Fig. 2.6, we show the one-dimensional profile. The solid line represents the electron density (in cm^{-3}) as a function of the radius. In order to compare this profile with a β-model, the values for n_o and R_c of the β-model are obtained by fitting the solid line in Fig. 2.6 with the analytical profile. The best fitting β-model is also shown in Fig. 2.6 where the core radius corresponds to $1/14$ of the virial radius (or $p = 14$ in the notation used above).

We fix the temperature for the β-model case to the average over the halo particles in the simulation. This average corresponds to $T_{halo} \approx 10^6$ K. With all these ingredients, the fluxes for this halo can be derived from the simulation and the analytical model. For the simulation case we find $S_{\rm ff} = 3.67 \times 10^{-9}$ Jy, while the β-model predicts a larger flux $S_{\rm ff} = 2.80 \times 10^{-8}$ Jy (a factor 7.5 larger). In terms of ΔT, the maximum temperature distortion is about a few μK (at 1 GHz) at the center of the cluster, that is, within reach of future planed experiments like SKA. According to Burigana et al. (2004), [65], SKA could reach a sensitivity limit of 40 nJy in one hour of integration and with an angular resolution of 1 milliarcsecond in the 4-20 GHz band. More massive and denser clusters would produce an even stronger signal making the study of free-free emission in clusters at radio frequencies an interesting and useful way to study the intracluster medium. In Fig. 2.7 we show a map of the free-free signal at 1 GHz in an area containing a more massive cluster at redshift $z = 0.15$ extracted from the 300 Mpc simulation. In this case, the free-free distortion is of the order of 1 mK in

the cluster regions. At higher frequencies, the temperature distortion decreases as ν^{-2}. That is, at 30 GHz, the temperature distortion would be of the order of 1 μK.

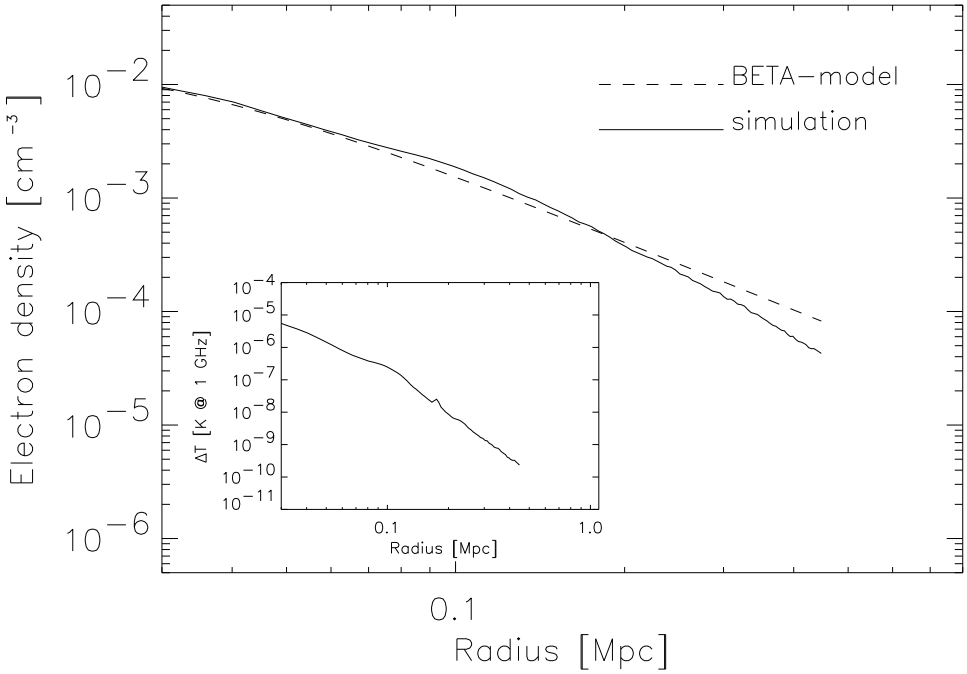

Figure 2.6 Density profile extracted from the most massive halo in the 50 h^{-1} Mpc simulation box at $z = 1.6$. The solid line shows the average electron density profile in concentric shells. For comparison, a β-model is shown (dashed line). The model corresponds to a core radius $R_c \sim 40$ kpc and $p = 1/14$. The smaller box shows the temperature distortion produced by this halo as a function of the radius and at $\nu = 1$ GHz. The maximum distortion is $\Delta T/T_{\rm CMB} \approx 10^{-6}$.

2.6 Discussion

Our results show that there is a significant free-free signal at all redshifts up to the time of reionization. Our predictions are based on analytical models and they are compared with N-body simulations. Some assumptions made in our model need to be improved, like, for instance, the fact that all low mass haloes remain ionized at all times.

Another important improvement is to substitute the β-model (in the analytical

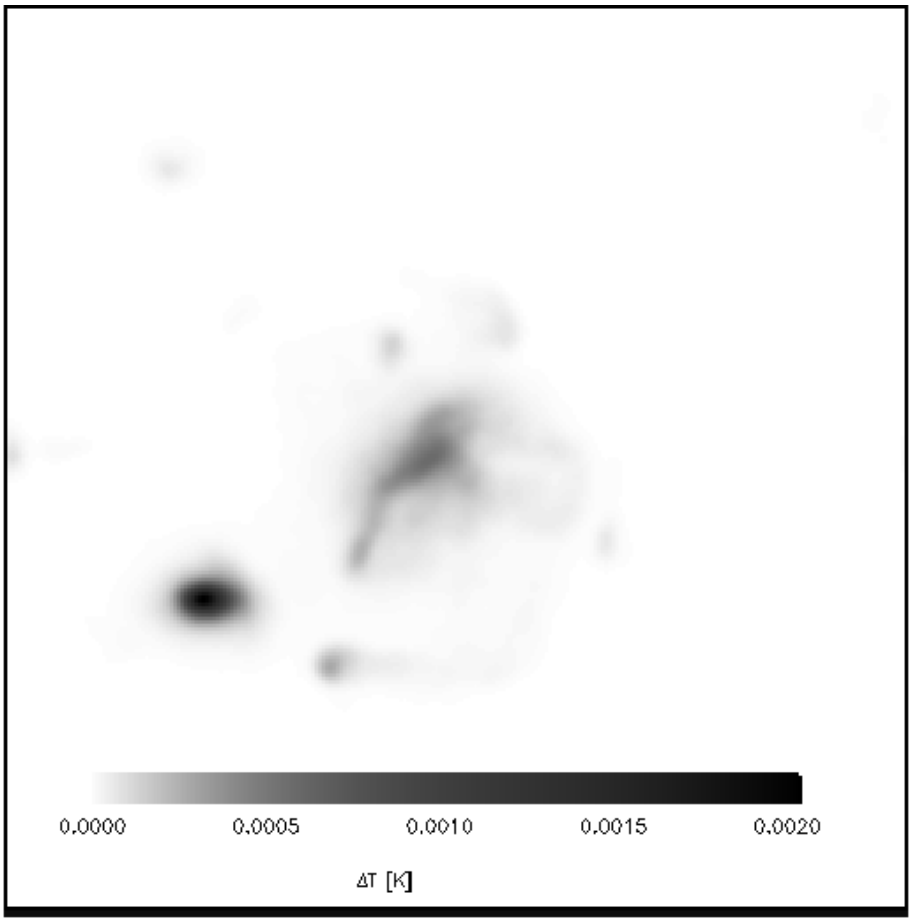

Figure 2.7 Free-free distortion for a massive halo ($M = 6.6 \times 10^{14} h^{-1} M_{\odot}$) at redshift $z = 0.15$. The greyscale shows the distortion in K and at 1 GHz. The field of view is $\approx 40'$. The total flux in this region is $S_{\rm ff} = 2.83 \times 10^{-5}$ Jy.

calculations) by a more accurate description of the gas in massive haloes. In particular, the model of Ascasibar & Diego (2008), [86], assumes a steeper and non-isothermal profile for the gas distribution that could boost the free-free signal. This model is in better agreement with high resolution X-ray profiles in galaxy clusters, [86, 99], and with the SZ effect, [100, 101], than the β-model.

Another issue that need to be addressed in the future is the fact that the free-free effect is significant for a wide range of halo masses. This fact, combined with the high range of redshifts, makes the computation of the free-free from simulations a very demanding task from the computational point of view.

2.6.1 Comparison with earlier results

It is interesting to compare our results (based on numerical and analytical analysis) with those found in the literature that use only analytical methods (Haiman & Loeb 1997, [102], Oh 1999, [71], Cooray & Furlanetto 2004, [79]). The main difference between our analysis and previous ones is that we have focused on the better understood regime at lower redshifts and higher masses. Cooray & Furlanetto (2004) shows how the free-free signal has the maximum contribution at redshift $z \leq 3$. The free-free signal is integrated from the beginning of the reionization ($z \sim 12$ in Oh 1999 and $z \sim 13$ in Cooray & Furlanetto 2004) until present while we consider only a redshift range ($0 < z < 7$) in which the Universe can be considered as fully ionized (on large scales). Also, in this work we focus more on massive haloes which are the ones that can be considered as fully ionized at all times (for $z < 7$). In earlier works, only low mass haloes where considered in the calculations of the free-free signal. The modeling of the low mass haloes is more difficult since they are more sensitive to non-linear phenomena. In a future work, we will extend our analysis to higher redshifts to include the transition between a neutral and a ionized Universe and a more careful modeling of the low mass haloes.

In Oh (1999) (see also Oh & Mack 2003, [60]), a model is proposed for the ionizing sources. The model includes the production rates of recombination line photons $\dot{N}_{\rm recomb}$ and ionizing photons $\dot{N}_{\rm ion}$. It makes a clear distinction between virialized (collapsed) structure that undergo a starburst phase and a diffuse gas that is constantly being re-ionized. A halo mass function is used to compute the number of active haloes (or haloes with a starburst, and ionizing UV flux) and the duration of the starburst is set to a constant interval of $t_0 = 10^7$ years. Our model is, instead, much more simplistic and assumes that all haloes are fully ionized. This assumption certainly fails in the low mass halo regime.

In Oh (1999), [71],the emissivity ϵ_ν is computed combining an expression for the luminosity of the haloes $L_\nu(M, z)$ and the rate formation of ionizing photons. In this model, the temperature is fixed to 10^4 K.

In our case, we used a combination of a β-model plus the mass function combined with a scaling law for the temperature in the analytical case. In the N-body simulation, no assumptions are made about the gas profile or its temperature since these values are extracted directly from the simulation. Recent

models, [82], show that the gas is seldom heated up to the virial temperature in systems with $T < 10^6$ K. Instead they are accreted in *cold flows* (with $T \sim 10^4$ K). The cold flow mechanism is not implemented in our N-body simulations resulting in smaller free-free signal from the smallest haloes.

The N-body simulation includes the contribution from both, compact haloes and diffuse IGM. In the work by Oh (1999), (and later by Oh & Mack 2004), a clear distinction is made between the contribution from small ionized haloes (that remain ionized for a limited amount of time before becoming neutral again) and the diffuse IGM. The authors introduce a cutoff flux S_c corresponding to the minimum mass able to be ionized and with a temperature of $T_e = 10^4$ K. The minimum mass for the ionized haloes with this temperature evolves with redshift as $M_* \sim 10^8(1+z/10)^{-3/2}\ h^{-1}M_\odot$. In our case, the temperature is derived from the simulation and is, in general, larger than the temperature used in Oh (1999) and Cooray & Furlanetto (2004). As a consequence, our higher temperatures will predict a lower free-free signal from haloes. As we mentioned earlier, in a future work we plan to include mechanisms such as cooling that would reduce the temperature of the haloes (and hence would boost the free-free signal).

The distortion over the CMB temperature from haloes derived by Oh (1999) is $\Delta T_{\rm ff} = 3.4 \times 10^{-3}$ K at 2 GHz. This result was obtained with no cutoff in the flux of point sources ($S_c = 0$). On the other hand, an estimation of the flux coming from the diffuse IGM renders a much smaller temperature distortion ($\Delta T_{\rm ff} = 6.0 \times 10^{-6}$ K at 2 GHz) a result later confirmed by Cooray & Furlanetto (2004). Cooray & Furlanetto (2004) obtain a value of $\Delta T_{\rm ff} \approx 5.0 \times 10^{-3}$ K for the halo contribution also at 2 GHz, [79]. Comparing these numbers with our analytical predictions (see Fig. 2.2), we obtain a lower signal at 2 GHz when the temperature of the haloes is computed with the scaling law Eq. (2.3.7) ($\approx 1.73 \times 10^{-3}$ K). Fixing the temperature to $\sim 10^4$ K the results agree better ($\approx 7 \times 10^{-3}$ K).

CHAPTER 3

The contribution of star-forming galaxies to the cosmic radio background

Recent measurements of the temperature of the sky in the radio band, combined with literature data, have convincingly shown the existence of a cosmic radio background with an amplitude of ~ 1 K at 1 GHz and a spectral energy distribution that is well described by a power law with index $\alpha \simeq -0.6$. The origin of this signal remains elusive, and it has been speculated that it could be dominated by the contribution of star-forming galaxies at high redshift if the far infrared-radio correlation $q(z)$ evolved in time. We fit observational data from several different experiments by the relation $q(z) \simeq q_0 - \beta \log(1+z)$ with $q_0 = 2.783 \pm 0.024$ and $\beta = 0.705 \pm 0.081$ and estimate the total radio emission of the whole galaxy population at any given redshift from the cosmic star formation rate density at that redshift. It is found that star-forming galaxies can only account for $\sim$13 percent of the observed intensity of the cosmic radio background.

3.1 Introduction

Although the detection of diffuse radio emission dates back to Jansky (1933), [103], the origin of the cosmic radio background (CRB) is still a mystery. The recent data obtained by the Absolute Radiometer for Cosmology, Astrophysics and Diffuse Emission (ARCADE 2) has revived the interest in this question, de-

tecting a diffuse background at frequencies between 3 and 10 GHz that is more then $5\,\sigma$ above the COBE/FIRAS measurement of the temperature of the cosmic microwave background (CMB) and well in excess of current estimates based on radio source counts. More precisely [76], the inferred value of the antenna temperature as a function of frequency can be expressed as

$$T(\nu) = \frac{h\nu/k}{\exp(h\nu/kT_{\rm CMB}) - 1} + T_R \left(\frac{\nu}{\nu_0}\right)^{\alpha-2} \tag{3.1.1}$$

where $T_{\rm CMB} = 2.729 \pm 0.004$ K denotes the thermodynamic temperature of the CMB, $T_R = 1.19 \pm 0.14$ K is the normalization of the radio background at $\nu_0 = 1$ GHz, and $\alpha = -0.62 \pm 0.04$ is the spectral index of the CRB, consistent with synchrotron emission from normal galaxies (see e.g. Condon 1992, [50]).

The observed emission is most likely of extragalactic origin, [104], and several candidates have been considered by Singal et al. (2010), [105]. Radio source counts detected by current surveys, sensitive to flux densities above $S_{1.4\,\rm GHz} \gtrsim 10$ μJy, cannot explain more than $\sim$ 10 per cent of the signal, [106–108], and low-surface brightness sources missed by these surveys may contribute, at most, an additional 15 per cent. Diffuse emission in regions far from galaxies is ruled out due to the overproduction of X-rays and γ-rays, so the only possible explanation is that the cosmic radio background is dominated by faint sources below the threshold of 10 μJy, [105].

According to Singal et al. (2010), radio supernovae make a negligible contribution, and radio-quiet quasars may be responsible for only a few per cent of the emission. Thermal bremsstrahlung from the hot gas in galaxy clusters has been shown to contribute about $0.01 - 0.02$ K at $\nu = 1$ GHz (see e.g.Ponente et al. 2011, [109]), and the most reasonable candidate to explain the bulk of the CRB seems to be the population of ordinary star-forming galaxies at high redshift.

Some authors, [71, 79], have tried to estimate the contribution of free-free emission from star-forming galaxies to the radio background by resorting to phenomenological prescriptions to relate halo mass and star formation activity at different redshifts.
However, if the far infrared-radio correlation (FRC) observed for local galaxies holds at all redshifts, there must be a tight relation between the radio and infrared backgrounds, [110, 111]. From the measured intensity of the latter, one concludes that the contribution of star-forming galaxies must be of the order of $5 - 10$ per cent.

During the last years, the advances in infrared and sub-millimetric instrumentation have made it possible to investigate the evolution of the FRC over a large fraction of the age of the Universe, and several recent studies (e.g. Ivison et al. 2010a, Ivison et al. 2010b, Michałowski, Hjorth & Watson 2010, [112–114]) suggest that the correlation is linear at all times, but the normalization is offset towards increasing radio loudness at high redshifts, boosting the expected signal from star-forming galaxies by a significant amount. In the present work, we make a quantitative estimate of the contribution of star-forming galaxies to the CRB. The prescription followed to assign radio luminosities as a function of the instantaneous star formation rate is detailed in Sect. 3.2. The evolution of the far infrared-radio correlation is discussed in Sect. 3.3, and the implications for the cosmic radio background are shown in Section 3.4. Our main conclusions are briefly summarized in the Sect. 5.2 in Chapter 5.

3.2 Radio emission from individual galaxies

In normal galaxies, radio emission is always associated to star formation, see e.g. Condon (1992), [50], or Introduction, Sect. 1.9. Young, massive stars produce intense ultraviolet radiation that ionizes the surrounding medium, and thermal bremsstrahlung from these free electrons (often referred to in the radio literature as *free-free* emission) makes a significant contribution to the galaxy spectra in the few-GHz range. On the other hand, stars with $M > 8\ \mathcal{M}_{\odot}$ explode as Type II and Type Ib supernovae at the end of their life cycle. Supernova remnants are thought to accelerate most of the relativistic electrons in normal galaxies, and they constitute the main source of the synchrotron emission that dominates at low frequencies.

Assuming a pure Hydrogen plasma with an electron temperature $T_e \sim 10^4$ K, the free-free luminosity of a galaxy is approximately given by

$$\frac{L_{\rm ff}}{3.2 \times 10^{-39}\ {\rm erg\ s^{-1}\ Hz^{-1}}} \approx \left(\frac{\nu}{\rm GHz}\right)^{-0.1} \left(\frac{n_e}{\rm cm^{-3}}\right)^2 \left(\frac{V_e}{\rm cm^3}\right) \qquad (3.2.1)$$

where ν denotes the photon frequency, n_e is a characteristic electron density, and V_e represents the total volume occupied by the radio-emitting, ionized HII regions, [71, 115]. This volume is set by the condition that the number of ionizing photons Q emitted by the stars per unit time is equal to the recombination

rate

$$Q = n_e^2 \, \alpha_B \, V_e \tag{3.2.2}$$

with $\alpha_B = 2.6 \times 10^{-13}$ cm^3 s^{-1} being appropriate for case-B recombination at $T_e \sim 10^4$ K. According to stellar population synthesis models, e.g. Leitherer & Heckman (1995) and Mollá, García-Vargas & Bressan (2009), [116, 117],

$$\frac{Q}{1.5 \times 10^{53} \text{ s}^{-1}} \approx \frac{\Psi}{\mathcal{M}_\odot \text{ yr}^{-1}} \tag{3.2.3}$$

where Ψ is the current star formation rate (SFR) of the galaxy, assuming a Salpeter, [118], initial mass function (IMF) between 0.1 and 100 $\mathcal{M}_\odot$. In the end, the predicted free-free luminosity

$$\frac{L_{\text{ff}}}{1.8 \times 10^{27} \text{ erg s}^{-1} \text{ Hz}^{-1}} \approx \frac{\Psi}{\mathcal{M}_\odot \text{ yr}^{-1}} \left(\frac{\nu}{\text{GHz}}\right)^{-0.1} \tag{3.2.4}$$

scales roughly proportionally with the instantaneous star formation rate.

Computing the synchrotron luminosity from first physical principles is much more involved, since it requires knowledge of the amount of cosmic rays injected by supernovae, their spectrum, and the conditions of the surrounding medium (most notably, its density structure and the intensity of the magnetic field). Observationally, [50], non-thermal synchrotron emission is about 10 times more luminous than the free-free continuum at $\nu = 1$ GHz, and its spectral index is close to ~ 0.7 for a broad range of star-forming galaxies. In addition, there is a tight correlation between the synchrotron luminosity and the thermal radiation emitted by the dust in the infrared, which is powered by the stellar ultraviolet light and is thus another tracer of the star formation rate. The observed far infrared-radio correlation suggests (but see e.g. Lacki, Thompson & Quataert 2010 and Lacki & Thompson 2010 for a different point pf view, [119, 120]) that synchrotron emission is also proportional to the SFR, implying that

$$\frac{L_{\text{syn}}}{1.8 \times 10^{28} \text{ erg s}^{-1} \text{ Hz}^{-1}} \approx \frac{\Psi}{\mathcal{M}_\odot \text{ yr}^{-1}} \left(\frac{\nu}{\text{GHz}}\right)^{-0.7}. \tag{3.2.5}$$

3.3 Evolution of the FRC

Since most of the contribution of normal galaxies to the cosmic radio background observed today is due to their synchrotron emission, with thermal bremsstrahlung (see e.g. Oh 1999, Seiffert et al. 2011, Ponente et al. 2011,

[71, 77, 109]) providing only a minor correction at the level of a few percent, equation (3.2.5) has a crucial importance. In particular, the intensity of the CRB is extremely sensitive to the evolution in time of the relation between SFR and radio luminosity.

It is not clear, though, whether the far infrared-radio correlation should evolve with redshift, and current observational evidence is far from being conclusive. While several recent studies (e.g. Ibar et al. 2008, Sargent et al. 2010, [121, 122]) are consistent with no evolution in the FRC, some others report systematic trends with redshift (e.g. Vlahakis, Eales & Dunne 2007, Seymour et al. 2008 and Michałowski, Hjorth & Watson 2010, [114, 123–125]).

The main source of uncertainty is that normal galaxies are rather faint in the radio band. According to equation (3.2.5), only the most intense starbursts, with instantaneous SFR in excess of $\Psi \gtrsim 30\ \mathcal{M}_\odot\ yr^{-1}$, would be detectable at $z \geq 1$ by current surveys, whose sensitivity at 1.4 GHz is of the order of $\sim 10\ \mu$Jy.

One possible solution (see e.g. Marsden et al. 2009, Pascale et al. 2009, Patanchon et al. 2009, [129–131]) is to stack the confusion-limited and sensitivity-limited radio images at the positions of thousands of infrared-selected galaxies. In doing so, one increases the signal-to-noise ratio and reduces the contribution of radio-loud active galactic nuclei (*AGN*), probing a population that is more representative of normal galaxies. This procedure has been applied by Ivison et al. (2010a), [112], to a mid infrared-selected sample of galaxies, obtaining that

$$q \equiv \log \frac{L_{\rm IR}\ /\ 3.75 \times 10^{12}\ {\rm W}}{L_{1.4\,{\rm GHz}}\ /\ {\rm W\ Hz^{-1}}} \propto (1+z)^{\gamma} \tag{3.3.1}$$

with $\gamma = -0.15 \pm 0.03$. Both the total infrared luminosity $L_{\rm IR}$ (defined from 8 to 1000 μm)[1] and the radio power $L_{1.4\,{\rm GHz}}$ are given at the rest-frame of the source, using a k-correction based on spectral templates. A similar analysis, [113], is consistent with no evolution, $\gamma = -0.04 \pm 0.03$, but discarding the least reliable data at $z < 0.5$ yields $\gamma = -0.26 \pm 0.07$.

Alternatively, one may detect high-redshift star-forming galaxies by observing their rest-frame infrared dust emission, shifted towards sub-millimeter wavelengths. Based on a sample of 76 sub-millimeter galaxies with measurements in the radio band, Michałowski, Hjorth & Watson (2010) conclude, in agreement with previous studies (e.g. Kovacs et al. 2006 and Murphy 2009, [132, 133]) that the radio emission of high-redshift galaxies scales linearly with the SFR, but the

[1] The difference with e.g. the far-infrared band (from 60 to 100 μm) is about a factor of two.

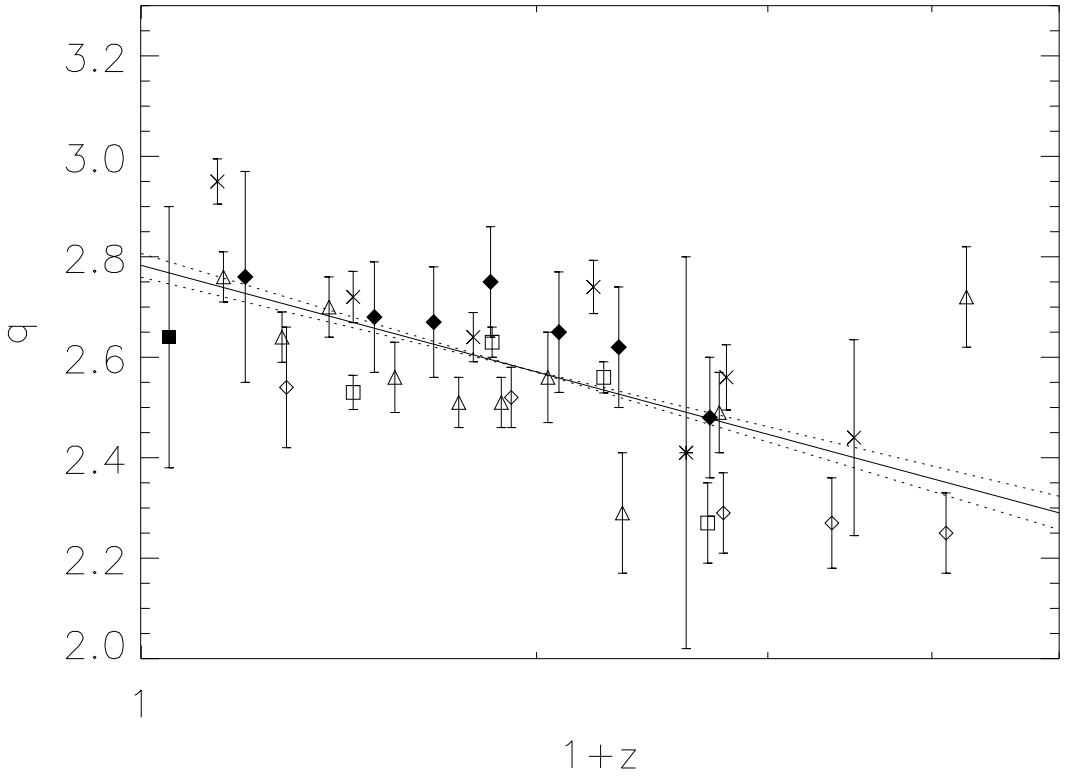

Figure 3.1 Evolution of the far infrared-radio correlation. Least-squares fit (solid line) with 1σ limits (dash lines) to the observational data from (Bell 2003, full squares, [126]), (Murphy et al. 2009, stars, [127]), (Michałowski, Hjorth & Watson 2010, open diamonds, [114]), (Sargent et al. 2010, triangles, [122]), (Bourne et al. 2011, full diamonds, [128]), (Ivison et al. 2010a, crosses, [112]) and (Ivison et al. 2010b, open squares, [113]).

normalization is about a factor of two higher than for local samples.

Although selection effects (e.g. Sargent et al. 2010, [122]) and potential biases arising from spectral templates, [128], cannot be completely excluded, a combination of different data sets is fairly well reproduced by

$$q(z) = q_0 - \beta \log(1+z) \tag{3.3.2}$$

with $q_0 = 2.783 \pm 0.024$ and $\beta = 0.705 \pm 0.081$ (see Fig. 3.1). Assuming that $L_{\rm IR} \propto \Psi$ and that the constant of proportionality does not vary with redshift, this implies that the synchrotron luminosity of a given galaxy scales as

$$\frac{L_{\rm syn}}{1.8 \times 10^{28}\,{\rm erg\,s^{-1}\,Hz^{-1}}} \approx \frac{\Psi}{\mathcal{M}_\odot\,{\rm yr^{-1}}} \left(\frac{\nu}{\rm GHz}\right)^{-0.7} (1+z)^{\beta} \tag{3.3.3}$$

In other words, we assume that the infrared luminosity is an unbiased tracer of the SFR and that all the evolution of the FRC is due to the conversion between SFR and radio luminosity.

3.4 The cosmic radio background

The specific intensity of the cosmic background at any given frequency is given by the integral along the line of sight

$$I_\nu = \frac{c}{4\pi H_0} \int_0^\infty \frac{\epsilon_{\nu'}(z)}{(1+z)\,E(z)}\,\mathrm{d}z \tag{3.4.1}$$

of the average emissivity per unit volume $\epsilon_{\nu'}$. In this formula, c and H_0 denote the speed of light and the Hubble constant, respectively,

$$E(z) = \sqrt{\Omega_M(1+z)^3 + \Omega_\mathrm{k}(1+z)^2 + \Omega_\Lambda} \tag{3.4.2}$$

reflects the cosmological expansion, and $\nu' = \nu(1+z)$ is the initial frequency at which the photons observed today with a frequency ν were emitted. We adopt a WMAP7 (seven-year observation) cosmology with $\Omega_M = 0.27$, $\Omega_K = 0$, $\Omega_\Lambda = 0.73$, and $H_0 = 71$ km s^{-1} Mpc^{-1}, [9], and compute the brightness temperature of the CRB as

$$T(\nu) = \frac{c^2\,I_\nu}{2k\nu^2} \tag{3.4.3}$$

using the Rayleigh-Jeans approximation, where k is the Boltzmann constant.

By definition, the average emissivity at a given redshift is the sum

$$\epsilon_{\nu'}(z) = \int_0^\infty n(\Psi, z)\; L_{\nu'}(\Psi)\;\mathrm{d}\Psi \tag{3.4.4}$$

of the contributions of all the galaxies at that redshift, with $n(\Psi, z)$ representing the number density of galaxies with SFR between Ψ and $\Psi + \mathrm{d}\Psi$ at redshift z. As long as the relation between luminosity and instantaneous star formation rate is linear, $L_{\nu'} = \kappa(\nu', z)\,\Psi$, as indicated by equations (3.2.4) and (3.3.3), one can express the total emissivity

$$\epsilon_{\nu'}(z) = \kappa(\nu', z) \int_0^\infty n(\Psi, z)\;\Psi\;\mathrm{d}\Psi = \kappa(\nu', z)\;\dot{\rho}_*(z) \tag{3.4.5}$$

in terms of the cosmic SFR density $\dot{\rho}_*$, [111]. The emissivity of the free-free and synchrotron components can be taken into account simultaneously as

$$\epsilon_{\nu'}(z) = \left[\kappa_\mathrm{ff}(\nu', z) + \kappa_\mathrm{syn}(\nu', z)\right]\;\dot{\rho}_*(z) \tag{3.4.6}$$

with

$$\frac{\kappa_\mathrm{ff}(\nu', z)}{1.8\times 10^{27}\ \mathrm{erg\,s^{-1}\,Hz^{-1}}\,\mathcal{M}_\odot^{-1}\,\mathrm{yr}} = \left(\frac{\nu'}{\mathrm{GHz}}\right)^{-0.1} \tag{3.4.7}$$

and

$$\frac{\kappa_{\rm syn}(\nu', z)}{1.8 \times 10^{28}\,{\rm erg\,s^{-1}\,Hz^{-1}}\,\mathcal{M}_\odot^{-1}\,{\rm yr}} = \left(\frac{\nu'}{\rm GHz}\right)^{-0.7}(1+z)^{\beta} \tag{3.4.8}$$

where $\beta = 0$ for a non-evolving far infrared-radio correlation, and $\beta = 0.705 \pm 0.0801$ to fit the data plotted in Figure 3.1.

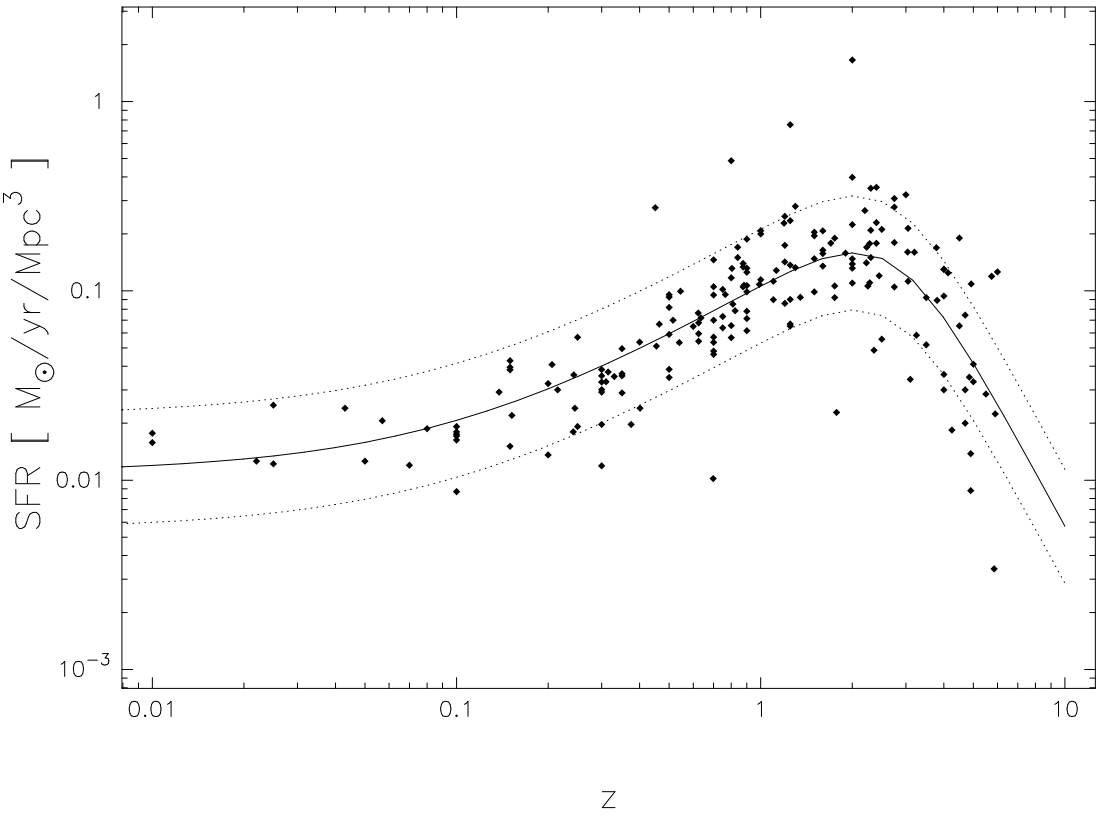

Figure 3.2 Cosmic star formation history. The solid line shows the best fit provided by expression (3.4.9) to the data points compiled by Michałowski, Hjorth & Watson (2010), [114], and dotted lines illustrate an uncertainty of a factor of 2.

The evolution of the cosmic SFR density has been extensively studied during the last decade, and several compilations of observational data exist in the literature (e.g. Somerville, Primack & Faber 2001, Ascasibar et al. 2002, Hopkins 2004, Hopkins & Beacom 2006, Michałowski, Hjorth & Watson 2010, [114, 134–137]. In the present work, we have adopted the parametrization of Cole et al. (2001), [138],

$$\frac{\dot{\rho}_*(z)}{\mathcal{M}_\odot\ {\rm yr^{-1}\ Mpc^{-3}}} = \frac{a + bz}{1 + \left(\frac{z}{c}\right)^d} \tag{3.4.9}$$

and fit the observational data points reported in Table A.4 of Michałowski, Hjorth & Watson (2010)[2]. The optimal values $(\,a, b, c, d\,) = (\,0.011,\, 0.097,\, 2.73,\, 3.96\,)$

[2]Conversion to a Salpeter IMF between 0.1 and $100\mathcal{M}_\odot$ and a WMAP7 cosmology (following the pre-

have been obtained by means of the FiEstAS sampling technique, [139], a Monte Carlo integration scheme based on the Field Estimator for Arbitrary Spaces (FiEstAS, [140, 141]). The resulting cosmic star formation history is plotted as a solid line in Fig. 3.2.

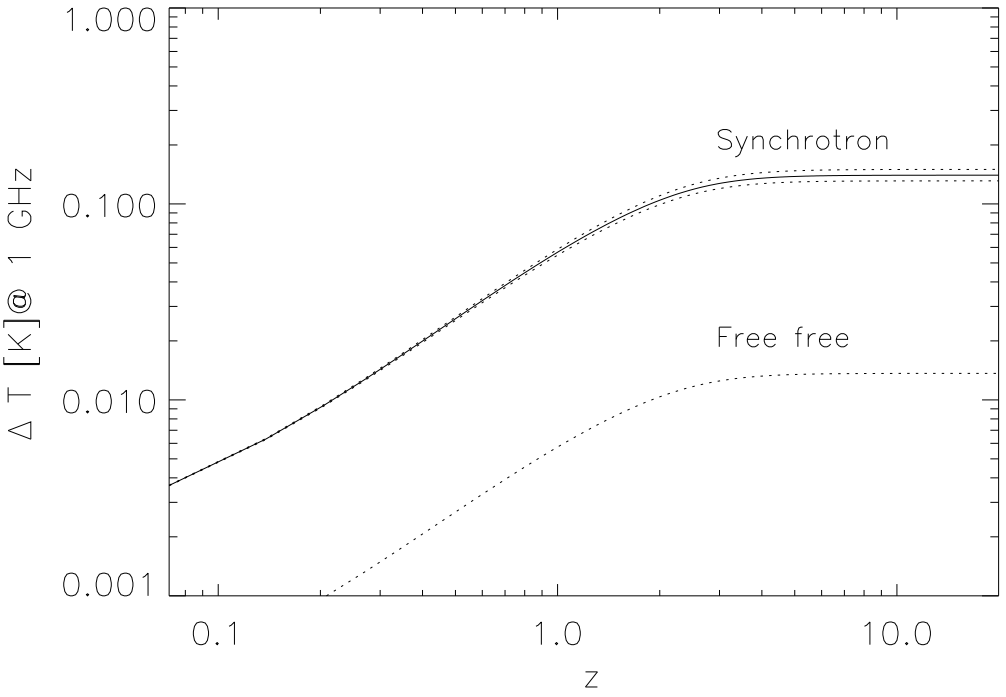

Figure 3.3 Integrated radio emission, observed at 1 GHz, from normal galaxies up to redshift z. ΔT refers to the excess signal above the CMB temperature. The solid line shows the contribution of synchrotron emission, assuming $\beta = 0.705$, and the errors associated to the least-squares fit (~ 0.01 at the end of the integration) are indicated by the dashed lines. The contribution of free-free emission is plotted as a dotted line.

Combining expressions (3.4.1), (3.4.3), (3.4.5), (3.4.7), and (3.4.9), we estimate that the contribution of free-free emission from star-forming galaxies to the cosmic radio background is

$$\frac{T_{\rm ff}}{0.0137\ {\rm K}} = \left(\frac{\nu}{\rm GHz}\right)^{-2.1} \tag{3.4.10}$$

whereas, using expression (3.4.8), synchrotron emission yields

$$\frac{T_{\rm syn}}{0.0817\ {\rm K}} = \left(\frac{\nu}{\rm GHz}\right)^{-2.7} \tag{3.4.11}$$

scription in Ascasibar et al. 2002, [135]) amounts to a negligible correction.

for $\beta = 0$ and

$$\frac{T_{\rm syn}}{0.1402\ {\rm K}} = \left(\frac{\nu}{\rm GHz}\right)^{-2.7} \tag{3.4.12}$$

for $\beta = 0.705$.

As can be seen in Fig. 3.3, the signal is dominated by galaxies at $z < 3$, due to the combined effects of distance dimming and the declining behavior of the cosmic star formation rate at high redshift.

CHAPTER 4

Systematics in lensing reconstruction

Non-parametric lensing methods are a useful way of reconstructing the lensing mass of a cluster without making assumptions about the way the mass is distributed in the cluster. These methods are particularly powerful in the case of galaxy clusters with a large number of constraints. The advantage of not assuming implicitly that the luminous matter follows the dark matter is particularly interesting in those cases where the cluster is in a non-relaxed dynamical state. On the other hand, non-parametric methods have several limitations that should be taken into account carefully. We explore some of these limitations and focus on their implications for the possible ring of dark matter around the galaxy cluster CL0024+17. We project three background galaxies through a mock cluster of known radial profile density and obtain a map for the arcs (θ map). We also calculate the shear field associated with the mock cluster across the whole field of view (3.3 arcmin). Combining the positions of the arcs and the two-direction shear, we perform an inversion of the lens equation using two separate methods, the biconjugate gradient, and the quadratic programming (QADP) to reconstruct the convergence map of the mock cluster. We explore the space of the solutions of the convergence map and compare the radial density profiles to the density profile of the mock cluster. When the inversion matrix algorithms are forced to find the exact solution, we encounter systematic effects resembling ring structures, that clearly depart from the original convergence map. Overfitting lensing data with a non-parametric method can produce ring-like structures similar to the alleged one in CL0024.

4.1 Introduction

Gravitational lensing is one of the most powerful probes of dark matter. In particular, galaxy clusters host the strongest gravitational potentials in the Universe, hence they are rich in gravitational lensing effects. The distortions produced in the images of background galaxies by a galaxy cluster can be used to reconstruct the mass distribution of the cluster, which is believed to be largely dominated by dark matter. Two regimes are distinguished according to the strength of the lensing distortion. The weak lensing regime refers to small distortions that usually need to be studied in a statistical way. Large distortions, on the other hand, can be studied individually (or in pairs) and they are referred to as strong lensing. Strong lensing occurs when the projected surface mass density is on the order of the critical mass density Σ_{crit}. In this scenario, a gravitational lens bends the light in such a way that it can produce multiple images (arcs) of the same background galaxy. Each multiple image can be used as a constraint of the mass distribution. The mass distribution has to be such that, when projected back into the source plane, the multiple images concentrate (or focus) into the same point. In most cases, the number of multiple images is small, which results in few constraints. If only strong lensing is available and the number of constraints is small, one needs to rely on parametric methods. However, more and more often new data reveals large numbers of multiple images around a single cluster. The cluster A1689 is probably the most spectacular example to date where hundreds of arcs can be seen around the cluster, [142, 143]. When the number of constraints is sufficiently large, non-parametric methods become competitive with the parametric ones and with the advantage that no *a priori* assumption is made about the mass distribution of the cluster. Non-parametric methods applied to lensing mass reconstruction have been studied in the past, [144–154]. On the positive side, in cases where the number of constraints is large, the results obtained with the parametric and non-parametric methods agree well (Diego et al. 2005b) probing, among other things, that the dark matter does trace the luminous matter and the usefulness of non-parametric methods as a way of testing that the assumptions made in the parametric methods are well founded. Non-parametric methods have been used as well to combine weak and strong lensing data in the same analysis, [146, 148, 151, 152, 155–157].

On the other hand, non-parametric methods have a series of limitations. In this

paper we explore one of these limitations related to the limited resolution in the mass reconstruction and its connection with the accuracy in the reconstructed arc positions.

The results of this paper may have implications for the results of Jee et al. (2007) , [31], who use a non-parametric method and find an unusual ring of dark matter around the cluster. While we do not question the validity of these interesting results, we explore the possibility that spurious structures might appear when using non-parametric methods if the limitations of parametric methods are not taken into account in the analysis.

4.1.1 A ring of dark matter around CL0024+17?

The cluster CL0024+17 ($z = 0.395$) was one of the first for which strong lensing was observed, [158]. Four strongly lensed arcs can be clearly seen around the tangential critical curve (see also Smail et al. 1996 and Broadhurst et al. 2000, [159, 160]). These arcs have been used to constrain the mass in the central region of the cluster, [160–163]. These mass constraints have been compared with those derived from X-ray measurements with CHANDRA, [164], and XMM-Newton, [165]. These authors estimated that the X-ray masses are a factor 3-4 lower than the lensing masses. This discrepancy has been interpreted as a sign that the cluster is not in hydrostatic equilibrium.

In Jee et al. (2007) , the authors reconstruct the mass of the cluster out to 100 arcseconds from its center. This corresponds to a physical size of 0.389 Mpc for an object located at $z \simeq 0.4$. In their analysis, they combine strong and weak lensing with a non-parametric method. The authors find a dark matter ring surrounding the cluster core, at $r \approx 75$ arcseconds from the center (Fig. 10 in Jee et al. 2007). The authors suggest that this ring might be the result of a high speed collision between two clusters along the line of sight, [166], in a scenario similar to the 'bullet cluster', [29], but with the difference that in that case the collision is perpendicular to the line of sight.

Whether the existence of the dark matter ring is real or not has been debated by many other authors like Milgrom & Sanders (2008), Qin, Shan & Tilquin (2008), Zu Hone, Lamb & Ricker (2009), Zitrin et al. (2009), Umetsu et al. (2010),

[167–171]. Milgrom & Sanders (2008) reconstruct the radial profile of the mass assuming a model based on modified Newtonian dynamics (or MOND). The authors claim that a ringlike structure appears at the MOND transition region (see figs. 3 and 4 in their paper). According to the authors, CL0024 can be considered as a robust probe of MOND. In Qin, Shan & Tilquin (2008), the authors study the distribution of galaxies in CL0024, which, being collisionless, should exhibit a similar ring-like pattern. On the basis of 295 counts, the authors find no evidence of a ring in the distribution of galaxies. In a different paper, Zu Hone, Lamb & Ricker (2009) use a hydrodynamical simulation of two colliding clusters to compute the radial profiles after the collision. They find no evidence of either a dip or ring in the radial profile outside the core radius after the collision. They conclude that a ring-like feature could only be explained by an unlikely and highly tuned set of initial conditions before the collision.

To reanalyze the lensing data for CL0024, Zitrin et al. (2009) analyze this cluster using data from the Hubble Space Telescope (HST) instrument ACS/NIC3. The dark matter distribution profile was reconstructed using a SL parametric method based on six free parameters. The results presented in Fig. 1 and Fig. 2 of their paper reveal neither a dip nor ring in the profiles. Finally, Umetsu et al. (2010) combine a large field of view data set from the SUBARU telescope with data from HST ACS/NIC3, finding no evidence of the ringlike structure after the mass reconstruction (see Fig. 21 of their paper).

In this paper, we revisit the debate using a non-parametric method similar to that used in Jee et al. (2007) but applied to simulated data (weak and strong lensing). The advantage of using simulations is that the underlying dark matter distribution and the position and redshifts of the background sources are perfectly known. This offers the unique possibility of comparing the optimal solution with the multiple possible solutions obtained by the non-parametric method. We can also explore the space of solutions obtained when the minimization is done under different assumptions and compare with the original mass distribution.

In Sections 4.2 and 4.3, we introduce the fundamentals of the gravitational lensing and the non-parametric method used in this paper for the mass reconstruction. In Section 4.4, we describe the mock data used in our analysis. In Section

4.5, we present the results obtained by our non-parametric method and compare the different solutions with the optimal one. Finally, in Section 4.6, we discuss our results and in Section 5.3 our conclusions.

4.2 Gravitational lensing basics

Basics for gravitational lensing have been given in Sect. 1.8, where it can be seen as a direct consequence of the dark matter paradigm and the halo formation. However, some technical notion on the mass recontruction method used for this work are given in the next subsection. More details are given in Appendix B.

4.2.1 Parameter-free lensing reconstruction

Here we adopt formalism and notation of Diego et al. (2005a) and Diego et al. (2007).

The mass reconstruction described in those papers is based on a parameter-free method where the lens plane is divided into a finite number of cells N_c and Eq. (1.8.1) can be written in algebraic form. The deflection angle α at a position θ is computed from the net contribution of the discretized mass distribution m_i at the positions θ_i

$$\alpha(\theta) = \frac{4G}{c^2}\frac{D_{ls}}{D_{os}D_{ol}}\sum_{N_c} m_i(\theta_i)\frac{\theta-\theta_i}{|\theta-\theta_i|^2}. \tag{4.2.1}$$

The number of cells in the gridded mass must be carefully choosen. The discretization of the lens plane affects the spatial resolution of the mass reconstruction, as we discuss in more detail later.

All the positions of the pixels hosting a strong lens image can be described by the vector θ of dimension N_θ. For each pixel in the θ vector and for a given discretized mass distribution, a corresponding β pixel can be traced back to the source plane. The relation between all these elements can be written in algebraic form

$$\theta = \Upsilon M + \beta, \tag{4.2.2}$$

where θ (and β) are vectors containing the x and y components of the N_θ pixels of the arcs (and sources), M is the vector of the masses inside the N_c cells, and

the matrix Y has the dimension of $(2N_\theta \times N_c)$. The description of this matrix is given in Diego et al. (2005a).

Eq. (4.2.2) is a system of $2N_\theta$ linear equations whose solution can be achieved using the methods described in Diego et al. (2005a). The unknowns of the problem are the masses in the M vector and the central positions of the background sources. Both vectors can be united into a single one X, rendering the simpler equation

$$\theta = \Lambda X, \tag{4.2.3}$$

where Λ is a matrix similar to Y but with an extra sparse block containing 1 and 0.

Weak lensing data can be modeled in a similar way. The two components of the shear are computed through the matrices that represent the contribution of each mass cell:

$$\begin{pmatrix} \gamma_1 \\ \gamma_2 \end{pmatrix} = \begin{pmatrix} \mathbf{\Delta_1} \\ \mathbf{\Delta_2} \end{pmatrix} M. \tag{4.2.4}$$

A detailed description of the matrices Y, Δ_1 and Δ_2 is presented in Appendix B.1.

After including the weak lensing regime, the joint system of linear equations can be explicitly written down as

$$\begin{pmatrix} \theta_x \\ \theta_y \\ \gamma_1 \\ \gamma_2 \end{pmatrix} = \begin{pmatrix} \mathbf{Y_x} & \mathbf{I_x} & \mathbf{0} \\ \mathbf{Y_y} & \mathbf{0} & \mathbf{I_y} \\ \mathbf{\Delta_1} & \mathbf{0} & \mathbf{0} \\ \mathbf{\Delta_2} & \mathbf{0} & \mathbf{0} \end{pmatrix} \begin{pmatrix} M \\ \beta_x \\ \beta_y \end{pmatrix}, \tag{4.2.5}$$

where the element ij in the matrix I_x is 1 if the θ_i pixel comes from the β_j source, and is 0 otherwise. The matrix 0 is the null matrix. Eq. (4.2.5) can be written in the more compact form

$$\Phi = \mathbf{\Gamma} X, \tag{4.2.6}$$

where Φ is the vector containing the positions of the arcs and the shear measurements, Γ is a non-square matrix, and X is the vector of the unknowns.

Written in this simple form, the lensing problem could, in principle, be resolved after the inversion of Eq. (4.2.6), $X = \Gamma^{-1}\Phi$.

4.3 Inversion of the lens equation

The vector X can be found by inverting Eq. (4.2.6). However, the matrix $\mathbf{\Gamma}$ is often non-invertible. This is actually not a problem as we seek an approximate solution with a more physical meaning than the exact solution. One of the assumptions made in the parametric method is that the background galaxies are infinitely small. The exact solution of the system of linear equations would reproduce an unphysical situation where the background galaxies are *point-like*. On the other hand, an approximate solution of the system has the benefit that the predicted background sources are not point-like but extended. In addition, an approximate solution allows for some error that is needed to compensate for the other *wrong* assumption made in non-parametric methods, namely, the assumption that the mass distribution is discretized. The predicted size of the background sources can be controlled in the solution by setting an error level or *residual*, R, in the system of linear equations

$$\mathbf{R} \equiv \Phi - \mathbf{\Gamma} X. \tag{4.3.1}$$

In the case of WL, the physical meaning of the residual is the associated error in the determination of the reduced shear.

As discussed in Diego et al. (2005a), a powerful way to find an approximate solution to the system is through the bi-conjugate gradient algorithm, which minimizes the square of the residual

$$\begin{aligned} \mathbf{R^t C^{-1} R} &= (\mathbf{\Phi} - \mathbf{\Gamma X})^t \mathbf{C^{-1}} (\mathbf{\Phi} - \mathbf{\Gamma X}) \\ &= \left(\mathbf{\Phi}^t \mathbf{C^{-1}} \mathbf{\Phi} - 2\mathbf{\Phi}^t \mathbf{C^{-1}} \mathbf{\Gamma X} + \mathbf{X}^t \mathbf{\Gamma}^t \mathbf{C^{-1}} \mathbf{\Gamma X} \right), \end{aligned} \tag{4.3.2}$$

where $\mathbf{C}$ is the covariance matrix of the residual R and among other things includes the relative weights of the SL and WL data. As discussed in Diego et al. (2007), this residual can be described (to first order) by a Gaussian distribution with a diagonal covariance matrix. This is however an approximation. The elements of the residual are correlated with each other, in particular those

elements corresponding to the SL part of the data. The elements of the WL part of the residual are far more weakly correlated with each other and the diagonal approximation is a far more valid for this part. For the time being, we assume that the covariance matrix is diagonal and later discuss its implications. The diagonal approximation has been also assumed in previous works, including Jee et al. (2007) . The elements of the diagonal corresponding to the SL data are set to σ_{SL} and the elements of the diagonal corresponding to the WL data are set to σ_{WL}. We adopt $\sigma_{SL} \sim 1$ arcsecond (in radians) and $\sigma_{WL} = 0.3$ (or equivalently 30%). As discussed in Diego et al. (2007), the value of σ_{SL} has a physical meaning. Its value is connected with the angular size of the sources.

An alternative to the bi-conjugate gradient is the non-negative quadratic programming (QADP). A brief description of bi-conjugate and quadratic programming is given in Appendix B.2.

Both methods have advantages and disadvantages: the bi-conjugate gradient is extremely fast, although the final solution may contain unphysical negative masses. On the other hand, the non-negative quadratic programming algorithm does not produce a solution with negative masses, but it is significantly slower than the bi-conjugate gradient (its typical computation time is a few hours compared with a few minutes to reach similar accuracy). In both cases, a threshold $R^2 \approx \epsilon$ is defined to set the level at which the minimization stops.

The method has one drawback when applied to our problem: one can not choose ϵ to be arbitrary small. If one chooses ϵ to be very small, the algorithm will try to find a solution that focuses the arcs into N_s sources with unphysically small sizes. The mass distribution that accomplishes this, is usually very biased relative to the correct one: it usually has a lot of substructure with large mass fluctuations in the lens plane. One must then choose ϵ with some carefully selected criteria. Since the algorithm will stop when $R^2 < \epsilon$, we should choose ϵ to be an estimate of the expected error associated with the sources not being point-like and the reconstructed mass being discretized. Instead of defining ϵ in terms of R^2, the parameter ϵ should be defined in terms of the residual of the conjugate gradient algorithm r_k (see Eq. B.2.7 in Appendix B.2). This would accelerate the minimization process significantly since we would not need to calculate R at each step but use the already estimated r_k. Both residuals are connected by the relation

$$r_k = \Gamma^T R. \tag{4.3.3}$$

Imposing a prior on the size of the sources means that we expect the residual of the lens equation, R, to take typical values on the order of the expected dispersion (or size) of the sources at the measured redshifts. Hence, we can define a $R_{\rm prior}$ of the form

$$R^i_{\rm prior} = \sigma^{\rm i}_{\rm prior} * RND, \tag{4.3.4}$$

where the index i runs from 1 to N_θ and $\sigma_{\rm i}$ is the dispersion (prior) assumed for the source associated with pixel i and RND is a random number normally distributed with zero mean and unity variance. We can then estimate ϵ as

$$\epsilon = r^{\rm T}_{\rm k} r_{\rm k} = R^T_{\rm prior} \Gamma \Gamma^{\rm T} R_{\rm prior}. \tag{4.3.5}$$

Following Diego et al. (2005a), we construct $R_{\rm prior}$ assuming that the source galaxies can be described as Gaussians with $\sigma = 30h^{-1}$ kpc. In our particular problem (a grid with $N_{\rm c} = 32 \times 32$ cells), this results in a value $\epsilon \approx 2 \times 10^{-10}$. One has to be careful not to choose a too small σ. They should be larger than the typical size of a galaxy. Only when the number of grid points, $N_{\rm c}$, is large enough, can the gridded version of the real mass distribution focus the arcs into sources that are similar in size to real ones. If $N_{\rm c}$ is not large enough, the gridded version of the true mass focuses the arcs into sources that are larger than the real sources. This is explained in more detail below.

The choice of the threshold is a crucial point when performing the mass reconstruction. We illustrate in the next few sections how this affects both the final mass estimation and the positions of the sources.

4.4 Simulation of mock lensing data

We now describe the simulated data consisting of a simple cluster and lensing (both strong and weak) data set. The use of simulated data gives us the unique advantage of being able to compare the reconstructed mass with the true underlying simulated mass and check for biases and systematics.

For the cluster, we assume a single Navarro-Frenk-White, (NFW, [172]) profile for the radial density. We choose the simplest possible profile in order to avoid the effects of the uncertainties caused by the complexity of the mass distribution. We also assume the same redshift of CL0024 ($z = 0.4$), while the field of

view corresponds to the field of view of the ACS field (FOV=3.3 arcmins). The resulting mass in the whole field of view is $M(\text{FOV}) \sim 4.8 \times 10^{14} \mathcal{M}_{\odot}$, while when we consider core radii within 30″, we have $M(< 30'') \sim 1.28 \times 10^{14} M_{\odot}$ (the mass reconstruction in Jee et al. 2007 yields $M(r < 30'') \approx (1.79 \pm 0.13) \times 10^{14} M_{\odot}$).

The strong and weak lensing data are computed using the full resolution of our simulated cluster (in the reconstruction process, the lens plane is divided with a grid that effectively reduces this resolution).

For the strong lensing data, we assume the same number of background sources ($N_s = 3$) identified in Jee et al. (2007) and that their redshifts are $z_1 = 1.675$, $z_2 = 1.27$, and $z_3 = 2.84$. We carefully chose the position of the background sources in trying to mimic the strong lensing data set used by Jee et al. (2007) , although this is not really relevant to our work. They identify five arcs from source 1, two arcs from source 2 and two arcs from source 3, making a total of nine. Most of the arcs are tangential, particularly those originating from source 1, which indicates that this source has to be positioned very close (in projection) to the density peak of the lens. In our case, our simulated strong lensing data set consists of seven arcs, three of which originate from source s_1 (two tangential and one radial), two from source s_2 (one tangential and one radial), and two from source s_3 (one tangential and one radial). The map of the lensed images is represented in Fig. 4.1 (top panel), with the labels identifying the original sources.

The shear data is computed assuming that the density of available background galaxies is lower toward the center of the cluster, where the presence of the cluster itself makes it harder to estimate the reduced shear. For all the shear data points, we assume a Gaussian noise of 30%. In addition to the cluster itself, the magnification bias has to be taken into account. Magnification acts on galaxies (enhancing their flux) but also expanding the area of the sky behind the cluster. In Broadhurst et al. (2005a), [143], the latter effect is estimated and showed that a net deficit of background galaxies is expected (see also Umetsu et al. 2011, [173]). The resulting shear field is shown in Fig. 4.1 (bottom panel).

4.4.1 Simulated vs real data

In Jee et al. (2007) , the authors consider a FOV of 3.5×3.5 arcminutes that is gridded in a 52×52 regular grid, but with the four corner points removed.

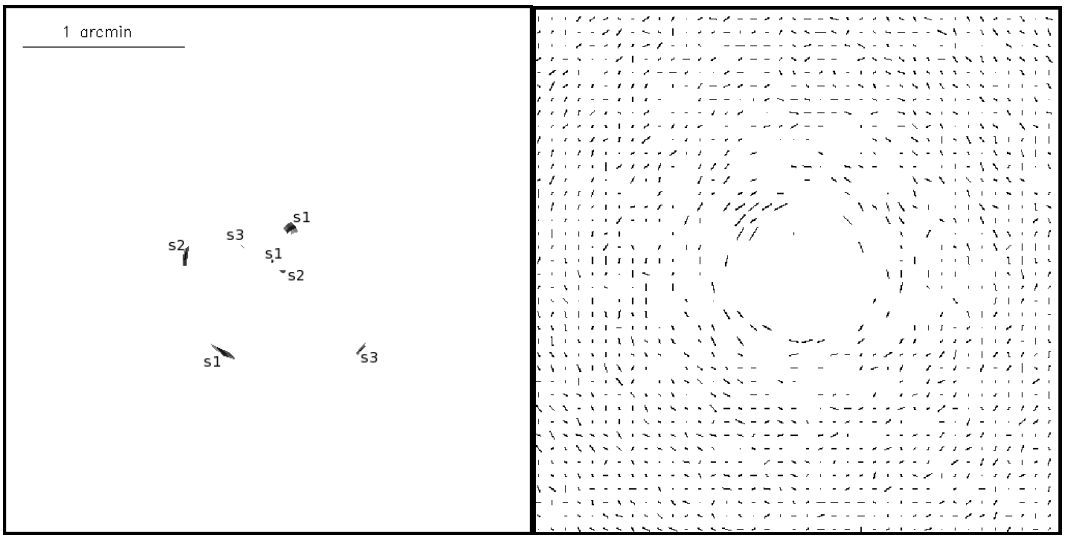

Figure 4.1 *Left panel:* The lensed arcs (θ map) originated from three sources in the background (not shown in the figure). The total number of pixels forming the arcs is $N_\theta = 288$. *Right panel:* shear field derived from the lens and used for the weak lensing computation. The inner points have been removed to mimic the contamination from cluster member galaxies. Total number of shear points is $N_{\rm shear} = 1301$, needed to set the dimension of the lensing matrix. All points have a Gaussian noise of 30%.

We consider a slightly smaller FOV (3.3×3.3 arcminutes) and divide the FOV using a 32×32 regular grid. We chose the side of the grid to be 32 to ensure that the number of constraints is comparable to the number of unknowns and hence have a more stable system of equations. A larger number of grid points will only introduce unnecessary noise in the reconstructed solution.

In Jee et al. (2007) , the strong lensing constraints are derived from 132 *knots* identified in the lensed images and the weak lensing constraints are based on an ensemble of 1297 background galaxies with photometric redshifts $z_{\rm phot} \geq 0.8$. In our simulated data, we instead consider all the pixels of our lensed images (288 pixels) for the strong lensing, while for the weak lensing we create a simulated vectorial field in 1301 positions.

The solution in Jee et al. (2007) is found after a minimization process involving the strong and weak lensing data, a regularization term and a model for the lensing potential. The regularization term improves the smoothness of the recovered solution and in principle helps to reduce the overfitting problem. The method is based on the maximum entropy method (MEM), which has a positive prior that forces the improved solution to remain positive. Here, we also

Figure 4.2 Simulated observed arcs (black) versus predicted ones from the optimal solution (white). The difference between the two sets of θ positions is representative of the error expected when recovering the solution.

use a minimization process but instead of a regularization term we stop the minimization process at a point that avoids overfitting the data. An interesting discussion of this point can be found in Jee et al. (2007) . They perform a *delensing* of the arcs from one particular source. The resulting recovered sources are reported in Fig. 14 in their paper, where the orientation, parity, and size of the images are strongly consistent among the different recovered sources. Nonetheless, the positions of the the delensed images do not overlap. The same authors report: *' When we forced the two locations to coincide in our mass reconstruction, the smoothness of the resulting mass map was compromised'*. This might indicate a tension between the recovered solution and the corresponding goodness of fit. Formally the solution is not an optimal one in the sense that the recovered source positions do not coincide but seem to be good enough to ensure that the recovered sources resemble the real ones.

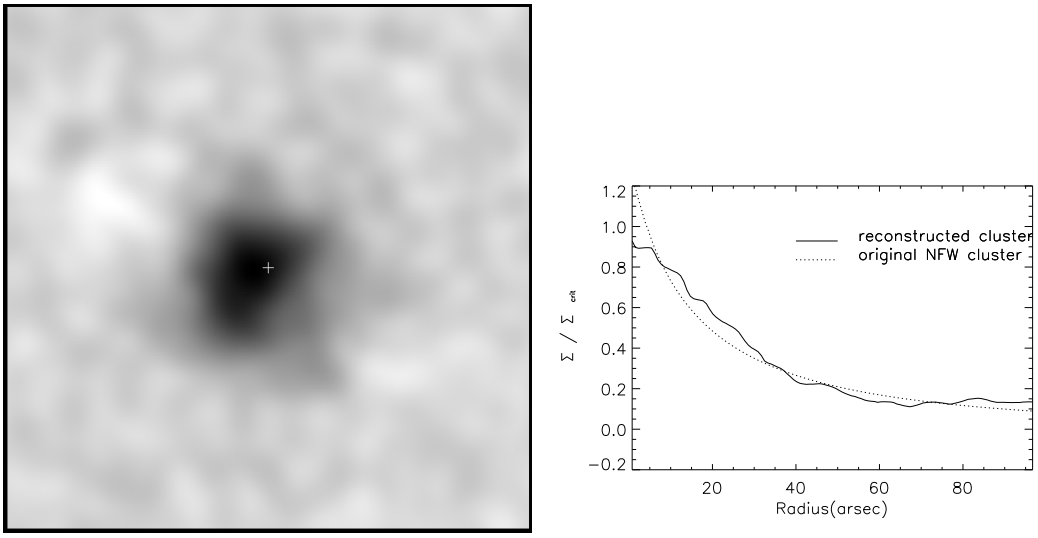

Figure 4.3 Mass reconstruction obtained with the BGA and no overfitting $\epsilon = 2 \times 10^{-10}$. *Top panel*: mass map after smoothing with a Gaussian. The mass inside the FOV is $M_{3.3'} = 6.1 \times 10^{14} M_{\odot}$, while the mass inside the core radius of 30″ is $M_{30''} = 1.39 \times 10^{14} M_{\odot}$. *Bottom panel*: Surface mass density profile (in units of Σ_{crit}) as a function of radius. Darker areas correspond to higher masses.

4.5 The optimal solution

With the simulated data, a very interesting exercise can be done before attempting the mass reconstruction. Since we know the true underlying mass and the positions of the background sources, we can predict where the arcs should appear when we assume the *optimal* solution possible for X assuming a uniform grid with 32×32 cells. This solution consists of the mean mass in each cell corresponding to the true underlying mass and the three real positions. In Fig. 4.2, we show the true strong lensing or θ-map used to reconstruct the mass, compared with the predicted one derived from the optimal solution X. The black arcs are obtained from the equation $\theta = \Gamma M + \beta$, where the matrix Γ is built from the real θ positions and the 32×32 cells, the vector β contains the real positions of the background sources, and the vector M contains the mean mass sampled in the 32×32 cells.

The first interesting conclusion we can derive from this exercise is that the arcs predicted from the optimal solution differ significantly from the true observed arcs. This is unsurprising as the optimal solution lacks the resolution of the true underlying mass and hence we should expect a different set of strong lensed

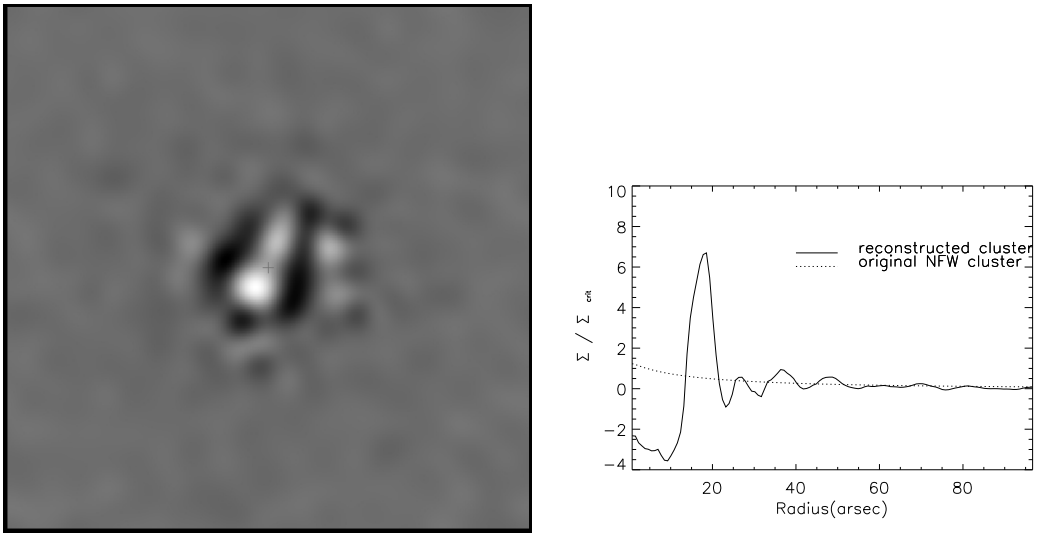

Figure 4.4 Plots for $M_{3.3'} = 4.34 \times 10^{14}\mathcal{M}_{\odot}$ and $M_{30''} \approx 1.9 \times 10^{14}\mathcal{M}_{\odot}$. Overfitting case. It shows the solution obtained with the BGA when the method is forced to find a nearly exact solution to the problem ($\epsilon = 2 \times 10^{-15}$). The density profile inside the core radius does not follow the profile of the input NFW cluster. Different density peaks and dips can be seen around the center of the FOV. Darker areas correspond to higher masses.

arcs. To reproduce the observed arcs, the solution has to *bend* the light in a different way. This can only be achieved with a mass distribution that is different (i.e biased away) from the true one.

This exercise summarizes the entire philosophy behind this paper: *using a non-parametric method with a uniform cell size, it is impossible to predict correctly the strong lensing data with an unbiased solution of the true underlying mass*. By default, the non-parametric method makes the *incorrect* assumption that the mass distribution is discrete and ignores the details of the mass distribution on scales smaller than the cell size. Hence, the derived solution has to be biased by the method in order to fit the data and compensate for this incorrect assumption. The best we can hope for is a solution that resembles the true underlying mass distribution but is unable to fit the observed data perfectly. This margin of error in the description of the observed data will then compensate the original error made by assuming that the mass is discretized. However, we note that we seek a solution as close as possible to the true solution, which can only be achieved when a realistic error, R, is allowed in the minimization of the system of linear equations given in Eq. (4.3.1).

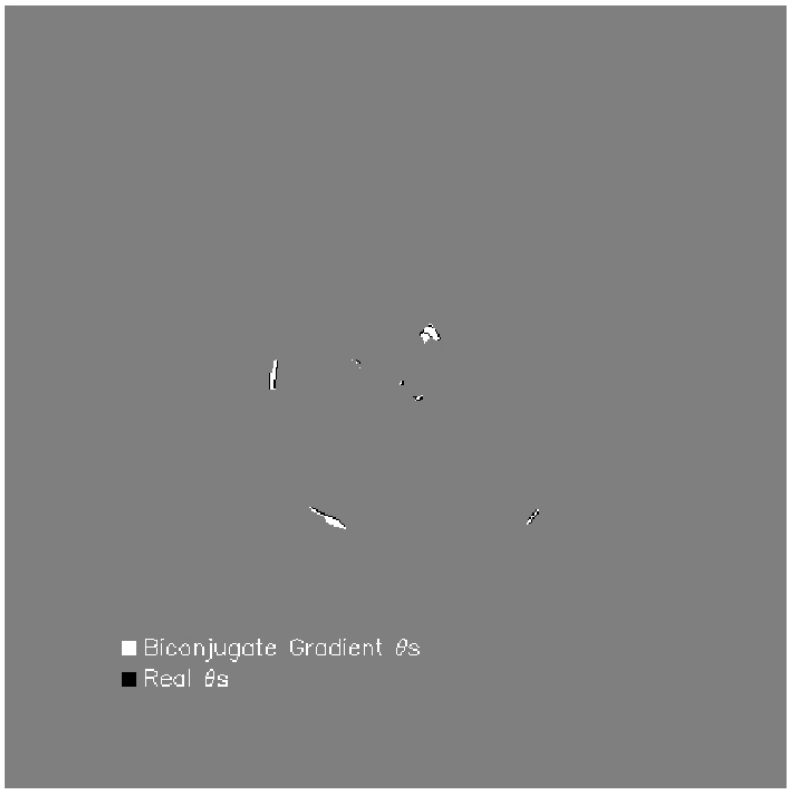

Figure 4.5 Black color indicates the observed (or true) arcs and in white we show the predicted arcs obtained with the solution shown in Fig. 4.4.

4.6 Mass reconstruction

To solve Eq. 4.2.6, the lens plane is divided into a regular grid of 32×32 cells. This number is smaller than the number of constraints provided by the weak and strong lensing data. The mass in each cell plus the positions of the background strong lensing galaxies form a vector of unknown variables X that has 1030 elements (1024 for the mass cells and 6 for the three sources, each one with the x and y coordinates of the position of the background galaxy).

4.6.1 The bi-conjugate gradient algorithm solution

The bi-conjugate gradient algorithm (BGA) is a fast and powerful algorithm for finding the solutions of a system of linear equations. As mentioned earlier, rather than finding the exact solution, we seek an approximated one with an error large enough to compensate for the discretized mass and that the back-

ground galaxies are not point-like. The minimization is stopped at a point where $R^2 \approx \epsilon$. The choice of ϵ is based on the physical size of the background galaxies and also that the optimal solution should not reconstruct the data perfectly as discussed in the previous subsection. A value of ϵ can be computed from the equation

$$\epsilon = \sum_{i}^{N_\theta} r_{\rm k}^2, \tag{4.6.1}$$

where $r_{\rm k} = \Gamma^{\rm T} R_{\rm SL,prior} + \Gamma^{\rm T} R_{\rm WL,prior}$ contains an estimate of the physical size of the background galaxies ($R_{\rm SL,prior}$) and the error in the weak lensing measurements ($R_{\rm WL,prior}$, see previous sections for the definition of ϵ and its relation to $r_{\rm k}$).

Once the value of ϵ is estimated, we can solve for the mass and position of the background sources. In Fig. 4.3, we show the mass reconstruction obtained with the BGA for a value of $\epsilon = 1 \times 10^{-10}$ (computed in Eq. 4.6.1, corresponding to a $\sigma_{\rm SL} \sim 1.2$ arcsec and $\sigma_{\rm WL} = 0.3$ or 30%). The total recovered mass inside the FOV is $M(< 3.3') = 6.1 \times 10^{14} M_\odot$, while $M(r < 30'') = 1.39 \times 10^{14} M_\odot$. The radial density profile is shown in the bottom panel of the figure, where it is compared with the true mass profile.

Values of ϵ significantly smaller than $\sim 10^{-10}$ would produce an *overfitting* of the data, introducing systematics in the final mass reconstruction. A typical case of overfitting is shown in Fig. 4.4, where the threshold value of ϵ has been lowered several orders of magnitude ($\epsilon = 2 \times 10^{-15}$). This value pushes the solution to the limit of the BGA and allows us to predict almost perfectly the observed data. However, this solution is clearly biased with respect to the true underlying mass as is clear when looking at the density profile (bottom panel).

The mass map shown in Fig. 4.4 is obviously a poor solution in the sense that it deviates significantly from the underlying mass distribution. However, from the point of view of the system of linear equations it is a good solution because it is able to reproduce the data accurately. This is shown in Fig. 4.5, where the observed arcs are compared to the predicted ones by the overfitting solution. This result should be compared with the case in Fig. 4.2 showing the opposite situation where the closest representation of the mass distribution leads to an error in the predicted strongly lensed arcs. The conclusion we can extract from this example is that a simultaneous (*unbiased*) reconstruction of the mass and the

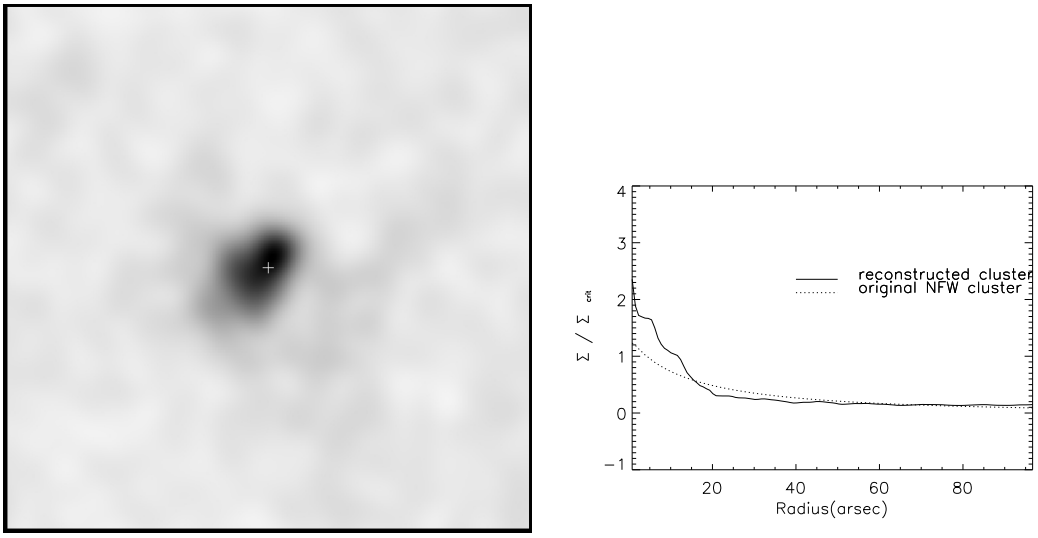

Figure 4.6 Plots for $M_{3.3'} = 5.92 \times 10^{14}\mathcal{M}_{\odot}$ and $M_{30''} = 1.22 \times 10^{14}\mathcal{M}_{\odot}$. Mass reconstruction obtained with the QADP after 100 iterations. This case corresponds to a reasonable value of ϵ and can be compared with the BGA solution shown in Fig. 4.3. The QADP recovers a higher mass in the central region (Σ/Σ_{crit}) than the BGA.

lensing data is impossible with a non-parametric method that lacks the details of the mass distribution.

4.6.2 The quadratic programing algorithm solution

The solution X derived from the BGA might predict negative masses, which could lead to large fluctuations in the mass density profile as the negative fluctuations have to be compensated for by larger positive fluctuations. However, Hoekstra et al. (2011), [174, and references within] report that *cosmic noise* (an induced shear effect by uncorrelated halos and large-scale structure) has to be taken into account when estimating the error bars in any cluster mass reconstruction that might lead to a negative convergence in the regime of the weak lensing. So a negative convergence is not completely unrealistic.

To avoid the large fluctuations at small radii exhibited by the biconjugate gradient, which can indicate a non-physical solution, we use the quadratic programming algorithm (QADP, see Appendix B.2), which prevents negative masses from appearing in the solution. This method resembles the maximum entropy method introduced in Jee et al. (2007) , since both impose a positive prior on the mass.

The QADP has a smooth behavior in the inner regions, where no large fluctuations are found, even in the crucial areas of the lens plane where the transition between the WL and SL regimes is observed. In addition, QADP provides an independent solution that should agree with the one derived by the BGA.

The number of iterations of the algorithm can be directly related to ϵ. The overfitting solution obtained by the QADP algorithm converges only after a large number of iterations ($\sim 10^4 - 10^5$) or equivalently after defining a small value for ϵ.

In Fig. 4.6, we show the solution obtained with QADP after 100 iterations. This result can be compared with the one in Fig. 4.3. The QADP recovers a higher mass than the BGA in the central region.

In Fig. 4.7, we show the overfitting case obtained with QADP with a large number of iterations ($N_{\rm iter} = 10^5$, or similarly, with a very small value for ϵ). In this case, the mass is pushed away from the center towards larger radii in a similar way to what was observed using the BGA. This is more clearly evident in the density profile. A peak in the density is observed at $r = 20''$ and an additional bump at $r = 50''$. The way in which the WL and SL are weighted is different in both methods. The overfitting solution differs significantly from the true mass (and also from Jee's reconstruction in the central part). The overfitting solution is dominated in our case by the WL part of the data (as in Jee et al. 2007). As shown in Fig. 5.1, the WL alone case shows a mass deficit at the center that is compensated for by the ring in the outer regions. Whether a similar situation occurs in Jee et al. (2007) is unclear but we note that Jee's mass reconstruction predicts a lower mass at the center than that of Zitrin et al. (2009), [170], (as seen in figure 21 of Umetsu et al. 2010,[171]).

In Jee et al. (2007) , their Fig. 10 shows the radial mass density profile of the cluster, with a Σ_c given at a fiducial redshift of $z_f = 3$. The authors state that the resulting profile does not match any conventional analytic profile. The density, peaking at the center with the value of $\Sigma/\Sigma_c = 1.3$, rapidly decreases from the center to the end of the core radius at $r = 50''$. The profile then remains *almost* constant around a value of $\Sigma/\Sigma_c = 0.7$. Only at radius $r = 70''$ from the center is an increment observable, extending out to $r = 80''$ with a peak at $r = 75''$.

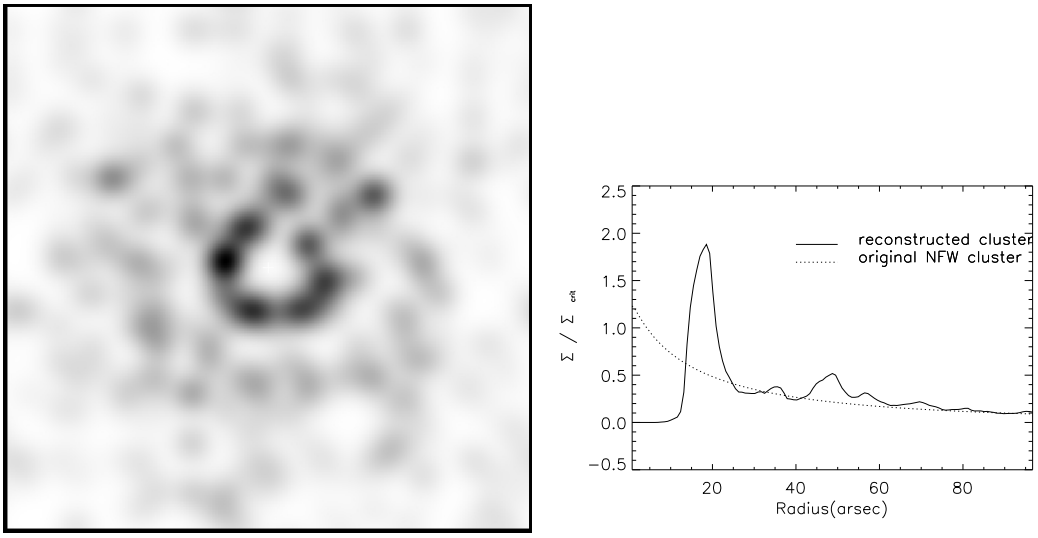

Figure 4.7 Plots for $M_{3.3'} = 6.81 \times 10^{14} \mathcal{M}_{\odot}$ and $M_{30''} = 1.59 \times 10^{14}$. Mass reconstruction obtained with QADP and after 10^5 iterations (overfitting case). The density peaks at $r \sim 15''$ and a bump is observed at $r \sim 50''$. Darker areas correspond to higher masses.

This is what the authors refer to as the *bump*. In two dimensions, this bump appears like a ring structure, separated from the core by 20″.

A plateau was detected by Jee et al. (2007) at $r \sim 50''$, that was not found by Umetsu et al. (2010), who instead measured a monotonically decreasing density. This plateau might depend on the initial guess. The WL part of the data displays this plateau more than the SL data, especially in those regions where WL constraints are weaker. The role that the prior plays in determining the regularization term in the MEM has to be investigated in more detail and leaves questions open on how the choice of the prior could affect the radii outside the central core.

CHAPTER 5

Conclusions

The last chapter is left for the conslusions derived from the previous chapters 2, 3 and 4.

5.1 Conclusions about the free-free signal from galaxy groups and clusters

As can be seen in Fig. 2.3, the mean free-free signal is larger for lower mass haloes. On the other hand, large mass haloes have larger individual free-free fluxes but they are much less abundant. Consequently their contribution to the mean signal decreases quickly with increasing mass.

An interesting result was shown in Fig. 2.4 where the explicit dependency of the average temperature distortion with the mass is shown for different redshifts intervals. From this plot, it is clear that the average signal is most sensitive to halo masses smaller than 10^{12} solar masses. Also, from the same figure we can conclude that haloes contribute to the average free-free signal at all redshifts up to the reionization time.

Even though groups and clusters are expected to contribute less than less massive haloes to the average signal, it should be possible to detect clusters through their free-free signal on a one by one basis opening the door for interesting studies of the intra-cluster medium at radio wavelengths. In this line, Cooray & Furlanetto (2004), [79], discussed the possibility of detecting the signal from clumps of IGM with ARCADE. In Burigana et al (2004), [65], the model by Oh (1999), [71], for unresolved free-free emitters has been exploited arriving to the indication that the SKA project will be able to detect them with deep exposures.

Future experiments might focus on the detectability of individual groups and/or clusters through their free-free signature. This signal can be combined with others (SZ, X-rays) in multiwavelength studies.

5.2 Discussion and conclusions on the contribution of star-forming galaxies to the cosmic radio background

In the present work, we have considered the relationship between the cosmic star formation rate and the radio background from star-forming galaxies in the light of recent measurements of the far infrared-radio correlation at different redshifts, attempting to give a further look into the significant missing flux that has been reported by the ARCADE2 team.

Our main result is that normal galaxies can *not* be responsible for the observed signal.

Although we think this conclusion is fairly robust, there is always some room for uncertainty. Radio emission in local galaxies has been thoroughly studied, and its properties are well known (see e.g. Condon 1992, [50]), but different gas compositions and/or temperatures may affect the conversion factor between SFR and radio emission by a significant amount, of the order of several tens of percent.

On the other hand, we use the cosmic star formation rate density to constrain the average emissivity of the universe, [111]. In contrast to radio source counts, where a population of faint objects below the detection threshold is very difficult to rule out, [105, 108], it would be extremely unlikely that our proposed fit underestimates the average SFR by more than a factor of two (dotted lines in Fig. 3.2). Uncertainties in the IMF cancel out with the production rate of ionizing photons given by Eq. 3.2.3 and are not expected to affect the present analysis significantly.

The most important source of uncertainty is the possible evolution of the far infrared-radio correlation. Current observations seem to be compatible with $\beta = 0.705 \pm 0.081$, increasing the expected emission from normal galaxies by about 70 per cent with respect to the case of no evolution. Using an extreme value $\beta = 1$ would boost the signal by only an additional 35 percent.

Nonetheless, it is worth noting that the high-redshift points in Figure 3.1 (in the

sample of Michałowski, Hjorth & Watson 2010, Murphy et al. 2009) are dominated by sub-millimeter galaxies. There is some discussion in the literature that these sources, whose contribution to the total SFR at $z \sim 1-2$ is only of the order of ten per cent (see Figure 4 in Michałowski, Hjorth & Watson 2010), may be radio-bright compared to normal galaxies and introduce some evolution in the observed FRC that does not apply to star formation as a whole[1] In fact, one would expect on theoretical grounds that the FRC of normal galaxies evolved in the opposite direction ($\beta < 0$). On the one hand, star formation at $z \sim 1$ is heavily obscured by dust, and the approximation that all the ultraviolet luminosity is re-radiated in the infrared is very good. In the local universe, some fraction of the ionizing photons is able to escape, and the infrared luminosity per unit SFR should be lower. On the other hand, galaxies at high redshift should produce less radio emission because the energy density of the CMB scales as $(1+z)^4$, and the relativistic electrons injected by supernovae lose more energy through inverse Compton scattering (see e.g. Carilli & Yun 1999, Carilli et al. 2008, Murphy et al. 2009, [127, 175, 176]). Both effects, especially the latter, would only strengthen our conclusions, and the estimate with $\beta = 0.705$ should arguably be regarded as an upper limit.

According to our results, radio emission from star-forming galaxies could explain up to ~ 13 per cent of the intensity of the CRB. Even taking all the possible uncertainties into account, we are still far from the 1.19 Kelvin reported by ARCADE2 at 1 GHz. Although evolution of the FRC at $z < 3$ has to be further investigated, current data strongly suggest that it only results in a relatively minor boost to the contribution of normal galaxies, and hence we can rule them out as the main source for the radio background. As shown in Fig. 3.3, the contribution of galaxies at higher redshifts is negligible.

Since relatively bright point sources, as well as Galactic or extragalactic diffuse emission have also been ruled out, (Singal et al. 2010 and references therein, [105]), there are few alternatives left to explain the observed cosmic radio background. Some possibilities are:

1. The ARCADE2 measurement is incorrect, or it is contaminated by Galactic foregrounds. Being perfectly consistent with independent measurements

[1] Just by removing the Michałowski, Hjorth & Watson (2010) data from the least-squares fit, the best value of β decreases to 0.57 ± 0.093. Furthermore, the data at $z < 1$ are compatible with $\beta = 0$ (see the discussion in Sargent et al 2010).

at longer wavelengths, [177–179], we think this possibility is unlikely.

2. Faint star-forming galaxies at high redshift are extremely radio bright, perhaps due to an enhanced magnetic field or AGN activity with respect to the brightest objects at that redshift [the possibility favored by 105].

3. There is a new population of numerous and faint radio sources waiting to be discovered.

To sum up, the nature of the cosmic radio background poses an exciting challenge for radio astronomy, to be faced in the upcoming era of Expanded Very Large Array (EVLA) and Square Kilometre Array (SKA).

5.3 Discussion and conclusions on non-parameter lensing reconstruction of CL0024

The interesting analysis of Jee et al. [31] appears to detect a dark matter ring around the core of CL0024. This ring might have been caused by a recent high speed collision between two massive clusters along the line of sight. If confirmed, CL0024 would be an interesting laboratory to test different physical phenomena. We have explored the possibility that spurious ring-like structures might appear as a consequence of overfitting lensing data in a non-parametric way. We show how the optimal (unbiased) solution should produce a fit to the data significantly poorer than the minimal χ^2 solution. This error is necessary to account for the initial error introduced when neglecting the impact of the small-scale fluctuations on the mass distribution. We demonstrate our argument by using a simulated data set where all the variables are known a priori and the reconstructed mass can be compared with the original one. The simulation shows how overfitting the data introduces artifacts in the reconstructed solution, which can resemble the ring-like structure found in Jee et al. [31]. The methods in Jee et al. [31] and the one used in this work are different in some aspects but both methods share many common key features such as the lens plane is divided into a regular grid and the parameters to be constrained are basically those for convergence in the pixels. Hence both methods should also have the same systematic effects and in particular be sensitive in a similar way to overfitting.

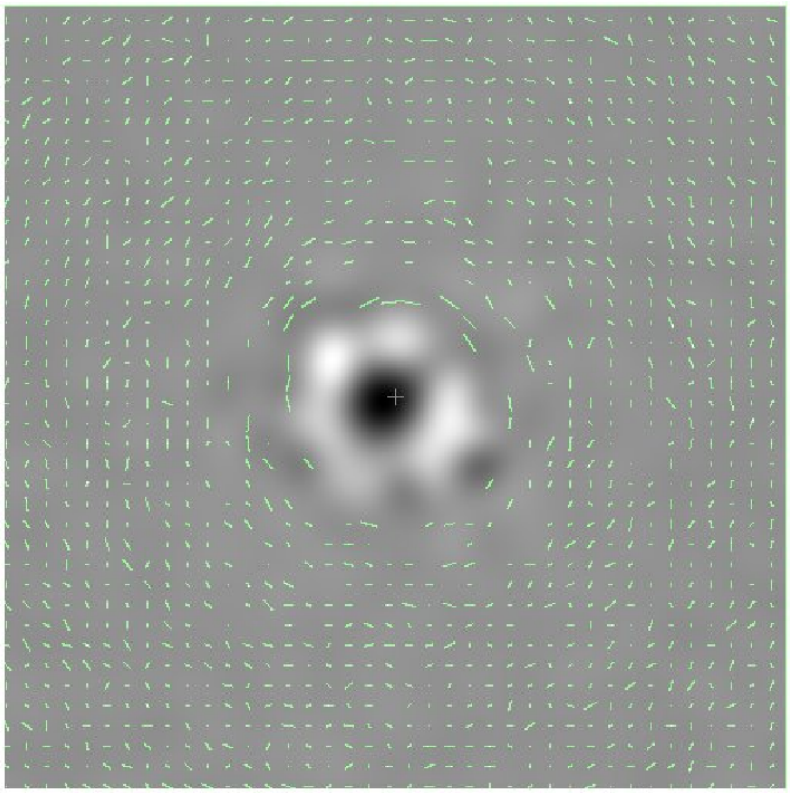

Figure 5.1 Reconstructed image for the case where only weak lensing data is used in the reconstruction. A clear ring of matter appears in the area where the density of weak lensing data gets reduced. Whiter colors indicate more mass.

Another interesting feature shown by the simulations that needs to be investigated more (with the actual data) is that when the density of weak lensing data is non-uniform across the field of view, there is a tendency for the overfitted solution to increase the mass density in the areas with fewer weak lensing data. We show one example in Fig. 5.1, where only the simulated weak lensing data is used to find the solution. The plot shows the WL data overlaid on the overfitted solution found for this case. In the case of CL0024, we expect a lower density of WL points toward the center of the cluster owing to contamination by the cluster members. While the SL data constraints the inner central region of the cluster, the outer regions are basically constrained by the WL data alone. In-between these two regions, the density of WL data points should show a gradient, and the effect of the non-uniformity of the WL data points might have a negative effect on the solution. The reality of the ringlike structure will need to be investigated in more detail.

We note that the covariance matrix of the residual might not necessarily be diag-

onal. As discussed in section 7 of Diego et al. [157], the elements of the residual are correlated with each other, in particular the strong lensing part of the residual. The elements of the WL portion of the residual are more weakly correlated with each other, and the diagonal approximation is in this case more valid. This is particularly true in our case where the error assigned to the WL measurements is the predominant one (30%). Since the WL data are more relevant to understanding the ring-like structure, we adopt the diagonal approximation for the covariance matrix. In addition, the second reason why we prefer to adopt this approximation in this paper is that Jee et al. [31] assumed that the data are uncorrelated (the covariance matrix is diagonal for an uncorrelated residual). The issue of the effect of the covariance matrix in lensing reconstruction has not been addressed by any method (to the best of our knowledge) and we plan to do so in a future paper. Another interesting point that deserves discussion is that in Jee et al. [31] a regularization term is included in the analysis, among other things, to prevent overfitting. This regularization term, however, does not guarantee that overfitting is prevented. The main objective of the regularization term is to favor solutions that are smooth by introducing a prior that represents a smoothed version of the solution. If we consider the extreme case where the reconstructed solution converges to the prior in their regularization term (this is not an unrealistic scenario because the prior is updated at each iteration and based on the previous solution), the regularization term tends to zero forcing the other terms in χ^2 to be even smaller and hence closer to an overfitting situation. The SL and WL terms to be minimized are the ones that really constrain the model and can still be too small even for smooth solutions. Our work shows that a good solution obtained with our non-parametric method should predict arcs significantly different from the ones observed. Only when overfitting is allowed can the reconstructed data closely reproduce the observations (see Figs. 4.2 and 4.5 above).

Our work shows the validity and usefulness of non-parametric methods but also shows some of its limitations, in particular that one should not be too ambitious when fitting the data.

CHAPTER 6

Resumen en castellano

En este ultimo capítulo se presenta el resumen en castellano de los capítulos anteriores.

6.1 Introducción

6.1.1 Estructura a gran escala

El concepto de estructura a gran escala del Universo fue desarrollado en los primeros años del siglo XX. Einstein formuló la teoría de la Relatividad General (RG), encontrando un punto de contacto con las ideas de Ernst Mach sobre los movimentos en sistemas de referencia inerciales. Einstein, como Mach, estaba convencido de que las fuerzas de inercia que siente un sistema tienen que ser producidas por el movimento relativo respecto a un cuerpo fijo. El problema era que en una métrica de Minkowski, donde el tensor metrico es $n_{ij} = (1, -1, -1, -1)$, las fuerzas inerciales son sentidas también fuera del alcance de masas fijas. En una época donde lo que se sabía del Universo era limitado sólo al Sistema Solar y a las galaxias más cercanas, el primero que pensó en la presencia de una masa fija alrededor de lo que se podía oservar fue de Sitter. Einstein y de Sitter llegaron a la conclusión de que, aunque no observada, hay masa distribuida de manera *homogénea* en el Universo, y la distribución de materia es la que da origen a la curvatura del espacio-tiempo. Además, el Universo tiene que ser *isótropo*, porque no puede existir una dirección del movimento privilegiada que contradijera la no existencia de un sistema de referencia absoluto. El concepto de un Universo donde la materia está distribuida de forma homogénea y en el cual cada observador ve lo mismo que otros ha sido

identificado como *Principio Cosmológico* de Einstein.

Se llegó a la idea que en el entorno de nuestra galaxia había otras que no son más que réplicas de ella en una estructura extendida donde los cúmulos de materia se alternan con vacíos.

No pasó mucho tiempo desde que las observaciónes empezaron a confirmar el modelo de Einstein y de Sitter (como el mapa de *nebulae* de Charlier 1922 en la sección 1.1). Edwin Hubble llegó a una primera estimación de la distribución de galaxias en base a sus propias magnitudes m

$$\frac{dN(m)}{dm} \propto 10^{0.6m}, \tag{6.1.1}$$

comprobando la uniformidad de la materia a gran escala.

6.1.2 El Universo estático

En la teoría de la RG, la relación que liga la métrica del espacio-tiempo con el contenido de materia es

$$R_{ij} - \frac{1}{2} g_{ij} R = 8\pi G T_{ij}, \tag{6.1.2}$$

donde los índices van desde 0 a 3, R_{ij} y R son el tensor y el scalar de Ricci respectivamente, g_{ij} es el tensor métrico y T_{ij} es el tensor de energía-impulso. En presencia de materia que ejerce presión, para un fluido en reposo, el tensor T_{ij} es un tensor diagonal con los elementos de la diagonal principal (ρ, p, p, p). Esto reduce el número de ecuaciones del sistema 6.1.2 a 10.

La Ec. 6.1.2 se puede reducir a una forma más sencilla si se considera un elemento de fluido en un espacio-tiempo de Minkowski, para el cual las velocidades no son relativisas. Es la ecuación de Poisson

$$\nabla \mathbf{g} = -4\pi G(\rho + 3p). \tag{6.1.3}$$

Indicando con R el término de la curvatura del espacio-tiempo, la Ec. de Poisson 6.1.3, para un universo estático, homogéneo e isótropo tiene las soluciones

$$\begin{array}{rcl} \frac{4}{3}\pi G(\rho + 3p) & = & 0, \\ \frac{8}{3}\pi G\rho - \frac{1}{R^2} & = & 0. \end{array} \tag{6.1.4}$$

En el intento de conciliar la teoría de la RG con el descubrimiento de la estructura a gran escala del Universo, Einstein se dio cuenta de que la primera de

las soluciones del sistema 6.1.4 preveía una presión o una densidad negativa. Einstein introducjo un término constante en la Ec. 6.1.2

$$R_{ij} - \frac{1}{2}g_{ij}R - \Lambda g_{ij} = 8\pi G T_{ij}, \tag{6.1.5}$$

donde Λ representa la *constante cosmológica*. El papel de la constante cosmológica es introducir una presión negativa cuando su densidad se mantiene constante

$$\rho_\Lambda = \frac{\Lambda}{8\pi G}, \quad p_\Lambda = -\rho_\Lambda. \tag{6.1.6}$$

En el modelo estándar de la cosmología, el termino Λ se usa para indicar la presencia de una energía oscura que, al igual que la constante introducida por Einstein, ejerce una presión negativa.

6.1.3 La expansión del Universo

La expansión del Universo se describe con el factor de escala en función del tiempo, $a(t)$. Una coordenada de tipo *comóvil* indica una distancia que no evoluciona con la expansión del Universo. Una coordenada de tipo *propio* es una función del tiempo

$$l(t) = l_0 a(t). \tag{6.1.7}$$

El parámetro de Hubble se define como $H \equiv \dot{a}/a$, y de lo cual se sigue la ley de Hubble

$$v = \dot{l} = l_0 \dot{a} = l\frac{\dot{a}}{a} = Hl, \tag{6.1.8}$$

que nos indica que las velocidades de recesión de los objectos lejanos son proporcionales a sus distancias. El valor de H se da en unidades de Km seg^{-1} Mpc^{-1}. Muchas medidas en cosmología usan un valor sin dimensiones del parámetro de Hubble, definido como $h \equiv H/(100\text{Km sec}^{-1}\,\text{Mpc}^{-1})$. El valor actual del parámetro de Hubble es $h = 0.72$.

La métrica de *Robertson-Walker* es la que describe dos eventos separados en el espacio-tiempo en un Universo que cambia su factor de escala

$$ds^2 = dt^2 - a(t)^2\left[\frac{dr^2}{1-Kr^2} + r^2(d\theta + \sin^2\theta d\phi^2)\right], \tag{6.1.9}$$

El valor de la curvatura K puede ser -1,0 y +1. El caso $K = -1$ se corresponde un universo parecido a un hiperboloide, abierto y de tamaño infinito. El caso

$K = 0$ se corresponde a un universo de tipo plano, infinito, y euclídeo en 4 dimensiones. El caso $K = 1$ se corresponde a un universo cerrado, pero sin bordes, de volúmen finito, de tipo esférico.

Las ecuaciones dinámicas para el factor de escala son las siguentes:

$$\frac{\ddot{a}}{a} = -\frac{4}{3}G(\rho + 3p) + \frac{\Lambda}{3}, \tag{6.1.10}$$

$$H^2 = \left(\frac{\dot{a}}{a}\right)^2 = \frac{8}{3}G\rho + \frac{k}{a^2} + \frac{\Lambda}{3}. \tag{6.1.11}$$

Para un modelo donde la densidad de materia es mayor que la curvatura y Λ, la Ec. 6.1.11 toma una forma más sencilla:

$$\left(\frac{\dot{a}}{a}\right)^2 = \frac{8}{3}G\rho. \tag{6.1.12}$$

En el caso que la cantidad de materia en un volúmen no aumenta o disminuye, su varía rescala como el factor de escala $\rho \propto a^{-3}(t)$. Sustituyendo esta relación en la Ec. 6.1.12 y separando las variables de integración, se obtiene que $a \propto t^{2/3}$, con el tiempo igual a:

$$t = \frac{2}{3H} = \frac{1}{(6\pi G\rho)^{1/2}}. \tag{6.1.13}$$

En un escenario de tipo Big Bang, el factor de escala llega a cero en un entorno del tiempo $t = 0$, con una densidad divergente.
El factor de escala tiene un papel en la definición del *redshift* (desplazamento al rojo) de tipo cosmológico

$$1 + z = \frac{a_0}{a_e} \tag{6.1.14}$$

donde el factor de escala a_0 se refiere al presente y a_e se refiere al momento de la emisión de la radiación. El factor de escala a_0 siempre es mayor o igual que el factor de escala a_e, ya que estamos en un universo en expansión, así que el redshift z siempre es un número mayor que cero.
Con la introducción del redshift, la Ec. 6.1.11 se puede escribir con el uso de los *parámetros de densidad*

$$H^2 = \left(\frac{\dot{a}}{a}\right)^2 = \left(\frac{\dot{z}}{1+z}\right) = H_0^2\left[\Omega(1+z)^3 + \Omega_R(1+z)^2 + \Omega_\Lambda\right], \tag{6.1.15}$$

donde los parámetros de densidad son

$$\Omega = \frac{8\pi G\rho_0}{3H_0^2}, \tag{6.1.16}$$

$$\Omega_R = \frac{1}{(a_0 H_0 R)^2}, \tag{6.1.17}$$

$$\Omega_\Lambda = \frac{\Lambda}{3H_0^2}, \tag{6.1.18}$$

para la materia, para la curvatura y para la energía oscura (Λ) respectivamente. El parámetro de densidad de la materia se puede escribir también en función de la densidad crítica $\rho_{\rm crit} = 3H_0^2/(8\pi G)$,

$$\Omega = \frac{\rho_0}{\rho_{\rm crit}}, \tag{6.1.19}$$

donde la relación entre ρ_0 y $\rho_{\rm crit}$ es un índice de la curvatura del Universo.

De la Ec. 6.1.15 se puede definir la función

$$E(z) \equiv \sqrt{\Omega(1+z)^3 + \Omega_R(1+z)^2 + \Omega_\Lambda}. \tag{6.1.20}$$

La *distancia comóvil* que un fotón viaja desde un redshift 0 a lo largo de la línea de visión es

$$D_C = \frac{c}{H_0}\int_0^z \frac{dz'}{E(z)}. \tag{6.1.21}$$

La *distancia comóvil transversa*, para un parámetro de curvatura $\Omega_R = 0$, es igual a la distancia comóvil, $D_M = D_C$. Para un universo abierto e infinito o cerrado, la distancia comóvil trasversa es una función del parámetro de curvatura. Se obtiene que $D_M > D_C$ para el modelo abiero y $D_M < D_C$ para el modelo cerrado.

Otras medidas de distancias de interés son la *distancia de diámetro angular*

$$D_A = a(t)D_M = \frac{D_M}{1+z}, \tag{6.1.22}$$

y la *distancia de luminosidad*

$$D_L = (1+z)D_M = (1+z)^2 D_A. \tag{6.1.23}$$

La distancia de luminosidad es la que liga la luminosidad L de una fuente al flujo recibido S

$$S = \frac{L}{4\pi D_L^2}. \tag{6.1.24}$$

El elemento de volúmen comvil se da por elemento de ángulo sólido $d\Omega$ y elemento de redshift dz

$$dV_C = \frac{c}{H_0}\frac{(1+z)^2 D_A^2}{E(z)} d\Omega dz \tag{6.1.25}$$

cuya integración, para un universo plano, es el volúmen de una esfera de radio D_M, $V_C = (4\pi/3)D_M^3$.

La *corrección de tipo k* tiene que ser introducida cuando se recibe un flujo diferencial de un objecto lejano, cuya luminosidad es una función de la frecuencia (longitud de onda)

$$S_\nu = (1+z)\frac{L_{\nu_e}}{L_\nu}\frac{L_\nu}{4D_L^2} \tag{6.1.26}$$

y

$$S_\lambda = \frac{1}{1+z}\frac{L_{\lambda_e}}{4D_L^2} \tag{6.1.27}$$

6.1.4 Crecimiento a través de inestabilidad gravitatoria

La cantidad básica para describir las inestabilidades gravitatorias es el *contraste de densidad* en la posición **x** al tiempo t,

$$\delta(\mathbf{x},t) = \frac{\rho(\mathbf{x},t)-\rho_b}{\rho_b}, \tag{6.1.28}$$

donde $\delta(\mathbf{x},t)$ es la densidad en ese punto y ρ_b es la densidad promedio. La coordenada **x** es de tipo comóvil. Para un fluido ideal sin presión, la ecuación del movimiento, la ecuación de Euler y la de Poisson son, respecto a una posición propia **r** y a una velocidad **u** que sigue la expansión de Hubble, las siguentes

$$\left(\frac{\partial\rho}{\partial t}\right)_{\mathbf{r}} + \nabla_{\mathbf{r}} + \rho\mathbf{u} = 0, \tag{6.1.29}$$

$$\left(\frac{\partial\mathbf{u}}{\partial t}\right)_{\mathbf{r}} + (\mathbf{u}+\nabla_{\mathbf{r}})\mathbf{u} = -\nabla_{\mathbf{r}}\Phi, \tag{6.1.30}$$

$$\nabla_{\mathbf{r}}^2\Phi = 4\pi G\rho. \tag{6.1.31}$$

Se puede pasar a las ecuaciones en coordenadas comóviles con los cambios $\mathbf{x} = \mathbf{r}/a(t)$, $\nabla = a\nabla_{\mathbf{r}}$ y $\mathbf{u} = \dot{a}\mathbf{v}(\mathbf{x},t)$ y se obtiene

$$\frac{\partial\delta}{\partial t} + \frac{1}{a}\nabla\cdot[(1+\delta)\mathbf{v}] = 0 \tag{6.1.32}$$

$$\frac{\partial\mathbf{v}}{\partial t} + \frac{\dot{a}}{a}\mathbf{v} + \frac{1}{a}(\mathbf{v}\cdot\nabla)\mathbf{v} = -\frac{1}{a}\nabla\phi \tag{6.1.33}$$

$$\nabla^2\phi = 4\pi G\rho_b a^2\delta. \tag{6.1.34}$$

Cuando el contraste de densidad es $\delta \ll 1$, las ecuaciones 6.1.32 y 6.1.33 se pueden escribir quitando los terminos en $\delta\mathbf{v}$ y δ^2 y se obtiene la evolución del contraste de densidad

$$\frac{\partial^2\delta}{\partial t^2} + 2\frac{\dot{a}}{a}\frac{\partial\delta}{\partial t} = 4\pi G\rho_b\delta. \tag{6.1.35}$$

Para un universo con componente de materia dominante (universo de tipo Einstein-de Sitter) $a \propto t^{2/3}$, entonces la evolución del contraste de densidad se puede esplicitar en función del tiempo

$$\frac{\partial^2\delta}{\partial t^2} + \frac{4}{3}\frac{\partial\delta}{\partial t} = \frac{2}{3t^2}\delta, \tag{6.1.36}$$

y la solución es

$$\delta = At^{2/3} + Bt^{-1}. \tag{6.1.37}$$

El primer término es el *modo creciente*, el segundo es el *modo decadente*.
Otra manera de describir la evolución del contraste de densidad es a través de la longitud de onda de Jeans. En presencia de una componente que ejerce presión (como la radiación acoplada con la materia en un universo denso), esa tiene que incluirse en la ecuación de la evolución del contraste

$$\frac{\partial^2\delta}{\partial t^2} + 2\frac{\dot{a}}{a}\frac{\partial\delta}{\partial t} = 4\pi G\rho_b\delta + \frac{c_s^2}{a^2}\nabla^2\delta \tag{6.1.38}$$

donde $c_s^2 \equiv dp/d\rho$ es la velocidad de las olas de sonido que se propagan en un medio. Descomponiendo el contraste en una serie de Fourier, la evolución de los modos δ_k es

$$\frac{d^2\delta_{\mathbf{k}}}{dt^2} + 2\frac{\dot{a}}{a}\frac{d\delta_{\mathbf{k}}}{dt} = \left(4\pi G\rho_b - \frac{k^2c_s^2}{a^2}\right)\delta_{\mathbf{k}}. \tag{6.1.39}$$

No hay evolución cuando el término entre paréntesis es nulo, es decir cuando al número de ondas es

$$k_{\mathrm{J}} = \frac{2a}{c_s}(\pi G\rho_b)^{1/2}. \tag{6.1.40}$$

Perturbaciones con una longitud propia mayor que la longitud de Jeans seguirán creciendo bajo el efecto de la propia gravedad, mientras que perturbaciones con una longitud de onda más corta que la de Jeans se comportan como osciladores hasta que materia y radiación son desacopladas.

Sobredensidades de simetría esférica que crecen en régimen de linealidad, llegan a un regimen de no-línealidad que produce sus colapso. Una sobredensidad de simetria esferica es parecida a un universo cerrado, por lo cual la posición y el tiempo son descritos por una solución de tipo cicloide

$$\delta \simeq \frac{3}{20}\left(\frac{6t}{B}\right)^{2/3}. \tag{6.1.41}$$

La esfera que contiene la sobredensidad está en expansión de acuerdo con el flujo de Hubble, pero llega a un punto de *inversion*, donde su sobredensidad

alcanza un valor de $\simeq 5.6$. Calculado en el regimen de línearidad ($\delta \propto t^{2/3}$) ese valor es $\simeq 1.06$. Después de la inversion, el sistema empieza a colapsar bajo su propia gravedad, pero no llega a una singularidad. El sistema se mantiene en uno estado de equilibrio gobernado por la condición de virialización, $V = -2K$, donde V es la energía potencial y K es la energía cinética. Dependiendo de donde se considera virializado el sistema (en un camino promedio o en el punto de maximo colapso), el contraste de densidad tiene un valor mayor que uno, $\simeq 147$ o $\simeq 178$. Ese valor suele ser llamado contraste de densidad critico, $\delta_{\rm crit}$ y tiene un papel importante en la teoría de Press-Schecther sobre el número de halos de materia oscura que se forman a lo largo de la expansión.

6.1.5 Radiación

En un escenario de tipo Bing Bang, con un Universo en evolución, su historia térmica depende de su cantidad de radiación.

La radiación está acoplada a la materia en el primer periodo del Universo, cuando este era extremadamente caliente y denso. En equilibrio térmico, los fotones exhiben un espectro de *cuerpo negro*

$$u(\omega)d\omega = \frac{\hbar}{\pi^2 c^3}\frac{\omega^3 d\omega}{e^{\hbar\omega/kT}-1}, \tag{6.1.42}$$

en función de la frecuencia angular ω. Integrando en todas las frecuencias la distribución de cuerpo negro, se obtiene la energía de radiación por unidad de volúmen

$$u = a_b T^4 \tag{6.1.43}$$

donde a_b es una constante y la temperatura varia como $T \propto (1+z)$. La densidad de la radiación es

$$\rho_{\rm rad} = \frac{a_b T^4}{c^2} = \frac{a_b}{c^2} T_0^4 (1+z)^4, \tag{6.1.44}$$

que puede ser comparada con la densidad de la materia

$$\rho(t) = \frac{1}{a^3(t)}\frac{3H_0^3}{8\pi G} \tag{6.1.45}$$

para encontrar el redshift al cual las dos densidades eran iguales

$$1 + z_{\rm eq} \simeq 3196, \tag{6.1.46}$$

al cual corresponde un tiempo de $2.6 \times 10^{10}\Omega^{-2}h^{-4}$ segundos. Antes de este tiempo, el Universo está dominado por la radiación, después está dominado

por la materia.

La temperatura T_0 es la temperatura medida en el fondo cósmico de microondas, $T_{\rm CMB} = 2.735 \pm 0.06$ Kelvin. El descubrimiento del fondo cósmico se produjo de manera casual en 1965 por parte de los ingenieros A. Penzias y R. Wilson. Al mismo tiempo, Dicke y Peebles habían formulado la teoría de una radiación de tipo fósil que tiene que estar presente en el Universo como prueba del acoplamiento entre materia y radiación a redshift muy alto. La observación de 1965 y después la medida de la temperatura de la radiación por el satelite COBE en 1991 confirmaron el modelo dinámico del Universo y abrió una nueva era para la cosmología.

Debido a la alta densidad y a la gran energía cinética de los fotones, la materia durante el acoplamiento se encuentra en uno estado ionizado. Los frecuentes choques impiden a los fotones llegar a regiones más lejanas que sus caminos promedios. Es un Universo de forma completamente ionizada y opaco a la luz. Su expansión, con la relativa bajada de la temperatura, conlleva dos efectos que se pueden considerar como ligados. El primero es el *desacoplamiento*, es decir que fotones y bariones no estan en equilibrio térmico y evolucionan de acuerdo a distintas propiedades térmicas. El desacoplamiento no ocurre de manera instantanea, se prolonga un cierto tiempo dando lugar a lo que se llama *superficie de último choque*. Los fotones están libres de viajar a grande distancias. Cuando esos fotones llegan a un observador, conservan información del último choque y su entorno. El redshift del desacoplamiento ha sido estimado en $z_{\rm dec} \simeq 1300$.

Tras el desacoplamiento radiación-materia, los iones y los electrones pueden combinarse para formar átomos de hidrógeno. Aunqueantes no existian átomos neutros, a esta primera formación se le da el nombre de *recombinación*. En el proceso de recombinación, también se produce una fracción de moléculas de hidrógeno H_2.

La presencia de fotones afecta la capacidad de los bariones de formar estructuras. Antes del desacoplamiento, bariones y fotones, estrechamentes correlacionados, tienen un recorrido medio muy corto. Pero los fotones pueden pasar de regiones más densas a menos densas y con esto *arrastran* los bariones.

Por fin, la evolución química de las especies en el Universo primordial crea una importante fracción de helio, que está estimada en el valor $Y_{\rm He} \simeq 0.25$, aunque medidas más recientes han subido su contenido a 0.28. La producción

de hidrógeno y helio en un contexto de tipo cosmológico, sin intervención de estructuras como estrellas o galaxias, tiene el nombre de *nuclosíntesis primordial*. Además de la produción de estos elementos, la nucleosíntesis llega a formar una pequeña, pero no despreciable fracción de isótopos pesados como deuterio y tritio (hidrógeno) y ^{3}He.

6.1.6 Materia oscura

Hasta ahora, con el término "materia" se ha identificado una componente muy fácil de trazar porque se está correlacionada a la emisión (o absorción) de radiación. Esta componente de la materia bariónica, en el modelo estándar está aceptado como una pequeña parte de una componente mucho mayor en número, que es la que rellena el parámetro de densidad Ω. A esa componente no se le da carácter emisor de radiación, y los efectos observables son de naturaleza puralezamente gravitatoria. Ya con el estudio a principios del siglo XX de los primeros sistemas ligados a través de la gravedad, como los cúmulos de Virgo y Coma, surgió la idea que solo la materia luminosa no era capaz de explicar las fuerzas atractoras observadas. Al pasar los años, con el creciente descubrimento de la dinámica del movimiento de las galaxias, la necesidad de introducir una teoría que conectara bien con las observaciones introdujo la necesidad de la existencia de la materia oscura. Sus propiedades han sido identificadas, pero todavía no se ha identificado con certidumbre los candidatos. SÓLo una mínima parte de materia oscura puede ser identificada con materia bariónica que no se puede observar (estrellas enanas marrón, cometas), la mayoría de materia oscura tiene que ser de otro tipo.

El candidado más acreditado hasta el presente es la materia oscura *fría* (CDM). El término frío se refiere a su propiedad de ser no-relativista, ya que no presenta una presión y actua sólo con gravedad. La sección de choque eficaz de ese tipo de materia es muy pequeña, también respecto a los choques que se producen en el acoplamiento materia-fotones a redshifts $z > z_{\rm dec}$, por lo cual, sobredensidades con longitud de onda más pequeña de la de Jeans no se ven afectadas por la presencia de fotones y crecen en regimén líneal también dentro del horizonte. Si n_f es el número de partículas de materia oscura, la estimación de la densidad puede dar el rango de masa

$$\rho_d = \frac{n_f m}{(1+z)^3} = \frac{3H_0^2\Omega_d}{8\pi G}. \tag{6.1.47}$$

Para un valor de Ω_d del orden de la unidad, la masa m tiene un rango de 2-10 GeV. Un posible candidado en ese orden de masa es la partícula con el nombre de *neutralino*, que aparece en la familia de partículas WIMP (*Weak Interaction Massive Particles*, partículas masivas de interaccíon debil). De los experimentos que intentan medir el neutralino, sólo uno ha mostrado una detección en el rango de masa 7-11 GeV.

Otro tipo de materia oscura fría es el *axión* que es de tipo bosónico, para el cual se prevé un rango de masa mucho más bajo, entre $10^{-6} - 1$ eV. Hasta ahora no se han detectado eventos que confirmen la existencia del axión.
Además de la materia oscura fría, ha tenido mucho éxito también la teoría de una materia oscura caliente, es decir, con velocidades relativistas y que ejerce una presión. El candiadato más razonable en este caso es una familia de neutrinos masivos, producidos en los decaimientos beta. Sin embargo, ese tipo de neutrino no podía explicar la constante de Hubble medida, ni podía explicar la formación de estructuras de tipo adiabático. Aunque se intenta reconciliar las observaciones con la presencia de materia oscura de tipo caliente (proponiendo otra familia de neutrinos), el modelo estándar está está basado en la existencia de materia oscura fría.
En los años 80, en los cuales se iba asentando la idea de la materia oscura, otras teorías alternativas iban siendo propuestas. La más importante es la teoría de la modificación de dinamica de Newton (MOND). MOND se realizó a partir de la medida de las curvas de velocidad de rotación de las galaxias. Las curvas se observaban constantes también a gran distancia del centro (en una teoría clásica, con sólo materia bariónica, tienen que caer como $v \propto r^{1/2}$). Para explicar eso, la materia oscura fue introducida como una componente presente en el halo alrededor del disco de la galaxia, que contenía la masa necesaria para mantener constante la velocidad. La teoría MOND dice que la fuerza es proporciónal a la aceleracíon sólo cuando esa acelaración es mayor a una constante a_0. Pero a una distancia para la cual la aceleración de Newton es más debil, la curva de velocidad rotacional es proporcional a esa constante, manteniéndose constante ella misma. MOND ha sido capaz de explicar varias curvas de rotación de galaxias lejanas de varios tipos, pero parece no tener la capacidad de explicar la fuerza de atracción de los cúmulos más masivos y de no tener un esquema para la formación de estructuras.

De aspecto parecido a MOND es la teoría de gravedad modificada, o MOG,

introducida en los ultimos años. En vez de una aceleración a_0 MOG introduce un par de parámetros que se ajustan al sistema que se estudia, una masa M_0 y un radio r_0. La constate gravitatoria G se sustituye por una función $G(r)$. Los autores de la MOG han declarado muchos éxitos de la teoría, el último de los cuales es la explicación del Bullet Cluster a través de únicamente materia bariónica. El caso del Bullet Cluster 1E0657-558 ha sido unas de las observaciones más importantes para la afirmación de la idea de la existencia de materia oscura. El choque de dos cúmulos en el plano del cielo ha permitido por primera vez medir una componente bariónica (gas caliente que emite en radios X) separada de una componente mas masiva (materia oscura, medida a través del efecto lente gravitatoria). Además de representar un laboratorio para la teoría de materia oscura, también la teorí MOG parece poder explicar la separación de las componentes y la masa que produce el efecto lente.

6.1.7 Estadística de un campo de densidad

En el espacio real se puede construir la *función de correlación a dos puntos*, que es la probabilidad de que dos objectos se encuentran en dos volúmenes V_1 y V_2 separados por una distancia r. La función de correlación se puede escribir en función de las sobredensidades de esos objectos. Cuando la distribución sigue una distribución Gaussiana, la función de correlación tiene su correspondiente transformada de Fourier. A cada sobredensidad real $\delta(\mathbf{r})$ le corresponde una serie con coeficientes en números de ondas $\delta_{\mathbf{k}}$. El espectro de potencias se define como

$$\mathcal{P}(k) \equiv \langle |\delta_{\mathbf{k}}|^2 \rangle, \tag{6.1.48}$$

o

$$\Delta^2(k) \equiv \frac{V}{(2\pi)^3} 4\pi k^3 \mathcal{P}(k), \tag{6.1.49}$$

y es la medida de cuánto varía el contraste de sobredensidad, respcto a un valor promedio, en diferentes escalas angulares. La función más sencilla para expresar el espectro de potencia es de tipo $\mathcal{P}(k) \propto k^n$. Ese tipo de espectro se presenta por fluctuaciones de materia oscura después de la era de la inflación y durante la era de la radiación. Las fluctuaciones crecen en todas las escalas, porque la radiación se está expandiendo por el horizonte así que su presión no contrasta los efectos de la gravedad para escalas mas grandes del mismo horizonte. Ese espectro se presenta para las sobredensidades resultantes después de la era de

la inflacion, por esto toma el nombre de *primordial* y por el hecho que las fluctuaciones crecen a todas las escalas, toma el nombre de *invariante*.

El espectro de potencias evoluciona según la escala de Jeans, que divide los modos crecientes de los que oscilan bajo la presión de radiación. Los modos que entran en el horizonte empiezan a oscilar por el efecto de la presión, así que fluctuaciónes de longitud corta se suprimen por efecto de la difusion de los fotones (*radiation drag* o *Silk damping*). Los modos que van entrando en el horizonte corresponden a los ks menores, así se crea un pico a la derecha del espectro, pico que se va moviendo hacia la izquierda a lo largo de la expansión de el horizonte. La supresión corresponde a una función $\mathcal{P}(k) \propto k^{-3}$, y se produce hasta que $a > a_{\rm eq}$. Desde este momento, la materia es la componente dominante del universo y todas las fluctuaciones siguen creciendo en regimén líneal.
La estadística Gaussiana permite una estimación de los halos de materia oscura que se forman a lo largo del tiempo por unidad de volúmen. Esta estadística tiene su importancia cuando a un halo de materia oscura se asocia una estructura bariónica. Dependiendo de la masa, esa estructura bariónica puede ser un grupo de galaxias o un cúmulo. Un grupo de galaxia tiene una masa más pequeña ($M < 10^{13}\mathcal{M}_{\odot}$) y es pobre en gas caliente (IGM). Los cúmulos son estructuras masivas (de hecho, las más masivas observadas, $M > 10^{13}\mathcal{M}_{\odot}$), y se caracterizan por la presencia de gas exstremadamente caliente ($\sim 10^7$ K) que emite en radio y en rayos X.

La teoría de Press y Schecther indica el número de halos que se forman en un volúmen comóvil a lo largo del redshift. Es la probabilidad de que un halo tenga una sobredensidad mayor que una densidad crítica δ_c en el momento del desacoplo. La probabilidad es la integral de una distribución de tipo Gaussiano, por lo cual la desviación estándar σ (sobre un radio de $8h^{-1}$ Mpc) es un dato observado

$$M\frac{dn}{dM} = \left(\frac{2}{\pi}\right)^{1/2} \frac{d\ln\sigma^{-1}}{d\ln M} v_c^{1/2} e^{-v_c/2}, \tag{6.1.50}$$

donde $v_c \equiv \delta_c/\sigma$.
La formación de estructuras a través del colapso gravitacional se conoce como formación de tipo *bottom-up* porque estructuras más pequeñas se forman antes y estructuras más masiva se forman después por mutua atracción. Una formación de estructuras del tipo contrario, $top - down$, en la cual estructuras masivas se forman al principio y las más pequeñas siguen después un proceso de

desintegración es prevista en un escenario de materia oscura caliente en modo adiabático.

Las observaciones indican una formación con materia oscura fría, además pruebas muy importantes para la teoriía de CDM se han realizado en los ultimos años a través de las *simulaciones cosmológicas*.

Una simulación cosmológica consiste en una distribución de elementos de materia en un volúmen y un conjunto de ecuaciones que describen su evolución en el tiempo. En este trabajo de tesis se ha usado el código GADGET-2 para desarollar una simulación cosmológica para rapresentar un conjunto de cúmulos de galaxias. GADGET-2 es una simulación de tipo N-cuerpos, en la cual se fija un número de elementos o *partículas* que pueden ser de naturaleza no-bariónica (materia oscura) o de naturaleza bariónica (gas o estrellas). Para cada de las n partículas se construye una función de Poisson que es la suma de las $n-1$ interaciónes entre dicha partículas y las otras. Para un número muy grande de partículas, el número de ecuaciones a resolver demasiado grande, considerando que por cada partícula en un volúmen hay que simular tres coordenadas de posición y tres de velocidad. Para reducir el número de ecuaciones por cada intervalo de integración, GADGET-2 usa el metodo del *tree* (arbol), descomponiendo el volúmen en subvolúmenes regulares. En cada subvolúmen se calcula una interacción promedio de las partículas. Cuando una partícula se encuentra lejana de un subvolúmen, no hay necesidad de cumplir el calculo de las interaciones de gravidad entre dicha partícula y las partículas del subvolúmen, sólo es necesario calcular la interación usando el sólo valor promedio. A través de un umbral definido por el usuario es posible intervenir sobre la descomposición en multipolos del volúmen cosmológico. En el caso de materia oscura, actúa sólo la interacción gravitatoria. En el caso de materia bariónica, hay que introducir ecuaciones por la viscosidad y los choques que se producen. En este caso se calcula la variación de la velocidad en función de términos de viscosidad artificial.

Aunque las ecuaciones usadas en un código de tipo N-body suelen ser más complicadas, la idea es que una simulación proporciona el conjunto de partículas en el volúmen en diferentes intervalos de tiempo. Los intervalos son decididos por el usuario y por cada intervalo se proporciona una lista de posiciones, velocidades, temperaturas y masa de cada partícula. Estas informaciones, reagrupadas en ficheros, dan un fotografía del universo simulado. Cuando se rep-

resentan, de acuerdo con la resolución espacial alcanzada, se identifican los aspectos peculiares de las estructuras a gran escala del Universo como nos sugieran las observaciones. Las simulaciones cosmológicas han sido una prueba crucial para la confirmación del modelo estándar, con materia oscura constituida en practicamente su totalidad de tipo no-bariónico, una nucleogénesis primordial que ha producido hidrógeno y helio con una proporción 3:1, formación de estructuras de tipo jerárquico por caída en potenciales gravitatorios, expansión del Universo de manera acelerada por la presencia de una presión debida a la existencia de la energía oscura.

6.1.8 Efecto lente gravitatoria

El efecto lente gravitatoria es una evidencia directa de la teoría de la relatividad general. Este efecto es debido a fuertes potenciales gravitatorios que producen distorsiones en la trayectoria de los fotones. Aunque toda masa es capaz de distorsionar el espacio, el efecto lente gravitatoria produce cantidades medibles de esa distorsión. Los primeros efectos de lente gravitatoria se midieron observando que dos galaxias, en posiciones muy diferentes del plano del cielo, se observaban con el mismo redshift y con el mismo espectro de emisividad. Pronto se identificaron esas galaxias como imágenes multiples de otra galaxia que no era visible. Este tipo de distorsión es conoscido como lente gravitatoria fuerte. El potencial gravitatorio necesario para producir una distorición tan grande se encuentra sólo en galaxias masivas y cúmulos de galaxias. En este caso se dice que el cúmulo es la lente. Aunque sólo cúmulos muy masivos son capaces de producir imágenes multiples de una misma fuente, potenciales gravitatorios más débiles (o el mismo potencial gravitatorio de un cúmulo masivo a grande distancia desde su centro) producen una distorsión coherente de las imágenes de las galaxias del fondo. Esa distorsión es una deformación de la imagen que se puede medir y cuantificar y toma el nombre de efecto lente débil.
Por el efecto de lente fuerte se puede usar la aproximación de *lente fina*, en la cual las distancias entre el observador y la lente y entre la lente y las galaxias del fondo son mucho mayores que el grosor del cúmulo-lente. Los elementos que entran en un sistema de lente fuerte son tres: las posiciones de las galaxias del fondo β, las posiciones de las imagines multiples θ y el ángulo de deflexión

α,

$$\beta = \theta - \frac{D_{LS}}{D_S}\alpha(\theta), \tag{6.1.51}$$

donde D_{LS} es la distancia angular entre lente y fuentes y D_S es la distancia angular entre observador y fuentes. Cuando las posiciones β están en el centro geométrico de la lente, las posiciones θ forman el *anillo de Einstein*.

En cada posición θ se reconstruye el potencial gravitatorio (bidimensional) a partir de las distancia entre esa posición y las otras posiciones θ'. Una vez que se han identificados las distancias entre sus componentes, el sistema tiene una cantidad definida que es la densidad crítica de superficie Σ_{crit}. En cada punto θ existe una densidad de superficie $\Sigma(\theta)$ (es una proyección en el cielo de una densidad de volúmen), entonces, para un mapa de θs existe un mapa de *convergencia*

$$\kappa = \frac{\Sigma(\theta)}{\Sigma_{crit}}. \tag{6.1.52}$$

El mapa de convergencia es un sinonimo de densidad de superficie, es decir, un sinónimo del potencial proyectado, $\kappa = (1/2)\nabla^2\psi$. Otra cantidad de un sistema de lente es la *magnificación*, definida como la variación de las posiciónes θs en función de las posiciónes βs.
La transición entre un regimen de lente fuerte y un regimen de lente débil puede ser pensada en función de la convergencia: un $\kappa \ll 1$ es indicativo un regimén de lente débil sin efectos de lente fuerte. Asociado al potencial gravitatorio está lo que llamamos *shear*, γ. El *shear* es la medida de la variación del potencial gravitatorio en función de las θs. El *shear reducido* $g = \gamma/(1-\kappa)$ es la medida de la distorsión coherente de la forma de las galaxias del fondo.

6.1.9 Procesos de radiación

Después del desacoplamiento entre materia y radiación, las fluctuaciónes de densidad son libres de crecer en regimen líneal y colapsar en regimen de no linealidad. El colapso aumenta la densidad de la materia bariónica, que por efecto de atracción gravitatoria se une en estructuras mas grandes. Si el desacoplamiento es a un redshift $z > 1000$, las primeras estructuras son a un redshift $z \sim 20$. Después de la recombinación, el gas de la nucleosintesis (hidrógeno y helio) se encuentra en un estado neutro. Las primeras estructuras dan lugar a las primeras regiones de formación estelar. Aunque muchas dudas quedan sobre el proceso de formación de las primeras estrellas, está claro que

fotones ionizantes empiezaron a escapar de las regiones estelares para propagarse en el medio poco denso alrededor. Una primera fase ve burbujas de gas ionizado alrededor de fuentes ionizantes. En una segunda fase las burbujas comienzan a solaparse de modo extendido y en una tercera fase la fracción de gas neutro se reduce a menos de 1 parte entre 10^3. La segunda fase se llama *reionización*. Al proceso de reionización se asocia un exceso de electrones, cuya densidad es n_e. La medida de la reionización se hace a través de la profundidad óptica τ, que es el producto de la densidad de electrones por la sección de choque Thomson (entre fotones y electrones), integrado en la línea de visión.
La presencia de electrones libres en el medio intergalactico es la causa de emisiones observadas en la banda de radio. La emisión de tipo *libre-libre*(o de tipo free-free) es una emisión de tipo térmica porque su espectro está relaciónado con la distribución de velocidades de Maxwell. El espectro libre-libre es casi plano, con una ligera dependencia de la frecuencia $\epsilon \propto \nu^{-0.1}$ debido al factor de Gaunt. La emisividad de libre-libre es una función de la densidad de electrones al cuadrado, y función inversa de la radiz de la temperatura, $\epsilon_{\rm ff} \propto n_e^2/T^{1/2}$. Por una temperatura tipica del medio ionizado de $T = 10^4$ K, la emisión libre-libre tiene un pico a $\nu_{\rm max} \simeq 1GHz$, aunque por la planitud de su espectro, su observación es posible alrededor de $\nu \simeq 100$ GHz donde no está tan dominado por emisión de synchrotron o polvo.
La emisión de tipo synchrotron se produce cuando los electrones libres interactuan con un campo magnetico presente en la galaxia. Por esto el synchrotron es una emisión de tipo no-térmico. La dependencia de la frecuencia es una ley de potencias mucho más pendiente de la de libre-libre. Una estimación por galaxias de tipo normal indica que $\epsilon_{\rm syn} \propto \nu^{-0.7}$. Los campos magneticos que aceleran los electrones son debidos a los restos de supernovas, entonces son una evidencia de regiones de formación estelar. Por esto la radiación de tipo libre-libre y la de synchrotron son dos componentes del mismo espectro de emisión de galaxias o cúmulos de galaxias. La pendiente del synchrotron permite que sea más fácil observarlo a frecuencias bajas. A frecuencias altas, una tercera fuente de emisión domina la de libre-libre y es la radiación de tipo infrarojo emitida por rl polvo. Aunque no causada por electrones libres, la presencia de polvo sigue siendo asociada a regiones de formación estelar, entonces las observaciónes han detectado una correspondencia entre la emisión de synchrotron (o radio) y la del polvo (infrarojo).

6.2 Capítulo 2

En este capítulo se presenta un resumen del articulo **La señal cosmológica de libre-libre de grupos de galaxias y cúmulos** escrito por Ponente, Diego, Sheth, Burigana, Ascasibar y Knollman y presentado en la revista Monthly Notices of the Royal Astronomical Society con referencia MNRAS, 2011, 410, 2353.
El articulo se pone como objetivo sacar un modelo para la emisión de tipo libre-libre de tipo cosmológico, es decir integrado en todo el espacio a partir de un redshift que incluya el proceso de reionización. Los reultados del artículo son relevantes para los nuevos projectos (SKA y ALMA) que contribuiran a dar mayor luz al marco de formación de las primeras estructuras. La ventana de observación es la banda radio a frecuencias de pocos GHz. En este contexto se ha introducido el experimento de ARCADE2 , que ha medido el fondo cósmico del cielo en bandas desde 3 a 10 GHz. Aunque el espectro de libre-libre es plano, cuando es observado en temperatura termodinamica, la señal aparece muy debil debido al cambio en temperatura con ley $\propto \nu^{-2}$.

La emissiviadad del libre-libre, en unidades de erg cm^{-3} s^{-1} Hz^{-1} sr^{-1} es

$$\epsilon_\nu = 5.4 \times 10^{-39} n_e^2 T_e^{-1/2} g_{\rm ff}(\nu, T_e) \exp\left(\frac{-h\nu}{kT_e}\right). \tag{6.2.1}$$

La emisión procedente de un único halo viene calculada usando el modelo β por la densidad de electrones en función del radio y usando relaciónes de escalas por el radio y la temperature en función de la masa. La masa del gas viene calculada como una fracción de la masa del halo que es de materia oscura.

Obtenida la función de emissividad de un halo, se puede estimar la abundancia de halos en redshift con una función de tipo Press-Schecther o su derivada de Sheth-Tormen. Hemos estimado la abundancia en un intervalo de masas $10^8 \leq M \leq 10^{16} h^{-1} \mathcal{M}_\odot$. Por el redshift de integración se ha usado un intervalo $0.05 \leq z \leq 7$ en el cual el proceso de reionización se puede considerar concluido. La función de masa de halos es una función monotóna decreciente: halos de masa pequeña se forman en mayor cantidad que halos de masas grandes, independentiemente del redshift. La masa mayor encontrada en nuestro modelo es $\sim 10^{15} \mathcal{M}_\odot$.

La estimación de la señal promedio de tipo libre-libre es la combinación de un modelo β de un sólo halo con la función de abundancias de halos. La emissividad es convertida en flujo y convertida en distorsión de temperatura sobre

la temperatura de fondo cósmico de microondas $\Delta T/T$. Una señal total tiene una distorsión de temperatura del orden de $\Delta T/T \simeq 10^3$ μK a la frecuencia de 1 GHz. La señal aparece más baja que la encontrada por Oh (1999) a partir de fuentes puntuales. En vez de usar la temperatura del virial por cada halo, hemos usado una temperatura fija de 10^4 K. Debida a la dependencia $\epsilon \propto T^{-1/2}$, esto ha permitido sacar un valor ligermente más alto por la distorsión.

No todos los rangos de masa dan la misma contribución a la señal. La mayor es dada por halos de masa entre $10^8 \leq M \leq 10^{12}$ que corresponden más a grupos de galaxias que a cúmulos. La contribución mayor de masas pequeñas se repite a todos los rangos de redshifts examinados.
La emisión libre-libre se ha calculado también a partir de una simulación cosmológica de un conjunto de 512^3 partículas de materia oscura y 512^3 partículas de gas con el código GADGET-2 . A una primera simulación de $300h^{-1}$ Mpc de volúmen comóvil ha seguido una segunda de $50h^{-1}$ Mpc. En la primera, cada partícula de materia oscura y gas tiene una masa de $M_{\rm DM} = 1.165 \times 10^{10} h^{-1} \mathcal{M}_\odot$ y $M_{\rm gas} = 0.17 \times 10^{10} h^{-1} \mathcal{M}_\odot$ respectivamente. En la simulación de $50h^{-1}$ Mpc esos valores son $M_{\rm DM} = 6.1 \times 10^7 h^{-1} \mathcal{M}_\odot$ y $M_{\rm gas} = 0.873 \times 10^7 h^{-1} \mathcal{M}_\odot$. Por cada partícula de gas, se ha calculada la densidad de electrones como una función de la masa de la partícula, y la temperatura ha sido calculada a partir de la energía interna asociada a cada partícula. De cada *caja* de la simulación, se proyecta un mapa del flujo en dos dimensiones. De cada proyección se calcula el valor promedio. La integración en redshift en este caso es la suma de los mapas. El valor de la señal de libre-libre sacado a 1 GHz de una simulación de $300h^{-1}$ es mucho menor que el valor calculado con el modelo analítico. La explicación es que el conjunto de tamaño de la simulación y partículas usadas no es lo suficiente para crear halos de masa pequeña. La prueba ha sido obtenida con el código Amiga Halo Finder (AHF) que ha estimado la masa por los conjuntos de partículas que se pueden considerar ligadas para formar halos. El rango de masa es $10^{11} \leq M \leq 10^{14}$ h^{-1} $\mathcal{M}_\odot$ que es capaz de recrear una distorsion de libre-libre de sólo $\Delta T/T \simeq 10^2$ μK. En la simulación de $50h^{-1}$ Mpc, la señal es aumentada en un factor 5.
Aunque la señal de libre-libre aparece debil, futuros experimentos como el SKA pueden alcanzar la sensibilidad para detectatar la parte central de halos que emiten en radio a través de libre-libre en un estadio en lo cual su temperatura del gas no es tan alta para emitir en rayos-X, tipicamente se habla de temperaturas asociadas a grupos de galaxias.

6.3 Capítulo 3

El capítulo contiene el articulo **La contribución de las galaxias con formación estelar al fondo cosmico en banda de radio** escrito por Ponente, Ascasibar & Diego, publicado en la revista Monthly Notices of the Royal Astronomical Sociey (MNRAS).

El objectivo del articulo es cuantificar la emisión radio de fondo a través de un modelo fenomenologico.
La medida del fondo cósmico de radio ha sido realizada por el equipo del proyecto Absolute Radiometer for Cosmology, Astrophysics and Diffuse Emission, ARCADE2 . El fondo difuso ha sido medido en bandas de radio desde 3 a 10 GHz, obteniendo

$$T(\nu) = \frac{h\nu/k}{\exp(kT_{\rm CMB}) - 1} + T_R \left(\frac{\nu}{\nu_0}\right)^{\alpha-2} \tag{6.3.1}$$

donde $T_{\rm CMB} = 2.729 \pm 0.0004$ K es la temperatura termodinamica del fondo cósmico de microondas, $T_R = 1.19 \pm 0.14$ K es el valor a 1 GHz del fondo cósmico de radio y $\alpha = -0.62 \pm 0.04$ es el indice espectral de la emisión de synchrotron. El valor de T_R parece ser mucho mayor (hasta 5σ) del precedente valor estimado por COBE/FIRAS. El equipo de ARCADE2 asegura que la señal es de tipo cosmológico (no de la Via Lactea), no es producida por gas extendido (IGM) y sólo puede ser causada por fuentes puntuales que corresponden a galaxias normales, en las cuales la actividad del agujero negro central es inexistente o despreciable. En el capítulo 2 se ha demostrado que la emisión de tipo libre-libre es demasiado debil para alcanzar 1 K a 1 GHz.
Usando el analisis en Condon (1992) que relaciona las emisiones de tipo libre-libre y de synchrotron a la tasa de formación estelar cosmica, se han podido obtener relaciónes entre la luminosidad de los dos efectos y la tasa formación estlar sacada de las ultimas observaciónes en varias bandas.

En primer lugar, manteniendo fija la tasa de formación estelar (SFR) la luminosidad de synchrotron es un factor 10 mayor que la luminosida de libre-libre, a una frecuencia de referencia (1 GHz). La frecuencia radio de 1.4 GHz es usada para definir el parámetro q, es decir la diferencia logaritmica entre la luminosidad en banda infraroja y en banda radio. El parámetro q toma el nombre de *correlación infrarojo-radio* (FRC) y es un parámetro defindido para las observaciónes. Pero sigue abierta la cuestion de si ese parámetro se mantiene constante o evolucióna en el redshift. Usando la estimación de q de varios autores,

hemos podido reducirlo a una forma líneal en logaritmo de $(1+z)$

$$q(z) = q_0 - \beta \log(1+z). \tag{6.3.2}$$

Bajo la suposición que la luminosidad de infrarojo no evoluciona con el redshift, el coeficiente β es un indice para la evolución en $(1+z)$ de la luminosidad de synchrotron,

$$L_{\rm syn} \rightarrow L_{\rm syn}(1+z)^{\beta}. \tag{6.3.3}$$

La evolución en redshift proporcióna una señal mayor a z altos (aunque suprimida por la mayor distancia de luminosidad), que se traduce en un señal total mayor cuando se integra en la línea de visión.
Para sacar la luminosidad de synchrotron hemos usado una parametrización de la SFR. Los cuatros parámetros de la estimación han sido sacados con un metodo de mínimos cuadrados pesados sobre un conjunto de datos observados. Una vez obtenidos todos los ingredientes para reconstruir una señal a lo largo de la lina de visión, por el libre-libre como por el synchrotron *estándar* y con dependencia de z. Los valores de temperatura sacados, en función de la frecuencia, son

$$\frac{T_{\rm ff}}{0.0137\ {\rm K}} = \left(\frac{\nu}{\rm GHz}\right)^{-2.1} \tag{6.3.4}$$

por el libre-libre,

$$\frac{T_{\rm syn}}{0.0817\ {\rm K}} = \left(\frac{\nu}{\rm GHz}\right)^{-2.7} \tag{6.3.5}$$

por el synchtroen estándar ($\beta = 0$) y

$$\frac{T_{\rm syn}}{0.1402\ {\rm K}} = \left(\frac{\nu}{\rm GHz}\right)^{-2.7} \tag{6.3.6}$$

por el synchtron con $\beta > 0$. El valor del modelo es $\beta = 0.705$. Aunque usando un limite superior $\beta = 1$, la señal de ARCADE2 de $T = 1.19$ K sigue siendo un exceso inexplicado.

6.4 Capitúlo 4

Este capitúlo propone el resumen del articulo **Errores sistematicos en la reconstruction a través de lente gravitatoria. ¿Hay anillos de materia oscura en el cielo?** presentado por Ponente e Diego y aceptado por la revista Astronomy & Astrophysics.

El trabajo se centra sobre el lensing gravitatorio de tipo *fuerte* y *debil* y sobre el metodo non-paramétrico para reconstruir el perfil de un cúmulo de galaxias a partir de los efectos que su potencial produce sobre las galaxias del fondo.

Los metodos no-paramétricos no usan suposiciones preliminares sobre la distribución de la masa en el cúmulo. Eso supone un metodo extremadamente poderoso al asumir que no hay ninguna información directa sobre la masa, su magnitud y su distribución, respecto a los resultados que se alcanzan. El metodo requiere muchas observaciones, así que sólo cúmulos para los cuales existen imágenes muy detailladas pueden ser analizados a través de metodos no-paramétricos. Unas de las reconstruciónes de cúmulos con metodos no-paramétrico más importante y descutida es la reconstrución del cúmulo CL0024+17 hecha por Jee et al. (2007). La peculiaridad de esa reconstrución es que en el mapa de convergencia aparece una primera estructura central (el *core*) y alrededor una estructura en anillo. Los autores reportan que una configuración como esa puede ser explicada con un choque de cúmulos como lo que pasa en Bullet Cluster, con la diferencia que se produce en este caso a lo largo de la línea di visión. En nuestro articulo se demonstra que, un metodo no-paramétrico introduce efectos systematicos cuando se intenta ajustar demasiado la solución a los datos reales. En el espacio de las soluciones, los efectos sistematicos reproducen estructuras parecidas a anillos.

Un problema que se resolve en modo no-paramétrico presenta un sistema

$$\Phi = \Gamma X, \tag{6.4.1}$$

donde el vecotor Φ contiene todas las posiciónes de los pixels que forman los arcos de lente fuerte (por N_θ pixels, el vecor tiene $2N_\theta$ elementos) y los gammas del campo de shear (también en este caso, para N_γ puntos de shear, el vector tiene el doble de puntos). El vector X es el vector de las soluciones, donde por soluciones se entiende un vector de masas M y un par de puntos (cordenada x y y) por cada fuente que se intenta reconstruir. La matriz Γ es la matriz (compuesta) que projecta un elemento (vector) del espacio de soluciones en un elemento del espacio de términos conocidos. Para conocer la solución X, hay que invertir el sistema 6.4.1. El vector de masas M depende del número de celdas en que se divide el plano de la lente. La lente tiene una distribución continua de masa, pero al introducir una red de celdas, de una distribución suave de masa se pasa a una distribución discretizada. En nuestro caso, el plano de la

lente, que tiene un tamaño angular fisico de 3.3 minutos de arco, se divide en una red de 32×32 celdas de tamaño fijo. La inversion del sistema de la lente se puede alcanzar con varios metodos, pero se han elegido dos, el algoritmo de *biconjugate gradient* (BGA) y el *quadratic programing*. El sistema 6.4.1 se puede escribir como

$$R \equiv \Phi - \Gamma X, \tag{6.4.2}$$

donde R es un vector de residuos. Mínimizar los residuos es equivalente a incontrar una solución aproximada del sistema. Esto es un concepto crucial en el proceso de reconstrucción, porque dejar un residuo no-nulo es equivalente a considerar un tamaño fisico puntual para las galaxias del fondo.

Para comprobar el nivel de sesgo que una reconstrucción no controlada introduce en la solución, se ha simulado un caso de lente gravitatoria con parámetros conocidos. El cúmulo ha sido creado con un modelo de Navarro-Fenk-White (NFW), con un perfil de densidad conocido, como conocido es el potential gravitatorio que produce los efectos de lente. Detras del cúmulo, se han posiciónado tres fuentes, porque en el caso de CL0024 el trabajo de Jee et al. (2007) ha identificado tres fuentes. El código usado por la simulación ha creado un mapa de θs, es decir un mapa de arcos. Aunque no es necesario, se ha intentado crear una disposición de los arcos muy parecida a la de l'imagen original del cúmulo CL0024 obtenida por la camara del telescopio espacial Hubble. El mapa de shear también ha sido simulado, y también en este caso se ha ajustado la simulación a el caso real.

Primero, el mapa de arcos y el mapa de shear vienen analizados con el BGA. En el BGA se tiene que introducir un parámetro, ϵ, que es la medida de cuanto se quiere mínimizar los residuos. El valor de ϵ, aunque no es cero, es muy pequeño. Se han hecho dos reconstrucciónes con el BGA, con los valores $\epsilon = 2 \times 10^{-10}$ y $\epsilon = 2 \times 10^{-15}$. En el primer caso, la distribución de masa aparece como un cúmulo central bien definido, que disminuye con un perfil de densidad muy parecido a el original de NFW. En el segundo caso, la estructura central aparece más pequeña y rodeada de un vacio de forma redonda. Alrededor del vacio aparece otra estructuras redonda.
La misma reconstrucción se ha hecho con el QADP, donde se introduce un número de iteraciónes que se requieren al algoritmo. Un número de 100 iteraciónes es suficiente para reconstruir una masa y un perfil parecidos a los del cúmulo simulado orginal. Aumentando el número de iteracióne a 10^5, se obser-

van las formaciónes de estructuras redondas al rededor de la parte central del campo de visión (en este caso, la zona central del cúmulo no tiene masa). En el intento de investigar la formaciónes de estructuras diferentes al perfil original de NFW, se ha obtenido una analisis de unicamente el campo de shear (lente debil) y se ha demostrado que structuras en anillo aparecen en la region de transición entre los datos de lente fuerte y los datos de lente debil. La distancia del anillo en el trabajo de Jee et al. (2007) indica su presencia a la misma transición.

6.5 Conclusiónes

Una señal de tipo libre-libre, aunque dificil a medir, es una herramienta util para un mapa de emisión de halos que alcanzan la masa de grupos de galaxias. Los calculos en el articulo presentado en capitúlo 2 dan una indicación de la sensibilidad necesaria para detectar grupos con futuros instrumentos. El modelo analitico desarrollado muestra ser robusto y capaz de ser adaptado en redshift y rango de masa. Aunque mejorable, el modelo analitico indica que masas pequeñas contribuyen mucho más a la emisión que masas grandes. También se muestra que la emisión por parte de gas extendido es despreciable, de acuerdo con las conclusiones de Oh (1999). Es interesante el hecho de poder combinar la emisión de libre-libre con otras emisiones como el efecto Sunyaev-Zeldovich o emisión en rayos-X de el mismo cluster. Aún más, las emisiones de gas ionizados se podrian combinar con la emisión en banda 21-cm de gas en estado neutro.

Hay varias conclusiones que se pueden sacar del modelo de synchrotron del capitúlo 3. En primer lugar la medida de ARCADE2 es incorrecta, contaminada por emissiones de nuestra Galaxia que no se han subtraido corectamente. Aunque parece que la subtración de emisiones galacticas son consistentes con otras medidas. Una segunda probabilidad muy favorecida por el mismo equipo de ARCADE2 es un incremento de la emisión de radio de galaxias lejanas que aparecen debiles en otras bandas. Una tercera hipótesis es la presencia de una población de galaxias muy poco brillantes en radio (no detectadas por las actuales capacidades de los instrumentos) y en gran número. Aún en este caso se espera que nuevos detectores como el *Extended Very Large Array*, (EVLA), o

futuros experimentos como el *Square Kilometre Array*, (SKA), pueden alacanzar la sensibilidad necesaria para descubrir esos objectos.

Una reconstruction a través de lente gravitatoria del cúmulo de galaxias Cl0024 ha sido presentada en el trabajo de Jee et al. (2007) . Los autores informan de la presencia de un anillo de materia oscura alrededor del centro del cúmulo, por ellos atribuido a un choque entre dos cúmulos a lo largo del línea de visión. En nuestro trabajo, se ha presentado una reconstrución con lente fuerte y debil a partir de datos simulados con un cúmulo de perfil conocido. El metodo de reconstrución de tipo no-paramétrico introduce una incertitubre en el resultado final que tiene que tenerse en cuenta. Cuando se intenta minimizar la incertidumbre, el sistema no es capaz de reconstruir el perfil original e introduce efectos sistematicos que en algunos casos parecen anillos al rededor de un parte central del cúmulo. Nuestro trabajo indica claramente que los efectos sistematicos se producen también cambiando los algoritmos de inversion de la matriz de la lente. Los metodos no-paramétricos se demuestran extremadamente poderosos en la reconstrucción de masa de cúmulos, pero no pueden ser forzados a encontrar una solución exacta.

APPENDIX A

Computing the mass function

In ST, the mass function is given in terms of the factor $\nu \equiv [\delta_c/\sigma_M]^2$, where δ_c is the overdensity contrast required for the perturbation to collapse, and σ_M is the rms fluctuation in the mass scale M. The function

$$\nu f(\nu) = M^2 \frac{n(M,z)}{\bar{\rho}} \frac{d\log M}{d\log \nu} \tag{A.0.1}$$

behaves like an almost universal function with respect to changes in redshift, [180]. The quantity $\bar{\rho} = 2.775 \times 10^{11} \Omega_M h^2 M_\odot$ Mpc^{-3} is today's average matter density.

This mass function accounts for the fact that the gravitational collapse of a halo is not exactly spherical but rather if follows a triaxial model. For a given cosmological model, the evolution of an ellipsoidal perturbation is determined by three parameters, namely the eigenvalues of the deformation tensor. These are the ellipticity e, the prolateness p and the density parameter δ. In their model, the collapse is traced independently over the three orthogonal axes and the virialization of the halo is defined as the time when it collapses along the three axes. Since each axis collapses independently from the others, collapse along each axis is frozen once it has shrunk by some critical factor.

The term $\nu f(\nu)$ in Eq. (A.0.1) is parametrized in the ST formalism as:

$$\nu f(\nu) = A \left(1 + \frac{1}{\nu'^p}\right) \left(\frac{\nu'}{2}\right)^{1/2} \frac{e^{-\nu'/2}}{\sqrt{\pi}}, \tag{A.0.2}$$

where $\nu' = a\nu$, $a = 0.707$, and $p = 0.3$. In the standard Press and Schechter mass function, [37], $p = 0$. $A \approx 0.3220$ is the normalization factor given by the constraint that the integral of $f(\nu)$ in the whole ν range must be equal to 1. For comparison, in the original formalism of Press and Schechter, the normalization is $1/2$.

In Eq. (A.0.2), the over-density parameter δ_c can be estimated, given a cosmological model, using the linear growth parameter $D(z)$ and $\delta_c(z)$ (see for example Mathiesen & Evrard 1998, [39]):

$$\delta_c = \frac{D_0)}{D(z)}\delta_c(z). \tag{A.0.3}$$

Similarly one could have considered $\delta_c(z) = \text{const}$ and $\sigma_M(z) = \sigma_M D(z)/D_0$ with the same results. The mass function, $n(M, z)$, can be easily derived from Eq. (A.0.1) and Eq. (A.0.2).

We assume a flat ΛCDM model ($\Omega_M + \Omega_\Lambda = 1$). In this case $\delta_c(z) = 1.6866[1 + 0.01256 \log_{10} \Omega_M(z)]$. The linear growth factor is given by Peebles (1980), [181],

$$D(x) = \frac{\sqrt{x^3 + 2}}{x^{3/2}} \int_0^x x'^{3/2}(x'^3 + 2)^{-3/2} dx', \tag{A.0.4}$$

where $x = a/[(1 - \Omega_\Lambda)/(2\Omega_\Lambda)]^{1/3}$. In Eq. (A.0.2) σ_M is the RMS fluctuation on the mass scale M:

$$\sigma_M^2 = \frac{1}{2\pi} \int_0^\infty dk k^2 P(k) W^2(kR). \tag{A.0.5}$$

The window function $W(kR)$ is a top hat function in Fourier space

$$W(kR) = \frac{3(\sin(kR) - kR\cos(kR))}{(kR)^3} \tag{A.0.6}$$

with R defined by $M = \frac{4}{3}\bar{\rho}R^3$. The power spectrum $P(k)$ can be parametrized as

$$P(k) = Ak^n T^2(k), \tag{A.0.7}$$

where A is the amplitude and $T(k)$ the transfer function. This choice for the amplitude makes it possible to introduce it in Eq. (A.0.5) with $R = 8h^{-1}$ Mpc to obtain the value of $\sigma_8 = 0.8$, while the index for primordial power spectrum is set to $n = 1$ (both values are from the fifth year of WMAP analysis, [182]). For the transfer function we use the expression given in Bardeen et al. (1986), [34],

$$T(k) = \frac{\ln(1+2.34q)}{2.34q} \left[1 + 3.89q + (16.1q)^2 + (5.46q)^3 + (6.71q)^4\right]^{-\frac{1}{4}}, \tag{A.0.8}$$

where $q = k(h^{-1}\mathrm{Mpc})/\Gamma$, and Γ is the shape parameter of the power spectrum ($\Gamma \sim \Omega_M h$). We have compared the mass functions obtained with this transfer function and the more elaborated one in [183] finding very small differences. For simplicity we use the Bardeen et al. (1986) transfer function.

APPENDIX B

Non-parametrics methods

B.1 How is built the Γ matrix

The Γ matrix is the basis of the Weak and Strong Lensing Analysis Package (WSLAP) and contains the information about how each cell in the grid contributes to either the j^{th} deflection angle or the k^{th} shear measurement. In the SL case, it also contains information about the source identity of the j^{th} pixel in a given lensed arc. All this information is organized in rows, each row corresponding to one constraint (deflection angle for SL and shear for WL). The final structure of Γ is

$$\mathbf{\Gamma} = \begin{vmatrix} \mathbf{Y_x} & \mathbf{1} & \mathbf{0} \\ \mathbf{Y_y} & \mathbf{0} & \mathbf{1} \\ \mathbf{\Delta_1} & \mathbf{0} & \mathbf{0} \\ \mathbf{\Delta_2} & \mathbf{0} & \mathbf{0} \end{vmatrix}. \tag{B.1.1}$$

The specific form of the **Y** and **Γ** matrices depends on the choice of basis system. For clarity purposes, we assume that this system is based on Gaussians positioned on the grid. This grid is a division of the lens plane into cells, where the mass in a cell is assumed to be distributed as a Gaussian of dispersion σ, which is proportional to the size of the cell. A proportionality factor ~ 2 gives very satisfactory results in terms of reproducing the constraints. The integrated mass at a given distance δ from the center of the cell is then

$$M(\delta) = 1 - \exp(\delta^2/2\sigma^2). \tag{B.1.2}$$

Since the basis has circular symmetry, the x and y components of the deflection angle α at the same point can be estimated easily as

$$\alpha_x(\delta) = Y_x = \lambda[1 - \exp(-\delta^2/1\sigma^2)]\frac{\delta_x}{\delta^2}, \tag{B.1.3}$$

$$\alpha_{\rm y}(\delta) = {\rm Y_y} = \lambda[1 - \exp(-\delta^2/1\sigma^2)]\frac{\delta_{\rm y}}{\delta^2}, \tag{B.1.4}$$

where the multiplying constant λ contains all the cosmological and redshift dependence

$$\lambda = 10^{15} M_\odot \frac{4G}{c^2}\frac{D_{\rm ls}}{D_{\rm ol}D_{\rm os}}h^{-1}\ {\rm rad}\ . \tag{B.1.5}$$

The factor $\delta_{\rm x}$ in Eq. (B.1.3) is just the difference (in radians) between the x position in the arc (x of pixel $\theta_{\rm x}$) and the x position of the cell j in the grid ($\delta_{\rm x} = \theta_{\rm x}(i) - \theta'_{\rm x}(j)$). Similarly, we can define $\delta_{\rm y} = \theta_{\rm y}(i) - \theta'_{\rm y}(j)$ and $\delta = \sqrt{\delta_{\rm x}^2 + \delta_{\rm y}^2}$.

The $\mathbf{\Delta_1}$ and $\mathbf{\Delta_2}$ matrices can be computed in a similar way but in this case, since we need to calculate the derivatives, the deflection angles $\alpha_{\rm x}$ and $\alpha_{\rm y}$ have to be computed at three points δ_1, δ_2, and δ_3. The first point, δ_1, is the same as δ above. The second and third points (δ_2 and δ_3) are one (or a few) pixel(s) left (or right) and up (or down) the pixel at δ_1, respectively. Then $\mathbf{\Delta}_1$ is just the difference

$$\mathbf{\Delta}_1 = \frac{1}{2}\frac{[\alpha_{\rm x}(\delta_3) - \alpha_{\rm x}(\delta_1)] - [\alpha_{\rm y}(\delta_3) - \alpha_{\rm y}(\delta_1)]}{\rm pix2rad}, \tag{B.1.6}$$

$$\mathbf{\Delta}_2 = \frac{\alpha_{\rm x}(\delta_3) - \alpha_{\rm x}(\delta_1)}{\rm pix2rad} = \frac{\alpha_{\rm y}(\delta_3) - \alpha_{\rm y}(\delta_1)}{\rm pix2rad}, \tag{B.1.7}$$

where pix2rad is the size of the pixel in radians. Since we included the factor $10^{15}M_\odot$ in λ (see Eq. B.1.5), the mass in the solution vector will be given in $10^{15}h^{-1}M_\odot$ units. The h^{-1} dependency exists because in λ we have the ratio $D_{\rm ls}/(D_{\rm ol}D_{\rm os})$, which goes as h.

The **0** (null) and **1** (0's and 1's) matrices on the right side of Γ add $2N_{\rm s}$ additional columns. The bottom part of thess columns consist entirely of 0's since the shear measurements are independent of the position β of the sources. The $N_\theta \times N_{\rm s}$ dimensional matrices **1** contain 1's in the ij positions ($i \in [1, N_\theta], j \in [1, N_{\rm s}]$), where the $i^{\rm th}$ θ pixel comes from the j source and 0's elsewhere.

B.2 Minimizing algorithms

B.2.1 Biconjugate gradient algorithm or BGA

The biconjugate gradient [184] algorithm is one of the fastest and most powerful algorithms for solving systems of linear equations. It is also extremely useful for finding approximate solutions for systems where no exact solutions exists

or where the exact solution is not the one we are interested in. The latter is our case. Given a system of linear equations

$$Ax = b, \tag{B.2.1}$$

a solution of this system can be found by minimizing the function

$$f(x) = c - bx + \frac{1}{2}x^T Ax, \tag{B.2.2}$$

where c is a constant. The gradient of the Eq. (B.2.2) is 0 when the same equation is at its minima

$$\nabla f(x) = Ax - b = 0. \tag{B.2.3}$$

That is, at the position of the minimum of the function $f(x)$ we find a solution to Eq. (B.2.1). In most cases, finding the minimum of Eq. (B.2.2) is much easier than finding the solution of the system in B.2.1, especially when no exact solution exists for B.2.1 or A does not have an inverse.

The biconjugate gradient finds the minimum of Eq. (B.2.2) (or equivalently, the solution of Eq. B.2.1) by following an iterative process that minimizes the function $f(x)$ in a series of steps no longer than the dimension of the problem. The beauty of the algorithm is that the successive minimizations are carried out on a series of orthogonal conjugate directions, p_{k}, with respect to the metric A. That is,

$$p_{\mathrm{i}} A p_{\mathrm{j}} = 0 \qquad j < i. \tag{B.2.4}$$

This condition is useful when minimizing in a multidimensional space because it guarantees that successive minimizations do not spoil the minimizations in previous steps.

By comparising Eq. (4.3.2) and Eq. (B.2.2), it is easy to identify the terms, $c = (1/2)\theta^{\mathrm{T}}\theta$, $b = \Gamma^{\mathrm{T}}$ and $A = \Gamma^{\mathrm{T}}\Gamma$. Minimizing the quantity R^2 is equivalent to solving Eq. (4.3.1). To see this, we only have to realize that

$$b - AX = \mathbf{\Gamma}^T(\mathbf{\Phi} - \mathbf{\Gamma X}) = \mathbf{\Gamma}^T\mathbf{R}. \tag{B.2.5}$$

If an exact solution for Eq. (4.3.1) does not exist, the minimum of R^2 will be a more accuratly approximated solution to the system. The minimum can be found easily: in the case of symmetric matrices A, the algorithm constructs two sequences of vectors r_{k} and p_{k} and two constants, α_{k} and β_{k}. To begin the algorithm, we need to make a first guess of the solution, namely X_0 and two vectors r_0 and p_0

$$\alpha_k = \frac{r_k^T r_k}{p_k^T A p_k}, \tag{B.2.6}$$

$$r_{k+1} = r_k - \alpha_k A p_k, \tag{B.2.7}$$

$$\beta_k = \frac{r_{k+1}^T r_{k+1}}{r_k^T r_k}, \tag{B.2.8}$$

$$p_{k+1} = r_{k+1} + \beta p_k \tag{B.2.9}$$

At every iteration, an improved estimate of the solution is given by

$$X_{k+1} = X_k + \alpha_k \beta_k. \tag{B.2.10}$$

The algorithm starts with an initial guess for the solution, X_1, and chooses the residual and the new search direction in the first iteration to be

$$r_1 = p_1 = b - AX_1. \tag{B.2.11}$$

We note that p_1 is nothing but ∇R^2. Thus, the algorithm chooses as a first minimization direction the gradient of the function to be minimized at the position of the first guess. It then minimizes in directions that are conjugate to the previous ones until either it reaches a minimum or the square of the residual R^2 is smaller than ϵ.

B.2.2 Quadratic programming algorithm (QADP)

The nonnegative quadratic programming algorithm used in this work has the peculiarity that it finds solutions, X, satisfying the condition $X \geq 0$. That is, negative masses are not allowed in the solution by construction. We follow the multiplicative updates proposed by Sha et al. [185].
The basic problem we wish to solve is to minimize the quadratic function

$$F(\mathbf{v}) = \frac{1}{2}\mathbf{v}^t \mathbf{A}\mathbf{v} + \mathbf{b}^t \mathbf{v}, \tag{B.2.12}$$

subject to the constraint $v_i \geq 0, \forall i$. In Eq. (B.2.12), the vector $\mathbf{v}$ is the unknown vector $\mathbf{X}$, $\mathbf{A} = \mathbf{\Gamma}^T \mathbf{\Gamma}$ and $\mathbf{b} = \mathbf{\Gamma}^T \mathbf{\Phi}$. We note that the elements of $\mathbf{X}$ are all positive, since the βs can be chosen all positive with respect to an appropriate system of reference. The matrix $\mathbf{A}$ can be decomposed into its positive and negative parts: $\mathbf{A} = \mathbf{A}^+ - \mathbf{A}^-$, where $A_{ij}^+ = A_{ij}$ if $A_{ij} > 0$ and 0 otherwise and $A_{ij}^- = -A_{ij}$ if $A_{ij} < 0$ and 0 otherwise (*nonnegative* matrices). The solution is iteratively updated by the rule

$$v_{k+1,i} = v_{k,i} \delta_i, \tag{B.2.13}$$

where the updat**ing** term is defined as

$$\delta_i = \frac{-b_i + \sqrt{b_i^2 + 4(\mathbf{A}^+\mathbf{v})_i(\mathbf{A}^-\mathbf{v})_i}}{2(\mathbf{A}^+\mathbf{v})_i}. \tag{B.2.14}$$

It is easy to see that generic quadratic programming problems have a single unique minimum. We denote as $\mathbf{v}^*$ this global minimum of $F(v)$. We attempt to prove that convergence of the iteration Eq. (B.2.14) corresponds to this minimum $\mathbf{v}^*$. At this point, one of two conditions must apply for each component v_i^*: either (i) $v_i^* > 0$ and $\partial F/\partial v_i(v_i^*) = 0$ or (ii) $v_i^* = 0$ and $\partial F/\partial v_i(v_i^*) \geq 0$. Now since

$$\frac{\partial F}{\mathbf{v}^*} = (\mathbf{A}^+\mathbf{v})_i - (\mathbf{A}^-\mathbf{v})_i + b_i, \tag{B.2.15}$$

the multiplicative updates in both cases (i) and (ii) take the value $\delta_i = 1$, where the minimum is a fixed point. Conversely, a fixed point of the iteration must be the minimum $\mathbf{v}^*$.

References

[1] P. J. E. Peebles. Principles of Physical Cosmology. In Peebles, P. J. E., editor, *Principles of Physical Cosmology by P.J.E. Peebles. Princeton University Press, 1993. ISBN: 978-0-691-01933-8*. 1993.

[2] J. A. Peacock. Large-scale surveys and cosmic structure. *ArXiv Astrophysics e-prints*, September 2003.

[3] T. Padmanabhan. Theoretical Astrophysics - Volume 1, Astrophysical Processes. In Padmanabhan, T., editor, *Theoretical Astrophysics - Volume 1, Astrophysical Processes, by T. Padmanabhan, pp. 622. Cambridge University Press, December 2000. ISBN-10: 0521562406. ISBN-13: 9780521562409. LCCN: QB461 .P33 2000*. December 2000. doi: 10.2277/0521562406.

[4] T. Padmanabhan. Theoretical Astrophysics - Volume 3, Galaxies and Cosmology. In Padmanabhan, T., editor, *Theoretical Astrophysics - Volume 3, Galaxies and Cosmology, by T. Padmanabhan, pp. 638. Cambridge University Press, December 2002. ISBN-10: 0521562422. ISBN-13: 9780521562423*. December 2002. doi: 10.2277/0521562422.

[5] David W. Hogg. Distance measures in cosmology, 1999. URL `http://www.citebase.org/abstract?id=oai:arXiv.org:astro-ph/9905116`.

[6] A. Ferrara and B. Ciardi. Enlightening the cosmic dark ages. In F. Melchiorri & Y. Rephaeli, editor, *Background Microwave Radiation and Intracluster Cosmology*, pages 253–+, 2005.

[7] C.V.L. Charlier. *Arkiv. för Mat. Astron. Fys.*, 16:1, 1922.

[8] E. P. Hubble. Extragalactic nebulae. *ApJ*, 64:321–369, December 1926. doi: 10.1086/143018.

[9] D. Larson, J. Dunkley, G. Hinshaw, E. Komatsu, M. R. Nolta, C. L. Bennett, B. Gold, M. Halpern, R. S. Hill, N. Jarosik, A. Kogut, M. Limon, S. S. Meyer, N. Odegard, L. Page, K. M. Smith, D. N. Spergel, G. S. Tucker, J. L. Weiland, E. Wollack, and E. L. Wright. Seven-year Wilkinson Microwave Anisotropy Probe (WMAP) Observations: Power Spectra and WMAP-derived Parameters. *ApJS*, 192:16–+, February 2011. doi: 10.1088/0067-0049/192/2/16.

[10] S. Weinberg. Gravitation and Cosmology: Principles and Applications of the General Theory of Relativity. In Weinberg, S., editor, *Gravitation and Cosmology: Principles and Applications of the General Theory of Relativity, by Steven Weinberg, pp. 688. ISBN 0-471-92567-5. Wiley-VCH , July 1972.* July 1972.

[11] Y. B. Zel'Dovich. Gravitational instability: An approximate theory for large density perturbations. *A&A*, 5:84–89, March 1970.

[12] J. C. Mather, E. S. Cheng, R. E. Eplee, Jr., R. B. Isaacman, S. S. Meyer, R. A. Shafer, R. Weiss, E. L. Wright, C. L. Bennett, N. W. Boggess, E. Dwek, S. Gulkis, M. G. Hauser, M. Janssen, T. Kelsall, P. M. Lubin, S. H. Moseley, Jr., T. L. Murdock, R. F. Silverberg, G. F. Smoot, and D. T. Wilkinson. A preliminary measurement of the cosmic microwave background spectrum by the Cosmic Background Explorer (COBE) satellite. *ApJ*, 354: L37–L40, May 1990. doi: 10.1086/185717.

[13] Y. B. Zel'Dovich, V. G. Kurt, and R. A. Syunyaev. Recombination of Hydrogen in the Hot Model of the Universe. *Soviet Journal of Experimental and Theoretical Physics*, 28:146–+, January 1969.

[14] S. Lepp and J. M. Shull. Molecules in the early universe. *ApJ*, 280:465–469, May 1984. doi: 10.1086/162013.

[15] J. Bernstein, L. S. Brown, and G. Feinberg. Cosmological helium production simplified. *Reviews of Modern Physics*, 61:25–39, January 1989. doi: 10.1103/RevModPhys.61.25.

[16] G. Steigman. Primordial Nucleosynthesis in the Precision Cosmology Era. *Annual Review of Nuclear and Particle Science*, 57:463–491, November 2007. doi: 10.1146/annurev.nucl.56.080805.140437.

[17] F. Zwicky. Die Rotverschiebung von extragalaktischen Nebeln. *Helvetica Physica Acta*, 6:110–127, 1933.

[18] S. Smith. The Mass of the Virgo Cluster. *ApJ*, 83:23–+, January 1936. doi: 10.1086/143697.

[19] J. R. Gott, III, D. N. Schramm, B. M. Tinsley, and J. E. Gunn. An unbound universe. *ApJ*, 194:543–553, December 1974. doi: 10.1086/153273.

[20] R. D. Peccei and H. R. Quinn. CP conservation in the presence of pseudoparticles. *Physical Review Letters*, 38:1440–1443, June 1977. doi: 10.1103/PhysRevLett.38.1440.

[21] L. D. Duffy and K. van Bibber. Axions as dark matter particles. *New Journal of Physics*, 11(10):105008–+, October 2009. doi: 10.1088/1367-2630/11/10/105008.

[22] T. S. van Albada, J. N. Bahcall, K. Begeman, and R. Sancisi. Distribution of dark matter in the spiral galaxy NGC 3198. *ApJ*, 295:305–313, August 1985. doi: 10.1086/163375.

[23] M. Milgrom. A modification of the Newtonian dynamics as a possible alternative to the hidden mass hypothesis. *ApJ*, 270:365–370, July 1983. doi: 10.1086/161130.

[24] M. Milgrom. A modification of the Newtonian dynamics - Implications for galaxies. *ApJ*, 270:371–389, July 1983. doi: 10.1086/161131.

[25] M. Milgrom. A Modification of the Newtonian Dynamics - Implications for Galaxy Systems. *ApJ*, 270:384–+, July 1983. doi: 10.1086/161132.

[26] C. Sivaram. Some aspects of MOND and its consequences for cosmology. *Ap&SS*, 215:185–189, May 1994. doi: 10.1007/BF00660076.

[27] J. W. Moffat. Scalar tensor vector gravity theory. *JCAP*, 3:4–+, March 2006. doi: 10.1088/1475-7516/2006/03/004.

[28] W. Tucker, P. Blanco, S. Rappoport, L. David, D. Fabricant, E. E. Falco, W. Forman, A. Dressler, and M. Ramella. 1E 0657-56: A Contender for the Hottest Known Cluster of Galaxies. *ApJ*, 496:L5+, March 1998. doi: 10.1086/311234.

[29] D. Clowe, M. Bradač, A. H. Gonzalez, M. Markevitch, S. W. Randall, C. Jones, and D. Zaritsky. A Direct Empirical Proof of the Existence of Dark Matter. *ApJ*, 648:L109–L113, September 2006. doi: 10.1086/508162.

[30] J. E. Forero-Romero, S. Gottlöber, and G. Yepes. Bullet Clusters in the MARENOSTRUM Universe. *ApJ*, 725:598–604, December 2010. doi: 10.1088/0004-637X/725/1/598.

[31] M. J. Jee et al. Discovery of a Ringlike Dark Matter Structure in the Core of the Galaxy Cluster Cl 0024+17. *ApJ*, 661:728–749, June 2007. doi: 10.1086/517498.

[32] J. R. Brownstein and J. W. Moffat. The Bullet Cluster 1E0657-558 evidence shows modified gravity in the absence of dark matter. *MNRAS*, 382:29–47, November 2007. doi: 10.1111/j.1365-2966.2007.12275.x.

[33] P. J. E. Peebles. Large-scale background temperature and mass fluctuations due to scale-invariant primeval perturbations. *ApJ*, 263:L1–L5, December 1982. doi: 10.1086/183911.

[34] J. M. Bardeen, J. R. Bond, N. Kaiser, and A. S. Szalay. The statistics of peaks of Gaussian random fields. *ApJ*, 304:15–61, May 1986. doi: 10.1086/164143.

[35] M. Tegmark, M. A. Strauss, M. R. Blanton, K. Abazajian, S. Dodelson, H. Sandvik, X. Wang, D. H. Weinberg, I. Zehavi, N. A. Bahcall, F. Hoyle, D. Schlegel, R. Scoccimarro, M. S. Vogeley, A. Berlind, T. Budavari, A. Connolly, D. J. Eisenstein, D. Finkbeiner, J. A. Frieman, J. E. Gunn, L. Hui, B. Jain, D. Johnston, S. Kent, H. Lin, R. Nakajima, R. C. Nichol, J. P. Ostriker, A. Pope, R. Scranton, U. Seljak, R. K. Sheth, A. Stebbins, A. S. Szalay, I. Szapudi, Y. Xu, J. Annis, J. Brinkmann, S. Burles, F. J. Castander, I. Csabai, J. Loveday, M. Doi, M. Fukugita, B. Gillespie, G. Hennessy, D. W. Hogg, Ž. Ivezić, G. R. Knapp, D. Q. Lamb, B. C. Lee, R. H. Lupton, T. A. McKay, P. Kunszt, J. A. Munn, L. O'Connell, J. Peoples, J. R. Pier, M. Richmond, C. Rockosi, D. P. Schneider, C. Stoughton, D. L. Tucker, D. E. vanden Berk, B. Yanny, and D. G. York. Cosmological parameters from SDSS and WMAP. *Phys. Rev. D*, 69(10):103501–+, May 2004. doi: 10.1103/PhysRevD.69.103501.

[36] J. Silk. Cosmic Black-Body Radiation and Galaxy Formation. *ApJ*, 151: 459–+, February 1968. doi: 10.1086/149449.

[37] W. H. Press and P. Schechter. Formation of Galaxies and Clusters of Galaxies by Self-Similar Gravitational Condensation. *ApJ*, 187:425–438, February 1974. doi: 10.1086/152650.

[38] R. K. Sheth and G. Tormen. Large-scale bias and the peak background split. *MNRAS*, 308:119–126, September 1999. doi: 10.1046/j.1365-8711.1999.02692.x.

[39] B. Mathiesen and A. E. Evrard. Constraints on Omega_0 and cluster evolution using the ROSAT log N-log S relation. *MNRAS*, 295:769–780, April 1998. doi: 10.1046/j.1365-8711.1998.01217.x.

[40] V. Springel. The cosmological simulation code GADGET-2. *MNRAS*, 364: 1105–1134, December 2005. doi: 10.1111/j.1365-2966.2005.09655.x.

[41] J. J. Monaghan and J. C. Lattanzio. A refined particle method for astrophysical problems. *A&A*, 149:135–143, August 1985.

[42] R. A. Gingold and J. J. Monaghan. Kernel estimates as a basis for general particle methods in hydrodynamics. *Journal of Computational Physics*, 46: 429–453, June 1982. doi: 10.1016/0021-9991(82)90025-0.

[43] D. S. Balsara. von Neumann stability analysis of smooth particle hydrodynamics–suggestions for optimal algorithms. *Journal of Computational Physics*, 121:357–372, 1995. doi: 10.1016/S0021-9991(95)90221-X.

[44] T. Quinn, N. Katz, J. Stadel, and G. Lake. Time stepping N-body simulations. *ArXiv Astrophysics e-prints*, October 1997.

[45] S. Borgani and A. Kravtsov. Cosmological simulations of galaxy clusters. *ArXiv e-prints*, June 2009.

[46] D. E. Osterbrock. Astrophysics of gaseous nebulae and active galactic nuclei. In Osterbrock, D. E., editor, *Research supported by the University of California, John Simon Guggenheim Memorial Foundation, University of Minnesota, et al. Mill Valley, CA, University Science Books, 1989, 422 p.* 1989.

[47] N. Y. Gnedin. Cosmological Reionization by Stellar Sources. *ApJ*, 535: 530–554, June 2000. doi: 10.1086/308876.

[48] I. T. Iliev, G. Mellema, U.-L. Pen, H. Merz, P. R. Shapiro, and M. A. Alvarez. Simulating cosmic reionization at large scales - I. The geometry of reionization. *MNRAS*, 369:1625–1638, July 2006. doi: 10.1111/j.1365-2966.2006.10502.x.

[49] H.A. Kramers. *Phil. Mag.*, 46:836, 1923.

[50] J. J. Condon. Radio emission from normal galaxies. *ARA&A*, 30:575–611, 1992. doi: 10.1146/annurev.aa.30.090192.003043.

[51] U. Klein, R. Wielebinski, and H. W. Morsi. Radio continuum observations of M82. *A&A*, 190:41–46, January 1988.

[52] J. E. Carlstrom and P. P. Kronberg. H II regions in M82 - High-resolution millimeter continuum observations. *ApJ*, 366:422–431, January 1991. doi: 10.1086/169576.

[53] P. C. van der Kruit. Observations of core sources in Seyfert and normal galaxies with the Westerbork synthesis radio telescope at 1415 MHz. *A&A*, 15:110–122, November 1971.

[54] A. R. Taylor. The Square Kilometre Array: A Science Overview. In M. P. van Haarlem, editor, *Perspectives on Radio Astronomy: Science with Large Antenna Arrays*, pages 1–1, 2000.

[55] R. Kurz and P. Shaver. The ALMA project. *The Messenger*, 96:7–11, June 1999.

[56] R. Schneider, R. Salvaterra, T. R. Choudhury, A. Ferrara, C. Burigana, and L. A. Popa. Detectable signatures of cosmic radiative feedback. *MNRAS*, 384:1525–1532, March 2008. doi: 10.1111/j.1365-2966.2007.12801.x.

[57] D. Scott and M. J. Rees. The 21-cm line at high redshift: a diagnostic for the origin of large scale structure. *MNRAS*, 247:510–+, December 1990.

[58] J. Miralda-Escude and M. J. Rees. Searching for the Earliest Galaxies Using the Gunn-Peterson Trough and the Ly alpha Emission Line. *ApJ*, 497:21–+, April 1998. doi: 10.1086/305458.

[59] D. Kunth, E. Terlevich, R. Terlevich, and G. Tenorio-Tagle. The Lyman-alpha emission in local Star-Forming Galaxies: Scenario and Connection with Primeval Galaxies. *preprint (astro-ph/9809096)*, September 1998.

[60] S. P. Oh and K. J. Mack. Foregrounds for 21-cm observations of neutral gas at high redshift. *MNRAS*, 346:871–877, December 2003. doi: 10.1111/j.1365-2966.2003.07133.x.

[61] P. Tozzi, P. Madau, A. Meiksin, and M. J. Rees. Radio Signatures of H I at High Redshift: Mapping the End of the "Dark Ages". *ApJ*, 528:597–606, January 2000. doi: 10.1086/308196.

[62] B. Ciardi and P. Madau. Probing beyond the Epoch of Hydrogen Reionization with 21 Centimeter Radiation. *ApJ*, 596:1–8, October 2003. doi: 10.1086/377634.

[63] S. R. Furlanetto, A. Sokasian, and L. Hernquist. Observing the reionization epoch through 21-centimetre radiation. *MNRAS*, 347:187–195, January 2004. doi: 10.1111/j.1365-2966.2004.07187.x.

[64] M. Zaldarriaga, S. R. Furlanetto, and L. Hernquist. 21 Centimeter Fluctuations from Cosmic Gas at High Redshifts. *ApJ*, 608:622–635, June 2004. doi: 10.1086/386327.

[65] C. Burigana, G. de Zotti, and L. Feretti. Sunyaev Zeldovich effects, free free emission, and imprints on the cosmic microwave background. *New Astronomy Reviews*, 48:1107–1117, December 2004. doi: 10.1016/j.newar.2004.09.044.

[66] N. Y. Gnedin and F. Prada. The Damping Wing of the Gunn-Peterson Absorption and Lyα Emitters in the Pre-Reionization Era. *ApJ*, 608:L77–L80, June 2004. doi: 10.1086/422390.

[67] R. A. Sunyaev and I. B. Zeldovich. The velocity of clusters of galaxies relative to the microwave background - The possibility of its measurement. *MNRAS*, 190:413–420, February 1980.

[68] M. G. Santos, A. Cooray, Z. Haiman, L. Knox, and C.-P. Ma. Small-Scale Cosmic Microwave Background Temperature and Polarization Anisotropies Due to Patchy Reionization. *ApJ*, 598:756–766, December 2003. doi: 10.1086/378772.

[69] I. T. Iliev, U.-L. Pen, J. R. Bond, G. Mellema, and P. R. Shapiro. The Kinetic Sunyaev-Zel'dovich Effect from Radiative Transfer Simulations of Patchy Reionization. *ApJ*, 660:933–944, May 2007. doi: 10.1086/513687.

[70] V. Jelić, S. Zaroubi, N. Aghanim, M. Douspis, L. V. E. Koopmans, M. Langer, G. Mellema, H. Tashiro, and R. M. Thomas. A cross-correlation study between the cosmological 21 cm signal and the kinetic Sunyaev-Zel'dovich effect. *MNRAS*, 402:2279–2290, March 2010. doi: 10.1111/j.1365-2966.2009.16086.x.

[71] S. P. Oh. Observational Signatures of the First Luminous Objects. *ApJ*, 527:16–30, December 1999. doi: 10.1086/308077.

[72] J. G. Bartlett and A. Stebbins. Did the universe recombine? *ApJ*, 371:8–13, April 1991. doi: 10.1086/169865.

[73] M. Bersanelli, M. Bensadoun, G. de Amici, S. Levin, M. Limon, G. F. Smoot, and W. Vinje. Absolute measurement of the cosmic microwave background at 2 GHz. *ApJ*, 424:517–529, April 1994. doi: 10.1086/173910.

[74] D. J. Fixsen, A. Kogut, S. Levin, M. Limon, P. Lubin, P. Mirel, M. Seiffert, and E. Wollack. The Temperature of the Cosmic Microwave Background at 10 GHz. *ApJ*, 612:86–95, September 2004. doi: 10.1086/421993.

[75] A. Kogut, D. Fixsen, S. Fixsen, S. Levin, M. Limon, L. Lowe, P. Mirel, M. Seiffert, J. Singal, P. Lubin, and E. Wollack. ARCADE: Absolute radiometer for cosmology, astrophysics, and diffuse emission. *New Astronomy Reviews*, 50:925–931, December 2006. doi: 10.1016/j.newar.2006.09.023.

[76] D. J. Fixsen, A. Kogut, S. Levin, M. Limon, P. Lubin, P. Mirel, M. Seiffert, J. Singal, E. Wollack, T. Villela, and C. A. Wuensche. ARCADE 2 Measurement of the Absolute Sky Brightness at 3-90 GHz. *ApJ*, 734:5–+, June 2011. doi: 10.1088/0004-637X/734/1/5.

[77] M. Seiffert, D. J. Fixsen, A. Kogut, S. M. Levin, M. Limon, P. M. Lubin, P. Mirel, J. Singal, T. Villela, E. Wollack, and C. A. Wuensche. Interpretation of the ARCADE 2 Absolute Sky Brightness Measurement. *ApJ*, 734:6–+, June 2011. doi: 10.1088/0004-637X/734/1/6.

[78] H. N. Sharpe. Heliosheath Synchrotron Radiation As A Possible Source For The Arcade 2 CMB Distortions. *arXiv:astro-ph/0902.0181v1*, February 2009.

[79] Asantha Cooray and Steven Furlanetto. Free-free emission at low radio frequencies. *ApJ*, 606:L5, 2004. URL `http://www.citebase.org/abstract?id=oai:arXiv.org:astro-ph/0402239`.

[80] C. Burigana, G. de Zotti, and L. Danese. Analytical description of spectral distortions of the cosmic microwave background. *A&A*, 303:323, November 1995.

[81] M. Zaldarriaga, L. Hui, and M. Tegmark. Constraints from the Lyα Forest Power Spectrum. *ApJ*, 557:519–526, August 2001. doi: 10.1086/321652.

[82] M. A. Fardal, N. Katz, J. P. Gardner, L. Hernquist, D. H. Weinberg, and R. Davé. Cooling Radiation and the Lyα Luminosity of Forming Galaxies. *ApJ*, 562:605–617, December 2001. doi: 10.1086/323519.

[83] G. B. Rybicki and A. P. Lightman. Radiative processes in astrophysics. In *New York, Wiley-Interscience, 1979. 393 p.* Wiley, 1979.

[84] W. J. Karzas and R. Latter. Electron Radiative Transitions in a Coulomb Field. *ApJS*, 6:167, May 1961. doi: 10.1086/190063.

[85] Y. Ascasibar, G. Yepes, V. Müller, and S. Gottlöber. The radial structure of galaxy groups and clusters. *MNRAS*, 346:731–745, December 2003. doi: 10.1111/j.1365-2966.2003.07116.x.

[86] Y. Ascasibar and J. M. Diego. A phenomenological model of galaxy clusters. *MNRAS*, 383:369–374, January 2008. doi: 10.1111/j.1365-2966.2007.12546.x.

[87] A. Cavaliere and R. Fusco-Femiano. X-rays from hot plasma in clusters of galaxies. *A&A*, 49:137–144, May 1976.

[88] J. M. Diego and S. Majumdar. The hybrid SZ power spectrum: combining cluster counts and SZ fluctuations to probe gas physics. *MNRAS*, 352:993–1004, August 2004. doi: 10.1111/j.1365-2966.2004.07989.x.

[89] A. Finoguenov, T. H. Reiprich, and H. Böhringer. Details of the mass-temperature relation for clusters of galaxies. *A&A*, 368:749–759, March 2001. doi: 10.1051/0004-6361:20010080.

[90] L. Verde, M. Kamionkowski, J. J. Mohr, and A. J. Benson. On galaxy cluster sizes and temperatures. *MNRAS*, 321:L7–L13, February 2001. doi: 10.1046/j.1365-8711.2001.04185.x.

[91] J. M. Diego, E. Martínez-González, J. L. Sanz, L. Cayón, and J. Silk. Constraining our Universe with X-ray and optical cluster data. *MNRAS*, 325: 1533–1545, August 2001. doi: 10.1046/j.1365-8711.2001.04557.x.

[92] A. Loeb. Contribution of Bremsstrahlung Emission from LY alpha Clouds to the Microwave Background Fluctuations. *ApJ*, 459:L5, March 1996. doi: 10.1086/309937.

[93] F. Miniati, A. Ferrara, S. D. M. White, and S. Bianchi. Ultraviolet background radiation from cosmic structure formation. *MNRAS*, 348:964–976, March 2004. doi: 10.1111/j.1365-2966.2004.07416.x.

[94] L. Hernquist and N. Katz. TREESPH - A unification of SPH with the hierarchical tree method. *ApJS*, 70:419–446, June 1989. doi: 10.1086/191344.

[95] M. Crocce, S. Pueblas, and R. Scoccimarro. Transients from initial conditions in cosmological simulations. *MNRAS*, 373:369–381, November 2006. doi: 10.1111/j.1365-2966.2006.11040.x.

[96] A. Refregier and R. Teyssier. Numerical and analytical predictions for the large-scale Sunyaev-Zel'dovich effect. *Phys. Rev. D*, 66(4):043002–+, August 2002. doi: 10.1103/PhysRevD.66.043002.

[97] M. Trenti and M. Stiavelli. Cosmic Variance and Its Effect on the Luminosity Function Determination in Deep High-z Surveys. *ApJ*, 676:767–780, April 2008. doi: 10.1086/528674.

[98] S. R. Knollmann and A. Knebe. AHF: Amiga's Halo Finder. *ApJS*, 182: 608–624, June 2009. doi: 10.1088/0067-0049/182/2/608.

[99] A. J. R. Sanderson, E. O'Sullivan, and T. J. Ponman. A statistically selected Chandra sample of 20 galaxy clusters - II. Gas properties and cool core/non-cool core bimodality. *MNRAS*, 395:764–776, May 2009. doi: 10.1111/j.1365-2966.2009.14613.x.

[100] J. M. Diego and Y. Ascasibar. Looking for the Sunyaev-Zel'dovich effect in the Virgo cluster from WMAP and ROSAT data. *MNRAS*, 389:1805–1814, October 2008. doi: 10.1111/j.1365-2966.2008.13685.x.

[101] J. M. Diego and B. Partridge. The Sunyaev-Zel'dovich effect in Wilkinson Microwave Anisotropy Probe data. *MNRAS*, 402:1179–1194, February 2010. doi: 10.1111/j.1365-2966.2009.15949.x.

[102] Z. Haiman and A. Loeb. Signatures of Stellar Reionization of the Universe. *ApJ*, 483:21–+, July 1997. doi: 10.1086/304238.

[103] K. G. Jansky. Radio Waves from Outside the Solar System. *Nature*, 132: 66–+, July 1933. doi: 10.1038/132066a0.

[104] A. Kogut, D. J. Fixsen, S. M. Levin, M. Limon, P. M. Lubin, P. Mirel, M. Seiffert, J. Singal, T. Villela, E. Wollack, and C. A. Wuensche. ARCADE 2 Observations of Galactic Radio Emission. *ApJ*, 734:4–+, June 2011. doi: 10.1088/0004-637X/734/1/4.

[105] J. Singal, Ł. Stawarz, A. Lawrence, and V. Petrosian. Sources of the radio background considered. *MNRAS*, 409:1172–1182, December 2010. doi: 10.1111/j.1365-2966.2010.17382.x.

[106] M. Gervasi, A. Tartari, M. Zannoni, G. Boella, and G. Sironi. The Contribution of the Unresolved Extragalactic Radio Sources to the Brightness Temperature of the Sky. *ApJ*, 682:223–230, July 2008. doi: 10.1086/588628.

[107] M. Massardi, A. Bonaldi, M. Negrello, S. Ricciardi, A. Raccanelli, and G. de Zotti. A model for the cosmological evolution of low-frequency radio sources. *MNRAS*, 404:532–544, May 2010. doi: 10.1111/j.1365-2966.2010.16305.x.

[108] T. Vernstrom, D. Scott, and J. V. Wall. Contribution to the diffuse radio background from extragalactic radio sources. *MNRAS*, 415:3641–3648, August 2011. doi: 10.1111/j.1365-2966.2011.18990.x.

[109] P. P. Ponente, J. M. Diego, R. K. Sheth, C. Burigana, S. R. Knollmann, and Y. Ascasibar. The cosmological free-free signal from galaxy groups and clusters. *MNRAS*, 410:2353–2362, February 2011. doi: 10.1111/j.1365-2966.2010.17611.x.

[110] D. B. Haarsma and R. B. Partridge. Radio Wavelength Constraints on the Sources of the Far-Infrared Background. *ApJ*, 503:L5+, August 1998. doi: 10.1086/311528.

[111] E. Dwek and M. K. Barker. The Cosmic Radio and Infrared Backgrounds Connection. *ApJ*, 575:7–11, August 2002. doi: 10.1086/341143.

[112] R. J. Ivison, D. M. Alexander, A. D. Biggs, W. N. Brandt, E. L. Chapin, K. E. K. Coppin, M. J. Devlin, M. Dickinson, J. Dunlop, S. Dye, S. A.

Eales, D. T. Frayer, M. Halpern, D. H. Hughes, E. Ibar, A. Kovács, G. Marsden, L. Moncelsi, C. B. Netterfield, E. Pascale, G. Patanchon, D. A. Rafferty, M. Rex, E. Schinnerer, D. Scott, C. Semisch, I. Smail, A. M. Swinbank, M. D. P. Truch, G. S. Tucker, M. P. Viero, F. Walter, A. Weiß, D. V. Wiebe, and Y. Q. Xue. BLAST: the far-infrared/radio correlation in distant galaxies. *MNRAS*, 402:245–258, February 2010. doi: 10.1111/j.1365-2966.2009.15918.x.

[113] R. J. Ivison, B. Magnelli, E. Ibar, P. Andreani, D. Elbaz, B. Altieri, A. Amblard, V. Arumugam, R. Auld, H. Aussel, T. Babbedge, S. Berta, A. Blain, J. Bock, A. Bongiovanni, A. Boselli, V. Buat, D. Burgarella, N. Castro-Rodríguez, A. Cava, J. Cepa, P. Chanial, A. Cimatti, M. Cirasuolo, D. L. Clements, A. Conley, L. Conversi, A. Cooray, E. Daddi, H. Dominguez, C. D. Dowell, E. Dwek, S. Eales, D. Farrah, N. Förster Schreiber, M. Fox, A. Franceschini, W. Gear, R. Genzel, J. Glenn, M. Griffin, C. Gruppioni, M. Halpern, E. Hatziminaoglou, K. Isaak, G. Lagache, L. Levenson, N. Lu, D. Lutz, S. Madden, B. Maffei, G. Magdis, G. Mainetti, R. Maiolino, L. Marchetti, G. E. Morrison, A. M. J. Mortier, H. T. Nguyen, R. Nordon, B. O'Halloran, S. J. Oliver, A. Omont, F. N. Owen, M. J. Page, P. Panuzzo, A. Papageorgiou, C. P. Pearson, I. Pérez-Fournon, A. M. Pérez García, A. Poglitsch, M. Pohlen, P. Popesso, F. Pozzi, J. I. Rawlings, G. Raymond, D. Rigopoulou, L. Riguccini, D. Rizzo, G. Rodighiero, I. G. Roseboom, M. Rowan-Robinson, A. Saintonge, M. Sanchez Portal, P. Santini, B. Schulz, D. Scott, N. Seymour, L. Shao, D. L. Shupe, A. J. Smith, J. A. Stevens, E. Sturm, M. Symeonidis, L. Tacconi, M. Trichas, K. E. Tugwell, M. Vaccari, I. Valtchanov, J. Vieira, L. Vigroux, L. Wang, R. Ward, G. Wright, C. K. Xu, and M. Zemcov. The far-infrared/radio correlation as probed by Herschel. *A&A*, 518:L31+, July 2010. doi: 10.1051/0004-6361/201014552.

[114] M. Michałowski, J. Hjorth, and D. Watson. Cosmic evolution of submillimeter galaxies and their contribution to stellar mass assembly. *A&A*, 514:A67+, May 2010. doi: 10.1051/0004-6361/200913634.

[115] R. H. Rubin. A Discussion of the Sizes and Excitation of H II Regions. *ApJ*, 154:391–+, October 1968. doi: 10.1086/149766.

[116] C. Leitherer and T. M. Heckman. Synthetic properties of starburst galaxies. *ApJS*, 96:9–38, January 1995. doi: 10.1086/192112.

[117] M. Mollá, M. L. García-Vargas, and A. Bressan. PopStar I: evolutionary synthesis model description. *MNRAS*, 398:451–470, September 2009. doi: 10.1111/j.1365-2966.2009.15160.x.

[118] E. E. Salpeter. The Luminosity Function and Stellar Evolution. *ApJ*, 121: 161–+, January 1955. doi: 10.1086/145971.

[119] B. C. Lacki, T. A. Thompson, and E. Quataert. The Physics of the Far-infrared-Radio Correlation. I. Calorimetry, Conspiracy, and Implications. *ApJ*, 717:1–28, July 2010. doi: 10.1088/0004-637X/717/1/1.

[120] B. C. Lacki and T. A. Thompson. The Physics of the Far-infrared-Radio Correlation. II. Synchrotron Emission as a Star Formation Tracer in High-redshift Galaxies. *ApJ*, 717:196–208, July 2010. doi: 10.1088/0004-637X/717/1/196.

[121] E. Ibar, M. Cirasuolo, R. Ivison, P. Best, I. Smail, A. Biggs, C. Simpson, J. Dunlop, O. Almaini, R. McLure, S. Foucaud, and S. Rawlings. Exploring the infrared/radio correlation at high redshift. *MNRAS*, 386:953–962, May 2008. doi: 10.1111/j.1365-2966.2008.13077.x.

[122] M. T. Sargent, E. Schinnerer, E. Murphy, H. Aussel, E. Le Floc'h, D. T. Frayer, A. Martínez-Sansigre, P. Oesch, M. Salvato, V. Smolčić, G. Zamorani, M. Brusa, N. Cappelluti, C. L. Carilli, C. M. Carollo, O. Ilbert, J. Kartaltepe, A. M. Koekemoer, S. J. Lilly, D. B. Sanders, and N. Z. Scoville. The VLA-COSMOS Perspective on the Infrared-Radio Relation. I. New Constraints on Selection Biases and the Non-Evolution of the Infrared/Radio Properties of Star-Forming and Active Galactic Nucleus Galaxies at Intermediate and High Redshift. *ApJS*, 186:341–377, February 2010. doi: 10.1088/0067-0049/186/2/341.

[123] C. Vlahakis, S. Eales, and L. Dunne. The far-infrared-radio relationship at high and low redshift. *MNRAS*, 379:1042–1048, August 2007. doi: 10.1111/j.1365-2966.2007.12007.x.

[124] R. J. Beswick, T. W. B. Muxlow, H. Thrall, A. M. S. Richards, and S. T. Garrington. An evolution of the infrared-radio correlation at very low flux

densities? *MNRAS*, 385:1143–1154, April 2008. doi: 10.1111/j.1365-2966.2008.12931.x.

[125] N. Seymour, M. Huynh, T. Dwelly, M. Symeonidis, A. Hopkins, I. M. McHardy, M. J. Page, and G. Rieke. Investigating the far-IR/radio correlation of star-forming Galaxies to z = 3. *MNRAS*, 398:1573–1581, September 2009. doi: 10.1111/j.1365-2966.2009.15224.x.

[126] E. F. Bell. Estimating Star Formation Rates from Infrared and Radio Luminosities: The Origin of the Radio-Infrared Correlation. *ApJ*, 586:794–813, April 2003. doi: 10.1086/367829.

[127] E. J. Murphy, R.-R. Chary, D. M. Alexander, M. Dickinson, B. Magnelli, G. Morrison, A. Pope, and H. I. Teplitz. Balancing the Energy Budget Between Star Formation and Active Galactic Nuclei in High-Redshift Infrared Luminous Galaxies. *ApJ*, 698:1380–1397, June 2009. doi: 10.1088/0004-637X/698/2/1380.

[128] N. Bourne, L. Dunne, R. J. Ivison, S. J. Maddox, M. Dickinson, and D. T. Frayer. Evolution of the far-infrared-radio correlation and infrared spectral energy distributions of massive galaxies over z= 0-2. *MNRAS*, 410: 1155–1173, January 2011. doi: 10.1111/j.1365-2966.2010.17517.x.

[129] G. Marsden, P. A. R. Ade, J. J. Bock, E. L. Chapin, M. J. Devlin, S. R. Dicker, M. Griffin, J. O. Gundersen, M. Halpern, P. C. Hargrave, D. H. Hughes, J. Klein, P. Mauskopf, B. Magnelli, L. Moncelsi, C. B. Netterfield, H. Ngo, L. Olmi, E. Pascale, G. Patanchon, M. Rex, D. Scott, C. Semisch, N. Thomas, M. D. P. Truch, C. Tucker, G. S. Tucker, M. P. Viero, and D. V. Wiebe. BLAST: Resolving the Cosmic Submillimeter Background. *ApJ*, 707:1729–1739, December 2009. doi: 10.1088/0004-637X/707/2/1729.

[130] E. Pascale, P. A. R. Ade, J. J. Bock, E. L. Chapin, M. J. Devlin, S. Dye, S. A. Eales, M. Griffin, J. O. Gundersen, M. Halpern, P. C. Hargrave, D. H. Hughes, J. Klein, G. Marsden, P. Mauskopf, L. Moncelsi, H. Ngo, C. B. Netterfield, L. Olmi, G. Patanchon, M. Rex, D. Scott, C. Semisch, N. Thomas, M. D. P. Truch, C. Tucker, G. S. Tucker, M. P. Viero, and D. V. Wiebe. BLAST: A Far-Infrared Measurement of the History of Star Formation. *ApJ*, 707:1740–1749, December 2009. doi: 10.1088/0004-637X/707/2/1740.

[131] G. Patanchon, P. A. R. Ade, J. J. Bock, E. L. Chapin, M. J. Devlin, S. R. Dicker, M. Griffin, J. O. Gundersen, M. Halpern, P. C. Hargrave, D. H. Hughes, J. Klein, G. Marsden, P. Mauskopf, L. Moncelsi, C. B. Netterfield, L. Olmi, E. Pascale, M. Rex, D. Scott, C. Semisch, N. Thomas, M. D. P. Truch, C. Tucker, G. S. Tucker, M. P. Viero, and D. V. Wiebe. Submillimeter Number Counts from Statistical Analysis of BLAST Maps. *ApJ*, 707:1750–1765, December 2009. doi: 10.1088/0004-637X/707/2/1750.

[132] A. Kovács, S. C. Chapman, C. D. Dowell, A. W. Blain, R. J. Ivison, I. Smail, and T. G. Phillips. SHARC-2 350 μm Observations of Distant Submillimeter-selected Galaxies. *ApJ*, 650:592–603, October 2006. doi: 10.1086/506341.

[133] E. J. Murphy. The Far-Infrared-Radio Correlation at High Redshifts: Physical Considerations and Prospects for the Square Kilometer Array. *ApJ*, 706:482–496, November 2009. doi: 10.1088/0004-637X/706/1/482.

[134] R. S. Somerville, J. R. Primack, and S. M. Faber. The nature of high-redshift galaxies. *MNRAS*, 320:504–528, February 2001. doi: 10.1046/j.1365-8711.2001.03975.x.

[135] Y. Ascasibar, G. Yepes, S. Gottlöber, and V. Müller. Numerical simulations of the cosmic star formation history. *A&A*, 387:396–405, May 2002. doi: 10.1051/0004-6361:20020303.

[136] A. M. Hopkins. On the Evolution of Star-forming Galaxies. *ApJ*, 615:209–221, November 2004. doi: 10.1086/424032.

[137] A. M. Hopkins and J. F. Beacom. On the Normalization of the Cosmic Star Formation History. *ApJ*, 651:142–154, November 2006. doi: 10.1086/506610.

[138] S. Cole, P. Norberg, C. M. Baugh, C. S. Frenk, J. Bland-Hawthorn, T. Bridges, R. Cannon, M. Colless, C. Collins, W. Couch, N. Cross, G. Dalton, R. De Propris, S. P. Driver, G. Efstathiou, R. S. Ellis, K. Glazebrook, C. Jackson, O. Lahav, I. Lewis, S. Lumsden, S. Maddox, D. Madgwick, J. A. Peacock, B. A. Peterson, W. Sutherland, and K. Taylor. The 2dF galaxy redshift survey: near-infrared galaxy luminosity functions. *MNRAS*, 326:255–273, September 2001. doi: 10.1046/j.1365-8711.2001.04591.x.

[139] Y. Ascasibar. FiEstAS sampling—a Monte Carlo algorithm for multidimensional numerical integration. *Computer Physics Communications*, 179: 881–887, December 2008. doi: 10.1016/j.cpc.2008.07.011.

[140] Y. Ascasibar and J. Binney. Numerical estimation of densities. *MNRAS*, 356:872–882, January 2005. doi: 10.1111/j.1365-2966.2004.08480.x.

[141] Y. Ascasibar. Estimating multidimensional probability fields using the Field Estimator for Arbitrary Spaces (FiEstAS) with applications to astrophysics. *Computer Physics Communications*, 181:1438–1443, August 2010. doi: 10.1016/j.cpc.2010.04.011.

[142] T. Broadhurst, N. Benítez, D. Coe, K. Sharon, K. Zekser, R. White, H. Ford, R. Bouwens, J. Blakeslee, M. Clampin, N. Cross, M. Franx, B. Frye, G. Hartig, G. Illingworth, L. Infante, F. Menanteau, G. Meurer, M. Postman, D. R. Ardila, F. Bartko, R. A. Brown, C. J. Burrows, E. S. Cheng, P. D. Feldman, D. A. Golimowski, T. Goto, C. Gronwall, D. Herranz, B. Holden, N. Homeier, J. E. Krist, M. P. Lesser, A. R. Martel, G. K. Miley, P. Rosati, M. Sirianni, W. B. Sparks, S. Steindling, H. D. Tran, Z. I. Tsvetanov, and W. Zheng. Strong-Lensing Analysis of A1689 from Deep Advanced Camera Images. *ApJ*, 621:53–88, March 2005. doi: 10.1086/426494.

[143] T. Broadhurst, M. Takada, K. Umetsu, X. Kong, N. Arimoto, M. Chiba, and T. Futamase. The Surprisingly Steep Mass Profile of A1689, from a Lensing Analysis of Subaru Images. *ApJ*, 619:L143–L146, February 2005. doi: 10.1086/428122.

[144] P. Saha and L. L. R. Williams. Non-parametric reconstruction of the galaxy lens in PG 1115+080. *MNRAS*, 292:148–+, November 1997.

[145] H. M. Abdelsalam, P. Saha, and L. L. R. Williams. Nonparametric Reconstruction of Abell 2218 from Combined Weak and Strong Lensing. *AJ*, 116:1541–1552, October 1998. doi: 10.1086/300546.

[146] S. L. Bridle, M. P. Hobson, A. N. Lasenby, and R. Saunders. A maximum-entropy method for reconstructing the projected mass distribution of gravitational lenses. *MNRAS*, 299:895–903, September 1998. doi: 10.1046/j.1365-8711.1998.01877.x.

[147] S. Seitz, P. Schneider, and M. Bartelmann. Entropy-regularized

maximum-likelihood cluster mass reconstruction. *A&A*, 337:325–337, September 1998.

[148] J.-P. Kneib, P. Hudelot, R. S. Ellis, T. Treu, G. P. Smith, P. Marshall, O. Czoske, I. Smail, and P. Natarajan. A Wide-Field Hubble Space Telescope Study of the Cluster Cl 0024+1654 at z=0.4. II. The Cluster Mass Distribution. *ApJ*, 598:804–817, December 2003. doi: 10.1086/378633.

[149] J. M. Diego, P. Protopapas, H. B. Sandvik, and M. Tegmark. Non-parametric inversion of strong lensing systems. *MNRAS*, 360:477–491, June 2005a. doi: 10.1111/j.1365-2966.2005.09021.x.

[150] J. M. Diego, H. B. Sandvik, P. Protopapas, M. Tegmark, N. Benítez, and T. Broadhurst. Non-parametric mass reconstruction of A1689 from strong lensing data with the Strong Lensing Analysis Package. *MNRAS*, 362: 1247–1258, October 2005b. doi: 10.1111/j.1365-2966.2005.09372.x.

[151] G. P. Smith, J.-P. Kneib, I. Smail, P. Mazzotta, H. Ebeling, and O. Czoske. A Hubble Space Telescope lensing survey of X-ray luminous galaxy clusters - IV. Mass, structure and thermodynamics of cluster cores at z= 0.2. *MNRAS*, 359:417–446, May 2005. doi: 10.1111/j.1365-2966.2005.08911.x.

[152] M. Bradač, P. Schneider, M. Lombardi, and T. Erben. Strong and weak lensing united. *A&A*, 437:39–48, July 2005. doi: 10.1051/0004-6361: 20042233.

[153] A. Halkola, S. Seitz, and M. Pannella. Parametric strong gravitational lensing analysis of Abell 1689. *MNRAS*, 372:1425–1462, November 2006. doi: 10.1111/j.1365-2966.2006.10948.x.

[154] M. Cacciato, M. Bartelmann, M. Meneghetti, and L. Moscardini. Combining weak and strong lensing in cluster potential reconstruction. *A&A*, 458:349–356, November 2006. doi: 10.1051/0004-6361:20054582.

[155] H. M. Abdelsalam, P. Saha, and L. L. R. Williams. Nonparametric Reconstruction of Abell 2218 from Combined Weak and Strong Lensing. *AJ*, 116:1541–1552, October 1998. doi: 10.1086/300546.

[156] P. Saha, L. L. R. Williams, and H. AbdelSalam. Cluster Reconstruction from Combined Strong and Weak Lensing. *ArXiv: astro-ph/9909249*, September 1999.

[157] J. M. Diego, M. Tegmark, P. Protopapas, and H. B. Sandvik. Combined reconstruction of weak and strong lensing data with WSLAP. *MNRAS*, 375:958–970, March 2007. doi: 10.1111/j.1365-2966.2007.11380.x.

[158] S. Wallington, C. S. Kochanek, and R. Narayan. Lens Inversion of the Giant Cluster Arc CL0024+1654. In *Bulletin of the American Astronomical Society*, volume 24 of *Bulletin of the American Astronomical Society*, page 1192, September 1992.

[159] I. Smail, A. Dressler, J.-P. Kneib, R. S. Ellis, W. J. Couch, R. M. Sharples, and A. Oemler, Jr. Hubble Space Telescope Observations of Giant Arcs: High-Resolution Imaging of Distant Field Galaxies. *ApJ*, 469:508–+, October 1996. doi: 10.1086/177799.

[160] T. Broadhurst, X. Huang, B. Frye, and R. Ellis. A Spectroscopic Redshift for the Cl 0024+16 Multiple Arc System: Implications for the Central Mass Distribution. *ApJ*, 534:L15–L18, May 2000. doi: 10.1086/312651.

[161] W. N. Colley, J. A. Tyson, and E. L. Turner. Unlensing Multiple Arcs in 0024+1654: Reconstruction of the Source Image. *ApJ*, 461:L83+, April 1996. doi: 10.1086/310015.

[162] J. A. Tyson, G. P. Kochanski, and I. P. dell'Antonio. Detailed Mass Map of CL 0024+1654 from Strong Lensing. *ApJ*, 498:L107+, May 1998. doi: 10.1086/311314.

[163] J. M. Comerford, M. Meneghetti, M. Bartelmann, and M. Schirmer. Mass Distributions of Hubble Space Telescope Galaxy Clusters from Gravitational Arcs. *ApJ*, 642:39–47, May 2006. doi: 10.1086/500824.

[164] N. Ota, E. Pointecouteau, M. Hattori, and K. Mitsuda. Chandra Analysis and Mass Estimation of the Lensing Cluster of Galaxies Cl 0024+17. *ApJ*, 601:120–132, January 2004. doi: 10.1086/380438.

[165] Y.-Y. Zhang, H. Böhringer, Y. Mellier, G. Soucail, and W. Forman. XMM-Newton study of the lensing cluster of galaxies CL 0024+17. *A&A*, 429: 85–99, January 2005. doi: 10.1051/0004-6361:20041296.

[166] O. Czoske, J.-P. Kneib, G. Soucail, T. J. Bridges, Y. Mellier, and J.-C. Cuillandre. A wide-field spectroscopic survey of the cluster of galaxies <ASTROBJ>Cl0024+1654</ASTROBJ>. I. The catalogue. *A&A*, 372:391–405, June 2001. doi: 10.1051/0004-6361:20010398.

[167] M. Milgrom and R. H. Sanders. Rings and Shells of "Dark Matter" as MOND Artifacts. *ApJ*, 678:131–143, May 2008. doi: 10.1086/529119.

[168] B. Qin, H.-Y. Shan, and A. Tilquin. Galaxy Distribution as a Probe of the Ringlike Dark Matter Structure in the Galaxy Cluster Cl 0024+17. *ApJ*, 679:L81–L83, June 2008. doi: 10.1086/589328.

[169] J. A. Zu Hone, D. Q. Lamb, and P. M. Ricker. Rings of Dark Matter in Collisions Between Clusters of Galaxies. *ApJ*, 696:694–700, May 2009. doi: 10.1088/0004-637X/696/1/694.

[170] A. Zitrin, T. Broadhurst, K. Umetsu, D. Coe, N. Benítez, B. Ascaso, L. Bradley, H. Ford, J. Jee, E. Medezinski, Y. Rephaeli, and W. Zheng. New multiply-lensed galaxies identified in ACS/NIC3 observations of Cl0024+1654 using an improved mass model. *MNRAS*, 396:1985–2002, July 2009. doi: 10.1111/j.1365-2966.2009.14899.x.

[171] K. Umetsu, E. Medezinski, T. Broadhurst, A. Zitrin, N. Okabe, B.-C. Hsieh, and S. M. Molnar. The Mass Structure of the Galaxy Cluster Cl0024+1654 from a Full Lensing Analysis of Joint Subaru and ACS/NIC3 Observations. *ApJ*, 714:1470–1496, May 2010. doi: 10.1088/0004-637X/714/2/1470.

[172] J. F. Navarro, C. S. Frenk, and S. D. M. White. The Structure of Cold Dark Matter Halos. *ApJ*, 462:563–+, May 1996. doi: 10.1086/177173.

[173] K. Umetsu, T. Broadhurst, A. Zitrin, E. Medezinski, and L.-Y. Hsu. Cluster Mass Profiles from a Bayesian Analysis of Weak-lensing Distortion and Magnification Measurements: Applications to Subaru Data. *ApJ*, 729:127–+, March 2011. doi: 10.1088/0004-637X/729/2/127.

[174] H. Hoekstra, J. Hartlap, S. Hilbert, and E. van Uitert. Effects of distant large-scale structure on the precision of weak lensing mass measurements. *MNRAS*, 412:2095–2103, April 2011. doi: 10.1111/j.1365-2966.2010.18053.x.

[175] C. L. Carilli and M. S. Yun. The Radio-to-Submillimeter Spectral Index as a Redshift Indicator. *ApJ*, 513:L13–L16, March 1999. doi: 10.1086/311909.

[176] C. L. Carilli, N. Lee, P. Capak, E. Schinnerer, K.-S. Lee, H. McCraken, M. S. Yun, N. Scoville, V. Smolčić, M. Giavalisco, A. Datta, Y. Taniguchi,

and C. M. Urry. Star Formation Rates in Lyman Break Galaxies: Radio Stacking of LBGs in the COSMOS Field and the Sub-μJy Radio Source Population. *ApJ*, 689:883–888, December 2008. doi: 10.1086/592319.

[177] C. G. T. Haslam, C. J. Salter, H. Stoffel, and W. E. Wilson. A 408 MHz all-sky continuum survey. II - The atlas of contour maps. *A&AS*, 47:1–+, January 1982.

[178] A. de Oliveira-Costa, M. Tegmark, B. M. Gaensler, J. Jonas, T. L. Landecker, and P. Reich. A model of diffuse Galactic radio emission from 10 MHz to 100 GHz. *MNRAS*, 388:247–260, July 2008. doi: 10.1111/j.1365-2966.2008.13376.x.

[179] A. E. E. Rogers and J. D. Bowman. Spectral Index of the Diffuse Radio Background Measured from 100 TO 200 MHz. *AJ*, 136:641–648, August 2008. doi: 10.1088/0004-6256/136/2/641.

[180] J. Tinker, A. V. Kravtsov, A. Klypin, K. Abazajian, M. Warren, G. Yepes, S. Gottlöber, and D. E. Holz. Toward a Halo Mass Function for Precision Cosmology: The Limits of Universality. *ApJ*, 688:709–728, December 2008. doi: 10.1086/591439.

[181] P. J. E. Peebles. The large-scale structure of the universe. In *Research supported by the National Science Foundation. Princeton, N.J., Princeton University Press, 1980. 435 p.* Princeton University Press, 1980.

[182] Dunkley, J. et al. Five-Year Wilkinson Microwave Anisotropy Probe Observations: Likelihoods and Parameters from the WMAP Data. *ApJS*, 180:306–329, February 2009. doi: 10.1088/0067-0049/180/2/306.

[183] D. J. Eisenstein and W. Hu. Baryonic Features in the Matter Transfer Function. *ApJ*, 496:605, March 1998. doi: 10.1086/305424.

[184] W. H. Press, S. A. Teukolsky, W. T. Vetterling, and B. P. Flannery. Numerical Recipes in Fortran 77. In *Numerical Recipes in Fortran 77, by Press, W. H. and Teukolsky and S. A. and Vetterling and W. T. and Flannery and B. P, pp. 992. Cambridge University Press. ISBN-10: 052143064X. ISBN-13: 978-0521430647*. 1997.

[185] Fei Sha, Lawrence K. Saul, and Daniel D. Lee. Multiplicative updates for nonnegative quadratic programming in support vector machines. In *Ad-*

vances in Neural Information Processing Systems 15, pages 1041–1048. MIT Press, 2002.